FABRICATION OF PEROVSKITE & DYE SENSITIZED SOLAR CELLS AND THEIR PARAMETRIC OPTIMIZATION

BY

MUHAMMAD YOUNAS

A Dissertation Presented to the

DEANSHIP OF GRADUATE STUDIES

KING FAHD UNIVERSITY OF PETROLEUM & MINERALS

DHAHRAN, SAUDI ARABIA

In Partial Fulfillment of the
Requirements for the Degree of

DOCTOR OF PHILOSOPHY

In

PHYSICS

April 2019

KING FAHD UNIVERSITY OF PETROLEUM & MINERALS

DHAHRAN- 31261, SAUDI ARABIA

DEANSHIP OF GRADUATE STUDIES

This thesis, written by **Muhammad Younas** under the direction of his thesis advisor and approved by his thesis committee, has been presented and accepted by the Dean of Graduate Studies, in partial fulfillment of the requirements for the degree of **DOCTOR OF PHILOSOPHY IN PHYSICS.**

Dr. Mohammad Ashraf Gondal
(Advisor)

Dr. Abdulaziz Husain M. Al-Aswad

Department Chairman

Dr. Khalil Harrabi
(Co-Advisor)

Dr. Salam A. Zummo
Dean of Graduate Studies

Dr. Zain Hassan Abdullah Yamani
(Member)

15/10/19

Date

Dr. Fahad A. Al-Sulaiman

(Member)

Dr. Osman M. Bakr

(Member)

DEDICATED TO MY PARENTS, FAMILY AND RESPECTFUL TEACHERS

ACKNOWLEDGMENTS

First of all, I want to thank ALMIGHTY ALLAH, the greatest, who gave me strength to carry on this project, all the praises for Him who guides us to the right path, the Merciful, the Beneficent. Prodigious esteem for the greatest leader of the world, the messenger of ALMIGHTY ALLAH, our Holy Prophet Hazrat Muhammad (PBUH); the benefactor of humanity.

I am greatly thankful to Department of Physics and Center of Research Excellence in Nanotechnology (CENT) of King Fahd University of Petroleum and Minerals (KFUPM), Kingdom of Saudi Arabia for giving me this opportunity to pursue my Ph.D.

I would like to express my gratitude and deepest regards to my thesis advisor Prof. Mohammad Ashraf Gondal for his scholarly guidance, sincere dedication, and utmost efforts to bring this work to complete in perfect manner. His phenomenal personality, dedication, passion and professionalism in his work gave me all the moral and technical support to complete my work. I would like to gratefully thank my committee members: Prof. Khalil Harrabi (my thesis co-advisor), Prof. Zain Hassan Abdullah Yamani, Dr. Fahad Al-Sulaiman and Dr. Osman M. Bakr (KAUST) for their valuable suggestions, technical and moral support at every stage of my Ph.D. I would like to pay special thanks to Dr. Amir Al-Ahmed for his help in my experimental work, characterization and discussions. I would also like to thank to Mr. Ayan A. Zhumekenov (KAUST) for his helpful discussions and suggestions for perovskite single crystals work. I would like to thank my Laser Research Group fellows, as well as Syed Amanullah from Chemical Engineering department and colleagues at CENT for their continuous support. Special

thanks to Dr. Muhammad Usman Iftikhar from Pakistan Space and Upper Atmosphere Research Commission (SUPARCO) for his beneficial guidance during my Ph.D. I want to acknowledge and thank the Center of Research Excellence in Nanotechnology (CENT) and Center of Research Excellence in Renewable Energy (CoRE-RE) at KFUPM for providing me the characterization facility to carry on my research.

Finally, I would like to thank my parents, wife, children, brother, sisters, teachers and friends for their support and prayers for my success.

TABLE OF CONTENTS

LIST OF TABLES

LIST OF FIGURES

LIST OF ABBREVIATIONS

DSSC	Dye Sensitized Solar Cell
UV-Vis	Ultraviolet Visible Spectroscopy
IV	Current Voltage
EIS	Electrochemical Impedance Spectroscopy
CE	Counter Electrode
I^-/I^{3-}	iodide/triiodide
mM	millimole
FTO	Fluorine doped tin oxide (SnO_2: F)
TiO_2	Titanium dioxide
WO3	Tungsten oxide
MWCNT	Multiwall carbon nanotube
CB	Conduction band
HOMO	Highest Occupied Molecular Orbital
LUMO	Lowest Unoccupied Molecular Orbital
PCE	Power Conversion Efficiency
J_{sc}	Current density
V_{oc}	Open circuit voltage
FF	Fill Factor
η	Efficiency
MAI	Methyl ammonium Iodide

BAI	Butyl ammonium Iodide
PAI	Propyl ammonium Iodide
MABr	Methyl ammonium Bromide
PbI_2	Lead Iodide
$PbBr_2$	Lead Bromide
GBL	gamma-Butyrolactone
DMF	Dimethylformamide
DMSO	Dimethyl sulfoxide
PEDOT:PSS	Poly(3,4-ethylenedioxythiophene) polystyrene sulfonate
PTAA	Poly[bis(4-phenyl) (2,4,6-trimethylphenyl) amine Poly(triarylamine)
PCBM	Phenyl-C61-butyric acid methyl ester
SEM	Scanning Electron Microscopy
EDX	Energy dispersive X-ray spectroscopy

ABSTRACT

Full Name : Muhammad Younas

Thesis Title : Fabrication of perovskite & dye sensitized solar cells and their parametric optimization

Major Field : Physics

Date of Degree : April 2019

Energy plays an important role in modernization, automation and economic growth of any country and society at large. It is predicted that by 2050, the energy consumption will rise to 23 terawatts from the current figure of 13 terawatt. Nearly 80% of the world energy requirement is catered by rapidly depleting fossil fuels, the excessive use of which triggers geological imbalances and environmental impairment due to the disposal of huge amounts of greenhouse gases in the fragile atmosphere. Escalating energy demands and ecological issues have encouraged researchers to focus on clean and eco-friendly energy sources. Solar energy enjoys the fact that it is easily attainable, most wide and approachable source of renewable energy on our planet. At present, the available photovoltaic cells are not cost effective nor very efficient. DSSCs and perovskite solar cells are third generation solar cells which is quite new version of photovoltaic devices. These emerging photovoltaics have various advantages over their silicon-based counterparts. In this thesis we focus on the most important parameters of photovoltaics i.e. reduction of cost, improvement of efficiency, and stability. We used novel co-sensitization and cost-effective approaches to enhance the efficiency by collecting the photogenerated electron to the external circuit. We used tungsten oxide (WO_3) and multiwall carbon nanotubes (MWCNT) with titanium dioxide (TiO_2) as a nanocomposite for the photoanode to reduce the recombination of

charges. Additionally, we used cost-effective MWCNT to replace expensive platinum (Pt) at counter electrode. By using these strategies, we reduced cost and improved different parameters for enhancement of efficiency. Furthermore, we used abundant and cost-effective perovskite materials to grow single crystals by using inverse temperature crystallization technique (ITC). We used a novel approach by mixing of 2D/3D perovskite materials and subsequently growth of single crystals using the ITC technique. We used the ITC technique concept to the carbon-based printed perovskite solar cells to grow larger crystals for improvement of efficiency. The carbon-based printed perovskite solar cells were fabricated using conventional way (poly crystalline) to fabricate solar cells and larger crystals using ITC techniques to confirm the improvement in the performance of the solar cells.

The key findings of this thesis research include the effectiveness of co-sensitization technique to enhance the efficiency of the DSSCs. The use of MWCNTs in photoanode enhance the efficiency of DSSCs due to reduction of recombination of charges. It is also found that MWCNTs can be used as counter electrode in DSSC due to its great stability and catalytic activity. The stability and catalytic activity of MWCNT measured and compared with conventional Pt counter electrodes. The key advantage of using MWCNT to replace conventional Pt in counter electrode is its cost which is much less than noble metal i.e. Pt. Furthermore, it is also found that 2D/3D mixed perovskite are more stable than 3D perovskite materials only.

Key words: Dye sensitized solar cells (DSSCs), Perovskite solar cells (PSC), Efficiency, Renewable energy, single crystal.

ملخص الرسالة

الاسم الكامل: محمد يونس

عنوان الرسالة: تصنيع الخلايا الشمسية perovskite والصباغة توعيتهم والأمثل parametric بهم

التخصص: علوم فيزيائية

تاريخ الدرجة العلمية: أبريل 2019

تلعب الطاقة دورًا مهمًا في التحديث والأتمتة والنمو الاقتصادي لأي بلد والمجتمع ككل. ومن المتوقع أنه بحلول عام 2050 ، سيرتفع استهلاك الطاقة إلى 23 تيرا واط من الرقم الحالي 13 تيراواط. يتم تلبية ما يقرب من 80٪ من احتياجات الطاقة العالمية من الوقود الأحفوري المستنفذ بسرعة ، ويؤدي الاستخدام المفرط له إلى اختلالات جيولوجية وضعف بيئي بسبب التخلص من كمية هائلة من غازات الدفيئة في الغلاف الجوي الهش. وقد شجع تصاعد الطلب على الطاقة والقضايا البيئية الباحثين على التركيز على مصادر الطاقة الجديدة النظيفة والصديقة للبيئة .تمتاز الطاقة الشمسية بحقيقة أنه يمكن الوصول إلى مصدر طاقة متجددعلى نطاق واسع ، وهو أوسع مصدر للطاقة المتجددة على كوكبنا. إن الخلايا الكهروضوئية المتوفرة ليست فعالة من حيث التكلفة أو أنها ليست ذات فعالية كبيرة DSSCs .والخلايا الشمسية perovskiteهي الجيل الثالث من الخلايا الشمسية وهو نسخة جديدة تماما من الأجهزة الضوئية. هذه الخلايا الكهروضوئية الناشئة لها مزايا مختلفة على نظائرها القائمة على السيليكون. في هذه الرسالة ، نركز على أهم ميزات الخلايا الكهروضوئية ، أي خفض التكلفة وتعزيز الكفاءة. استخدمنا أساليب جديدة للتوعية المشتركة وفعالة من حيث التكلفة لتعزيز الفعالية من خلال جمع الإلكترونات المزججة إلى الدائرة الخارجية. استخدمنا أكسيد التنغستن (WO3)والأنابيب النانوية الكربونية متعددة الجدران (MWCNT)مع ثاني أكسيد التيتانيوم (TiO2)كمركب نانوي لتصنيع الخيط الضوئي للحد من إعادة تجميع الرسوم. وعلاوة على ذلك ، استخدمنا MWCNTفعالة من حيث التكلفة لاستبدال البلاتين باهظة الثمن (حزب العمال). باستخدام هذه الاستراتيجيات ، قمنا بتخفيض التكلفة وتحسين البارامترات المختلفة لتعزيز الكفاءة. وعلاوة على ذلك ، استخدمنا مواد perovskiteوفيرة وفعالة من حيث التكلفة من أجل زراعة بلورات مفردة وتصنيع الخلايا الشمسية. استخدمنا نهجا جديدا من بلورات ثنائية متزايدة ثنائية / ثنائية البيروفسكايت لتعزيز الاستقرار وكذلك الكفاءة. بالإضافة إلى ذلك ، يتم تصنيع خلايا بيروفسكايت الشمسية المطبوعة المعتمدة على الكربون باستخدام تقنية تبلور درجة الحرارة العكسية

(ITC) ويتم مقارنة كفاءة كلا النوعين من خلايا بيروفسكايت الشمسية. معظم نتائج هذه الأطروحة منشورة أو قيد المراجعة.

النتائج الرئيسية لهذا البحث تتضمن أطروحة فعالية تقنية التوعية المشتركة لتعزيز كفاءة DSSCs. إن استخدام MWCNTs في الصورة الضوئية يعزز كفاءة DSSCs بسبب تقليل إعادة تجميع الرسوم. وجد أيضًا أن MWCNTs يمكن استخدامها كقطب مضاد في DSSC نظرًا لاستقرارها الكبير ونشاطها الحفاز. يتم قياس الثبات والنشاط الحفزي لـ MWCNT ومقارنتهما مع أقطاب Pt التقليدية. إن الميزة الرئيسية لاستخدام MWCNT لاستبدال Pt التقليدي في القطب المضاد هي تكلفتها التي تقل بكثير عن المعدن النبيل ، أي نقطة. علاوة على ذلك ، وجد أيضًا أن البيروفسكايت ثنائي الأبعاد / ثلاثي الأبعاد أكثر استقرارًا من مواد البيروفسكايت ثلاثية الأبعاد فقط.

الكلمات المفتاحية: الخلايا الشمسية الحساسة للصبغة (DSSCs) ، الخلايا الشمسية البيروفسكايت (PSC) ، الكفاءة ، الطاقة المتجددة ، الكريستال الأحادي

CHAPTER ONE

INTRODUCTION

1.1. Introduction

After Fukushima nuclear catastrophe which devastated Japan in 2011, numerous countries changed their strategies and began focusing on clean and more environmentally friendly sources of energy [1]. Photovoltaic technologies have distinct advantages over conventional technologies which are used these days, such as nuclear plants, for electricity generation. Renewable energy is one of the best alternatives to disengage from the fossil-based energy resource dependence to fulfill the global energy demands. Based on the report released by U.S energy information administration in 2018, renewable energy is the fastest growing source of world energy with an annual increase rate of 2.5% on average [2]. The advantages of using renewable energy are that it is secure, clean, environmentally friendly, and sustainable.

The Kingdom of Saudi Arabia receives incoming solar radiation of around 105 trillion kilowatt hours per day, some of the most concentrated sunlight in the world, which is comparable to 10 billion barrels of crude oil in energy terms. On average solar radiations of 2200 kWh (th)/m^2 is irradiated annually on the Arabian Peninsula [3]–[5].

Solar energy is one of the most abundant sources of renewable energy. Photovoltaic (PV) is one of the technologies that generate electricity by using solar energy and are mainly using silicon-based solar cell panels. This technology remains expensive compared to fossil fuel energy sources.

In the past decade, the emerging PV, especially Dye Sensitized Solar Cells (DSSCs) and perovskite solar cells (PSC) have emerged as the best alternative to the conventional silicon-based solar cell. It has the main advantage of low-cost energy production. However, there is still a big challenge to make these alternatives become more practical. Emerging PV can be fabricated by using either solution processable techniques (e.g. spin coating, ink-jet printing, and so on), or low-cost deposition technologies. Different types of designs and materials have been used in engineering solar cells. According to the National Renewable Energy Laboratory (NREL) the reported certified efficiency for DSSC is 11.9% and 23.7% for perovskite solar cells respectively [6], [7].

These materials play the same role as silicon by converting sunlight to photocurrent. Upon photon absorption, an exciton is generated, corresponding to an electron and hole added to the charge carrier's concentration. The excitons diffuse and their separation occurs at the electron and hole transporting material's interfaces. Then, these charge carriers are transported to the collecting electrode to produce electricity. In case the generation occurs far away from the interface the electron-hole pair ends up with a recombination process. DSSC suffers from a low energy conversion efficiency due to low absorption co-efficients of the dyes in the range of 400-900 nm [8]. To increase the efficiency of DSSC, various strategies have been investigated. These include co-sensitization of the different dyes, electron and hole transport composite materials etc [9]. Co-sensitization is an effective

technique to boost the power conversion efficiency (PCE) of these devices [10], [11]. It improves the absorption range and ultimately power conversion efficiency (PCE) of dye sensitized solar cells [12].

Many combinations of photosensitizers like porphyrin co-sensitized with ruthenium complex [13], organic dye co-sensitized with ruthenium complex [14], [15], or co-sensitization of phtalocyanine with an organic dye [16]–[18], and organic dye that has been co-sensitized with a different organic dyes [19], [20] have been employed. Yousheng Chen et al. used plural organic dyes, a hemicyanine dye, a merocyanine dye, and a squarylium cyanine dye and obtained an efficiency of 6.5% [19]. Daibin Kuang et al. used two organic dyes (SQ1 and JK2), and obtained a PCE of 6.4% [20]. Wenjun Wu et al. synthesized two indolium based organic dyes and used them in DSSCs [21]. They used their mixture in the ratio of 1:3 and obtained an overall PCE of 3.0% under AM 1.5G illumination. Kun-Mu Lee et al. synthesized a new metal-free organic dye for DSSC. They used the mixture of N719 and this newly synthesized dye and obtained a PCE of 5.1% [22]. Chi-Ming Lan et al. designed and used co-sensitization approach using a stepwise method for of a spirally configured zinc porphyrin sensitizer (LD12) with organic dye (CD5) for DSSC. The co-sensitized CD5 & LD12 devices showed PCE of 9.0% [12]. In addition, using nanorods in the DSSC could increase the interface between donor and acceptor and act as electron paths to the electrode. Different groups used ZnO nanorods to enhance the low efficiency of DSSC [23]–[25]. Despite of this progress and improvement, the efficiency of DSSC remains the limiting parameter toward its commercialization.

A recent addition in the field of photovoltaics is the lead halide perovskite solar cell, $CH_3NH_3PbX_3$ (X = Cl, I, and /or Br). The perovskite solar cells has demonstrated very

promising results, where the efficiency reached over 23%[6], [26], [27] . The perovskite solar cells can be fabricated easily and at low cost compared to other solar cells in the market. These devices can be prepared and processed from solution and using low temperature processes similar to those used in the printing industry. This has made them attractive for photovoltaic applications. Moreover, it is also possible to make the device semi-transparent since the perovskite films are very thin as well as light weight and can be flexible due to the use of plastic substrates [28].

The perovskite solar cells (PSC) operation mechanism (working principles) is not yet fully understood. The progress in this field requires more investigations. It is necessary to determine the different mechanisms in these devices e.g. operational, electronic, carrier separation, extraction, transportation and recombination. Finally, it makes possible the estimation of different perovskite materials combinations and evaluation of characteristics of these combinations. In addition to the absorber film the properties and mechanism of electrode contact, and the overall structure design of the new devices also need to be explored.

The aim of this thesis is to fabricate the PSC and DSSCs and optimize their parameters like open circuit voltage (V_{oc}), short circuit current (J_{sc}) and fill factor (FF), consequently improving the PCE. We aim to focus on the development of new cost-effective nanocomposite materials for the anode and cathode to improve the performance and reduce the cost of these photovoltaics. We also aim to develop new approaches like co-sensitization to enhance the photovoltaics performance.

1.2. Thesis Overview

In this section, the summary of each chapter has been provided.

1.2.1 Chapter 2

In chapter 2, a detailed comprehensive literature review for DSSC and PSC is given. The importance of solar cell technology for future utilization and necessity to eradicate the growing environmental issue like global warming is discussed. Furthermore, the pros and cons for various solar cell technologies e.g. silicon based, dye sensitized based and perovskite based is pointed out. The importance of DSSC and PSC in terms of cost-effective technologies is detailed. The current situation and prospects of both emerging photovoltaics is described in this chapter.

1.2.2 Chapter 3

In this chapter, the experimental details e.g. materials, fabrication methods, characterization parameters and equipment details of all experiments carried out for this thesis is provided. Section 3.1 is related to the co-sensitization of Z907 and SQ2 dyes. Section 3.2 discusses the details of using nWO_3-TiO_2 as a photoanode and MWCNT as counter electrode. Section 3.3 is related to the details of using nMWCNT-TiO_2 as a photoanode and MWCNT as counter electrode. Section 3.4 provides details pertaining to the details of perovskite single crystals.

1.2.3 Chapter 4

In this chapter, the detailed characterizations of the synthesized materials and fabricated thin films is provided. These characterizations include scanning electron microscope (SEM), energy dispersive X-ray spectroscopy (EDX), elemental mapping analysis, transmission electron microscope (TEM), X-ray diffraction (XRD), X-ray photoelectron

spectroscope (XPS), Raman Spectroscopy, optical microscope etc. Section 4.1 is related to the characterization of co-sensitization of Z907 and SQ2 dyes. Section 4.2 discusses the materials characterization details of nWO_3-TiO_2 as a photoanode and MWCNT as counter electrode . Section 4.3 is related to the characterization details of nMWCNT-TiO_2 as a photoanode and MWCNT as counter electrode. Section 4.4 provides to the characterization details of perovskite single crystals.

1.2.4 Chapter 5

This chapter provides the comprehensive results obtained for this thesis and their detailed discussions. These results includes characterization of device current-voltage (J-V) characteristics, ultra-violet visible (UV-Vis) spectroscopy, electrochemical impendence spectroscopy (EIS), cyclic voltammetry (CV) , Tafel studies, chronoamperometry, and Autolab studies. Section 5.1 is related to the results and discussions of co-sensitization of Z907 and SQ2 dyes. Section 5.2 discusses the results and discussion of using nWO_3-TiO_2 as a photoanode and MWCNT as counter electrode. Section 5.3 is related to the results and discussions details of using nMWCNT-TiO_2 as a photoanode and MWCNT as counter electrode. Section 5.4 provides results and discussions pertaining to perovskite single crystals.

1.2.5 Chapter 6

Chapter 6 offers a conclusion of the entire work carried out for this thesis along with recommendations for future progress and development.

CHAPTER TWO

LITERATURE REVIEW

In this chapter a detailed comprehensive literature review for DSSC and perovskite solar cells is given. The importance of solar cell technology for future utilization and necessity to eradicate the growing environmental issue like global warming is discussed. Furthermore, the pros and cons for various solar cell technologies e.g. silicon based, dye sensitized based and perovskite based has been pointed out. The importance of DSSC and PSC in terms of cost-effective technologies has been enlighten. The current situation and prospects of both emerging photovoltaics have been described in this chapter.

2.1 Third Generation Solar Cells

In the past decade, the research focus in the field of renewable energy technologies has accelerated greatly and is oriented towards sourcing alternatives to silicon-based solar cells, which suffer from high cost and difficult fabrication techniques. Third generation solar cells also called emerging photovoltaics especially DSSC and perovskite based photovoltaics attracted a lot of interest where many investigations were carried out and eventually led to an efficiency of 11.9% and 23.7 % respectively [6]. DSSC remains as a promising candidate owing to its advantages of low cost and easy solution processing. However, the relatively low efficiency is a serious problem facing by these solar cells. The fast recombination time of the electron and hole in addition to the short diffusion length are the key limiting factors. Nine years ago, an emerging new type of solar cells were

introduced. These are perovskite solar cells. Perovskite solar cells achieved remarkably high efficiencies in only nine years; in addition, it boasts further advantages such as low synthesis cost due to perovskite materials being abundantly available as well as easy fabrication process. The perovskite solar cell using two planar electrodes attained 15% efficiency [29], [30]. However, an organic solar cell using the same planar electrodes led to low efficiency 2.5%. The perovskite solar cells are the subject of intensive research where many parameters are being varied to maximize the efficiency. Perovskite materials, named after the Russian mineralogist L.A. Perovskite, have the general formula ABX_3 where the 'A' refers to organic cations, the 'B' refers to inorganic (group IV) cations (Sn, Pb), and the 'X' is an anion (group VII) (Cl, Br, I) [31], [32].

2.2 Dye Sensitized Solar Cells (DSSC)

In 1991, DSSC was first developed by Brian O' Regan and Michael Grätzel, where they fabricated the first high efficiency DSSC [33]. DSSC achieved an energy conversion efficiency of 7.1 %, which was further developed to reach 10%. Although the low cost is the key attraction of these solar cells for commercial applications, however, it faces stability issues when liquid electrolytes are being used for fabrication [34]. The working principle of DSSC is shown in Figure 1. In DSSC, there are three primary components. At the top, there is a transparent conducting glass with fluoride-doped tin dioxide (FTO) layer. On the back of this FTO, a mesoporous TiO_2 thin layer is tape casted generally using doctor blade method. The mp-TiO_2 has a large surface area. Usually, TiO_2 only absorbs a small fraction of the solar radiation (in the UV region) [35], [36]. Hence, the TiO_2 coated plate is soaked into a ruthenium or organic based dye solution to be absorbed dye into its pores. It is adsorbed into the TiO_2 surface and makes covalent bonds with TiO_2 molecules. To

select a proper combination of materials and suitable dye is sometimes difficult due to numerous commercially-available dyes and materials, each of them having various pros and cons [37]. The dye molecule used in the DSSC should match with the desired visible solar spectrum, possess high thermal stability, and have properly adhere to the surface of the applied semiconductor. In addition, they should have a sufficiently high redox potential to regenerate when used with a redox mediator [38]. The most common redox electrolyte used in the DSSC is iodine. However, there are other options like organic hole-transport material, polymer gels, solid-state, and quasi-solid state electrolytes [39]–[41]. Platinum (Pt) is usually used on the back electrode as a catalyst for the reduction of the oxidized electrolyte [42]. Along with all these parameters, fill factor (FF) is another important parameter that effects the efficiency of the DSSC. It depends on the various processes like electron transfer process at interface as well as the internal resistance of DSSC e.g. series resistance R_s and shunt resistance R_{sh}. To determine these parameters, we usually use electrochemical impedance spectroscopy (EIS). To interpret EIS data we use equivalent circuits which can be found in the following references [43], [44].

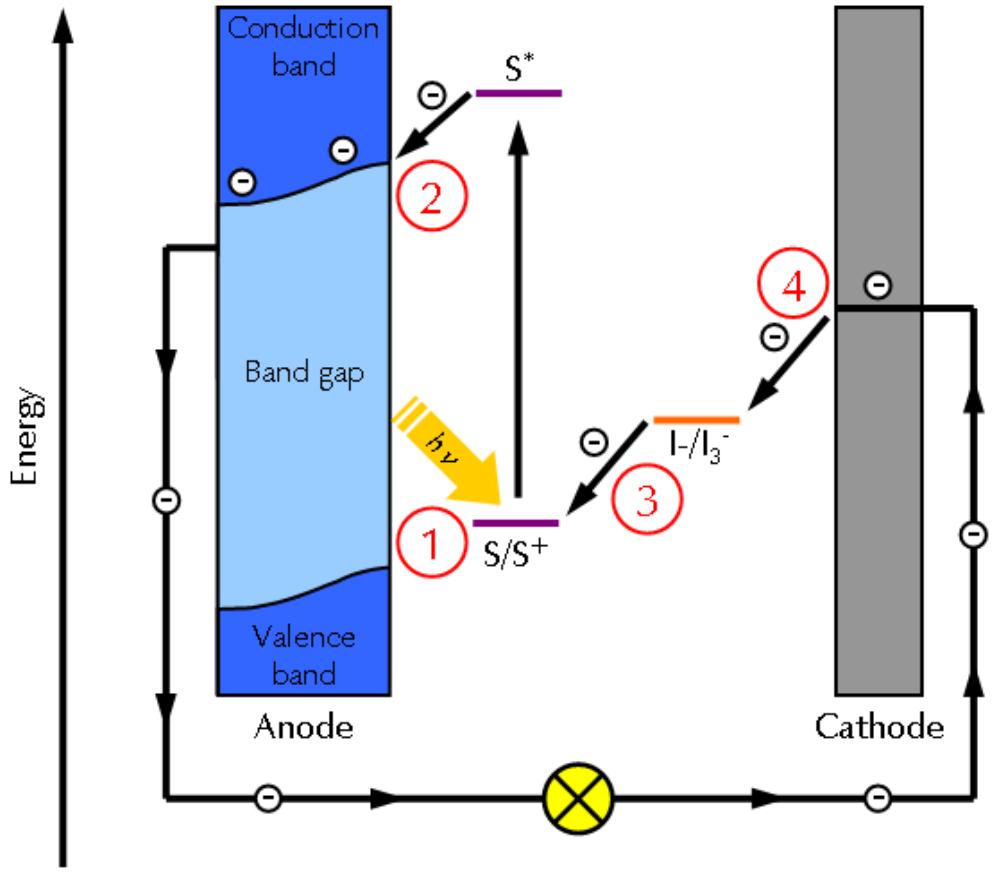

Figure 1 Nano crystalline dye sensitized solar cell [45].

As for the sensitizing dyes, cis-RuL2-(NCS)2 dye has been a viable candidate which can work in conjunction with the nanocrystalline TiO_2 films [46], because this dye has an absorption threshold near 800 nm and extends up to the near infra-red region of the solar spectrum. A black dye developed by Nazeeruddin et al. [47] shows the characteristics of the panchromatic sensitization in the visible to NIR region and the reported efficiency was around 10.2 % [48], Until now, the black dyes are expected to be the best in terms of photovoltaic performance in the whole light absorption range [49], [50]. Hwang et al. [51], with an organic (metal free) dye achieved a conversion efficiency of 9.1 %. The commonly used semiconducting material in DSSC are TiO_2, SnO_2, NbO_2, ZnO, and chalcogenides

which have been under extensive investigation. Furthermore, the most commonly used semiconducting material TiO_2 has different phases. Reference study on TiO_2 anatase and rutile phases was conducted and it was found that TiO_2 anatase is better than TiO_2 rutile [52]. TiO_2 has a few limitations like low charge transport which are covered by other semiconducting materials like zinc oxide. ZnO is one of the most promising semiconducting material for DSSC because of its high electron mobility and suitable band structure [53]. Furthermore, SnO_2 (Tin dioxide) is another interesting option with high charge mobility but it has a large band gap as compared to TiO_2 [54]. Surprisingly, the performance of SnO_2 based DSSC is much less than that of TiO_2 [55]. It is due to the fact that SnO_2 has a large band gap which reduces the number of generated photoelectrons. Tan et al. [56] synthesized ternary oxides Zn_2SnO_4 nanoparticles with large band gap (3.6 eV) for the first time. However, the PCE was only about 3.8% under simulated AM 1.5 illumination. This PCE is approaching to that of the ZnO based semiconducting solar cell (4.1%) [57]. In case of indium tin oxide ($InSnO_2$) films, the resistivity of the fabricated thin films is low due to the replacement of indium atoms with tin atoms, which releases one extra electron, and (ii) oxygen vacancies acting as two electron donors [58], [59]. Semiconducting materials having other morphologies have also been introduced to overcome the limitation of nanoparticles. For example TiO_2 nanowires have been tried [60] and it showed an efficiency of around 9.3 %. Zinc oxide (ZnO) nano wire arrays as shown in Figure 2 were applied for the first time applied in the DSSCs in 2005[61] and moderate efficiency has been achieved.

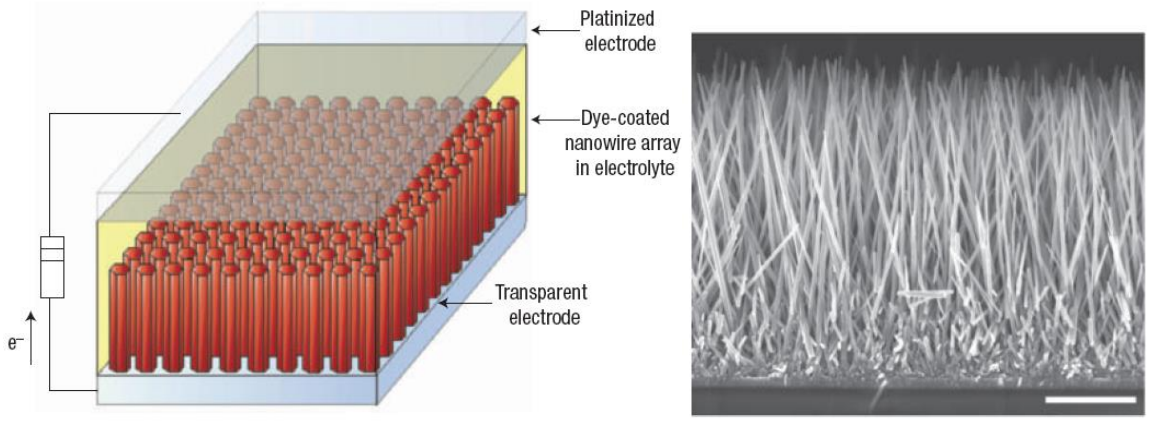

Figure 2 ZnO nanowire arrays for DSSC: A better vectorial charge transportation is expected in nanowire vs. nanoparticles [61].

Beside n-type semiconductors CuSCN and CuI are p-type semiconductors which were introduced for first time introduced by Tennakone et al. acting as hole-transport materials (HTM) [62]. The same was used by O'Regan and Schwartz [63]. Unfortunately, they achieved very low PCE of only <1%, due to these semiconductors forming voids in the TiO_2 inter crystallite. The CuI crystalline semiconductors are fast in crystal growth which interfere with the pores of TiO_2 due to its exceeding dimensions, ultimately effecting the dye absorption on these pores. Later Kumara et al. [64] used a promising crystal growth inhibitor triethylaminehydrothiocyannate (THT) and obtained cell efficiency of 3.75%. DSSC remains potential to compete with the traditional silicon based solar cells due to its low cost. Semiconducting materials such as TiO_2 used for the fabrication of DSSCs is abundant and inexpensive as compared to silicon material. In addition, they are not as sensitive to impurities during the synthesis process.

DSSC remains a promising candidate owing to its advantages of low cost and easy fabrication. Yet, the low efficiency is a serious problem facing by DSSC. The fast

recombination of charges in addition to the short diffusion length are the keys limiting factors of DSSCs. Nine years ago, a new type of solar cells, called perovskite solar cells (PSC) emerged as a promising candidate to overcome the limiting factors of DSSC. PSC gave a new route to achieve high efficiency along with the low cost and easy fabrication process. The general structure of the perovskite solar cells is given in the Figure 3a.

2.3 Perovskite Solar Cells (PSC)

Perovskite is a type of mineral composed of calcium titanium oxide ($CaTiO_3$). It was first found in the Ural Mountains in Russia by Gustav Rose in 1839 and is named after Russian scientist Lev Perovskite (1792–1856). He is the pioneer of the Russian Geographical Society (RGS). Any compound having the same structure as perovskite mineral is called perovskite structure. The general formula of perovskite structure is ABX_3, where A is an organic cation, B is an inorganic cation and X is an anion. A, B and X are very different in size [65]. This general structure can be given a number of different names from the following table 1.

Table 1 General structure of perovskite materials

A	B	X_3
Organo	Metal	Halide (or trihalide)
Methylammonium	Lead, Tin, Ge	Iodide (or triiodide)
	Plumbate	Chloride (or trichloride)

The lattice arrangement of perovskite is given in Figure 3b, but as in crystallography we can represent same structure in many ways, we must understand that we can present it in many other ways. The general way to represent perovskite is to keep large cation A in the center of the cube, B on the corners of the cube and X on the faces.

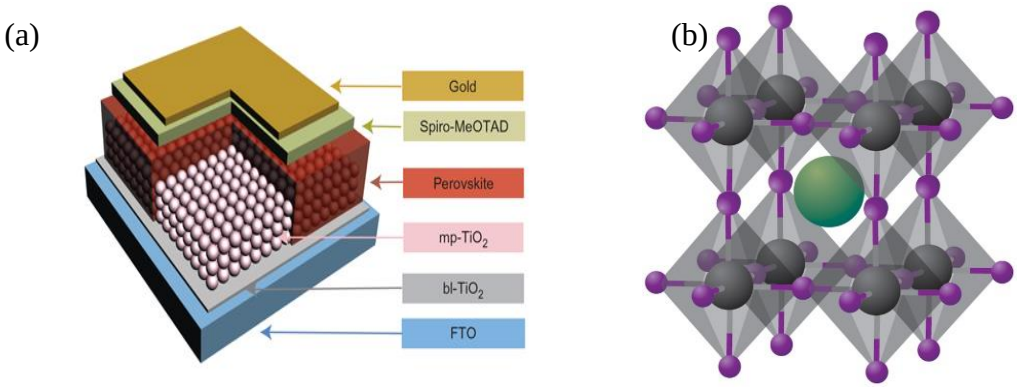

Figure 3 (a) Perovskite solar cell structure and (b) Perovskite crystal structure.

In 2009, the first report was published on Perovskite solar cell with the combination of $CH_3NH_3PbI_3$ absorber and an iodide/triiodide redox couple (Liquid electrolyte/$CH_3NH_3PbI_3$/TiO_2). The reported efficiency was 3.81% [66], [67]. By improving the titanium oxide surface morphology and processing of the perovskite materials along with keeping the liquid electrolyte unchanged (Liquid electrolyte/$CH_3NH_3PbI_3$ QD/TiO_2) Kim and co-workers were able to achieve an improved PCE of 6.5% [67], [68] . The perovskite solar cells based on liquid electrolyte shows a poor stability[69], [70]. To overcome this problem Kojima and co-workers offered a solution by changing liquid electrolyte with solid state HTM with the combination of Spiro-MeOTAD/$CH_3NH_3PbI_3$/mesoporous TiO_2 approaching an efficiency of 9.7% [67], [69].

In 2012, N. G. Park and T. N. Murakami & T. Miyasaka working in collaboration with M. Grätzel and co-workers used these solid-state HTM to fabricate perovskite solar cells [71] with maximum PCE between 8 to 10% in full simulation sun light conditions by using $CH_3NH_3PbI_{3-x}Cl_x$ mixed halide perovskite[69], [72], [73]. This efficiency was better than the best reported solid state DSSC having an efficiency of 7% [74].

In order to understand the charge separation phenomenon in perovskite solar cells, a femto-second transient absorption spectroscopic study was carried out with TiO_2 and Al_2O_3. No major spectral differences were observed between them. This fact introduced the possibility that perovskite solar cells may work even without an electron injecting layer. Then PSC was confirmed to work without mesoporous TiO_2 layer, where the combination with $CH_3NH_3PbI_3$ on Al_2O_3 (Spiro-MeOTAD/$CH_3NH_3PbI_{3-x}Cl_x$/mesoporous Al_2O_3) scaffold achieved an efficiency of 10.9%, a considerable success [75]. The efficiency was further improved up to 12.3% by optimizing the Al_2O_3 layer thickness and preparation conditions at low temperatures [76]. Furthermore, the efficiency improvement was also achieved with replacement of the polymer HTM to PTAA instead of Spiro-MeOTAD, because of their superior hole mobility and good film forming properties (PTAA/$CH_3NH_3PbI_{3-x}Br_x$/m-TiO_2) [77]. Since then, there has been a great deal of development in the PCEs of perovskite solar cells in the last couple of years. The efficiency reached up to 15% in the same year of 2013 with the combination Spiro-MeOTAD/$CH_3NH_3PbI_{3-x}Cl_x$/TiO_2, 2-step solution deposition where they improved the film formation of perovskite using two-step solution deposition method [29], [30], [78]. However, the certified efficiency was 14.1% by National Renewable Energy Laboratory (NREL) [6]. It was suspected that MAI provide acidic surroundings to the underlaying ETL

e.g. ZnO, which rapidly etch the surface of ZnO due to the reaction between MAI and ETL surface. This reaction was suppressed with two step method [79]. Similar results were obtained using a planar cell configuration in which the film thickness was very thin in order to eliminate the mesoporous TiO_2 scaffolding. The $MAPbI_{3-X}Cl_X$ perovskite material (Spiro-MeOTAD/$CH_3NH_3PbI_{3-x}Cl_x$/TiO_2, evaporated thin film p–i–n architecture) was deposited by a source containing two thermal evaporation processes. An efficiency of 15.4% was obtained [30]. Jeon et al. modified the method and introduced the solvent engineering method to achieve thick perovskite films (PTAA/$CH_3NH_3PbI_{3-x}Br_x$/mesoporous TiO_2) and obtained an efficiency of 16.2% with this process modification [2][80] . Then a confirmed efficiency of 17.9% was achieved in early 2014 by using the same combination PTAA/$CH_3NH_3PbI_{3-x}Br_x$/mesoporous TiO_2 by improving the film formation quality and other factors [80]. Subsequently, the PCE reached 19.3% by engineering the interface on a planar device by using yttrium-doped TiO_2 as an ETM (Spiro-MeOTAD/perovskite/yttrium-doped TiO_2) [81], [82]. By November 2014, a new record certified non-stabilized efficiency of 20.1% was achieved by the Korean Research Institute of Chemical Technology (KRICT) by using the combination of PTAA/$(FAPbI_3)_{1-x}(MAPbBr_3)_x$/mesoporous-$TiO_2$ [6], [27]. In 2016, the same institute (KRICT) achieved the certified efficiency 22.1%, which is now jumped to 23.7% in June 2018 by Institute of chemistry-Chinese academy of sciences[6].

All above mentioned PSCs are based on the regular structure, (i.e. FTO/TiO_2 or Al_2O_3/perovskite/Spiro-OMeTAD or PTAA/Au or Ag). However, recently solar cells with an inverted structure (i.e. ITO/PEDOT: PSS/perovskite/PCBM/Al) have attracted significant attention as well. It was first reported by Jeng et al. with a PCE of 4% [83]. At

the start of 2014, many research groups simultaneously reported power conversion efficiencies surpassing 10% [84], [85]. Recently, the PEC for this inverted structure has exceeded 17% [86], [87]. Researchers believe that the efficiency of this inverted structure could catch up with the PCE of the regular structure in the near future [88].

The stability of the perovskite solar cell has also been improved tremendously from 17 minutes (2009) to 3000 hours (2016), and that too under ambient conditions of open air and at room temperature. A detailed description of the aforementioned stability improvements can be found in [27], [89]. The stability of the inverted structure is better than regular TiO_2 structures (substrate/Spiro-MeOTAD/$CH_3NH_3PbI_3$/ TiO_2/Au or Ag). The stability can also be improved by using the mixed halide structure instead of single perovskite structure[90].

Perovskite solar cells are promising devices due to the low cost and very high efficiency as compared to its alternative, conventional semiconductor based solar cells. From this promising technology we are hopeful that the PCE of perovskite based solar cell can crosses the threshold of 25% for the single junction and even 30% by using tandem structures. These structures are applied by incorporating suitable low band gap material systems such as CIGS or Si [24], [91]–[93].

The above literature review can be concluded as there is significant room to work on DSSC for improvement of their efficiency and in parallel to work on its cost reduction. On the other hand, perovskite has good efficiency, however, there is need to enhance its stability. In this thesis we focus on these gaps to enhance the performance and stability of these photovoltaics. Additionally, we worked on the cost-effectiveness of these photovoltaics.

CHAPTER THREE

EXPERIMENTAL DETAILS

In this chapter, the experimental details (e.g. materials, fabrication methods, characterization parameters and equipment models etc.) of all experiments carried out for this thesis is provided.

3.1 Co-sensitization of Z907 and SQ2 dyes methodology

3.1.1 Materials

Fluorine doped tin oxide (SnO_2: F) FTO conductive glass substrates, anatase TiO_2 paste (Solaronix, T/SP **14451**), dyes (Ruthenizer 520-DN and Sensitizer SQ2), electrolyte (Solaronix, Iodolyte Z-50) and platinum paste (Solaronix, Plastisol T), were all procured from Solaronix (Switzerland).

3.1.2 Preparation of dye solutions

Seven different dye solutions were prepared in ethanol i.e. 0.5mM Z907, 0.5mM SQ2, (0.4mM Z907 + 0.1mM SQ2), (0.3mM Z907 + 0.2mM SQ2), (0.25mM Z907 + 0.25mM SQ2), (0.2mM Z907 + 0.3mM SQ2) and (0.1mM Z907 + 0.4mM SQ2). The structures and chemical names of both dyes are shown in Figure 4.

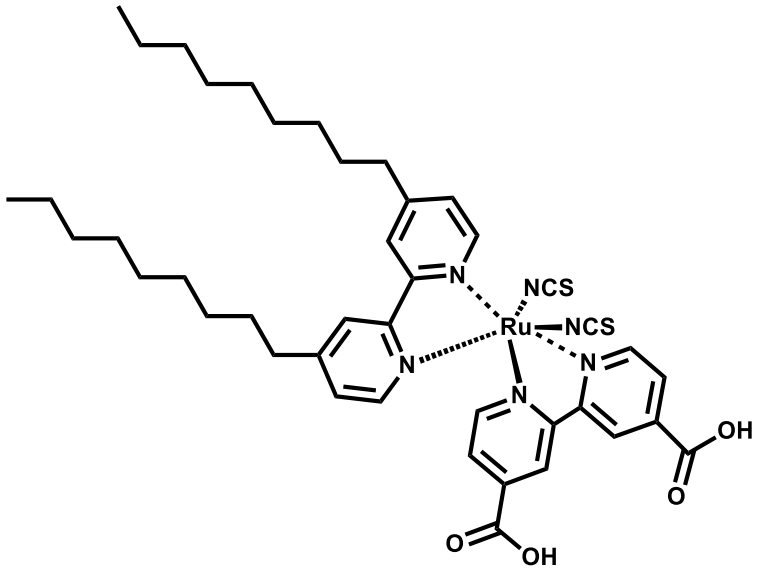

cis- diisothiocyanato-(2,2'-bipyridyl-4,4'-dicarboxylic acid)-(2,2'-bipyridyl-4,4'-dinonyl) ruthenium (II) [Z907]

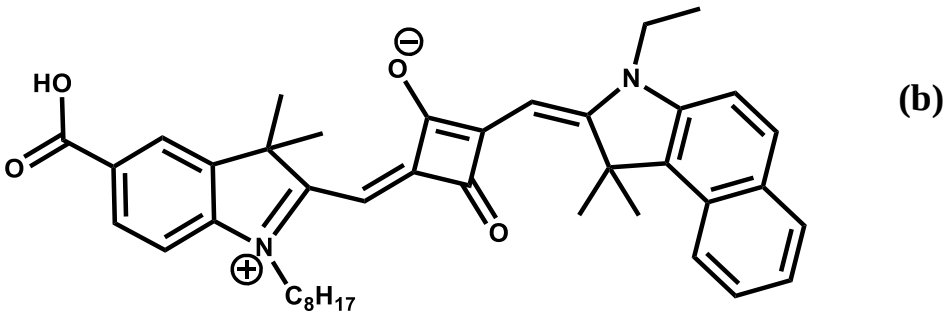

5-carboxy-2-[[3-[(2,3-dihydro-1,1-dimethyl-3-ethyl-1H-benzo[e]indol-2-ylidene)methyl]-2-hydroxy- 4-oxo-2-cyclobuten-1-ylidene]methyl]-3,3-dimethyl-1-octyl-3H-indolium [SQ2]

Figure 4 Structures and chemical names of (a) Z907 and (b) SQ2 dyes.

3.1.3 Fabrication of DSSC

The DSSC flow diagram is shown in Figure 5 for easy visualization. FTO conductive glass substrates were employed with TiO_2 paste by tape casting method, and then subsequently annealed at 200 ^oC for the first 10 min and 450 ^oC for next 20 min. After cooling to room temperature, TiO_2 deposited FTO conductive substrates were soaked in the respective dye solutions i.e., individual and mixture of dyes solution for 24h to obtain properly prepared photoanodes. After the sensitization, photoanodes were rinsed with methanol to remove the un-adsorbed dye. Similarly, the tape casting method was used for the preparation of platinum counter electrodes on conductive FTO glass substrates. The samples were then annealed at 450 ^oC for 15 min. The two electrodes were joined together with super glue gel (named as the original super glue by super glue corporation). Finally, the electrolyte was injected between the two joint electrodes to complete the fabrication of solar cells. In this work, the fabricated solar cells active area is 0.20 cm^2.

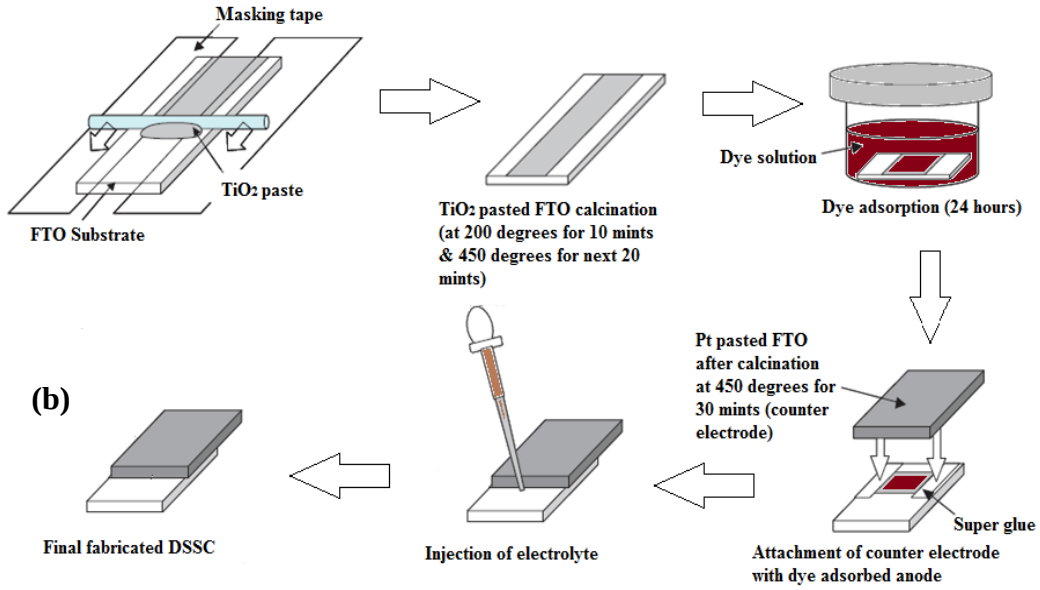

Figure 5 Flow diagram of DSSC fabrication.

3.2 nWO_3-TiO_2 as photoanode and MWCNT as counter electrode DSSCs methodology

3.2.1 Pastes preparation for photo-anode (nWO_3 -TiO_2)

Initially, WO_3 nanoparticles were synthesized by facile, one-pot precipitation reaction of the aqueous solution of sodium tungstate (Sigma Aldrich, USA) and acidic solution of hydrochloric acid (Sigma Aldrich, USA). A definite amount of sodium tungstate was dissolved in deionized (DI) water and then hydrochloric acid solution (prepared in deionized water) was added drop wise along with vigorous stirring. This mixture was carefully stirred at 25 ^oC on a magnetic stirrer to get a precipitate of WO_3 nanoparticles. The precipitate was stirred for about 3h and left for another 24 h at room temperature to form an absolute precipitate. This precipitate was filtered by suction pump, rinse with demineralized water and finally baked at 100 ^oC for 24 h. The dried powder was calcined for 6 h at 800 ^oC in a muffle furnace to get the crystalline WO_3 nanoparticles.

In the second stage of preparation, *n*WO_3-TiO_2 pastes with different WO_3-TiO_2 mass ratios (*n* = 1%, 3% and 5%) were prepared by mixing with polyvinylpyrrolidine (Sigma Aldrich, USA) as a binder, 1 ml ethanol (Sigma Aldrich, USA) as a solvent, 250 µl Triton X-100 (Sigma Aldrich, USA) as a dispersant, 60 µl acetylacetone (Sigma Aldrich, USA) as a surface modifier, and 40 µl acetic acid (Sigma Aldrich, USA) as acidification agent. Initially, *n*WO_3-TiO_2 and binder were weighed in precise amounts and mixed together and subsequently ethanol was added and this mixture was vigorously stirred for 15 minutes at 60 ^oC to get a smooth and homogeneous solution. Eventually, acetylacetone, triton X-100 and acetic acid were added in the above solution while stirring and heating at 60 ^oC and this stirring was continued for 3 h to get the *n*WO_3-TiO_2 pastes.

3.2.2 DSSCs fabrication

Prior to the fabrication of DSSCs, 1.5 cm^2 FTO (fluorine doped tin oxide: SnO_2/F) substrates were washed with ethanol, acetone and isopropyl alcohol respectively and were dried in oven at 100 ^oC for 30 minutes. The *n*WO_3-TiO_2 pastes were tape-casted on FTO substrates using doctor blade method, initially annealed at 200 ^oC for 10 minutes and subsequently at 500 ^oC for next 20 minutes to get uniform surface films. The annealed substrates were gradually cooled down to the room temperature and soaked in N719 dye solution for 48 h to get photo anodes. Similar cleaning, coating and annealing (450 ^oC for 30 minutes) methods were adopted to make the counter electrodes also. A specific amount of MWCNTs with outer diameter 10-20 nm, length 1-10 μm (Chengdu Organic Chemicals Co., Ltd, China) mixed with commercial titanium paste was used to make MWCNT counter electrode. The purpose of using TiO_2 paste in the back electrode is just as a binder and it should be noted that its role as a counter electrode (CE) as such is very weak (0.01% efficiency for [TiO_2/N719/TiO_2] as given in Table 4.3). In the fabrication of Pt counter electrode, platinum (Pt) paste was tape-casted on the conductive glass substrates (FTO) using similar method (doctor blade). Finally, the photoanode and the CE were joined with each other using super glue (Company name: Super glue corporation, Glue name: The original super glue) and finally the electrolyte (Iodolyte AN-50) was gently poured between the two joined electrodes. The active area of fabricated solar cells in this study is 0.25 cm^2. Ruthenium dye N719, TiO_2 paste (D/SP 14112) electrolyte Iodolyte (AN-50), conductive glass substrates FTO (fluorine doped tin oxide: SnO_2/F) (thickness 2.2 mm, 7 Ω/sq) were purchased from Solaronix, Switzerland.

3.2.3 Characterization details

The following instruments were used for the characterization studies: for XRD, Mini-XRD Rigaku Corporation (Model: MiniFlex II); for SEM TESCON (Model: Lyra3); for EDX and mapping analysis Lyra3 TESCON system with the accelerating voltage 20KV; for TEM analysis JEOL (Model: JEM-2100F); for XPS Thermo Scientific (Model: ESCALAB 250Xi); for J-V characterization solar simulator with data acquisition system (Keithley 2400) PV measurements Incorporation (Model: IV-5); for quantum efficiency measurements PV measurements Incorporation (Model: QEX-10); for UV-vis spectroscopy spectrophotometer JASCO (Model: V-670); and for Tafel/Chronoamperometry/cyclic voltammetry/ Electrochemical Impedance Spectroscopy (EIS) BioLogic Science Instruments (Model: VMP3 SAS). For EIS studies, a 10 mV AC signal in 1 Hz to 1 MHz frequency range with an applied bias in the range of 0 to 750 mV (larger than V_{oc} of fabricated DSSC) was used and EIS measurements were conceded in dark conditions. The solar simulator was equipped with standard simulated solar light (100 mW/cm^2).

3.2.4 Photo-catalytic degradation of MB dye

The radiation source for the photocatalytic studies is 100 W UV lamp (OmniCure), and the photocatalysts used were *n*WO_3-TiO_2 films on the FTO glass substrates with three different WO_3-TiO_2 mass ratios (*n* = 1%, 3% and 5%). During the irradiation process, we collected sample in regular intervals and to estimate the concentrations of degraded samples, we took absorption using the spectrophotometer and the analyzed dye samples were returned to the main photo-catalytic chamber. The percentage of degradation was calculated using the

formula [(C_o-C)/C_o] x 100). Here C_o is initial concentration and C represent instantaneous dye concentrations. To quantify the concentration of the dye in the aqueous solution, the intensity of the absorption peak of MB dye centered at 664 nm was used.

3.3 nMWCNT-TiO_2 as photoanode and MWCNT as counter electrode DSSCs methodology

3.3.1 Characterization details

The spectrophotometer (model: UV/Vis JASCO-670) has been used to acquire the ultraviolet-visible (UV-Vis) spectra of prepared dye solutions and dyes anchored to TiO_2 films on FTO conductive glass. The solar simulator (IV-5, Sr #83, PV Measurement, Incorporation) at Air Mass (AM) 1.5 G (1000 Wm^{-2}) with Source Meter (Keithley 2400) has been used to evaluate the IV characteristics of the fabricated DSSCs. The potentiostat VMP3 SAS (s/n: 0373 Bio-Logic Instruments) has been used to investigate the EIS (electrochemical impendence spectroscopy) properties under dark conditions of illumination, with a 10 mV amplitude AC signal having a frequency within the range of 10 Hz and 800 KHz. The applied bias was in the range of 0 and 750 mV larger than the V_{oc} of the DSSC.

3.3.2 Materials

FTO (SnO_2/F fluorine doped tin oxide, thickness 2.2 mm, 7 Ω/sq) conductive glass substrates, N3 dye (Ruthenium based dye), Titanium dioxide paste (Ti-Nanoxide T/SP, 14412), electrolyte Iodolyte (Z-50, 35112), were purchased from “Solaronix, Switzerland”. Multiwall carbon nanotubes with outer radius 5-10 nm and length ~1-10 μm was purchased from “Chengdu Organic Chemicals Co. Ltd, China”.

3.3.3 Preparation of pastes for photo-anode and counter electrode (n-MWCNT -TiO_2)

3.3.4 Preparation of photoanode

20mg/25ml MWCNT suspension was prepared in ethanol and the mixture was sonicated for 12 hours to get a proper dispersion of MWCNT in ethanol. For instance, in order to prepare 0.03% MWCNT-TiO_2, 38 µl of the above MWCNT suspension is added to 40 mg of TiO_2 paste and similarly for preparing 0.06%, 0.09% and 0.12% MWCNT in TiO_2, we had to add 76 µl, 114 µl, 152 µl of MWCNT suspension respectively in 40 mg of TiO_2. Nanocomposite of *n*-MWCNT-TiO_2 in four different mass ratios (MWCNT in TiO_2 wt % = 0.03, 0.06, 0.09 and 0.12) were prepared. The prepared MWCNT/TiO_2 composite pastes with varying wt% was deposited on cleaned FTO glass substrates first by casting scotch tape (Company: 3M) for the desired active area and then using doctor blade method for the deposition of the prepared pastes and sequentially annealed at 150 ^oC for 10 minutes and 475 ^oC for next 30 minutes. The thickness of prepared anodes films was found to be around 9 µm from SEM cross-sectional view.

3.3.5 Preparation of counter electrode

A specific amount of MWCNT was mixed with TiO_2 paste and a few drops of ethanol were added to the MWCNT-TiO_2 composite paste for good dispersion. The role of TiO_2 paste was like a binder which binds MWCNT together and works as an adhesive between MWCNT and FTO glass substrates. The prepared paste was deposited with the same tape casting and doctor blade method and calcined at directly 450 ^oC for 20 minutes to get the final CE for DSSC fabrication.

3.3.6 Fabrication of DSSCs

The photo anode substrates were soaked in the dye solution (N3 in ethanol: 0.5mM) for 24 hours. After 24 hours the photoanodes were removed from dye solution and rinsed with ethanol to remove unabsorbed dye. Finally, the photoanode and the counter electrode were joined together with super glue gel (Company: The original super glue corporation) and the electrolyte, Iodolyte Z-50 was poured between the two joined electrodes to complete the fabrication of DSSC. The active area of fabricated DSSC was 0.25cm^2.

3.4 Perovskite single crystals methodology

3.4.1 Materials

All chemicals and materials used in this study are analytical grade. The materials and equipments used in this study are listed in table 2 below:

Table 2 Materials and lab equipments used in this study.

Materials	Lab equipment
Methylammonium iodide (MAI)	Programmable Hotplate
Propylammonium iodide (PAI)	Micropipette
Butylammonium iodide (BAI)	Multimeter
Gamma-Butyrolactone (GBL)	Autolab potentiostat
Acetone	Mettler-Toledo weighing scale

3.4.2 Materials structures

The following are the structures of the used materials. All the three structures contain different carbon atoms as shown in Figure 6 below. The MAI has one carbon atom connected with three hydrogen atoms, BAI have three carbon atoms connected with seven hydrogen atoms, and PAI have four carbon atoms connected with nine hydrogen atoms.

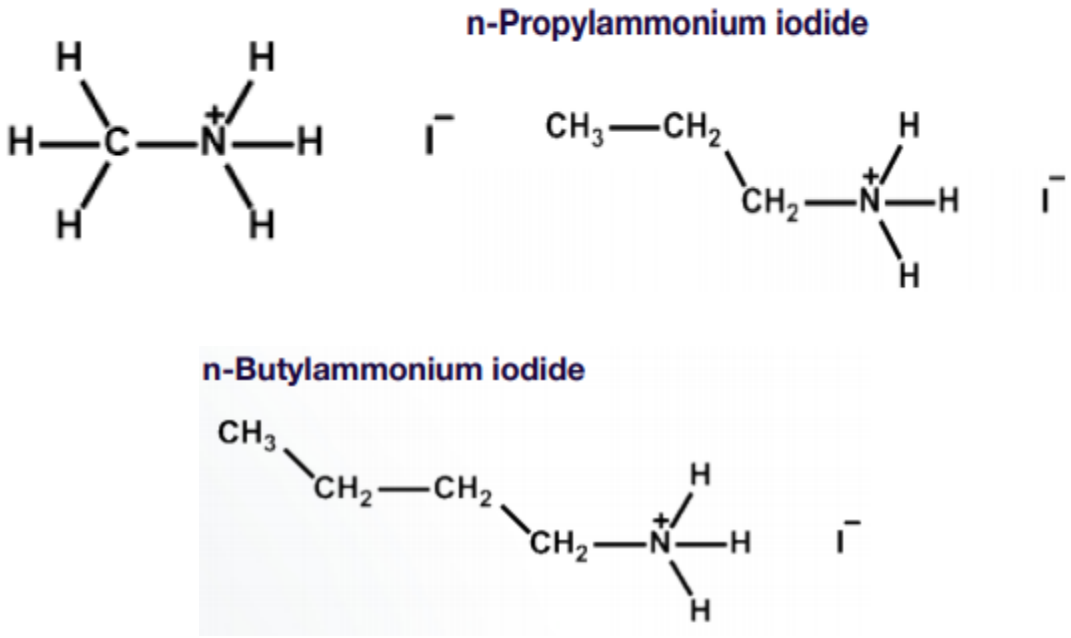

Figure 6 The structures for different perovskite materials used in this study.

3.4.3 Procedure

The following procedures (provided in 3.4.4) has been followed for preparation of perovskite solutions and single crystals.

3.4.4 Preparation of perovskite solutions.

Step 1: The perovskite materials were weighed for the preparation of 1 ml solution for each bottle. The following formula has been used for the weighing of perovskite materials.

Mass in Material (mg) = (Solvent in ml) (Materials in moles) (Molecular weight of material)

The weighing scale was used to measure the exact amount of each material. 1 ml GBL solution was poured into the measured amount of materials in each bottle. Finally, the materials were mixed using the magnetic stirrer at 70 ^{o}C for 30 mints.

Step 2: The prepared solutions were filtered with 0.45 micrometer PTFE filter to remove the big chunks if any in the dissolved materials in each bottle. Filtration has been carried out in fume hood with proper PPE to avoid any toxic side effects of the lead-based materials.

Three different perovskite solutions were prepared as shown in Figure 7. Each bottle made by different recipe of perovskite materials as given below.

- Bottle#1 $MAPbI_3$
- Bottle#2 BAI: $MAPbI_3$
- Bottle#3 PAI: $MAPbI_3$

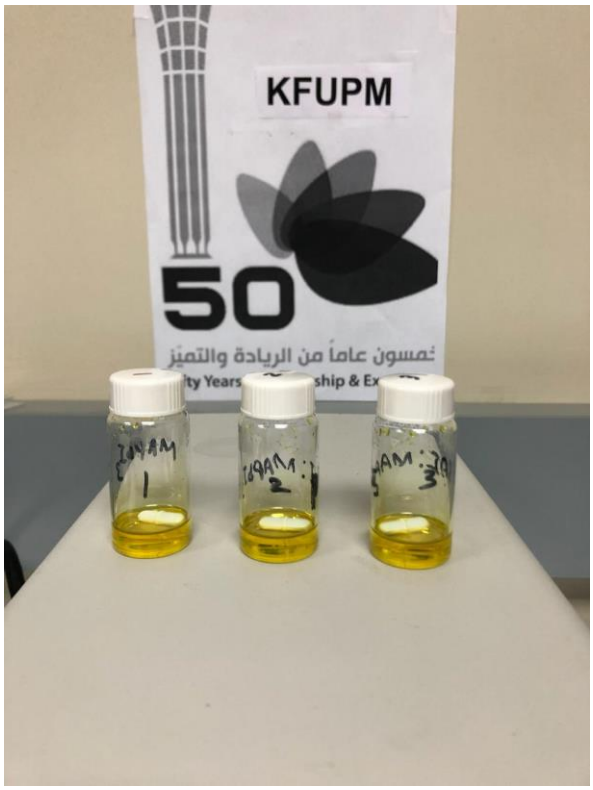

Figure 7 The prepared solutions for all three combinations i.e. $MAPbI_3$, BAI: $MAPbI_3$, and PAI: $MAPbI_3$.

3.4.5 Procedure for growth of perovskite single crystals

The perovskite single crystals were grown using the following steps.

Step 1: To grow bulk and thin single crystals all the prepared solutions are set on the programmable hot plate that was programmed to rise for 5 ^oC/h starting from 70 ^oC till 110 ^oC. After 8 hours the three bottles were examined for crystallization. The flow diagram to grow the perovskite bulk and thin single crystals are shown in Figure 8 and 9 below.

Step 2: The prepared bulk perovskite single crystals were harvested from the solutions. To harvest the bulk perovskite single crystals from the solutions we need to wash them with acetone to remove any existing solution on them. The solutions from the three bottles were

removed one by one, and acetone was added to the bottles to remove the residual perovskite solution from the crystals. All the harvested bulk crystals were marked with their identity on filter paper and size of each single crystal was measured. Maximum size of bulk perovskite single crystal was measured as ~7mm.

Step 3: The thin single crystals can be utilized directly on the ITO or FTO by just removing the other conducting glass plate which was used for cap casing. Maximum size of thin perovskite single crystal was measured as ~5mm.

Step 4: The perovskite single crystals were collected and dried in vacuum for 5 mintutes and pictures were taken as shown in Figures 89-94 respectively.

Figure 8 Growth of bulk and thin perovskite single crystals using programmable hotplate.

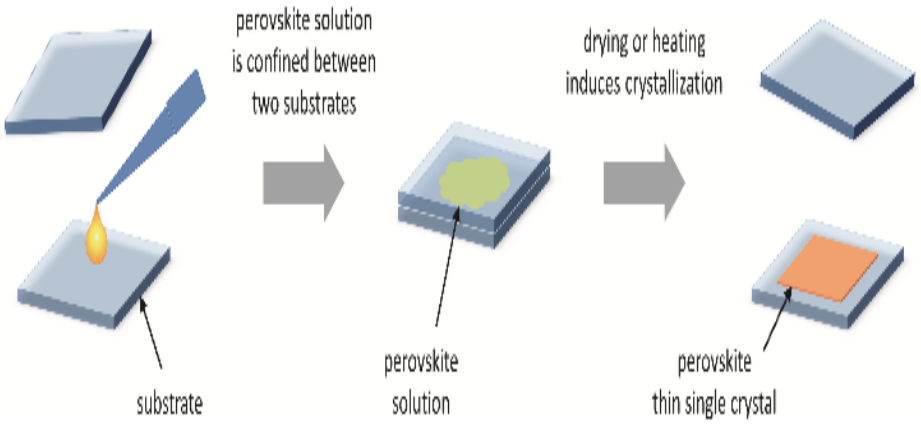

Figure 9 The flow diagram to grow thin perovskite single crystal [94].

CHAPTER FOUR

CHARACTERIZATION OF SYNTHESIZED MATERIALS AND FABRICATED THIN FILMS

In this chapter, the detailed characterizations of the synthesized materials and fabricated thin films has been provided. These characterizations include scanning electron microscope (SEM), energy dispersive X-ray spectroscopy (EDX), X-ray mapping analysis, transmission electron microscope (TEM), X-ray diffraction (XRD), X-ray photoelectron spectroscope (XPS), Raman Spectroscopy, optical microscopy etc.

4.1. Characterization for Co-sensitization of Z907 and SQ2 dyes

4.1.1 Scanning electron microscope cross-sectional view

The deposited TiO_2 film thickness on each substrate was analyzed and measured with the help of SEM cross-sectional images as shown in Figure 10. Each film shows an average thickness of 6 μm.

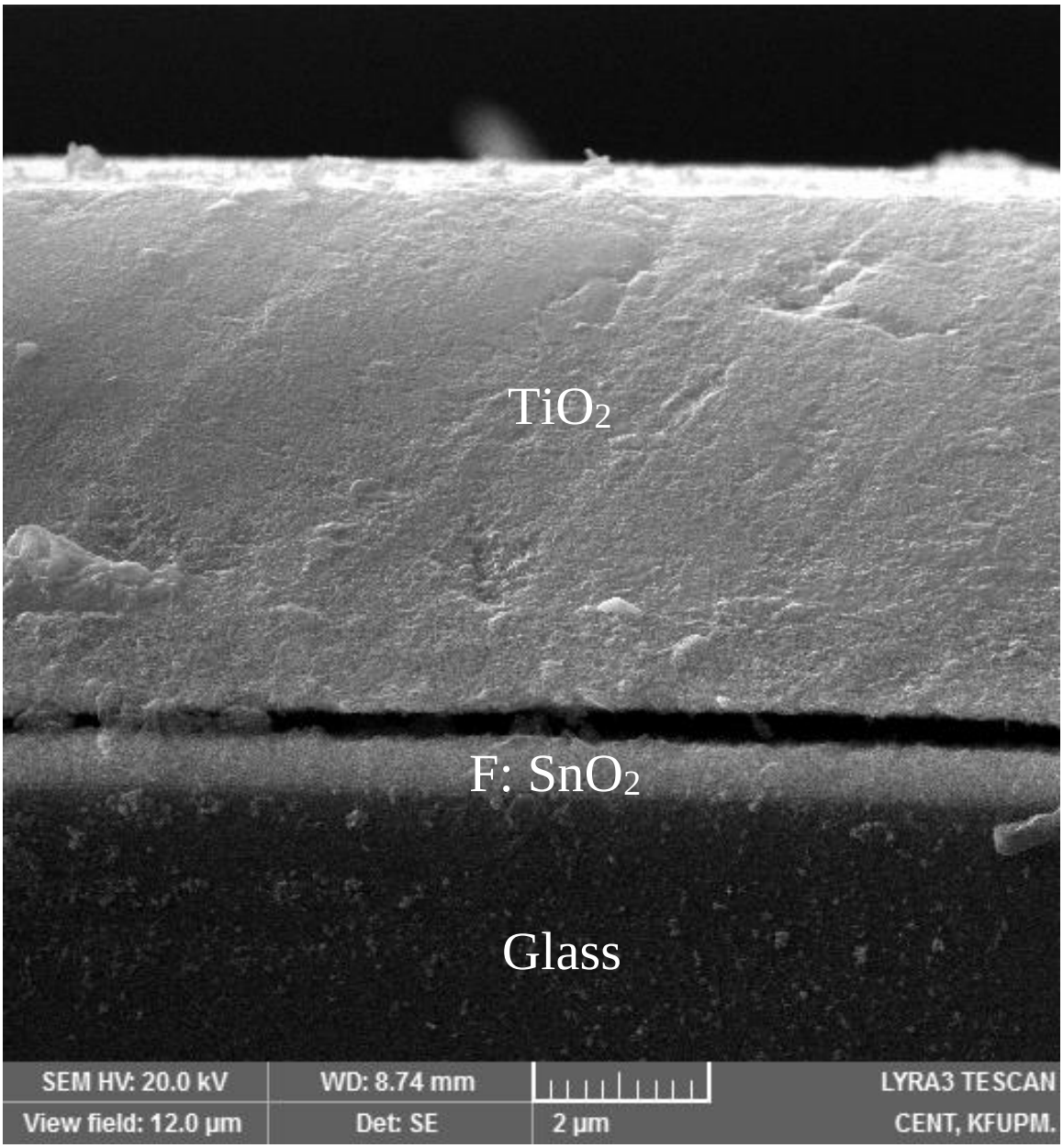

Figure 10 Cross-sectional image of TiO_2 film deposited on FTO glass substrate.

4.2. Characterization for nWO_3-TiO_2 as photo-anode thin films

4.2.1 Morphological and structural characterization of nWO_3-TiO_2 photo-anode

4.2.2 SEM, EDX, TEM and Mapping analysis

In order to study the surface morphology of the photo-anode (*n*WO_3-TiO_2 film), FE-SEM images were taken. Figure 11 (a-f) shows the FE-SEM images of *n*WO_3-TiO_2 films with three different WO_3-TiO_2 mass ratios (*n* = 1%, 3% and 5%) at two different magnifications. The FE-SEM images reveal that *n*WO_3-TiO_2 photo-anode film surfaces are homogeneous, porous and contain well dispersed nanoparticles of the size of 10-30 nm range on FTO conductive glass substrates. A good surface porosity, and consequent rise in the surface area, enables the enhanced dye loading on the *n*WO_3-TiO_2 surface. In addition to this, SEM images of pure MWCNTs, pure TiO_2 film, MWCNT incorporated TiO_2 and platinum back electrode films were taken and are shown in Figure 12 (a-d). Additionally, the elemental compositions of *n*WO_3-TiO_2 films with three different WO_3-TiO_2 mass ratios (*n* = 1%, 3% and 5%) were examined using EDX analysis and these results along with the corresponding elemental mapping are shown in Figure 13 (a-c) and Figure 14, 15 & 16**.** From this inspection**,** it is quite clear that *n*WO_3-TiO_2 composes of Ti, W and O, with a little trace of gold due to gold coating. Table 3 shows the weight and atomic percent of the elements for the specific scanned area in all three different thin films. In order to confirm the proper attachment of WO_3 on TiO_2 in of *n*WO_3-TiO_2 films, transmission electron microscope (TEM) images were taken for both pure TiO_2 as given in Figure 15 and 1%WO_3-TiO_2 films at three different magnifications provided in Figure 17 (b-d), which clearly indicate the formation of the nanocomposite of WO_3 and TiO_2 (*n*WO_3-TiO_2), with an average particle size of 10-20 nm. Also, the TEM images of 3%WO_3-TiO_2 and 5%WO_3-TiO_2 composition are provided in Figure 18, where the attachment of WO_3 in TiO_2 lattice is quite evident, which accounts for the improved characteristics of solar cell, when it is used as the

photoanode. Furthermore, the elemental mappings of *n*WO_3-TiO_2 films with three different WO_3-TiO_2 mass ratios (*n* = 1%, 3% and 5%) are also presented in Figure 14, 15 and 16 respectively. The elemental mapping clearly shows the uniform dispersion of WO_3 in TiO_2 nanoparticles.

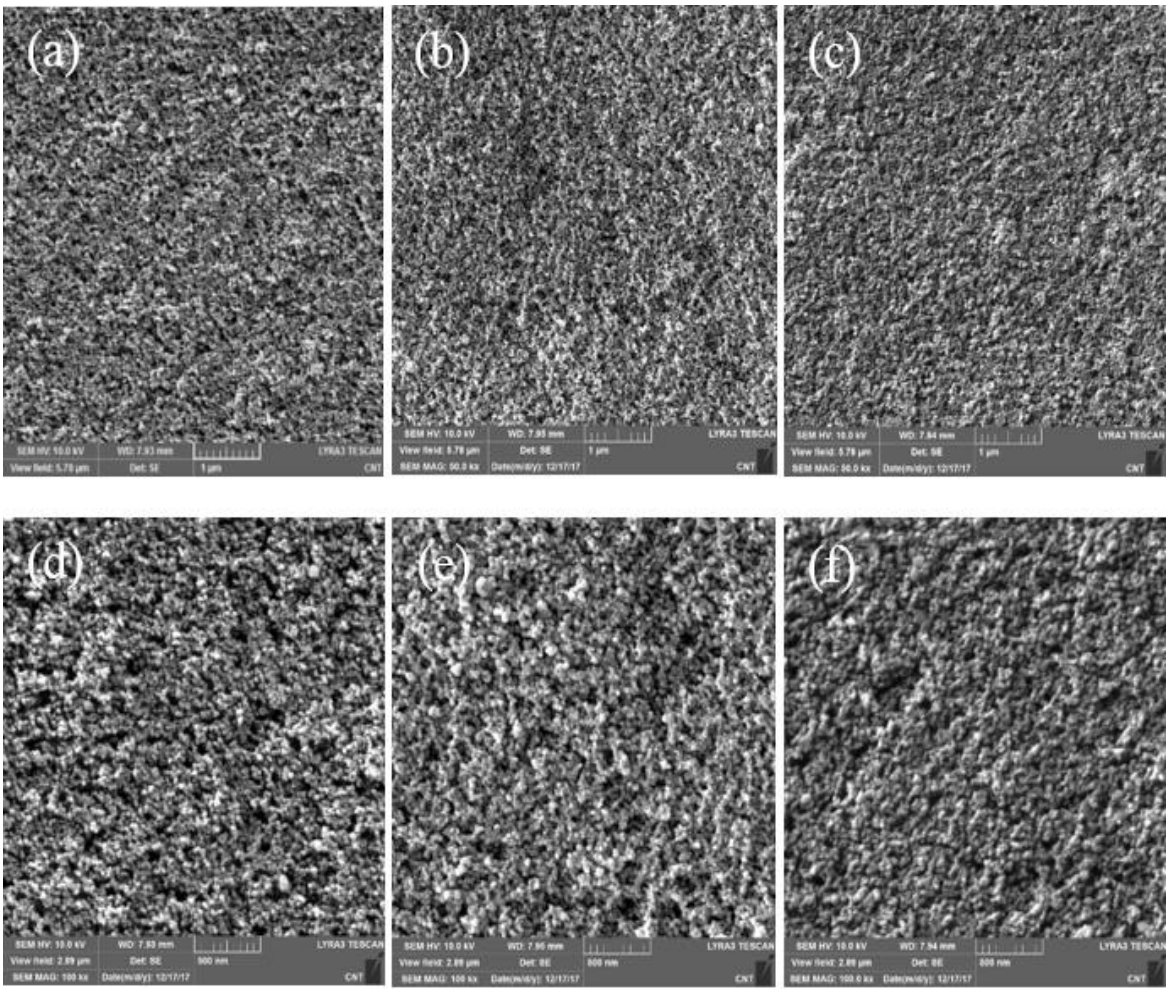

Figure 11 SEM images of (a, d) 1%WO_3-TiO_2 (b, e) 3%WO_3-TiO_2 (c, f) 5%WO_3-TiO_2 at the zoom factors of 50kx and 100kx.

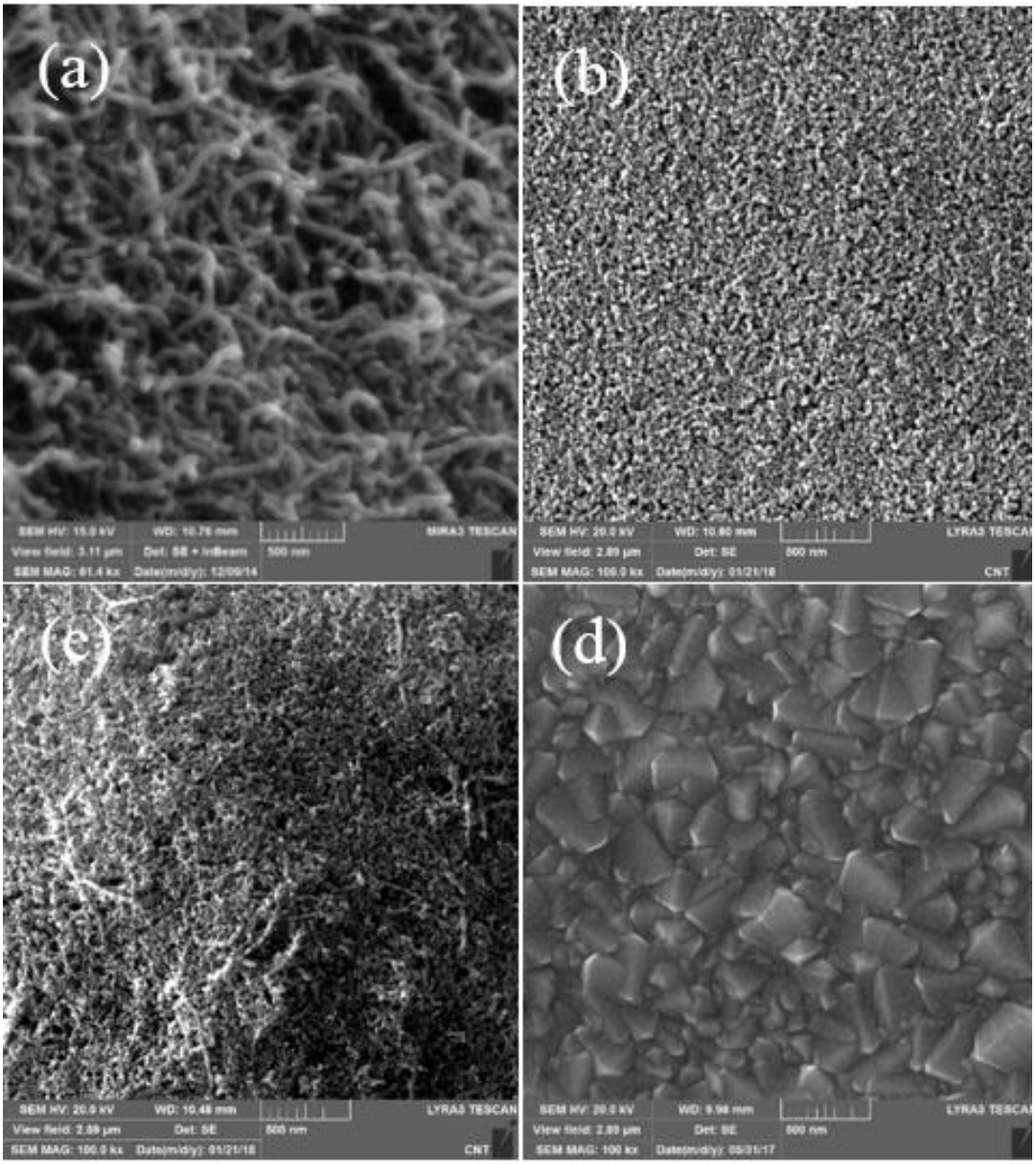

Figure 12 SEM images of (a) pure MWCNT (b) pure TiO_2 (c) MWCNTs incorporated TiO_2 counter electrode films and (d) Pt based counter electrodes film.

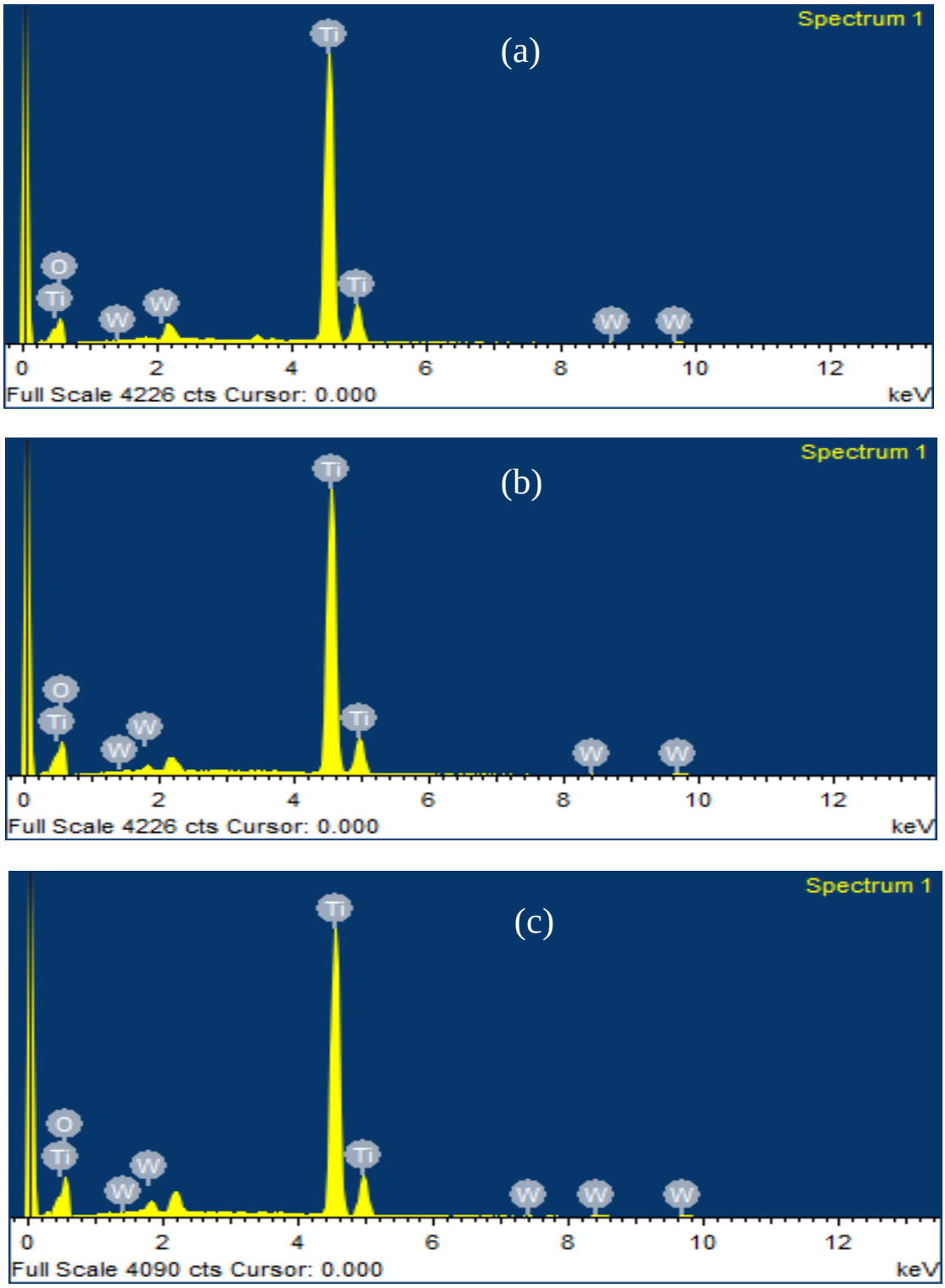

Figure 13 EDX analysis of (a) 1%WO_3-TiO_2 (b) 3%WO_3-TiO_2 (c) 5%WO_3-TiO_2 photo-anode films.

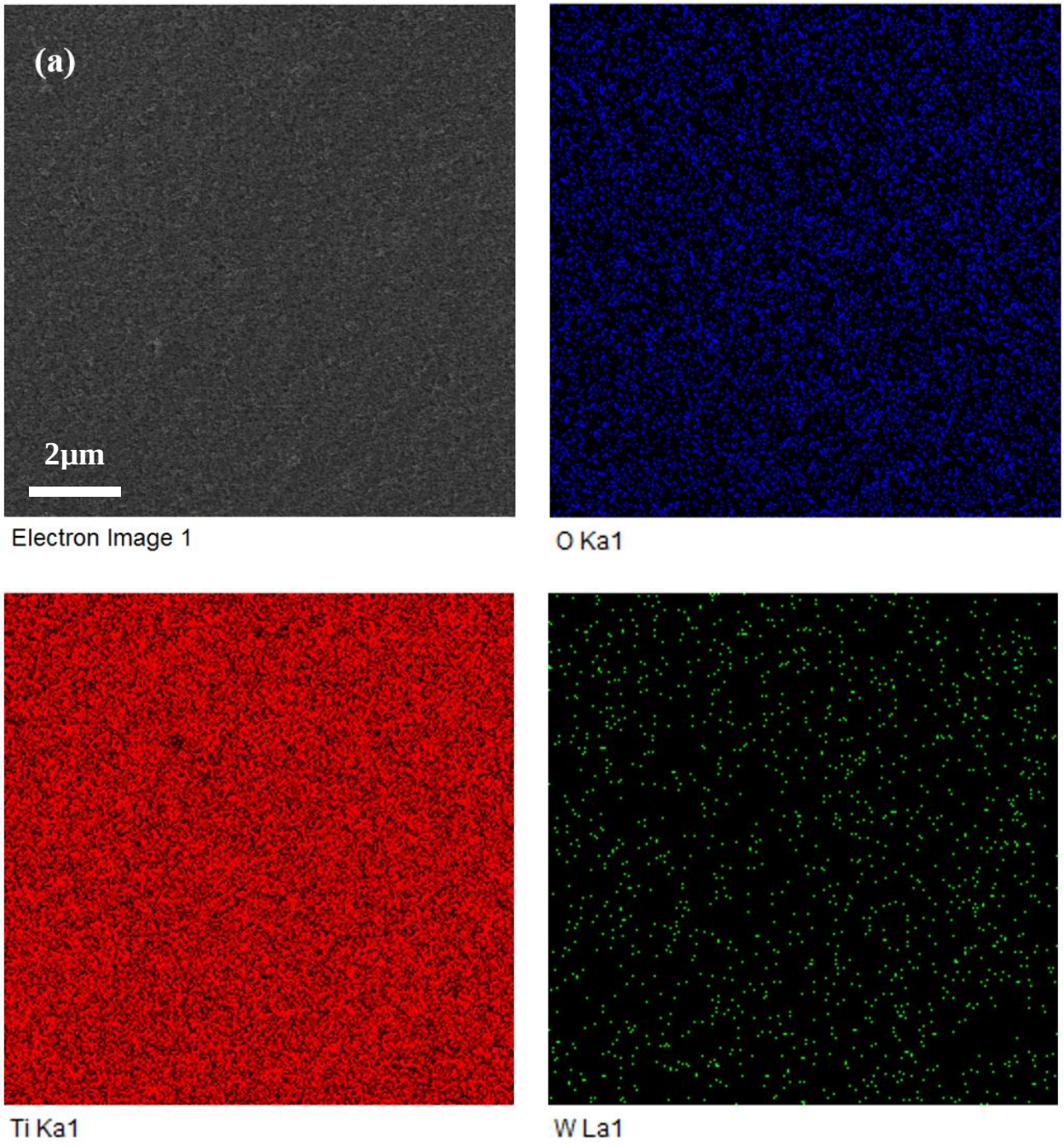

Figure 14 Elemental mapping analysis of 1%WO_3-TiO_2.

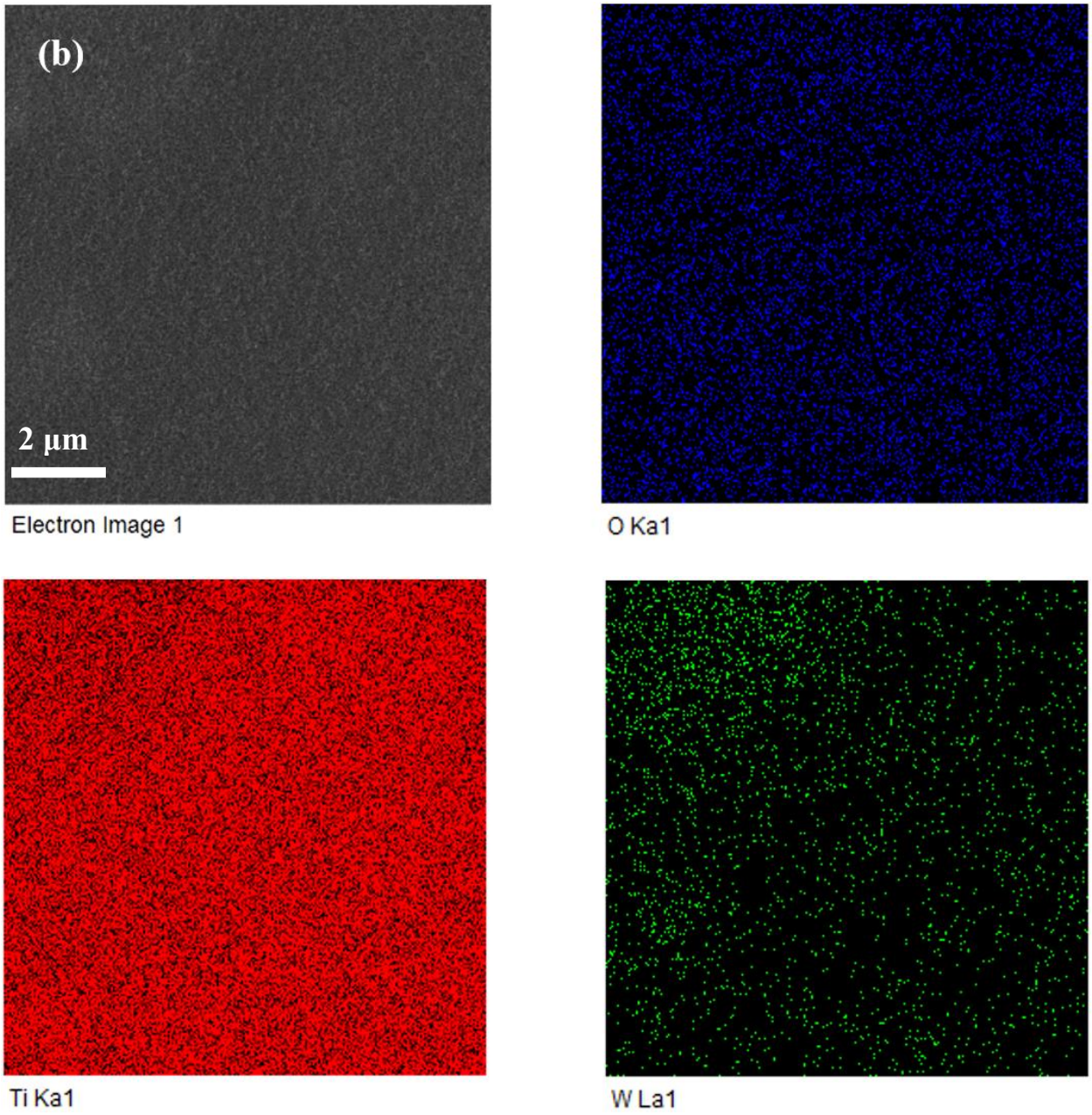

Figure 15 Elemental mapping analysis of 3%WO_3-TiO_2.

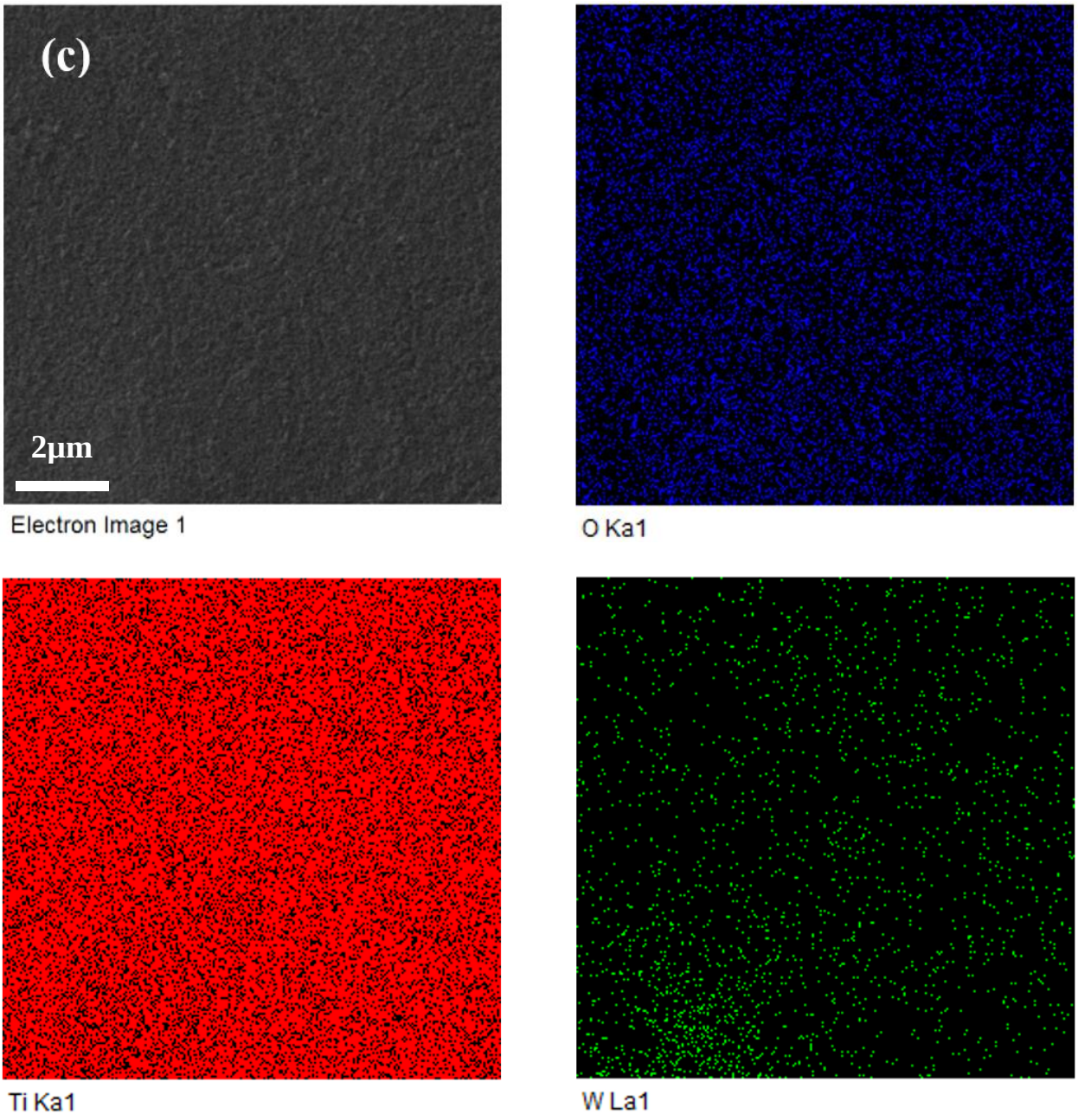

Figure 16 Elemental mapping analysis of 5%WO_3-TiO_2 photo-anode films.

Table 3 EDX elemental analysis of *n*WO_3-TiO_2 nanocomposite anode thin films

Percentage	1%WO_3-TiO_2		3%WO_3-TiO_2		5%WO_3-TiO_2	
Element	Weight (%)	Atomic (%)	Weight (%)	Atomic (%)	Weight (%)	Atomic (%)
O	35.43	62.25	40.38	67.36	42.00	69.27
Ti	64.22	37.69	58.22	32.44	54.99	30.29
W	0.35	0.05	1.40	0.20	3.01	0.43
Totals	100.00		100.00		100.00	

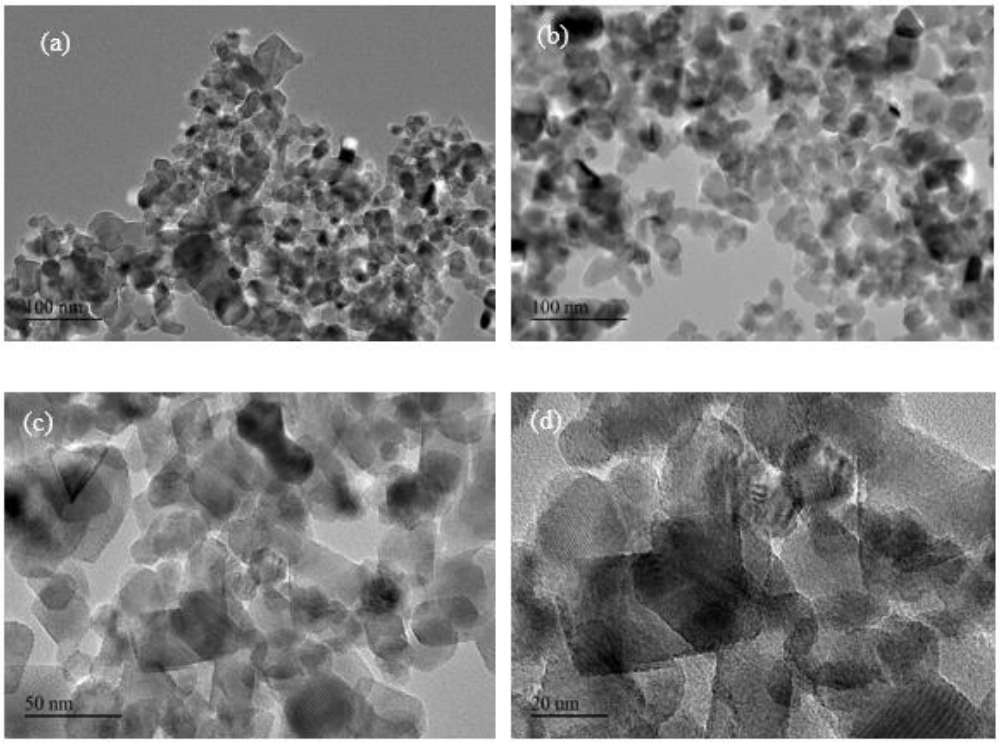

Figure 17 TEM images of (a) pure TiO_2 photo-anode film and, (b, c & d) for 1%WO_3-TiO_2, photo-anode films at different resolutions.

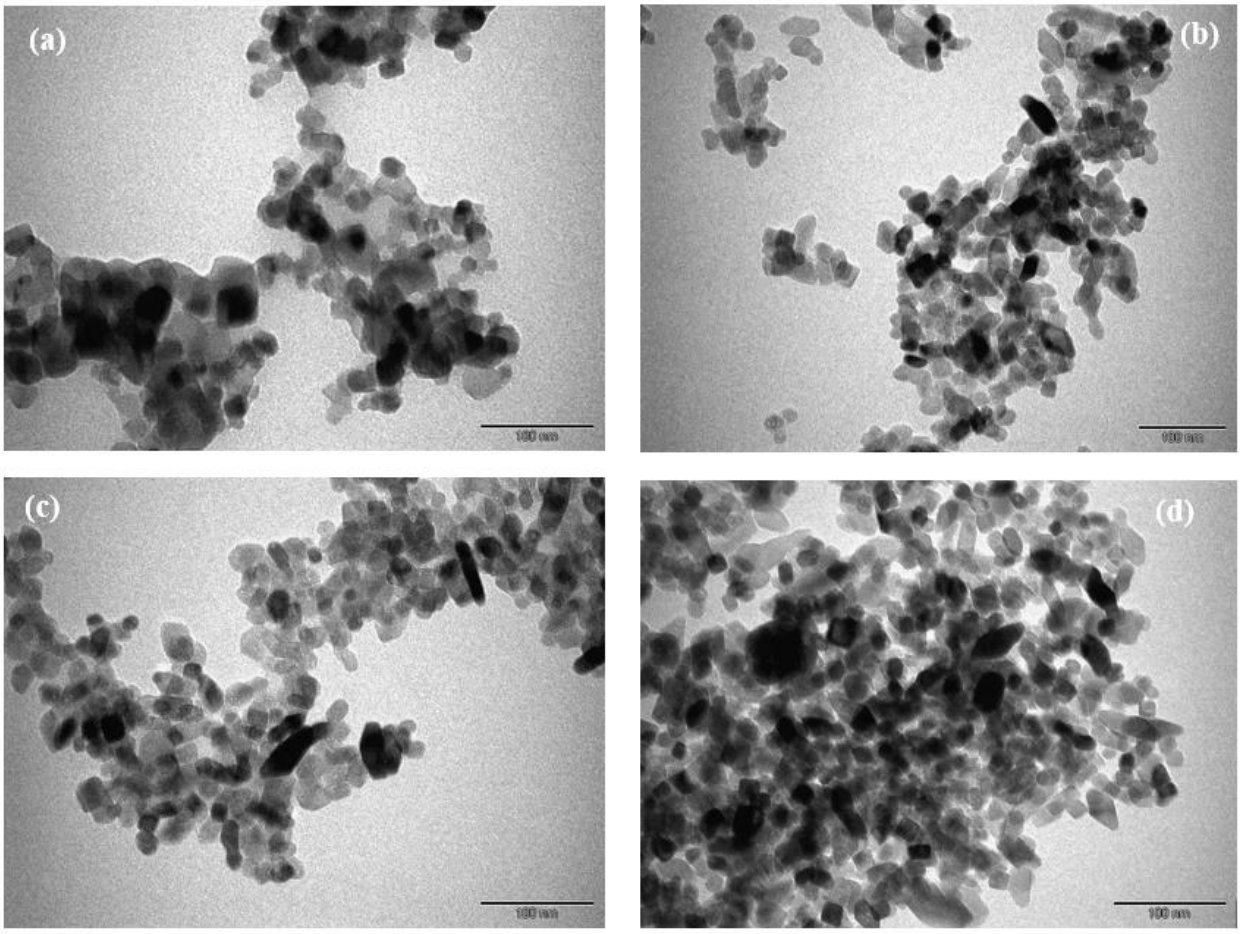

Figure 18 TEM images of (a) pure TiO_2 (b) 1%WO_3-TiO_2 (c) 3%WO_3-TiO_2 (d) 5%WO_3-TiO_2 photo-anode films.

4.2.3 XPS analysis

For further verification of elemental composition and chemical bonding between the atoms of *n*WO_3-TiO_2 photoanode films, X-ray photoelectron spectroscopy (XPS) study was carried out. Figure 19a shows the survey spectra of the photoanode (1%WO_3-TiO_2) of the best performing DSSC device, which clearly shows the presence of Ti, O, and W atoms, consistent with the EDX results. Figure 19 (b-d) shows the deconvoluted spectra of Ti 2p, O 1s and W 4f for 1%WO_3-TiO_2, and the component peak assignments of each of these

three elements accompanied by their full width half maximum (FWHM), area under the peak, and atomic percentages are listed in Table 4, which are in agreement with the literature [95], [96]. The deconvolution of Ti 2p peak shows two component peaks as shown in the Figure 19b. The XPS component peaks centered at 458.6 eV and 464.35 eV respectively for Ti $2p_{3/2}$ and Ti $2p_{1/2}$ can be assigned to Ti^{4+} [97], and the noticeable minor positive shift in the binding energies indicates the presence of WO_3 in the titanium lattice due to the establishment of W-O-Ti bonding [98]. The replacement of W^{6+} with Ti^{4+} is speculated because the ionic radius of W^{6+} (0.065 nm) is slightly larger than that of Ti^{4+} (0.062 nm) [99]. The three component peaks in Figure 19c of O 1s can be attributed to the metal oxides according to the assignments given in the literature [100], [101]. The peak corresponding to 531.58 eV may be ascribed to the Ti-O and W-O (crystal lattice oxygen) [102]. The deconvoluted W 4f XPS peak has three component peaks as shown in Figure 19d, whose assignment are listed in Table 4 based on the literature [103], [104], which shows the W $4f_{7/2}$ and W $4f_{5/2}$ peaks of tungsten component present in *n*WO_3-TiO_2 photoanode thin film. Also, the XPS analysis of 3%WO_3-TiO_2 and 5%WO_3-TiO_2 photoanodes are provided in Figure 20 and Figure 21 respectively. The component peak assignments of each of these elements along with their full width half maximum (FWHM), area under the peak, atomic percentages are listed in Table 5 and Table 6 for 3%WO_3-TiO_2 and 5%WO_3-TiO_2 respectively, which also shows the presence of Ti, O and W components in *n*WO_3-TiO_2 photoanode thin film and are in good agreement with the literature.

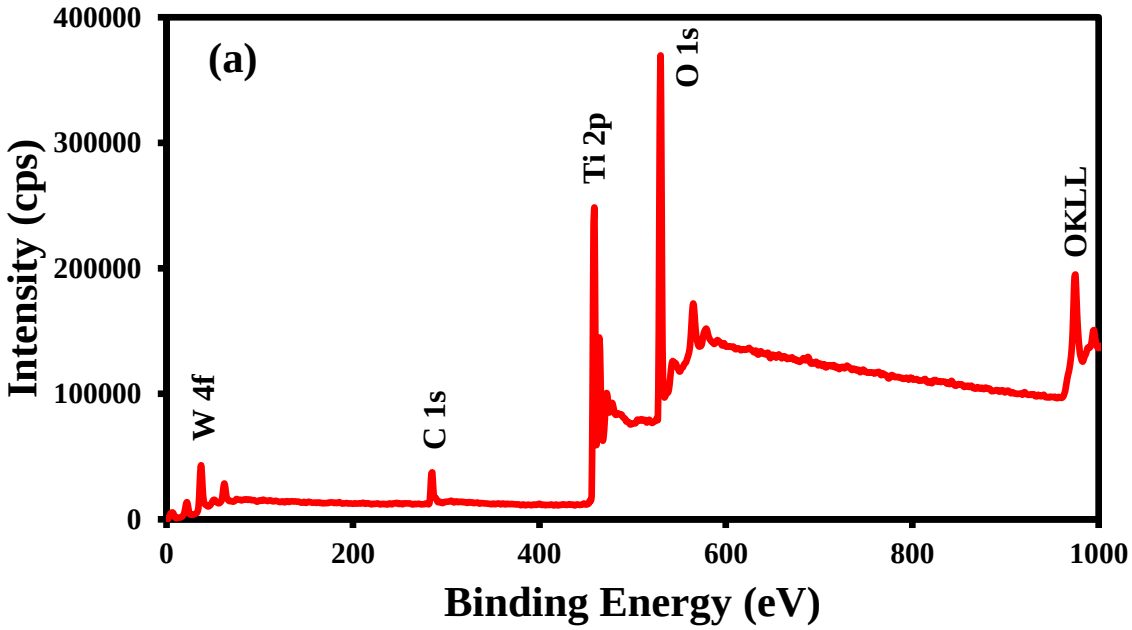
(a)
Intensity (cps)
400000
300000
200000
100000
0
W 4f
C 1s
Ti 2p
O 1s
OKLL
0
200
400
600
800
1000
Binding Energy (eV)

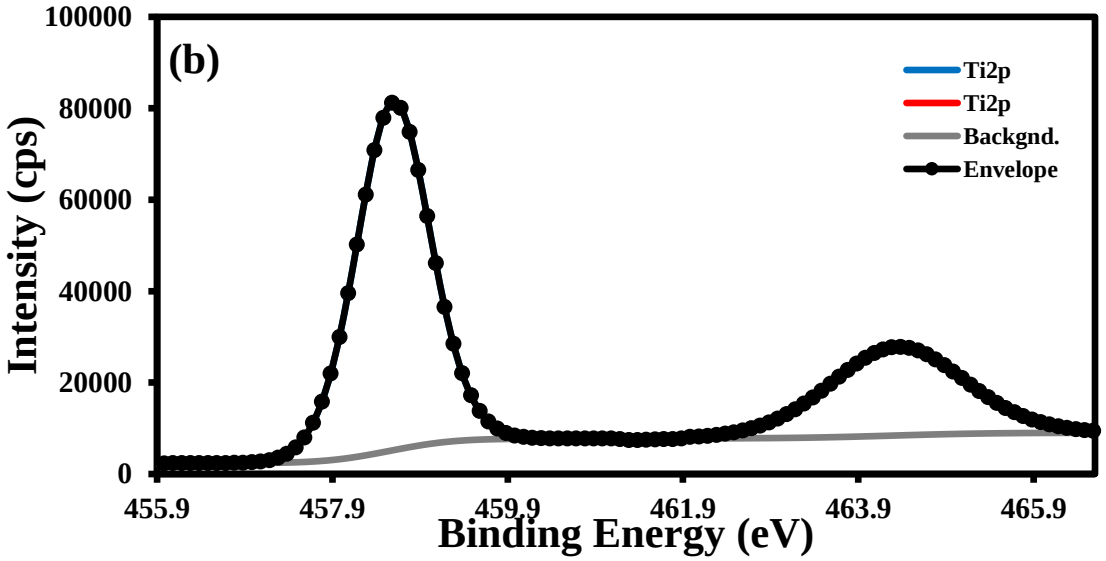
(b)
Intensity (cps)
100000
80000
60000
40000
20000
0
Ti2p
Ti2p
Backgnd.
Envelope
455.9
457.9
459.9
461.9
463.9
465.9
Binding Energy (eV)

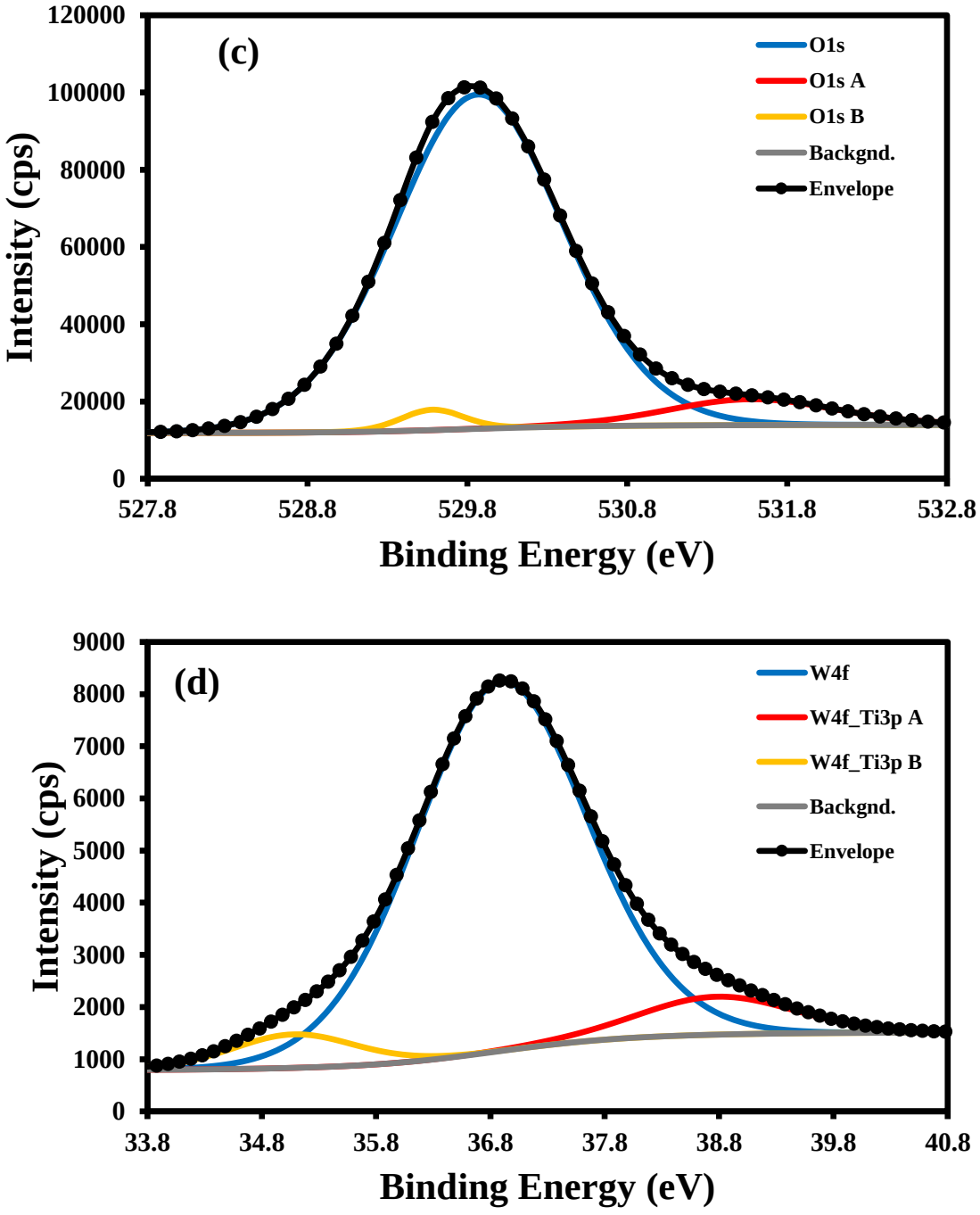

Figure 19 XPS spectra of 1%WO_3-TiO_2 thin film: (a) Survey spectra (b) deconvolution of Ti 2p peak (c) deconvolution of O 1s peak and (d) deconvolution of W 4f spectra.

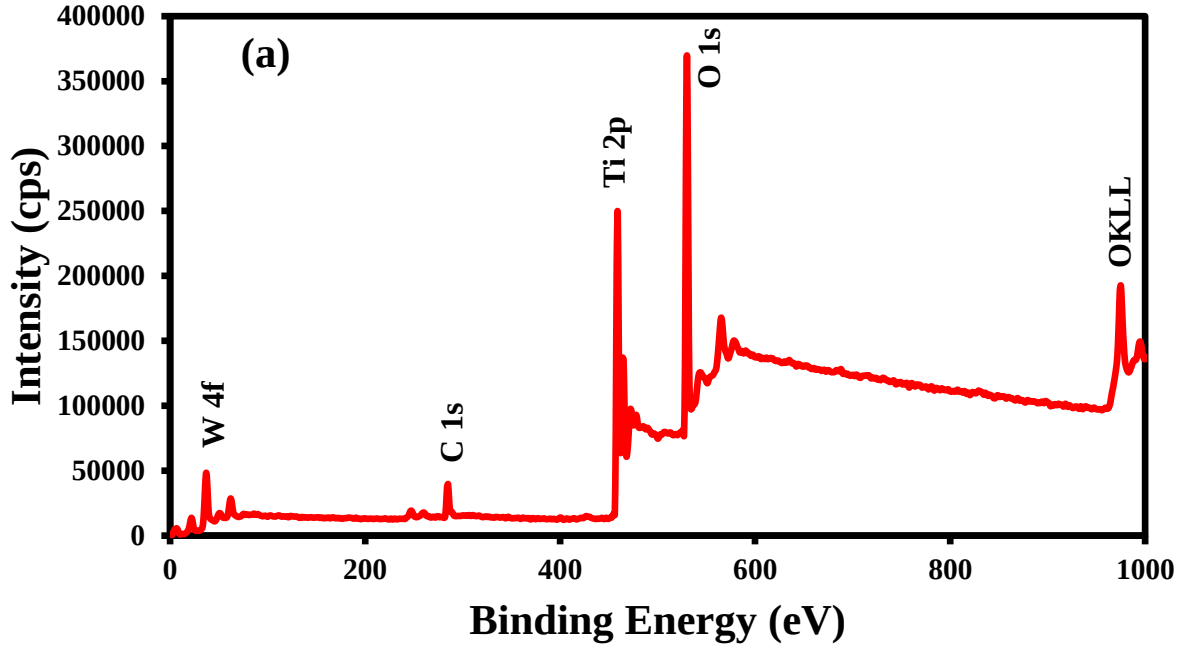
(a)
Intensity (cps)
Binding Energy (eV)
W 4f
C 1s
Ti 2p
O 1s
OKLL
400000
350000
300000
250000
200000
150000
100000
50000
0
0
200
400
600
800
1000

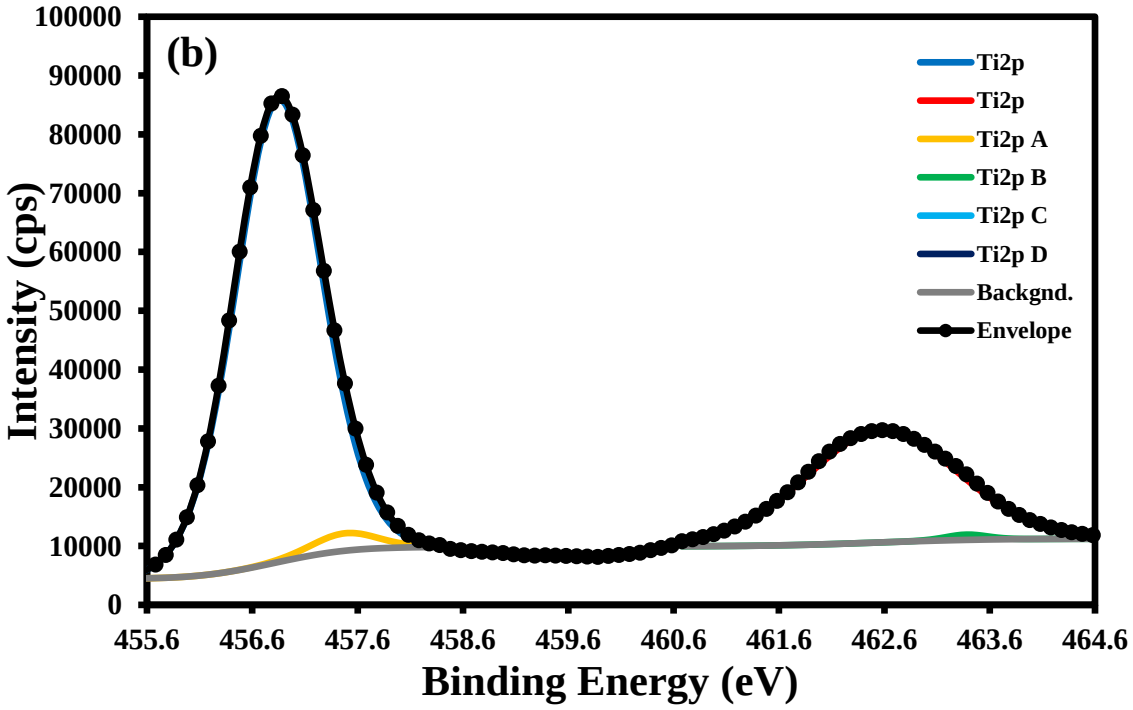
(b)
Intensity (cps)
Binding Energy (eV)
Ti2p
Ti2p
Ti2p A
Ti2p B
Ti2p C
Ti2p D
Backgnd.
Envelope
100000
90000
80000
70000
60000
50000
40000
30000
20000
10000
0
455.6
456.6
457.6
458.6
459.6
460.6
461.6
462.6
463.6
464.6

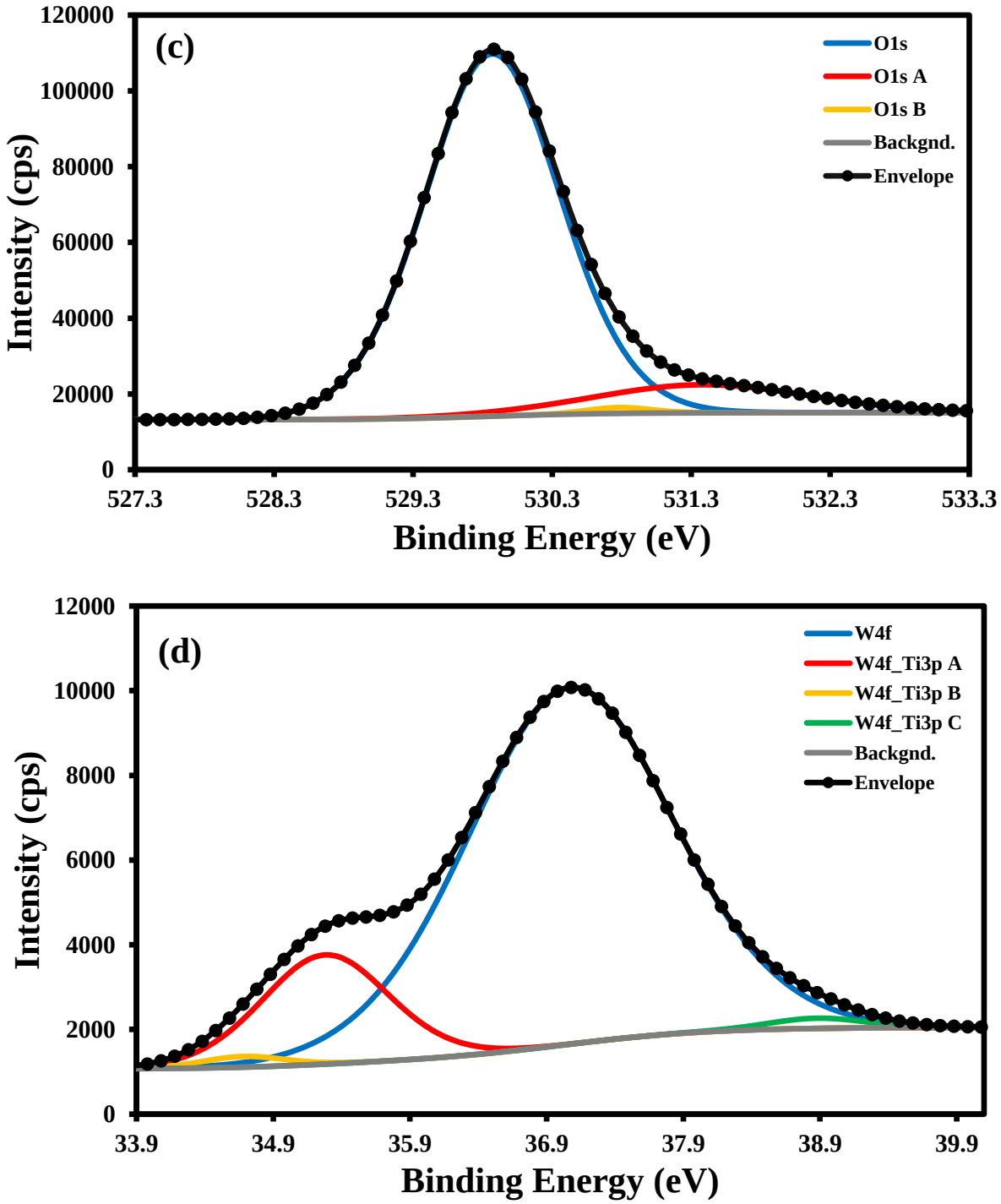

Figure 20 XPS spectra of 3%WO_3 doped TiO_2 thin film (a) Survey spectra (b) Ti 2p spectra(c) O 1s spectra (d) W 4f spectra.

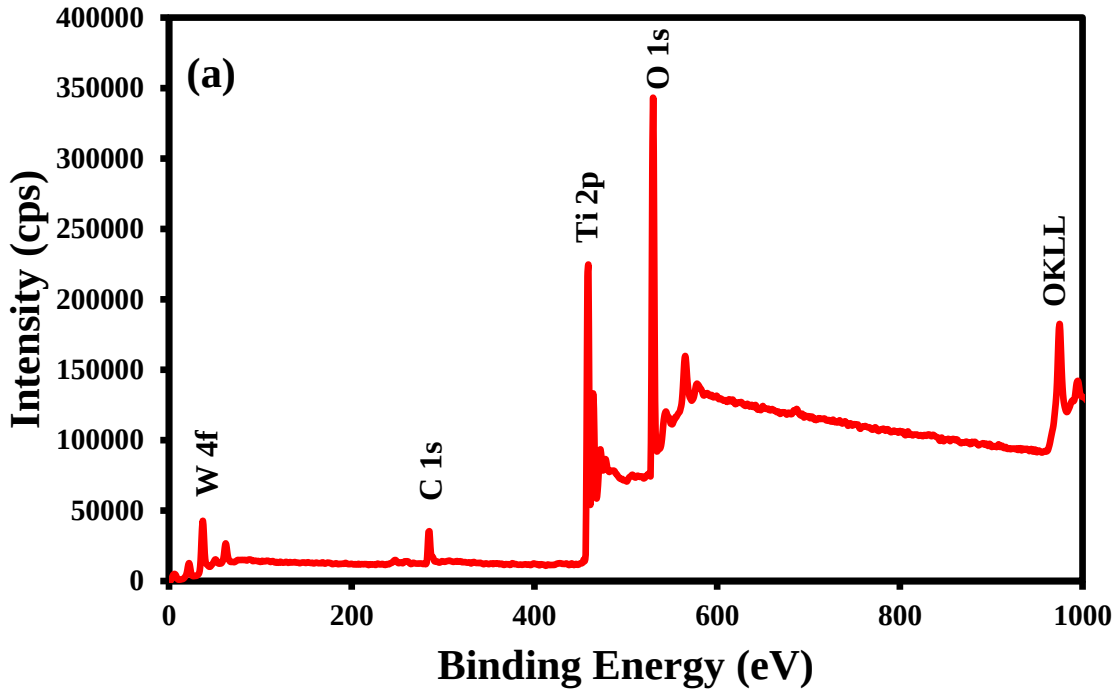
(a)
Intensity (cps)
Binding Energy (eV)
W 4f
C 1s
Ti 2p
O 1s
OKLL
400000
350000
300000
250000
200000
150000
100000
50000
0
0
200
400
600
800
1000

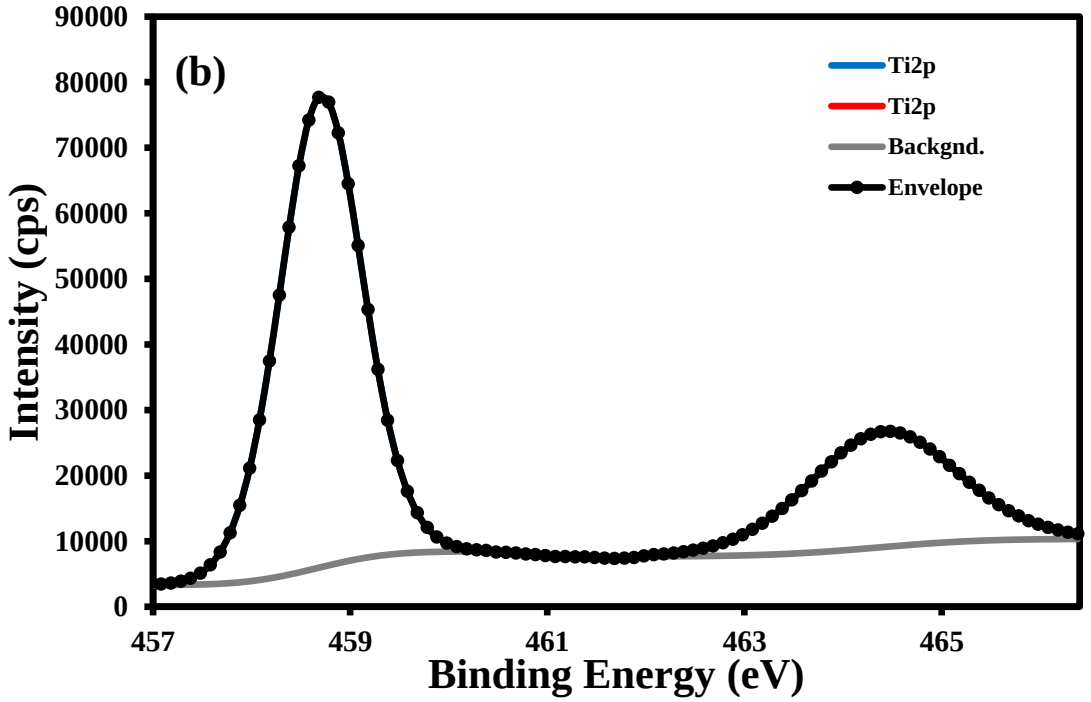
(b)
Intensity (cps)
Binding Energy (eV)
Ti2p
Ti2p
Backgnd.
Envelope
90000
80000
70000
60000
50000
40000
30000
20000
10000
0
457
459
461
463
465

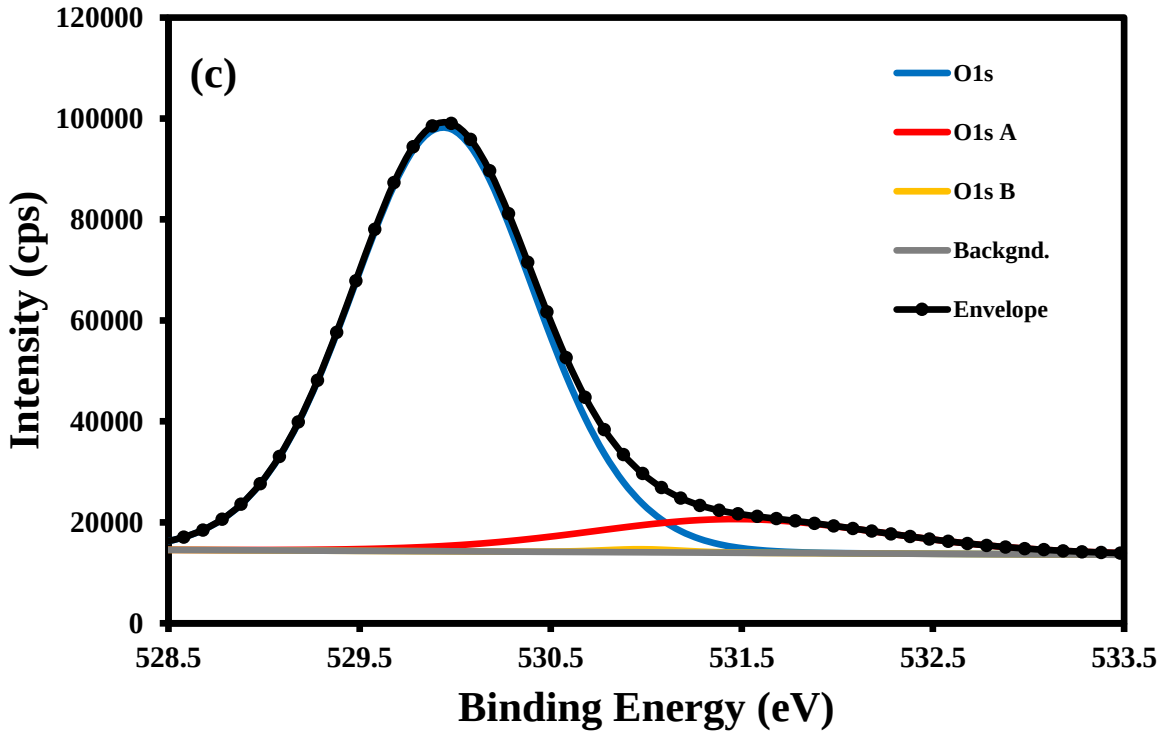

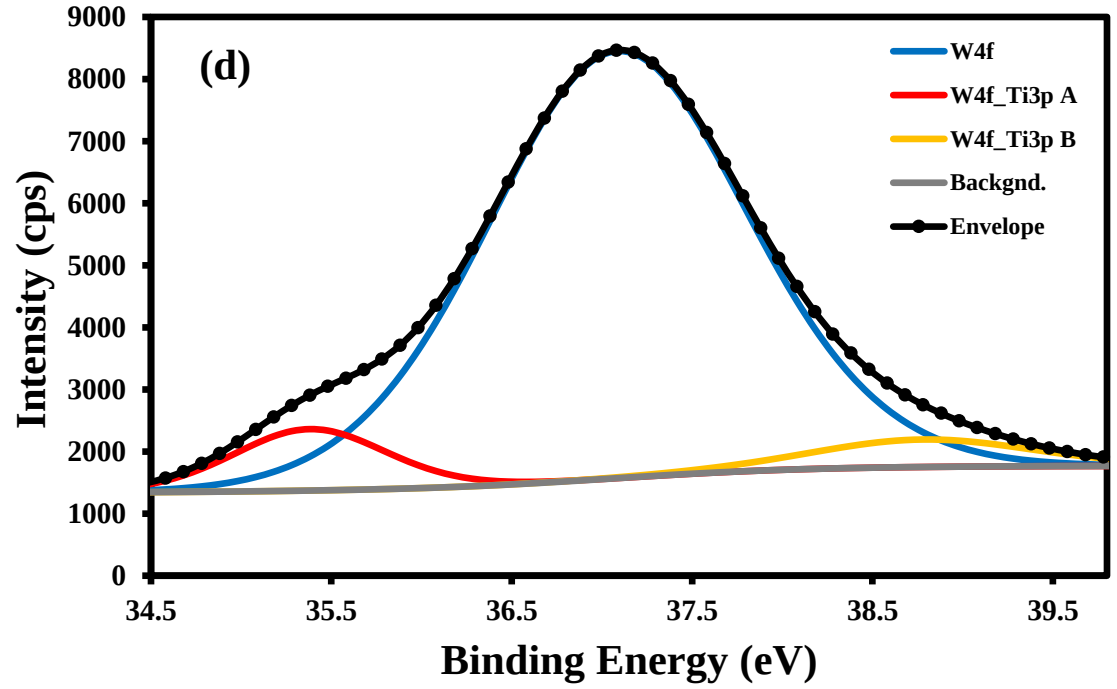

Figure 21 XPS spectra of 5%WO_3 doped TiO_2 thin film (a) Survey spectra (b) Ti 2p spectra (c) O 1s spectra (d) W 4f spectra.

Table 4 Assignments of component peaks of deconvoluted Ti 2p, O 1s and W 4f for 1%WO_3-TiO_2

Name	Peak BE	FWHM eV	Area (P) CPS.eV	Atomic %	Assignment
Ti2p	458.6	0.99	81885.97	68.33	TiO_2 ($2p_{3/2}$)
Ti2p	464.35	1.81	37906.29	31.67	TiO_2 ($2p_{1/2}$)
O1s	529.87	1.26	117857	91.03	TiO_2 (anatase)
O1s A	531.58	1.23	8963.04	6.93	Ti-O-W
O1s B	529.58	0.47	2649.06	2.05	TiO_2
W4f	36.89	1.78	13666.51	86.3	WO_3 ($4f_{7/2}$)
W4f_Ti3p A	38.78	1.62	1272.27	8.04	WO_3 ($4f_{5/2}$)
W4f_Ti3p B	35.08	1.29	896.53	5.66	W($4f_{5/2}$) metal

Table 5 Assignments of component peaks of deconvoluted Ti 2p, O 1s and W 4f for 3%WO_3-TiO_2

Name	Peak BE	FWHM eV	Area (P) CPS.eV	Atomic %	Assignment
Ti2p	456.85	0.98	83144.96	67.89	TiO_2 ($2p_{3/2}$)
Ti2p	462.58	1.75	35268.96	28.83	TiO_2 ($2p_{1/2}$)
Ti2p A	457.48	0.73	2350.28	1.92	TiO_2 ($2p_{3/2}$)
Ti2p B	463.38	0.47	448.46	0.37	TiO_2 ($2p_{1/2}$)

Ti2p C	456.48	0.45	838.87	0.68	TiO_2 ($2p_{3/2}$)
Ti2p D	462.08	0.47	373.88	0.31	TiO_2 ($2p_{1/2}$)
O1s	529.87	1.16	119620.6	88.56	TiO_2
O1s A	531.38	1.81	14535.06	10.77	Ti-O-W
O1s B	530.78	0.54	904.46	0.67	TiO_2 (anatase)
W4f	37.07	1.78	16208.66	82.35	WO_3 ($4f_{5/2}$)
W4f_Ti3p A	35.28	1.1	3062.69	15.56	W($4f_{7/2}$)
W4f_Ti3p B	34.68	0.71	195.13	0.99	W($4f_{5/2}$) metal
W4f_Ti3p C	38.88	0.83	216.22	1.1	WO_3 ($4f_{5/2}$)

Table 6 Assignments of component peaks of deconvoluted Ti 2p, O 1s and W 4f for 5%WO_3-TiO_2

			Area (P)		
Name	Peak BE	FWHM eV	CPS.eV	Atomic %	Assignment
Ti2p	458.7	0.99	77059.59	69.54	TiO_2 ($2p_{3/2}$)
Ti2p	464.41	1.79	33715.26	30.46	TiO_2 ($2p_{1/2}$)
O1s	529.94	1.14	103442.4	88.43	TiO_2 (anatase)
O1s A	531.48	1.83	13211.47	11.3	Ti-O-W
O1s B	530.98	0.49	315.79	0.27	TiO_2
W4f	37.08	1.71	12727.24	87.83	WO_3 ($4f_{5/2}$)
W4f_Ti3p A	35.38	1	1072.07	7.4	W($4f_{7/2}$)
W4f_Ti3p B	38.78	1.44	691.6	4.77	WO_3 ($4f_{5/2}$)

4.2.4 XRD analysis

The crystalline structures of nWO$_3$-TiO$_2$ films with three different WO$_3$-TiO$_2$ mass ratios (n = 1%, 3% and 5%) used in photo-anode were investigated using XRD and the results are depicted in Figure 22. It can be noticed from Figure 22 that the XRD peaks for nWO$_3$-TiO$_2$ grows as the mass ratio of WO$_3$ are increased in nWO$_3$-TiO$_2$ nanocomposite thin films. The diffraction peaks observed in Figure 19 are indexed and are labeled to differentiate the two merged XRD patterns. For the sake of comparison, the individual XRD patterns of the synthesized WO$_3$ and commercial TiO$_2$ (P25) were also recorded and shown in Figure 23. The observed XRD patterns are in close agreement with the standard spectra available in the literature and also, they tally with the XRD patterns of nWO$_3$-TiO$_2$ shown is Figure 22.

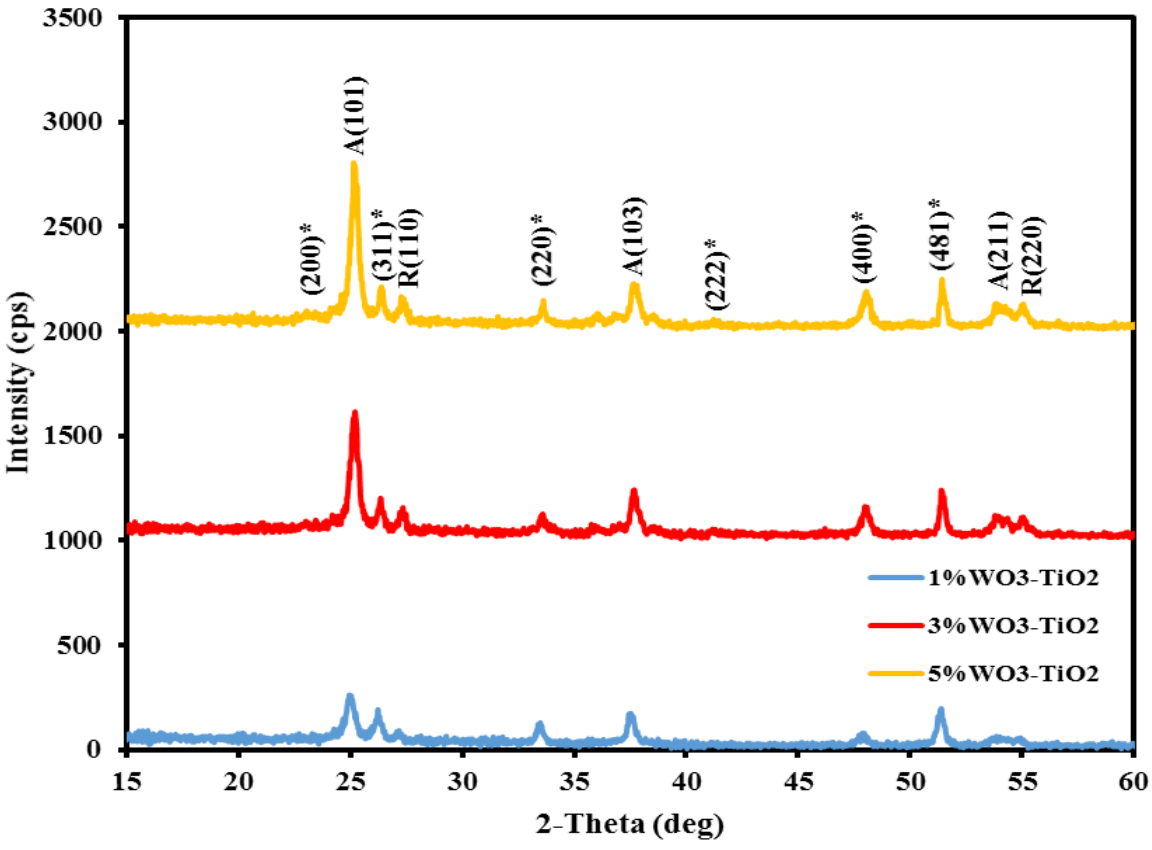

Figure 22 XRD analysis of 1%WO_3-TiO_2, 3% WO_3-TiO_2, and 5%WO_3-TiO_2, used as the photo-anodes in the fabrication of DSSCs. The XRD peaks that belong to WO_3 are marked with an asterisk (*), R and A stand for the rutile and anatase phases of TiO_2.

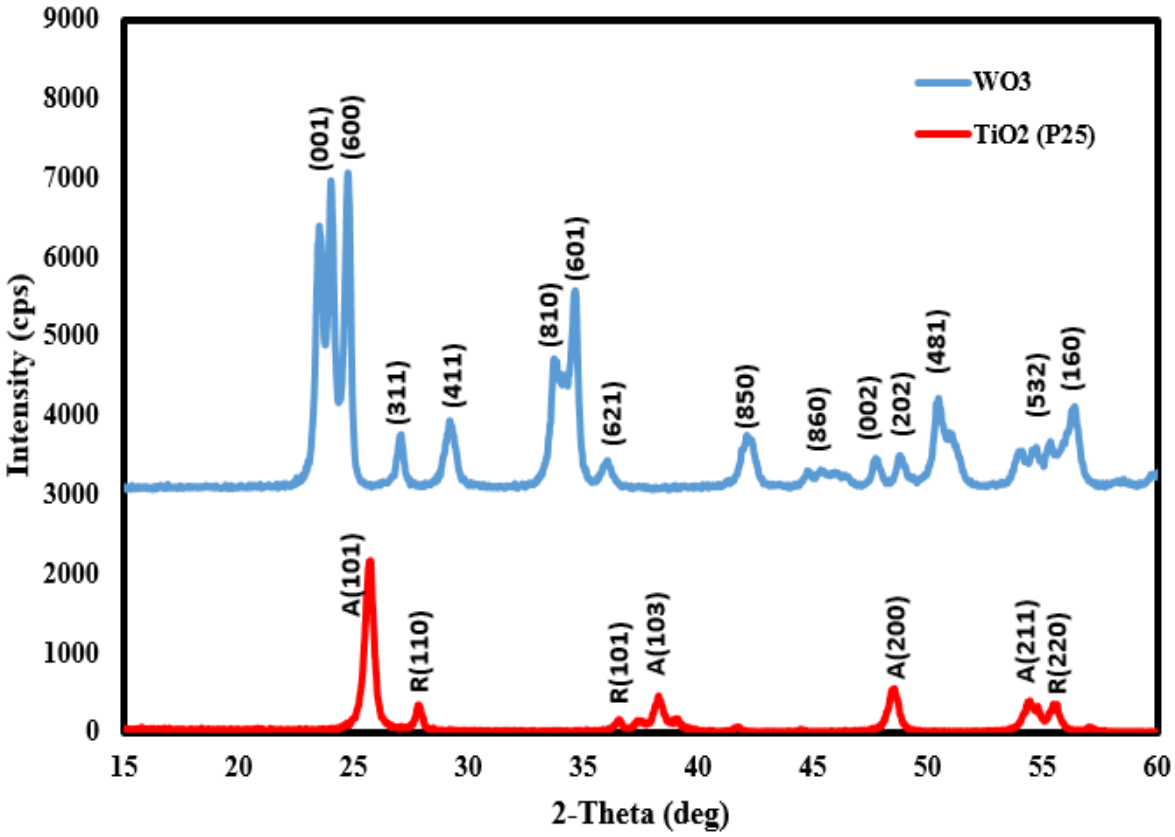

Figure 23 XRD analysis of pure WO_3 and pure TiO_2 (P25) powders.

4.3. Characterization of nMWCNT-TiO_2 nanocomposite photo-anode thin films

4.3.1 Morphological analysis of MWCNT-TiO_2 nanocomposite photo-anode

The morphological analysis of MWCNT-TiO2 nanocomposite photoanodes is provided in the section 4.3.2 below.

4.3.2 SEM, EDX, TEM and Mapping analysis

The shape, size and composition of the semiconducting material used in the photo anode of DSSC are key factors that profoundly influence the overall efficiency of DSSC, as these morphological characteristics of the surface of the photo anode are contributory factors for the effective surface area, the nature of dye loading, the formation of trap states below the conduction band, the diffusion length of the electrons in the semiconducting layer and the number of available trajectories that electrons can pass through [105], [106]. The enhanced surface area in the smaller size semiconducting particles in leads to higher dye adsorption, consequently the generation of more number of charge carriers and better photovoltaic efficiency as compared to the DSSC having photo anode with large particle size semiconducting material. However, having very small particle size may lead to increased number of grain boundaries, through which photoelectrons have to pass, hence the electron trapping probability becomes quite high [107], [108]. Moreover, the larger particles are prone to increased light scattering and hence the effective light intensity in the DSSC becomes less. Also the optimum thickness and the surface roughness of the coating on the photo anode are important factors to be considered, because the larger the thickness of the coating, the more is the absorbance of the dye, but at the same time the thicker coating imposes longer distance for the electrons to travel and this restricts the effective transportation of photo generated electrons to the electrode due to the increase of the charge transfer resistance. Although the thicker coating in the photo anode generates more photocurrent due to the increased building up of dye in the anode material, the light

transmittance and consequent light intensity reaching the system decreases. Hence, the optimum thickness should be based on the on the nature, size and the electron transport properties of the coated anode material.

The surface morphology of the coated films of pure TiO_2 and MWCNT-TiO_2 using scanning electron microscopic (SEM) images are shown in Figure 24a and 24b respectively, where the surface of TiO_2 is found to be quite porous, while in MWCNT-TiO_2 surface, MWCNT and TiO_2 particles are well dispersed. Also, the presence of a carbon peak in the EDX spectrum of MWCNT-TiO_2 in Figure 24c, confirms the anchoring of MWCNT on TiO_2 surface. More resolved surface morphological analysis of the photo anodes was conducted by tunneling electron microscope (TEM) images shown in Fig. 25a for TiO_2 and Figure 25(b-d) for MWCNT-TiO_2 with different resolutions, which gives further visual confirmation of dispersion of MWCNT in MWCNT-TiO_2 nanocomposite. The MWCNTs in photo anode are with 10-20 nm outer diameters and 1-10 μm length according to manufacturer's specification and from the TEM images, the particle size of TiO_2 is around 20 nm. It is quite clear from the TEM images in Figure 25b and 25c that many TiO_2 particles anchor on the outer surface of the long tubular MWCNT and this assembly ensures the efficient electron transport through MWCNTs. With this improved electron transport due to the presence of MWCNT, there is a possibility to increase the thickness of the coating and consequently to improve the building up of dye on the anode material and thereby increasing the photocurrent without compromising the electron injection to the electrode. The HRTEM image of MWCNT in Figure 25d shows that the spacing between adjacent MWCNT walls is around 0.346 nm. The X-ray mapping analysis in Figure 26 was carried out to verify the uniformity of the distribution of MWCNT in

TiO_2. It clearly shows the uniform distribution of MWCNT in the MWCNT-TiO_2 nanocomposite anode thin films.

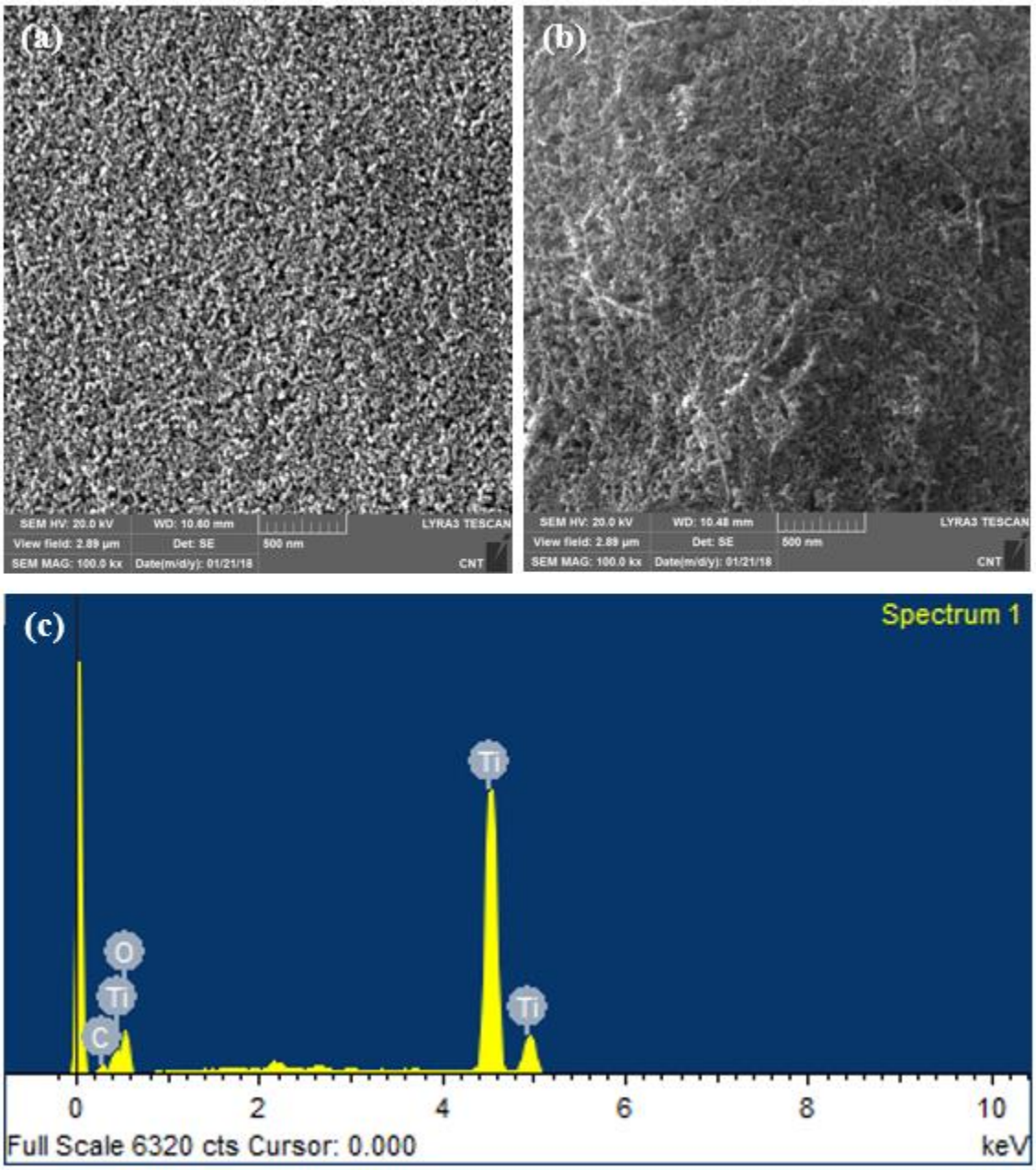

Figure 24 SEM images of **(a)** pure TiO_2 **(b)** MWCNT-TiO_2 nanocomposite **(c)** EDX analysis of MWCNT-TiO_2 anode film.

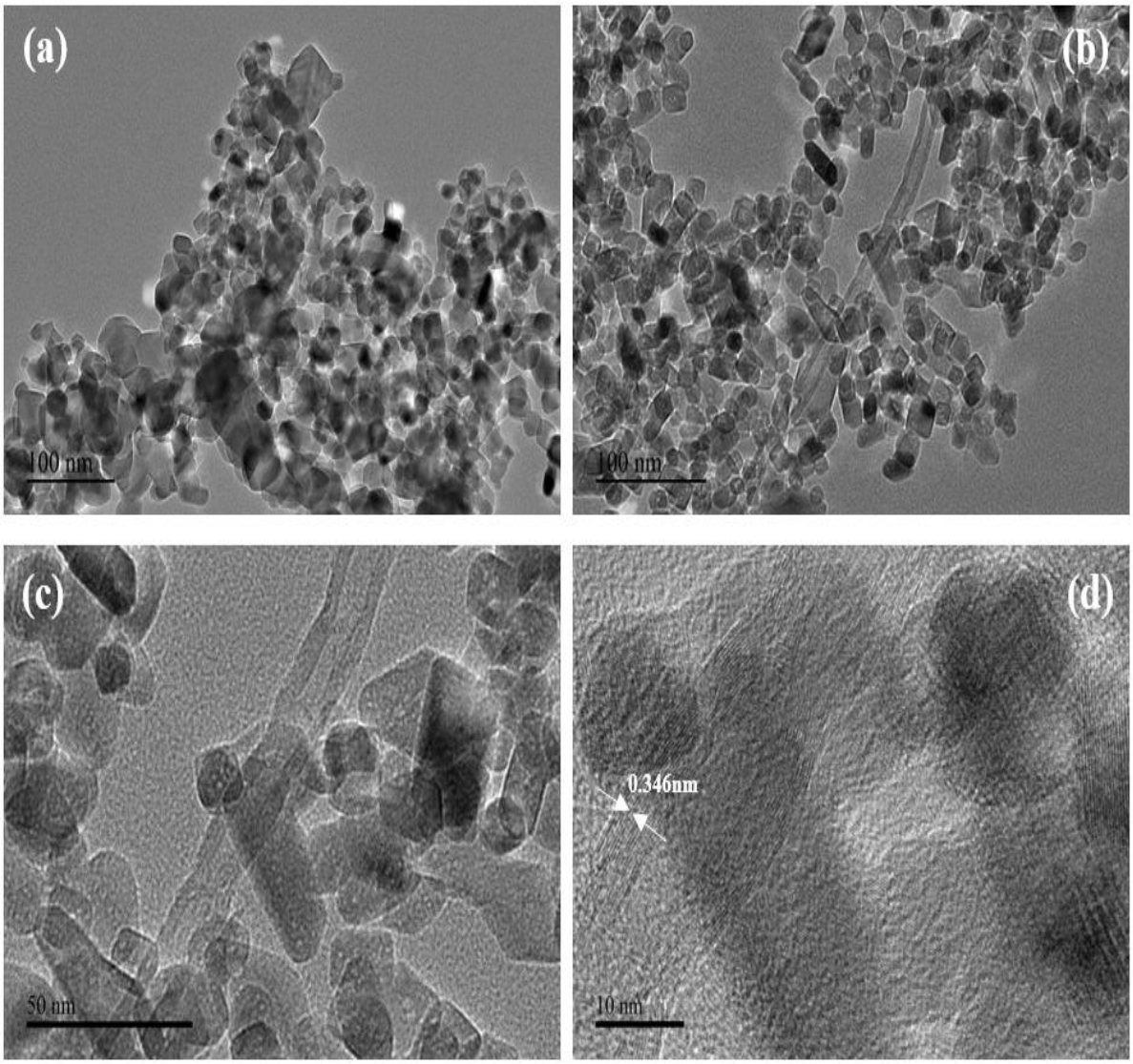

Figure 25 TEM images of **(a)** pure TiO_2 particles **(b, c & d)** MWCNT-TiO_2 nanocomposite at various resolutions.

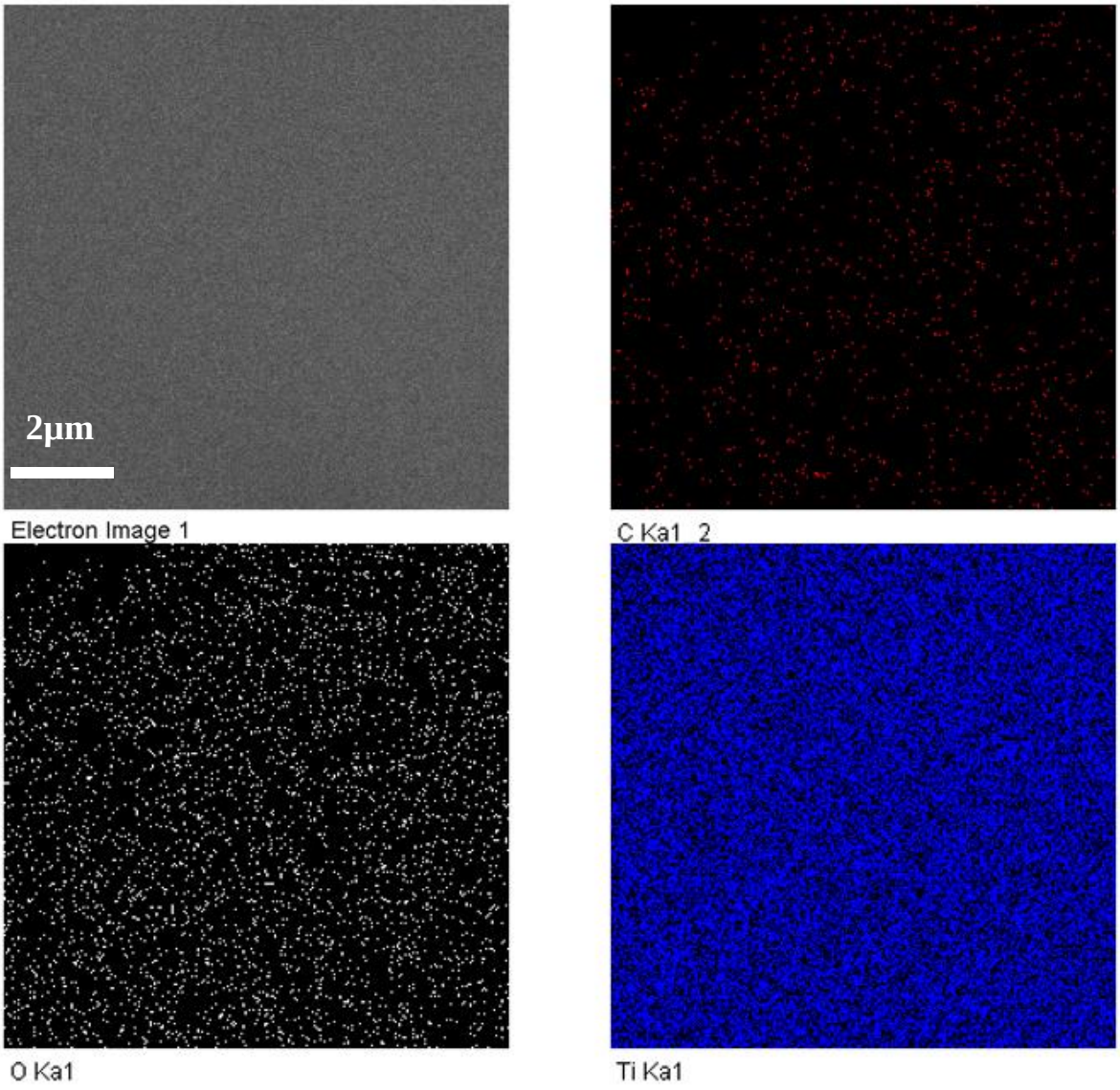

Figure 26 Mapping analysis of MWCNT-TiO_2 anode film for elemental dispersion.

4.3.3 XPS analysis of nMWCNT-TiO_2 photo-anode

The chemical states of Titanium (Ti), Oxygen (O) and Carbon (C) atoms in the MWCNT-TiO_2 composite environment and the possible bond formation between the host and the dopant atoms were investigated using XPS. The XPS survey scan in Figure 27a shows the presence of obvious Ti 2p, O 1s and C 1s peaks in the composite material, and in order to

get the intricate details, each of the peaks in the survey scan was deconvoluted to see the nature of component peaks. In Figure 27b, Ti 2p peak has two component peaks: Ti $2p_{3/2}$ centered at 459.38 eV and Ti $2p_{½}$ centered at 465 .08 eV, which appear due to the spin orbit coupling, and it can be observed that these two peaks are shifted towards higher binding energies compared to the Ti 2p peaks in pure TiO_2 which are at 458.67 eV and 464.42 eV respectively. This shifting of Ti 2p peaks indicates that Ti in MWCNT-TiO_2 composite is in a different chemical state compared to Ti in pure TiO_2 and this could be ascribed to the strong interaction between TiO_2 nanoparticles and MWCNT through Ti-O-C bonding [95], [109]. Also, in the deconvolution of O 1s peak in Figure 27c, there are two component peaks centered at 531.7 eV and 530.63 eV, which are attributed to the new chemical state of O atom in Ti-O and Ti-O-C bonds respectively in MWCNT-TiO_2. The intense Ti-O-C XPS peak of O 1s, centered at 531.18 eV and 532.18 eV indicates a strong bonding between MWCNTs and TiO_2 in MWCNT-TiO_2 composite [101], [110]. Finally, in the deconvolution of C 1s peak as shown in Figure 27d, the component peaks centered at 284.65 eV, 285.81 eV, 288.65 eV and 289.23 eV are attributed to the carbon atoms in the chemical state of C-C, C-O, C=O and O-C=O respectively in MWCNTs. The formation of Ti-O-C bond in the MWCNT-TiO_2 observed from the deconvolution of Ti 2p peak is desired as it introduces trap states in the MWCNT-TiO_2 composite. This trap state narrows down the band gap energy of MWCNT-TiO_2 composite and consequently transform the material into visible light active and makes the DSSC efficient under visible region of the solar spectrum. Also, Ti-O-C bond serves as a bridge for efficient charge transfer in the anode coating and thereby reduces the electron-hole recombination in the MWCNT-TiO_2 and increases the efficiency of the solar cell. Moreover, the anode films were prepared in

the open environment which may lead to the reduction of carbon into carbon oxides which further enhances the conductivity of the photoelectrons in the anode thin films [111]. The assignments of component peaks of deconvoluted Ti 2p, O 1s and C 1s are provided in table 7. Furthermore, the detailed XPS analysis of bare FTO glass substrate and pure TiO_2 along with their deconvoluted peaks information has been provided in Figures 28-33 and tables 8 and 9 respectively. The detailed XPS analysis of other nanocomposite samples with different MWCNT mass ratios i.e. 0.03%, 0.09% & 0.12% and their deconvoluted peaks information has been provided in Figures 34-45 and tables 10, 11 and 12 respectively.

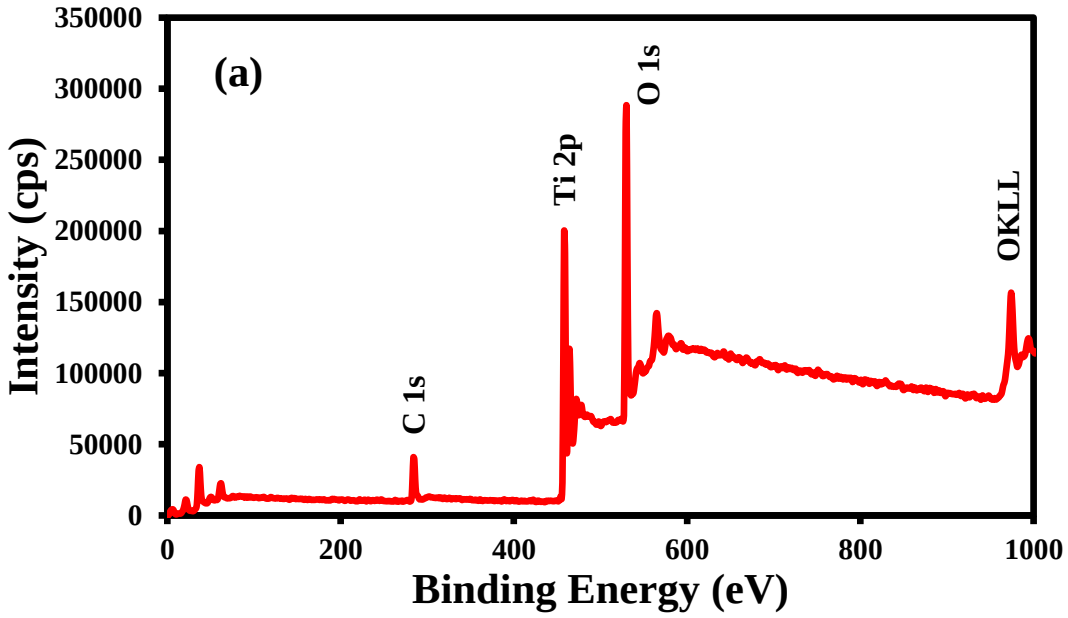

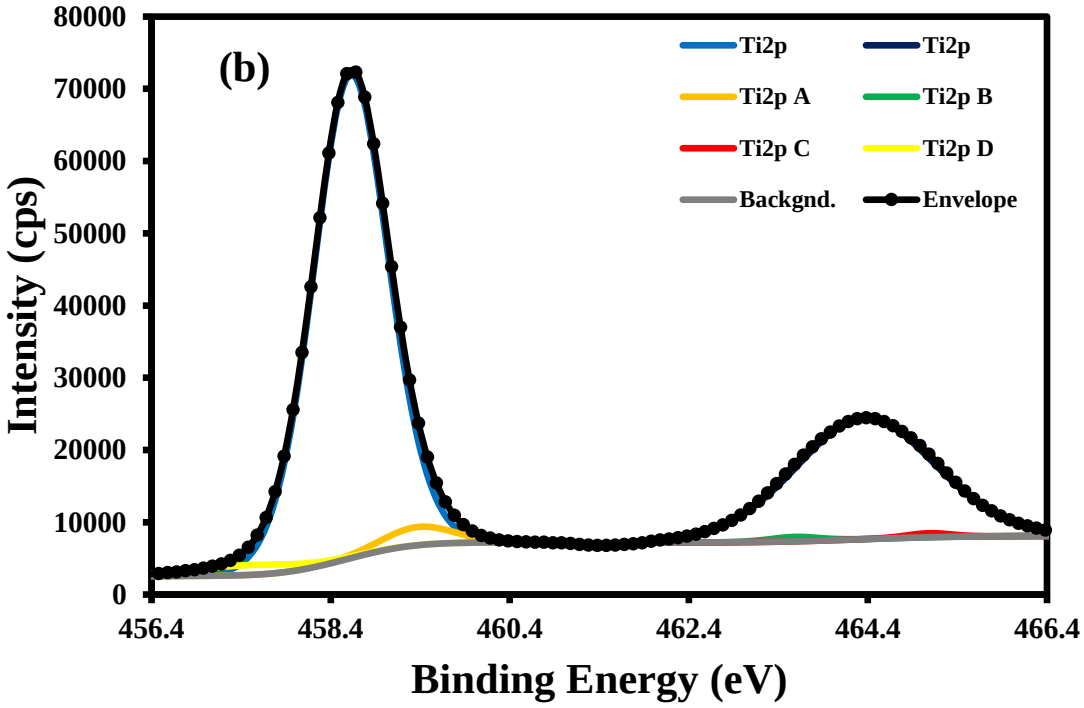
(b)
Ti2p
Ti2p
Ti2p A
Ti2p B
Ti2p C
Ti2p D
Backgnd.
Envelope
Intensity (cps)
80000
70000
60000
50000
40000
30000
20000
10000
0
456.4
458.4
460.4
462.4
464.4
466.4
Binding Energy (eV)

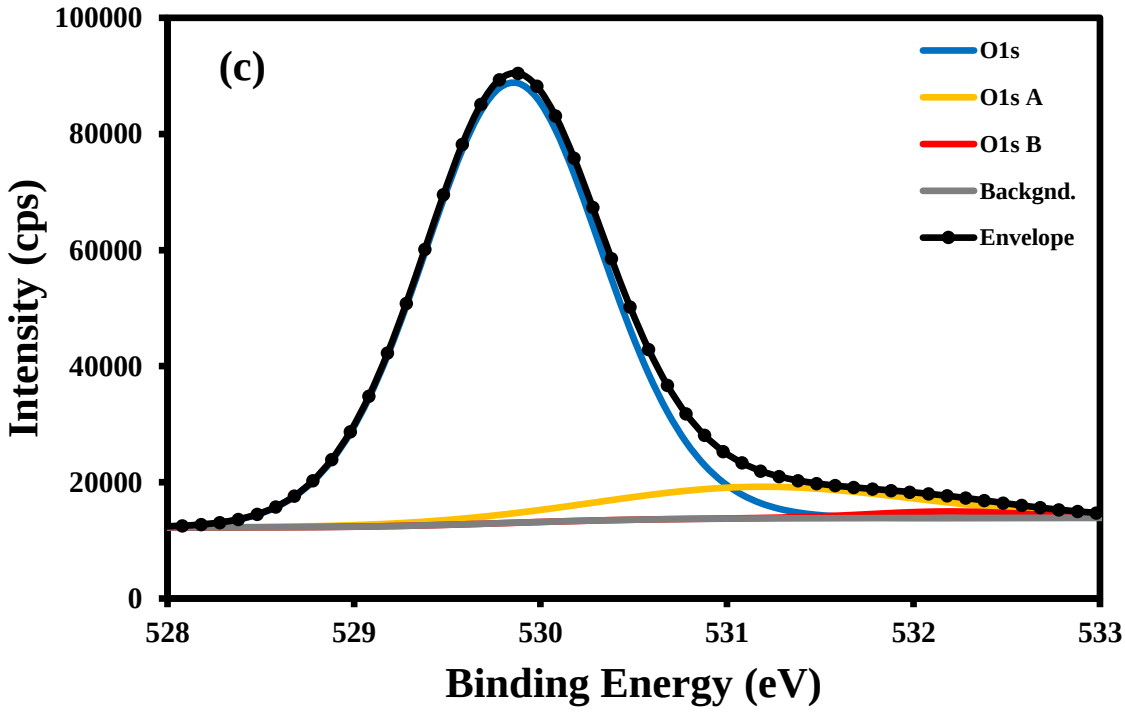
(c)
O1s
O1s A
O1s B
Backgnd.
Envelope
Intensity (cps)
100000
80000
60000
40000
20000
0
528
529
530
531
532
533
Binding Energy (eV)

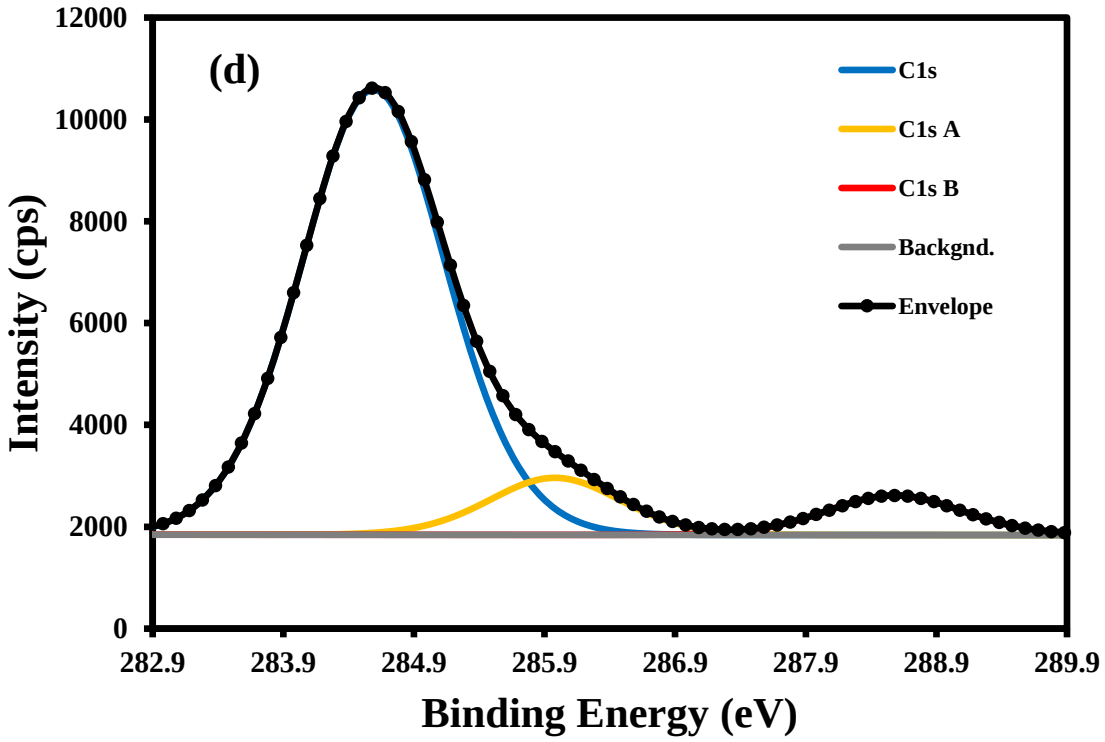

Figure 27 XPS spectra of 0.06%-MWCNT-TiO_2 thin film: **(a)** Survey spectra **(b)** deconvolution of Ti 2p peak **(c)** deconvolution of O 1s peak and **(d)** deconvolution of C 1s spectra.

Table 7 Assignments of component peaks of deconvoluted Ti 2p, O 1s and C 1s of 0.06%MWCNT-TiO_2

			Area (P)		
Name	Peak BE	FWHM eV	CPS.eV	Atomic %	Assignment
Ti2p	458.62	0.99	71521.17	64.8	TiO_2 ($2p_{3/2}$)
Ti2p	464.37	1.85	33400.89	30.3	TiO_2 ($2p_{1/2}$)
Ti2p A	459.38	0.94	2575.51	2.33	TiO_2 ($2p_{3/2}$)
Ti2p B	463.58	0.66	427.2	0.39	TiO_2 ($2p_{1/2}$)
Ti2p C	465.08	0.58	345.55	0.31	TiO_2 ($2p_{1/2}$)

Ti2p D	457.48	1.4	2069	1.87	TiO_2 ($2p_{3/2}$)
O1s	529.85	1.14	93671.26	87.85	SnO_2
O1s A	531.18	1.98	11734.1	11.01	Carbonates
O1s B	532.18	1	1213.18	1.14	Carbonates
C1s	284.59	1.31	12388.43	83.3	C-C
C1s A	285.98	1.19	1447.19	9.73	C-O
C1s B	288.58	1.23	1035.22	6.97	C=O

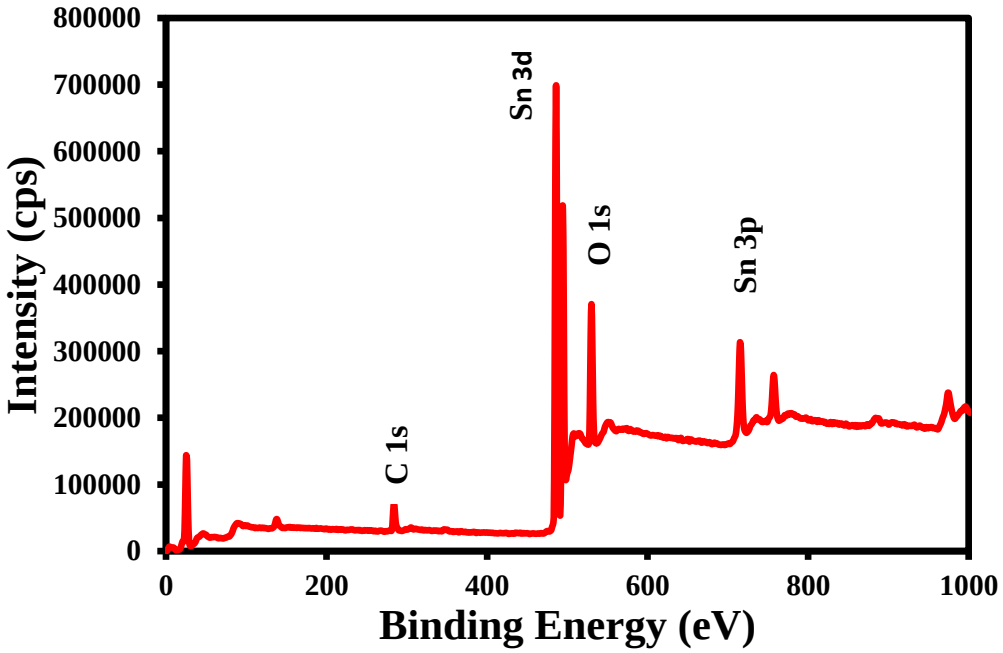

Figure 28 Survey spectra for Bare FTO glass.

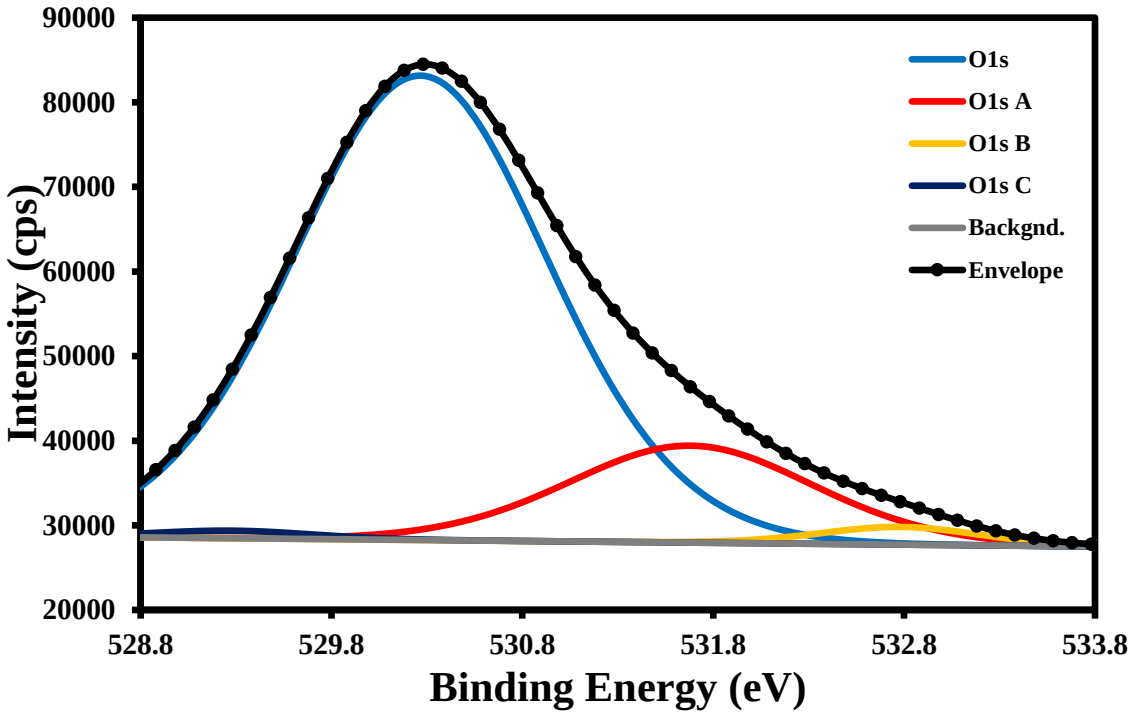

Figure 29 Deconvoluted peaks for O1s element of Bare FTO glass.

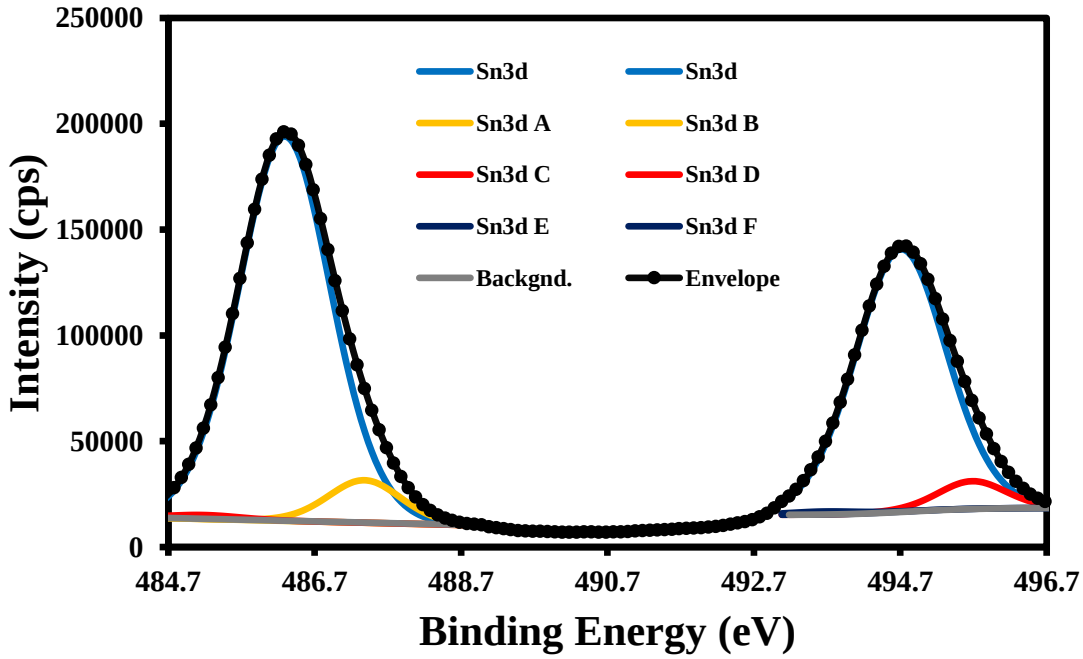

Figure 30 Deconvoluted peaks for Sn3d element of Bare FTO glass.

Table 8 Deconvoluted peaks information for Sn3d and O 1s for bare FTO

Name	Peak BE	FWHM eV	Area (P) CPS.eV	Atomic %
O1s	530.27	1.58	93931.5	81
O1s A	531.68	1.52	18855.24	16.27
O1s B	532.78	0.98	2221.06	1.92
O1s C	529.28	0.98	945.26	0.81
Sn3d	486.29	1.49	292391.6	54.61
Sn3d	494.71	1.47	197565.6	36.97
Sn3d A	487.38	1.17	25519.49	4.77
Sn3d B	487.38	1.22	0	0
Sn3d C	485.19	1.17	2382.53	0.44
Sn3d D	495.68	1.1	15494.25	2.9
Sn3d E	495.68	1.14	0	0
Sn3d F	493.66	1.1	1646.38	0.31

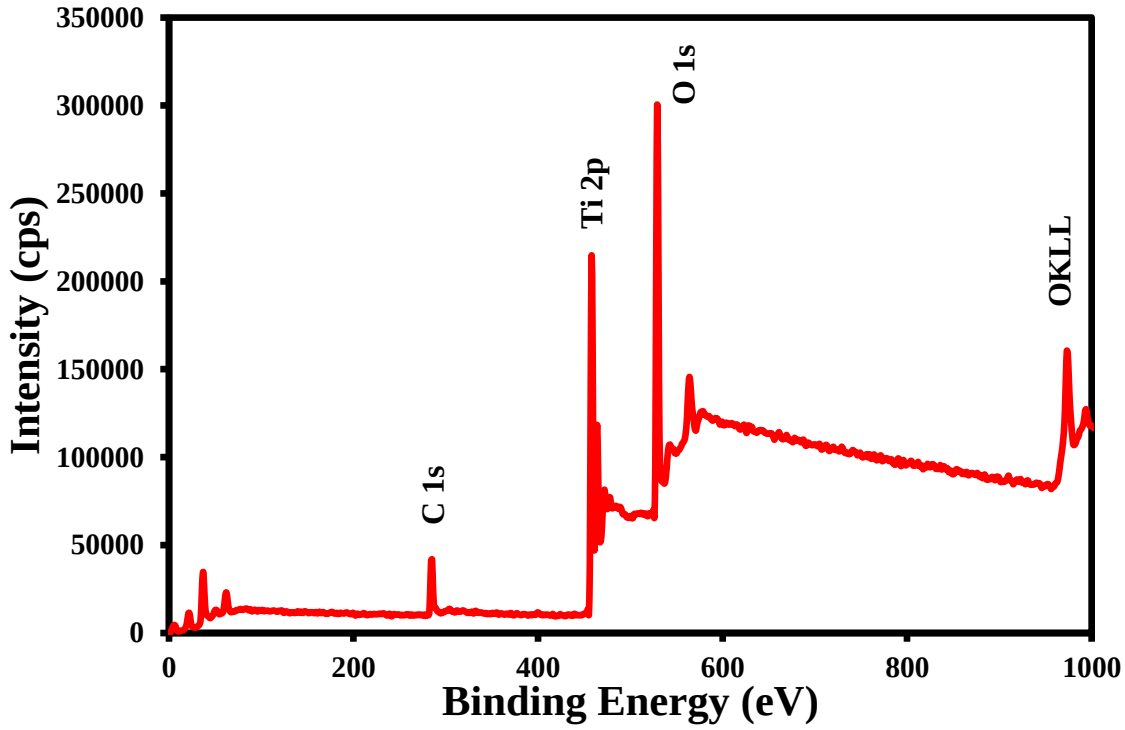

Figure 31 Survey spectra of pure TiO_2 thin film on FTO glass substrate.

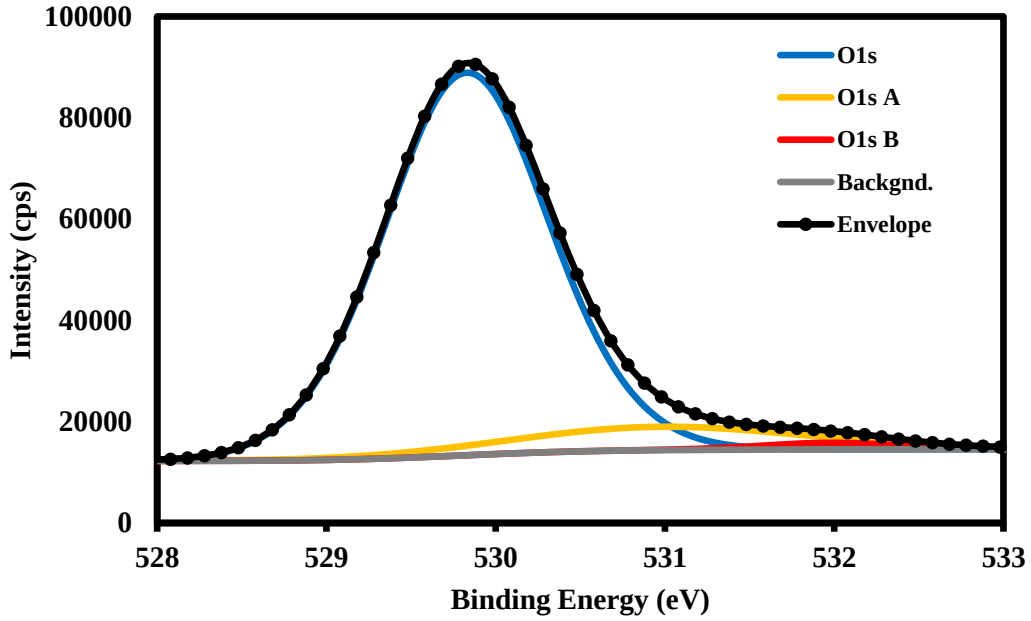

Figure 32 Deconvoluted peaks for O1s element of pure TiO_2 on FTO glass substrate.

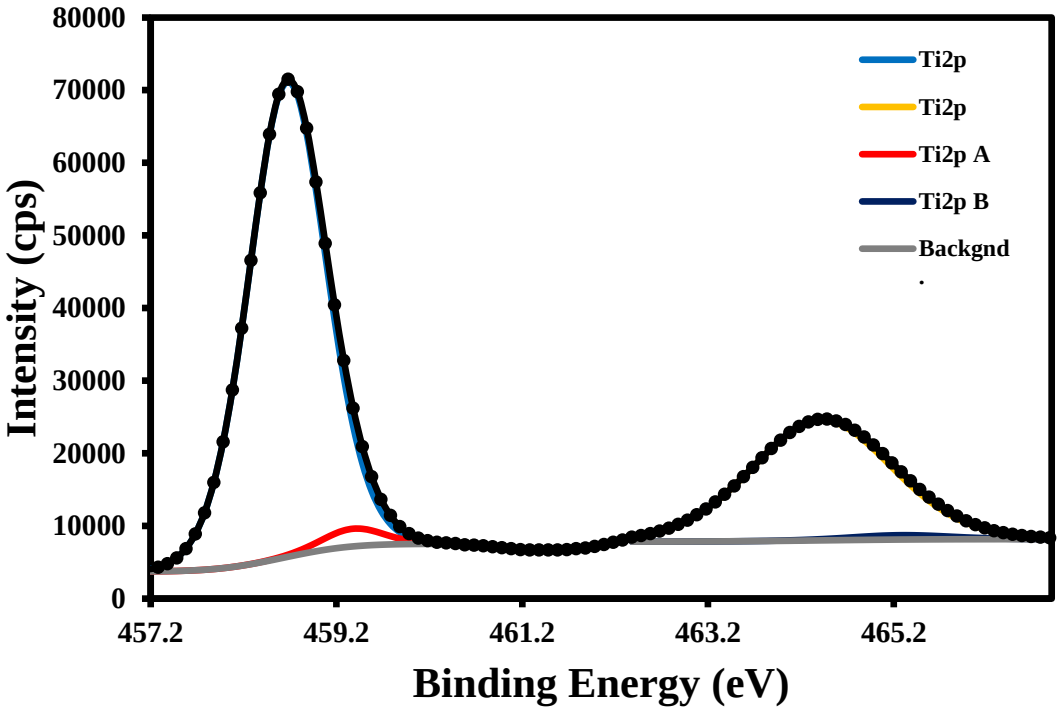

Figure 33 Deconvoluted peaks of Ti 2p element of pure TiO_2 on FTO glass substrate.

Table 9 Deconvoluted peaks information for Ti 2p and O 1s for pure TiO_2

			Area (P)	
Name	Peak BE	FWHM eV	CPS.eV	Atomic %
Ti2p	458.67	0.99	69966.37	66.75
Ti2p	464.42	1.8	31969.24	30.54
Ti2p A	459.38	0.77	2029.24	1.94
Ti2p B	465.28	1.25	811.25	0.78
O1s	529.83	1.15	93879.58	89.15
O1s A	530.98	2.03	10095.25	9.59
O1s B	531.98	0.94	1329.41	1.26

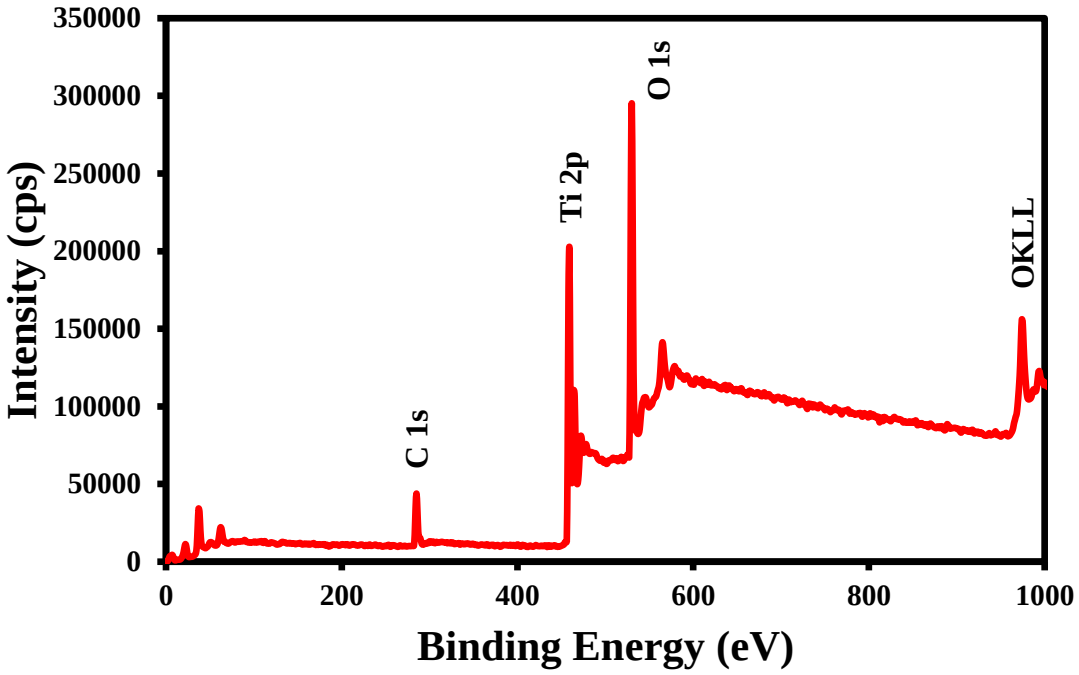

Figure 34 Survey spectra of 0.03%MWCNT-TiO_2 thin film on FTO glass substrate.

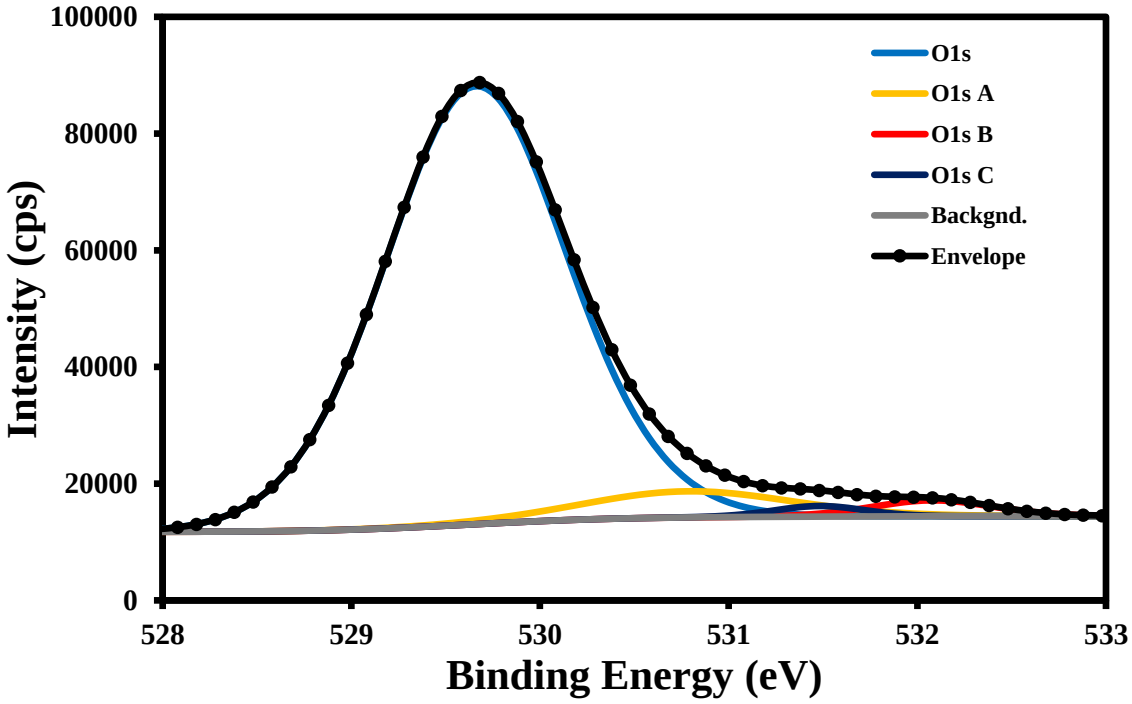

Figure 35 Deconvoluted peaks of O 1s element of 0.03%MWCNT-TiO_2 thin film on FTO glass substrate.

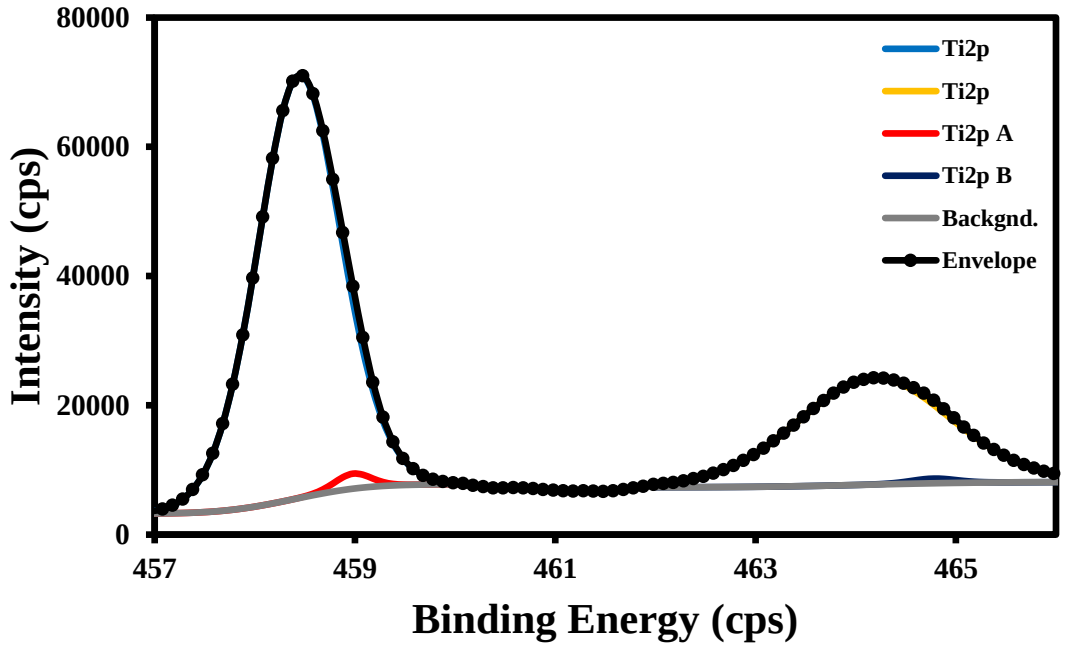

Figure 36 Deconvoluted peaks of Ti 2p element of 0.03%MWCNT-TiO_2 on FTO glass substrate.

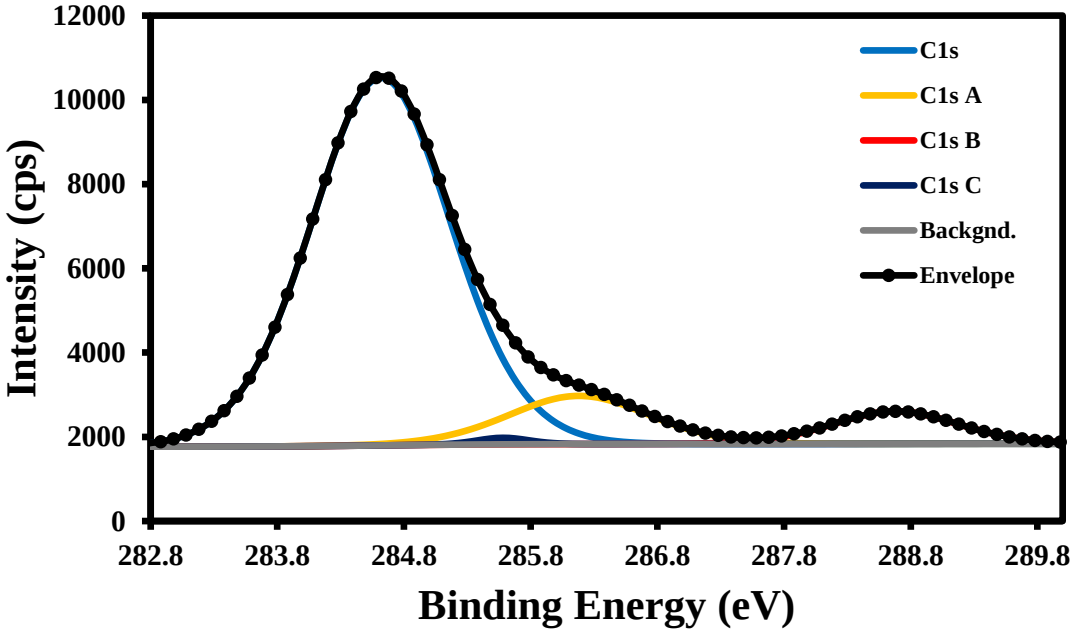

Figure 37 Deconvoluted peaks for C1s element of 0.03%MWCNT-TiO_2 on FTO glass substrate.

Table 10 Deconvoluted peaks information for Ti 2p, O 1s and C 1s for 0.03%MWCNT-TiO_2.

Name	Peak BE	FWHM eV	Area (P) CPS.eV	Atomic %
C1s	284.62	1.3	12289.17	82.07
C1s A	286.18	1.31	1622.08	10.84
C1s B	288.68	1.17	979.97	6.55
C1s C	285.58	0.49	81.04	0.54
O1s	529.66	1.14	92941.6	90.66
O1s A	530.78	1.29	6249.29	6.1
O1s B	532.08	0.75	2216.63	2.16
O1s C	531.48	0.56	1102.54	1.08
Ti2p	458.44	0.99	70041.65	67.43
Ti2p	464.18	1.82	32317.43	31.15
Ti2p A	458.98	0.43	1068.46	1.03
Ti2p B	464.78	0.52	406.18	0.39

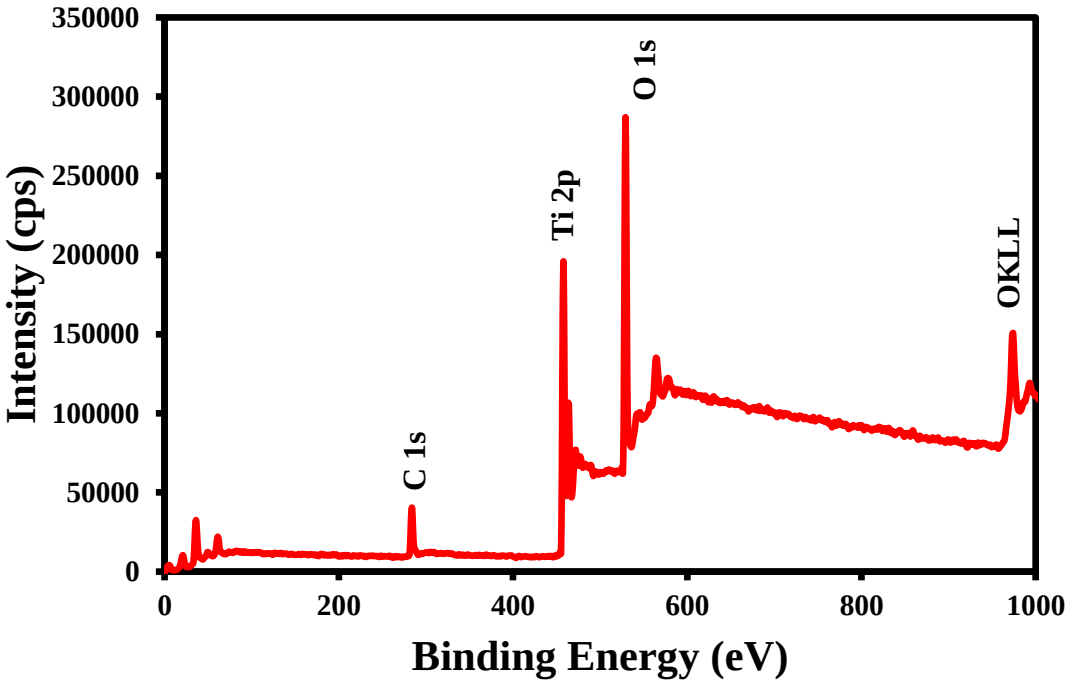

Figure 38 Survey spectra of 0.09%MWCNT-TiO_2

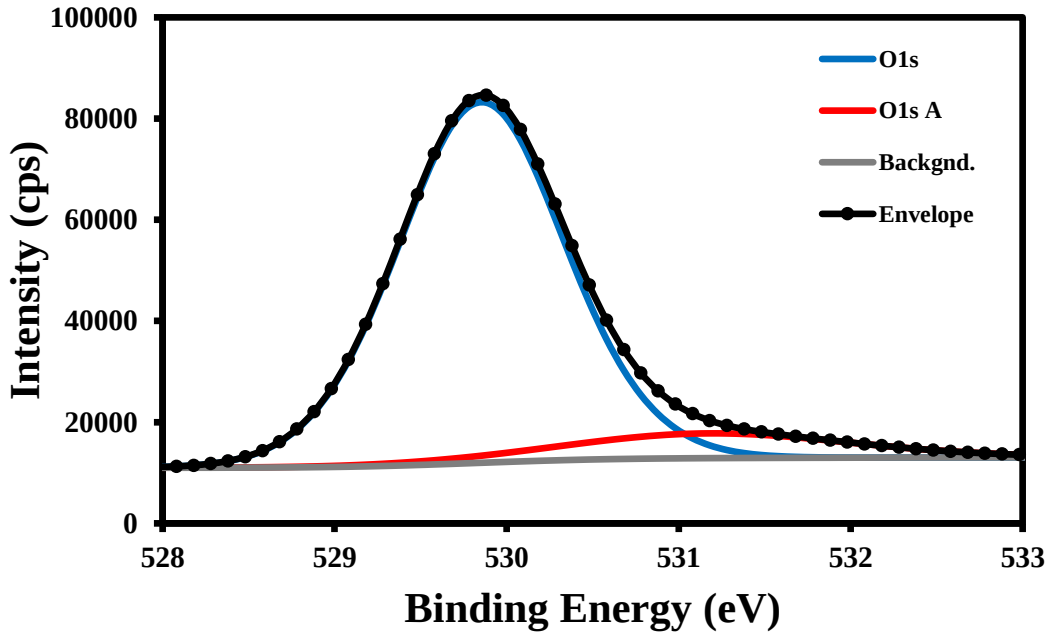

Figure 39 Deconvoluted peaks of O 1s element of 0.09%MWCNT-TiO_2 thin film on FTO glass substrate.

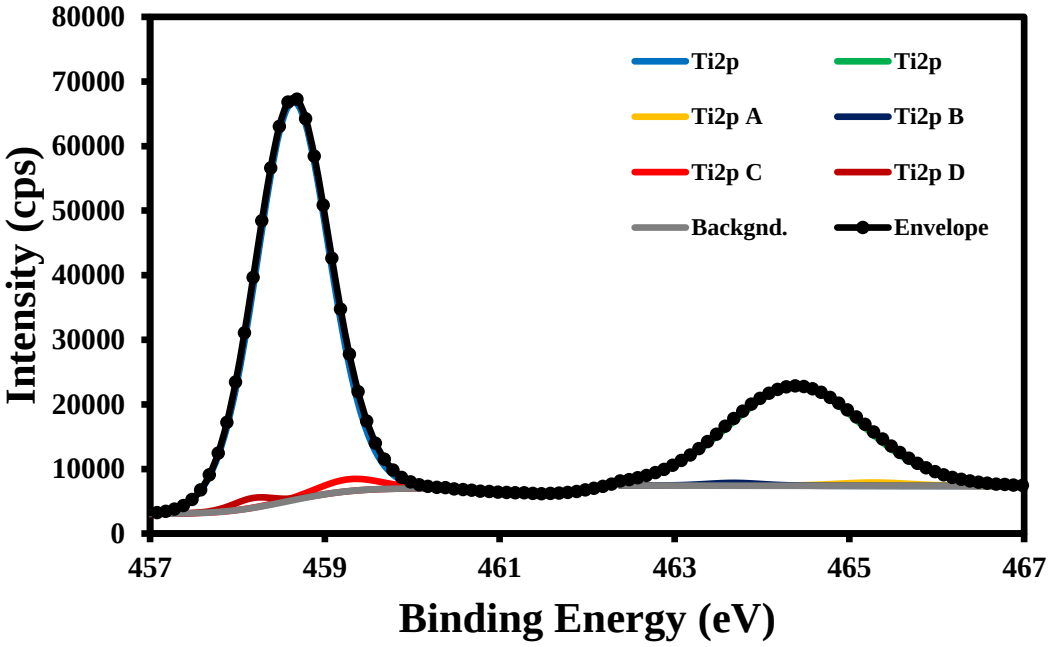

Figure 40 Deconvoluted peaks of Ti 2p element of 0.09%MWCNT-TiO_2 thin film on FTO glass substrate.

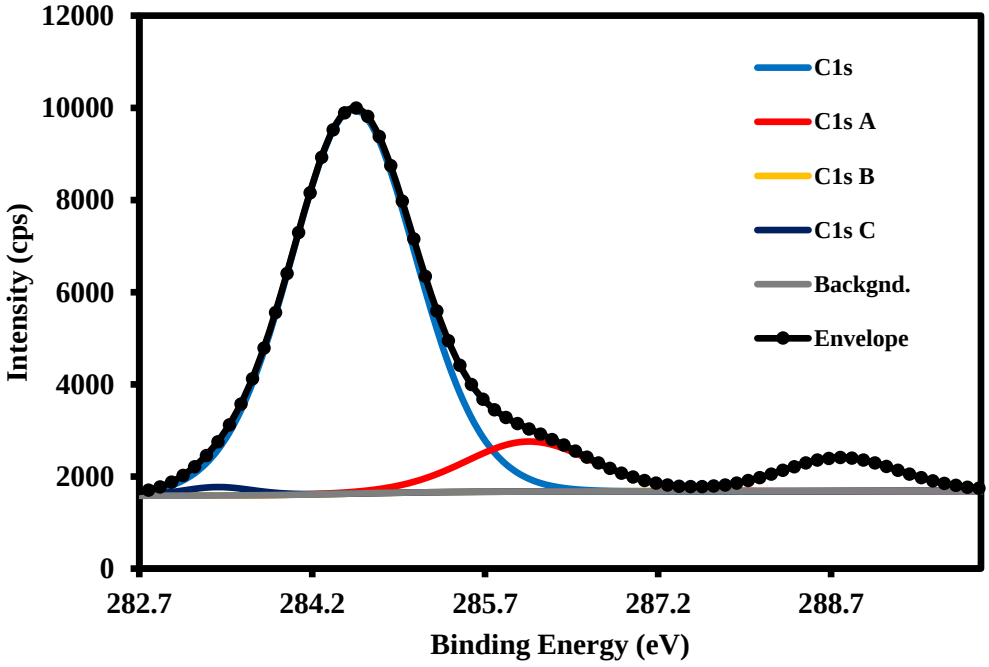

Figure 41 Deconvoluted peaks of C1s element of 0.09%MWCNT-TiO_2 thin film on FTO glass substrate.

Table 11 Deconvoluted peaks information for Ti 2p, O 1s and C 1s for 0.09%MWCNT-TiO_2

Name	Peak BE	FWHM eV	Area (P) CPS.eV	Atomic %
C1s	284.56	1.3	11694.76	81.6
C1s A	286.08	1.31	1538.75	10.74
C1s B	288.78	1.21	956.65	6.68
C1s C	283.38	0.71	141.43	0.99
O1s	529.85	1.14	88309.77	89.54
O1s A	531.18	1.94	10310.8	10.46
Ti2p	458.63	0.99	65865.27	66.14
Ti2p	464.39	1.82	30148.14	30.31
Ti2p A	465.28	1	562.43	0.57
Ti2p B	463.68	0.75	357	0.36
Ti2p C	459.28	0.85	1692.66	1.7
Ti2p D	458.18	0.56	924.84	0.93

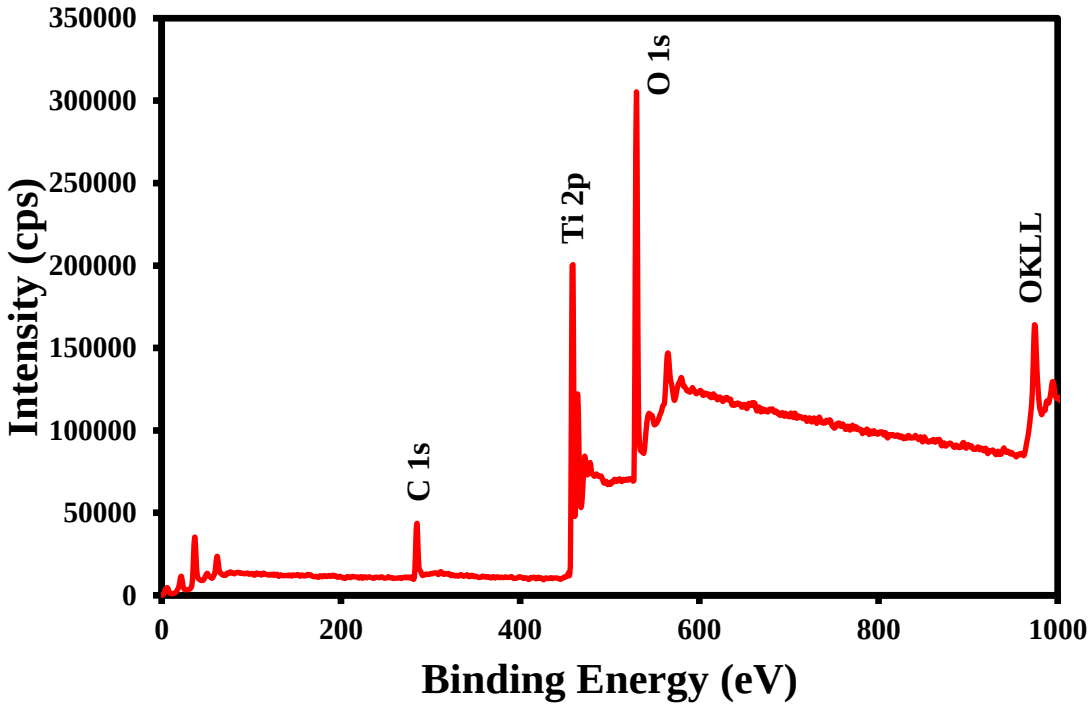

Figure 42 Survey spectra of 0.12%MWCNT-TiO_2

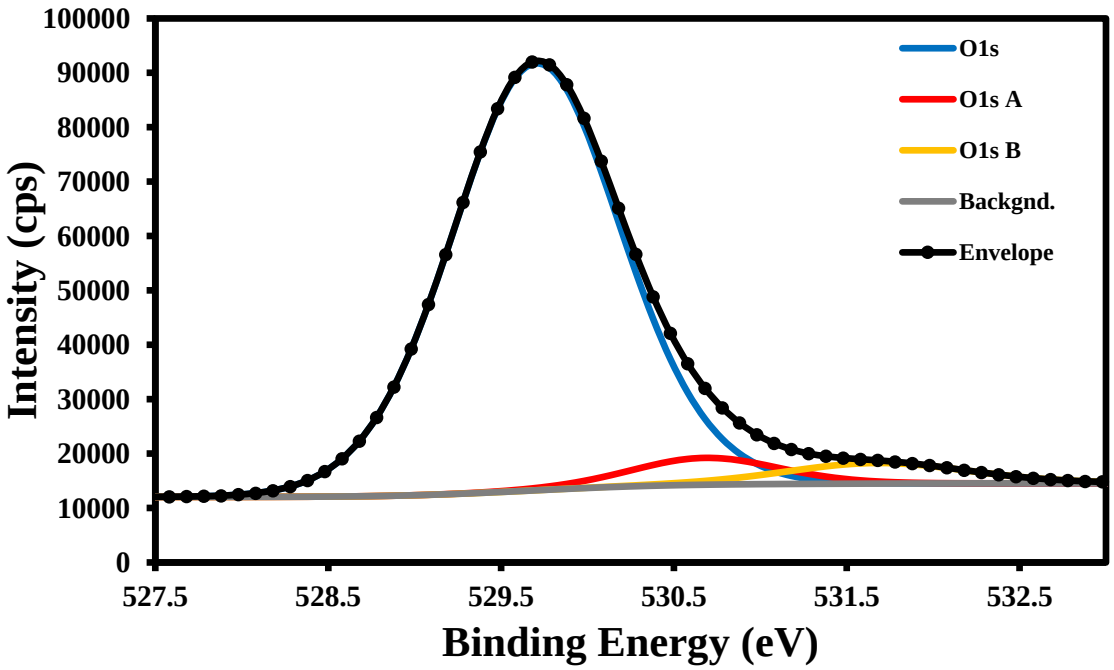

Figure 43 Deconvoluted peaks of O 1s element of 0.12%MWCNT-TiO_2 thin film on FTO glass substrate.

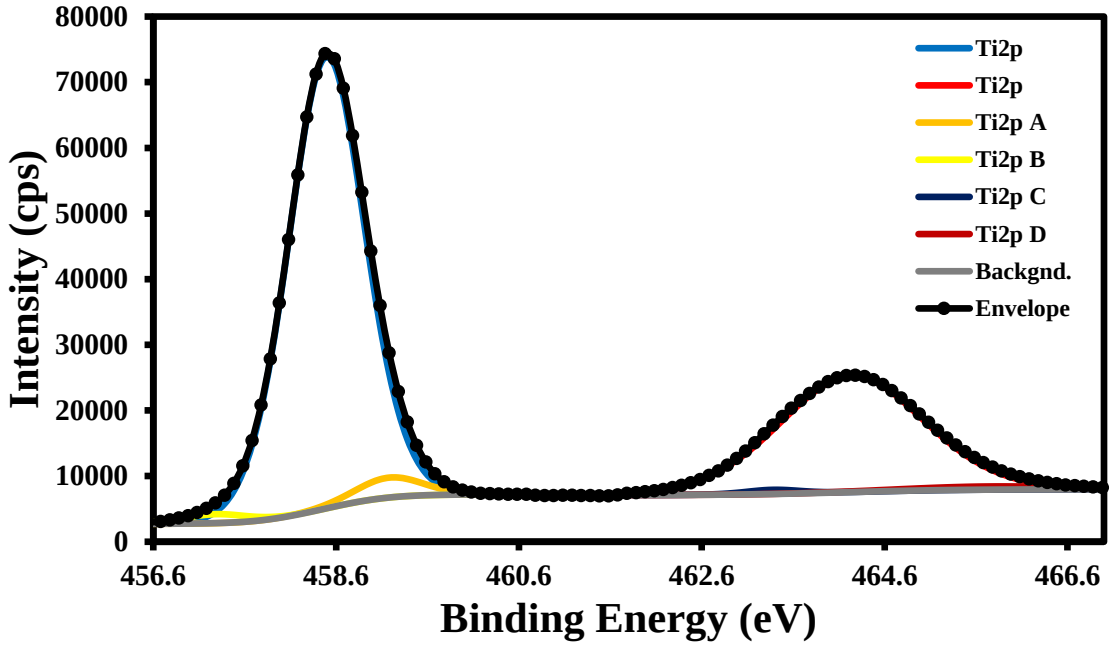

Figure 44 Deconvoluted peaks of Ti 2p element of 0.12%MWCNT-TiO_2 thin film on FTO glass substrate.

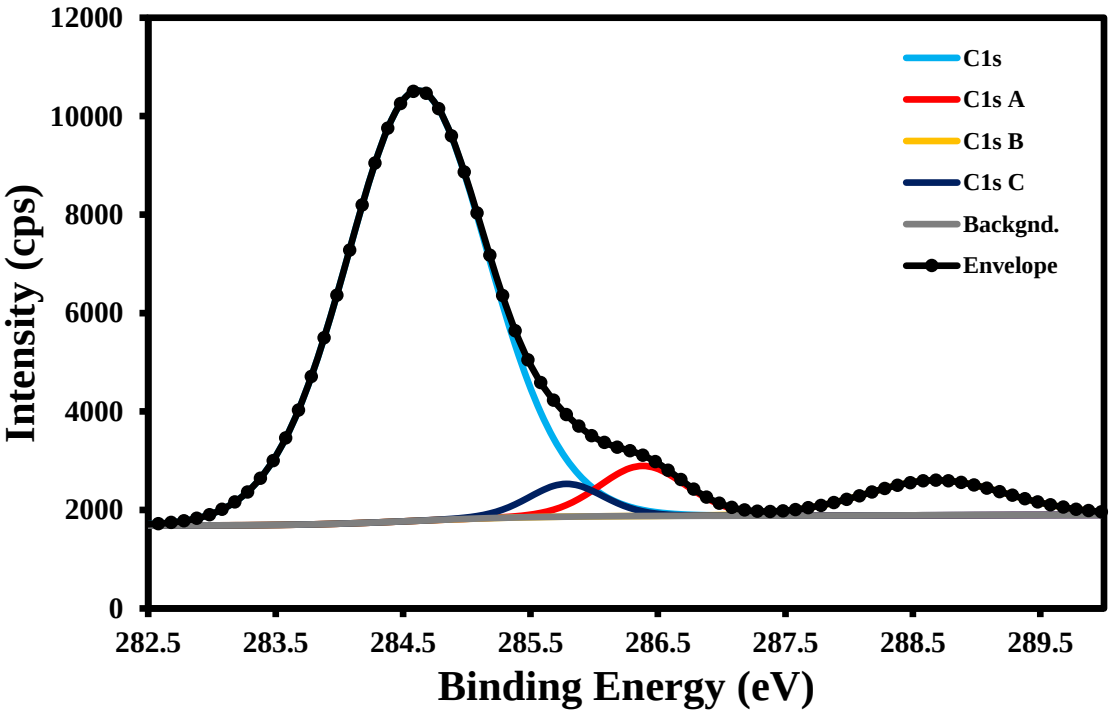

Figure 45 Deconvoluted peaks for C1s element of 0.12%MWCNT-TiO_2 thin film on FTO glass substrate.

Table 12 Deconvoluted peaks of Ti 2p, O 1s and C 1s for 0.12%MWCNT-TiO_2.

Name	Peak BE	FWHM eV	Area (P) CPS.eV	Atomic %
C1s	284.61	1.33	12569.54	83.59
C1s A	286.38	0.83	920.95	6.13
C1s B	288.68	1.35	1056.93	7.03
C1s C	285.78	0.7	487.99	3.25
O1s	529.7	1.15	98061.77	90.35
O1s A	530.68	1	5347.05	4.93
O1s B	531.68	1.25	5124.97	4.72
Ti2p	458.5	0.99	73763.37	63.98
Ti2p	464.24	1.87	35862.91	31.15
Ti2p A	459.18	0.87	2845.49	2.47
Ti2p B	457.28	0.83	1222.66	1.06
Ti2p C	463.38	0.7	476.02	0.41
Ti2p D	465.78	2.04	1069.83	0.93

4.3.4 XRD analysis

The XRD analysis for all the fabricated nMWCNT-TiO_2 nanocomposite thin films is carried out and presented in Figure 46, where the presence of peaks pertaining to the crystallographic planes of TiO_2 and MWCNT is quite evident. Particularly the relative intensity of (101) peak of TiO_2 increases with MWCNT concentration and this is because the diffraction intensity of (002) peak of MWCNT overlaps with that of (101) peak of TiO_2.

Furthermore, the crystal size is calculated from the XRD data which shows the crystal size is increased from 15nm in case to 0.03% MWCNT to 20nm for 0.12%MWCNT.

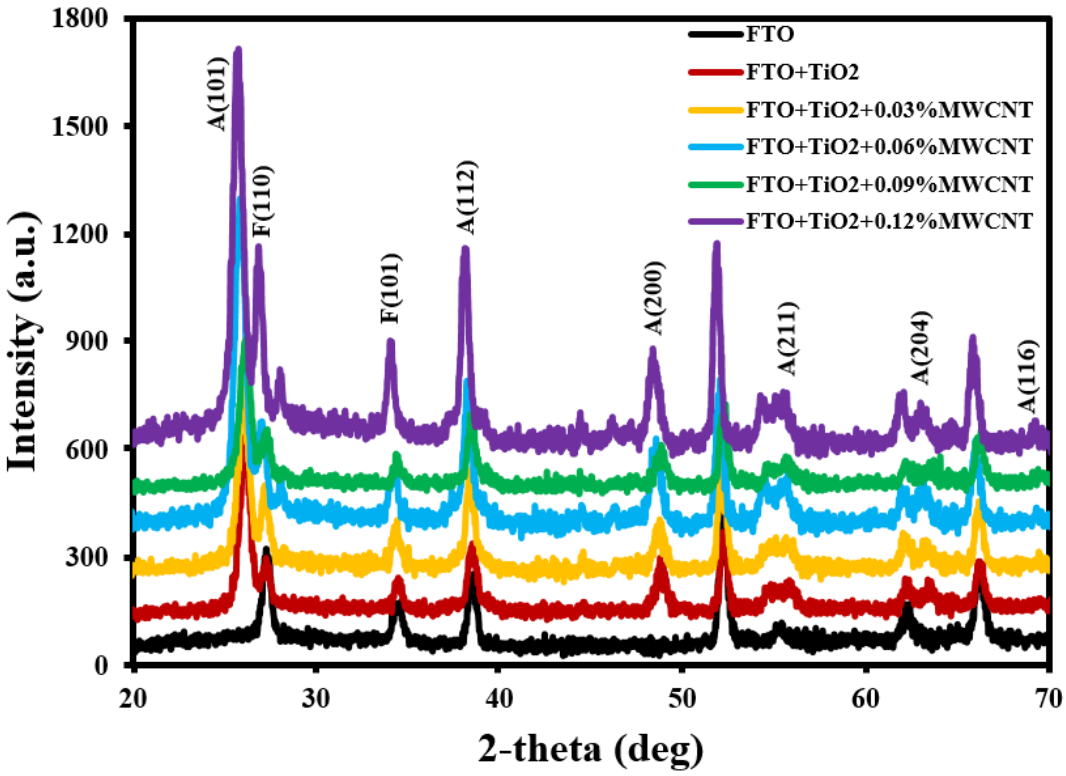

Figure 46 XRD analysis of nMWCNT-TiO_2 thin films. "A" represent peaks belongs to anatase phase of TiO2 and "F" represent peaks belongs to FTO.

4.3.5 Raman analysis

The Raman analysis is carried out using surface enhanced Raman spectroscopy to confirm the formation of composite in the fabricated thin films. Figure 47a shows the Raman spectrum of all the synthesized composite photoanodes, where we can see the presence of the peaks due to different Raman modes of vibration of TiO_2 in the energy range of 100-800 cm^{-1} along with D and G bands of MWCNT in the energy of 1000-1600 cm^{-1} [112], which confirm the presence of both materials. The peak intensity of D and G bands

increases as the amount of MWCNT increase. The magnified MWCNT peaks are provided in Figure 47b and 47c, which clearly show the presence of MWCNT and their different compositions.

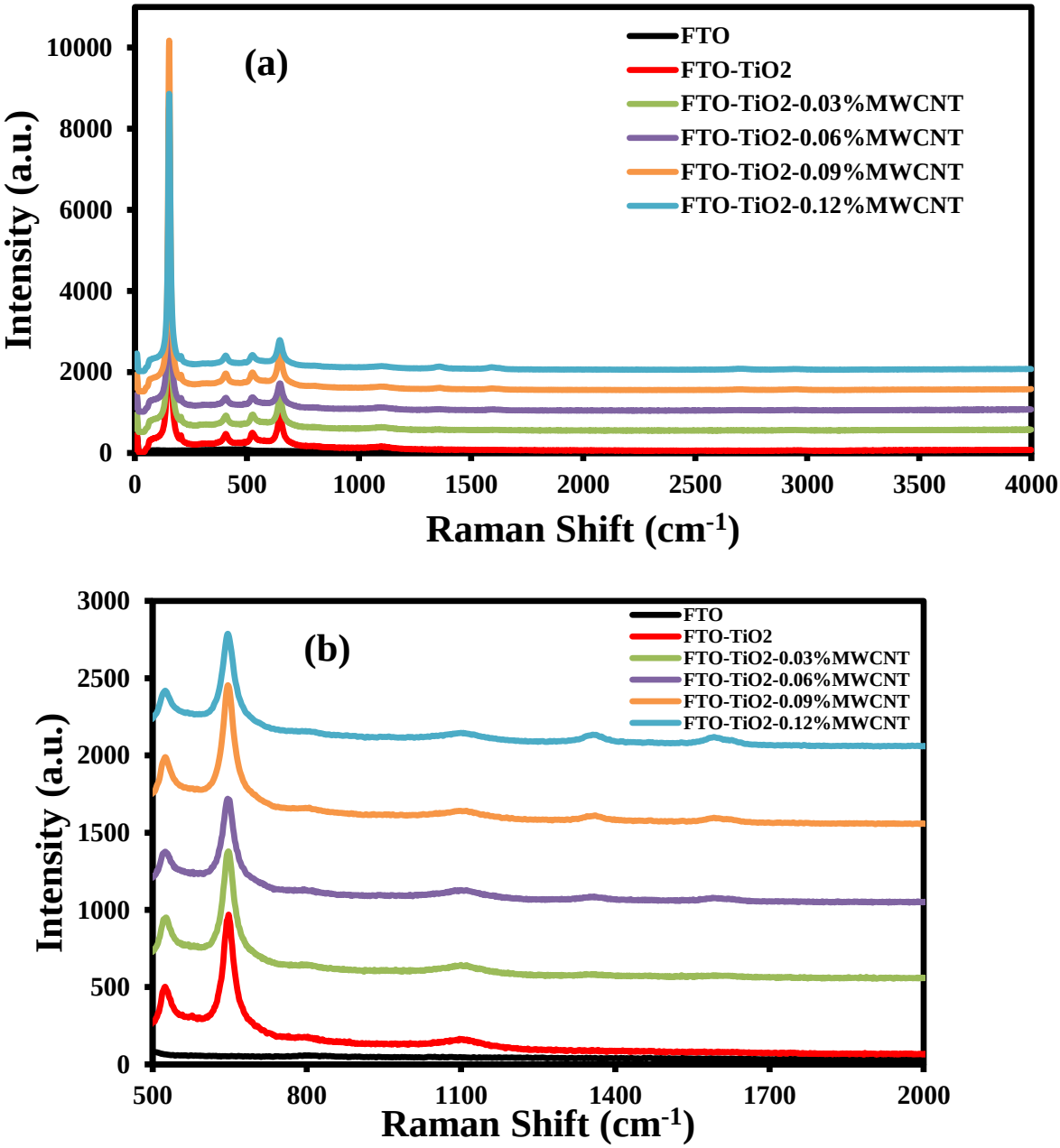

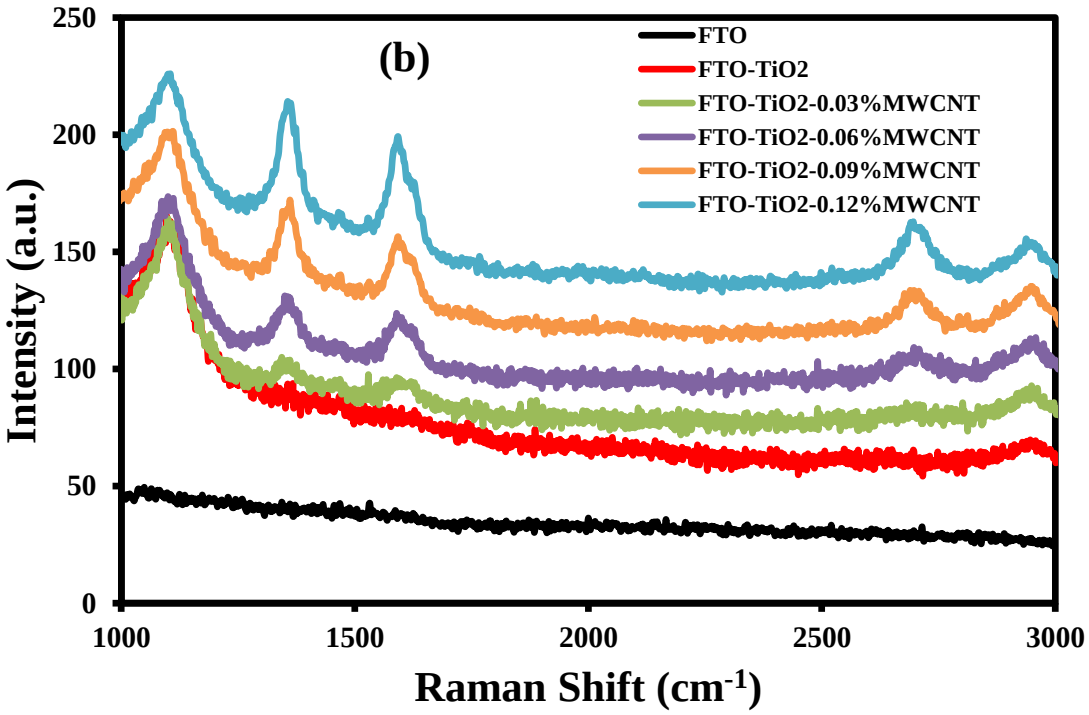

Figure 47 Raman analysis of nMWCNT-TiO2 thin films (a) for complete Raman spectra (b) for Raman shift from 500 cm^{-1} to 2000 cm^{-1}(c) for Raman shift 1000 cm^{-1} to 3000 cm^{-1}.

4.4. Characterization of perovskite single crystals

4.4.1 Optical Microscope analysis

The optical microscope analysis has been performed to see the surface of the grown thin crystals which are provided in the Figure 48 below. These images clearly show that there are no grain boundaries on the grown single crystals and that they have very smooth surfaces which shows the quality of single crystals.

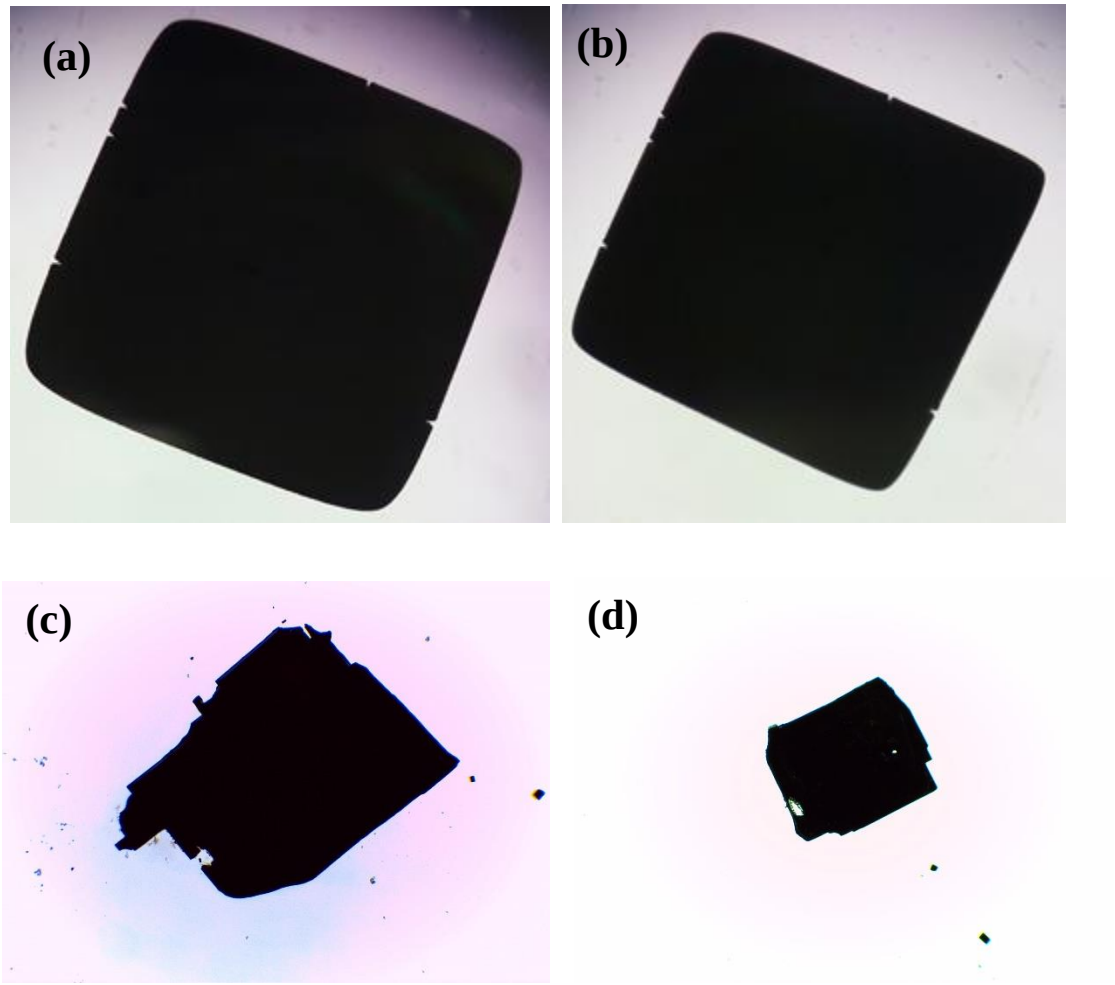

Figure 48 Optical microscope image of (a & b) $MAPbI_3$ (c) BAI: MAPbI3 (d) PAI: MAPbI3 perovskite thin single crystal between two ITO coated glasses.

4.4.2 Scanning electron microscope analysis

For the surface analysis of the grown single crystals we also carried out scanning electron microscopy. The applied voltage to capture SEM images was 20kV. The SEM images of all the three single crystals i.e. $MAPbI_3$, BAI: $MAPbI_3$ and PAI: $MAPbI_3$ are provided in Figures 49, 50 and 51 respectively.

4.4.3 $MAPbI_3$ SEM analysis

Figure 49 shows the SEM analysis of $MAPbI_3$ single crystal. From the SEM image we can observe there are no grain boundaries on the surface of single crystal. However, the surface is not very smooth and looks rougher.

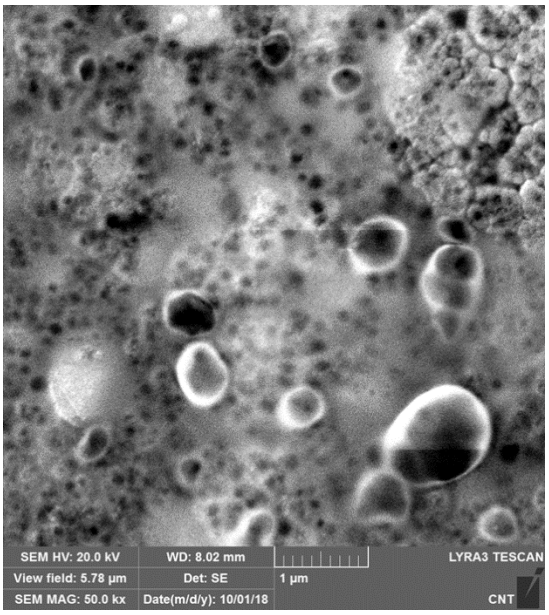

Figure 49 Scanning electron microscope image of the 3D $MAPbI_3$ perovskite bulk single crystal.

4.4.4 BAI: $MAPbI_3$ SEM analysis

Figure 50 shows the SEM analysis of BAI: $MAPbI_3$ single crystal. From the SEM image we can observe there are no grain boundaries on the surface of single crystal. Furthermore, the surface is very smooth and clear as compared to $MAPbI_3$ single crystals as shown in Figure 49. The broken line appeared on the surface of the single crystal due to high accelerating voltage i.e. 20kv.

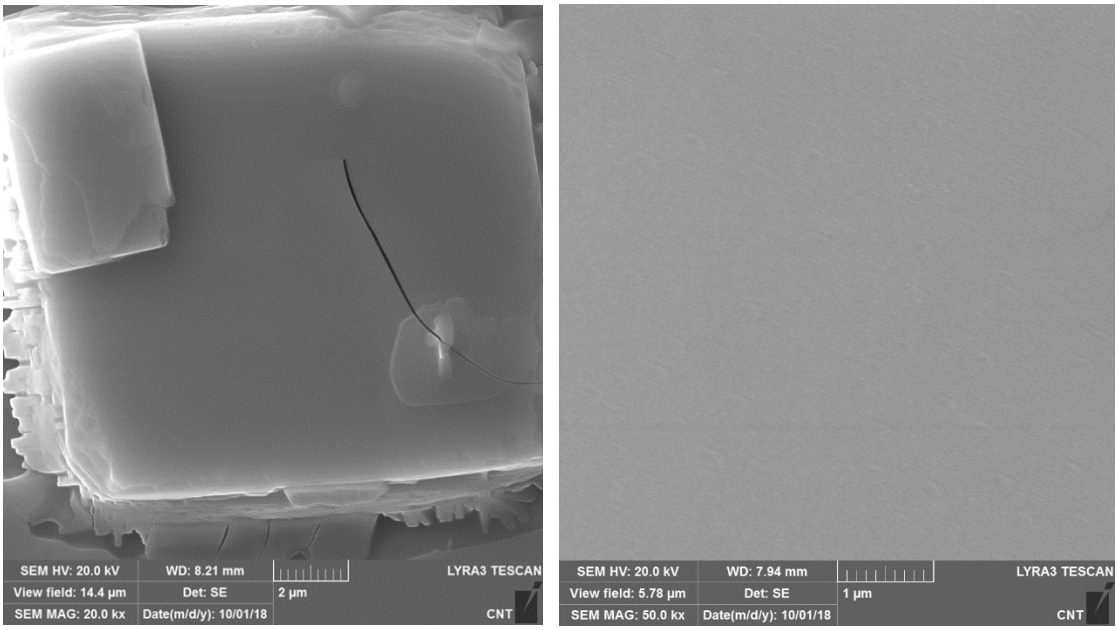

Figure 50 Scanning electron microscope image of the 2D/3D BAI: $MAPbI_3$ perovskite bulk single crystal.

4.4.5 PAI: $MAPbI_3$ SEM analysis

Figure 51 shows the SEM analysis of PAI: $MAPbI_3$ single crystal. From the SEM image we can observe there are no grain boundaries on the surface of single crystal. Furthermore, the surface is very smooth and clear as compared to $MAPbI_3$ single crystals as shown in Figure 49. The broken line appeared on the surface of the single crystal due to high accelerating voltage i.e. 20kv.

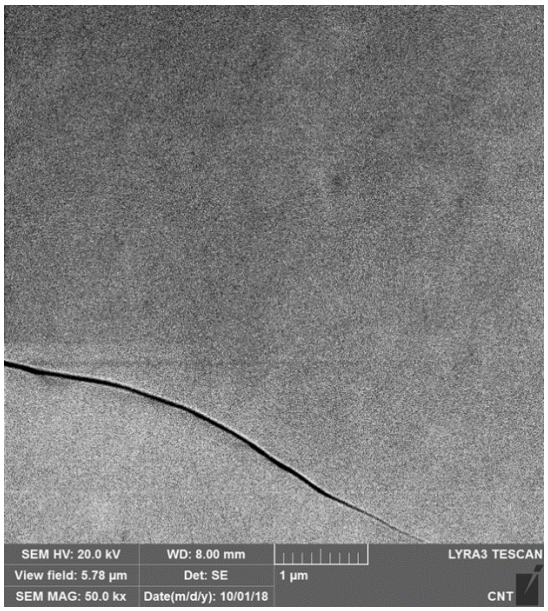

Figure 51 Scanning electron microscope image of the 2D/3D PAI: $MAPbI_3$ perovskite bulk single crystal.

4.4.6 Energy Dispersive X-ray spectroscopy (EDX)

EDX is a useful technique do the elemental analysis. Here we carried out the EDX analysis of grown single crystals to confirm their elements. The EDX conditions include 20kv as applied accelerating voltage. All the three types of crystals elements are confirmed and verified by EDX analysis. Their electron image, EDX spectrum and compositional states are provided below, where we can confirm the fact of having perovskite elements. The tables show the variation of different components in three types of single crystals.

4.4.7 $MAPbI_3$ EDX analysis

The EDX analysis of $MAPbI_3$ single crystal was carried out and its electron image and EDX spectra is provided in Figure 52. The selected area is scanned in four parts. Each area

shows the expected elements i.e. Carbon, Nitrogen, Lead and iodide. The detailed elemental stats are provided in table 13.

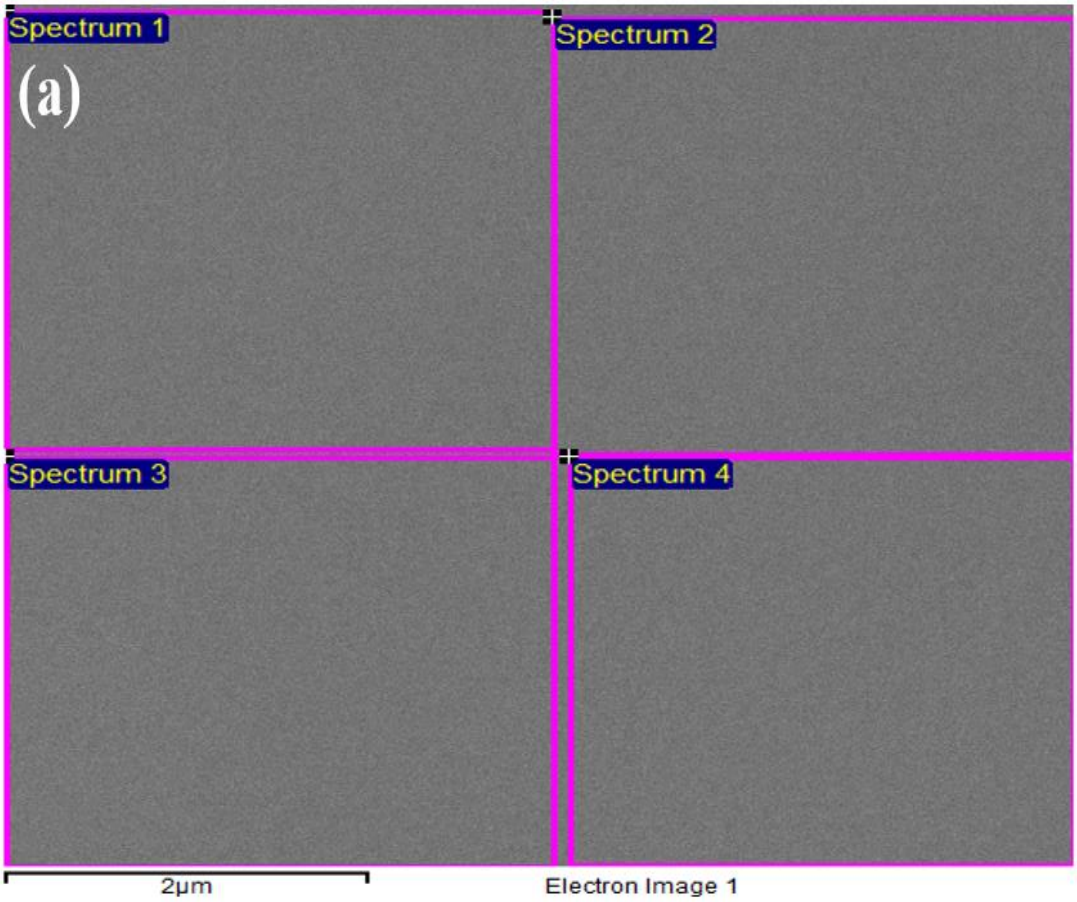

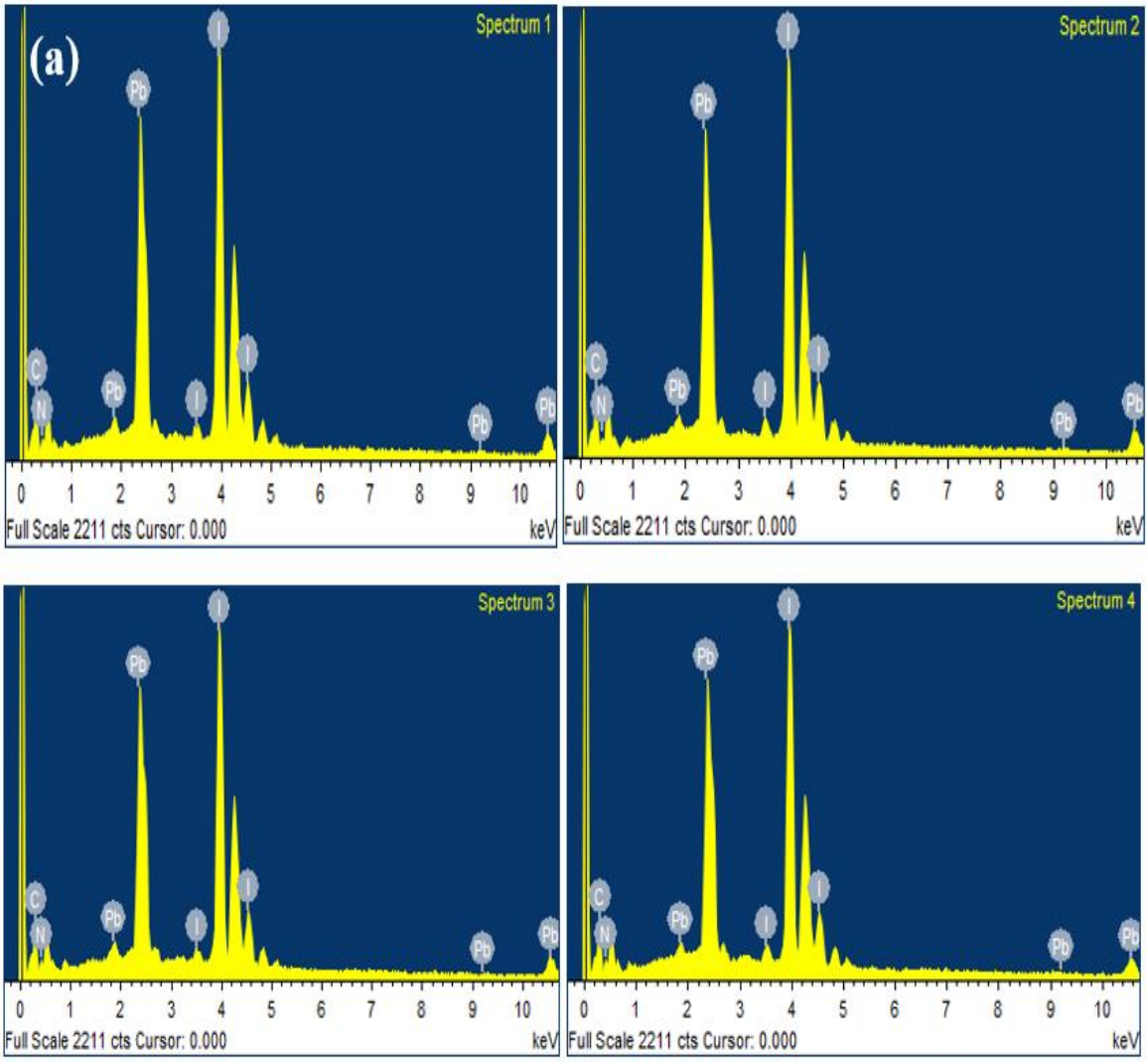

Figure 52 EDX analysis of $MAPbI_3$ perovskite bulk single crystal.

Spectrum	In stats.	C	N	I	Pb	Total
Spectrum 1	Yes	8.96	1.89	58.37	30.78	100.00
Spectrum 2	Yes	8.61	2.26	58.01	31.12	100.00
Spectrum 3	Yes	8.26	3.89	56.89	30.96	100.00
Spectrum 4	Yes	9.26	3.11	56.97	30.65	100.00
Mean		8.77	2.79	57.56	30.88	100.00
Std. deviation		0.43	0.89	0.74	0.21	
Max.		9.26	3.89	58.37	31.12	
Min.		8.26	1.89	56.89	30.65	

Table 13 EDX analysis of $MAPbI_3$ single crystal

4.4.8 BAI: $MAPbI_3$ EDX analysis

The EDX analysis of BAI: $MAPbI_3$ single crystal was carried out and its electron image and EDX spectra is provided in Figure 53. Four areas were selected for EDX scan. Each area shows the expected elements i.e. Carbon, Nitrogen, Lead and iodide. The detailed elemental stats are provided in table 14.

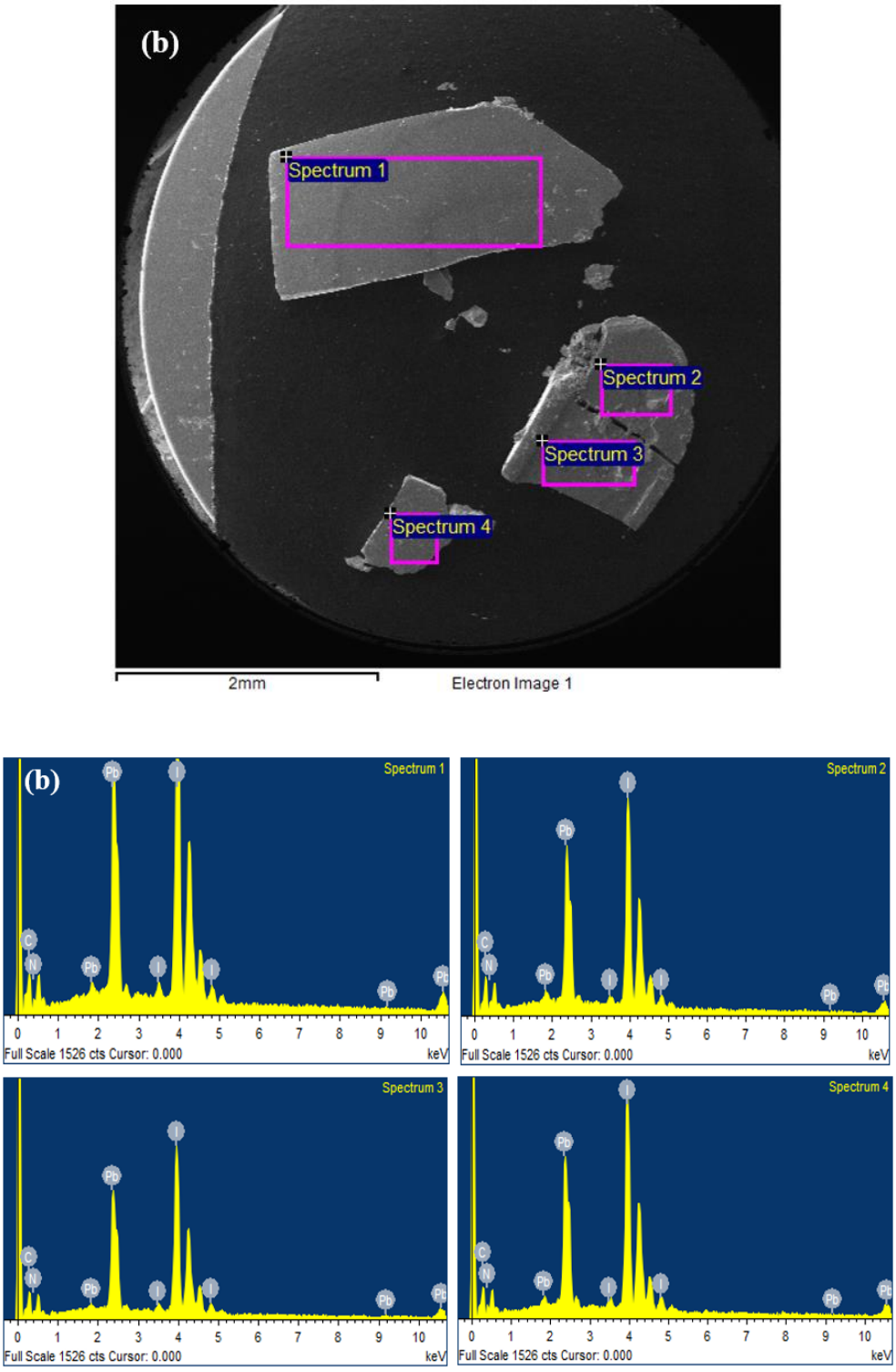

Figure 53 EDX analysis of BAI: $MAPbI_3$ perovskite bulk single crystal.

Table 14 EDX analysis of BAI: $MAPbI_3$ single crystal

Spectrum	In stats.	C	N	I	Pb	Total
Spectrum 1	Yes	7.64	2.41	60.49	29.46	100.00
Spectrum 2	Yes	10.92	3.06	57.38	28.64	100.00
Spectrum 3	Yes	10.49	2.02	58.55	28.94	100.00
Spectrum 4	Yes	9.11	3.81	58.28	28.80	100.00
Mean		9.54	2.82	58.67	28.96	100.00
Std. deviation		1.48	0.78	1.31	0.36	
Max.		10.92	3.81	60.49	29.46	
Min.		7.64	2.02	57.38	28.64	

4.4.9 PAI: $MAPbI_3$ EDX analysis

The EDX analysis of PAI: $MAPbI_3$ single crystal was carried out and its electron image and EDX spectra is provided in Figure 54. The selected area was scanned into four parts. Each area shows the expected elements i.e. Carbon, Nitrogen, Lead and iodide. The detailed elemental stats are provided in table 15.

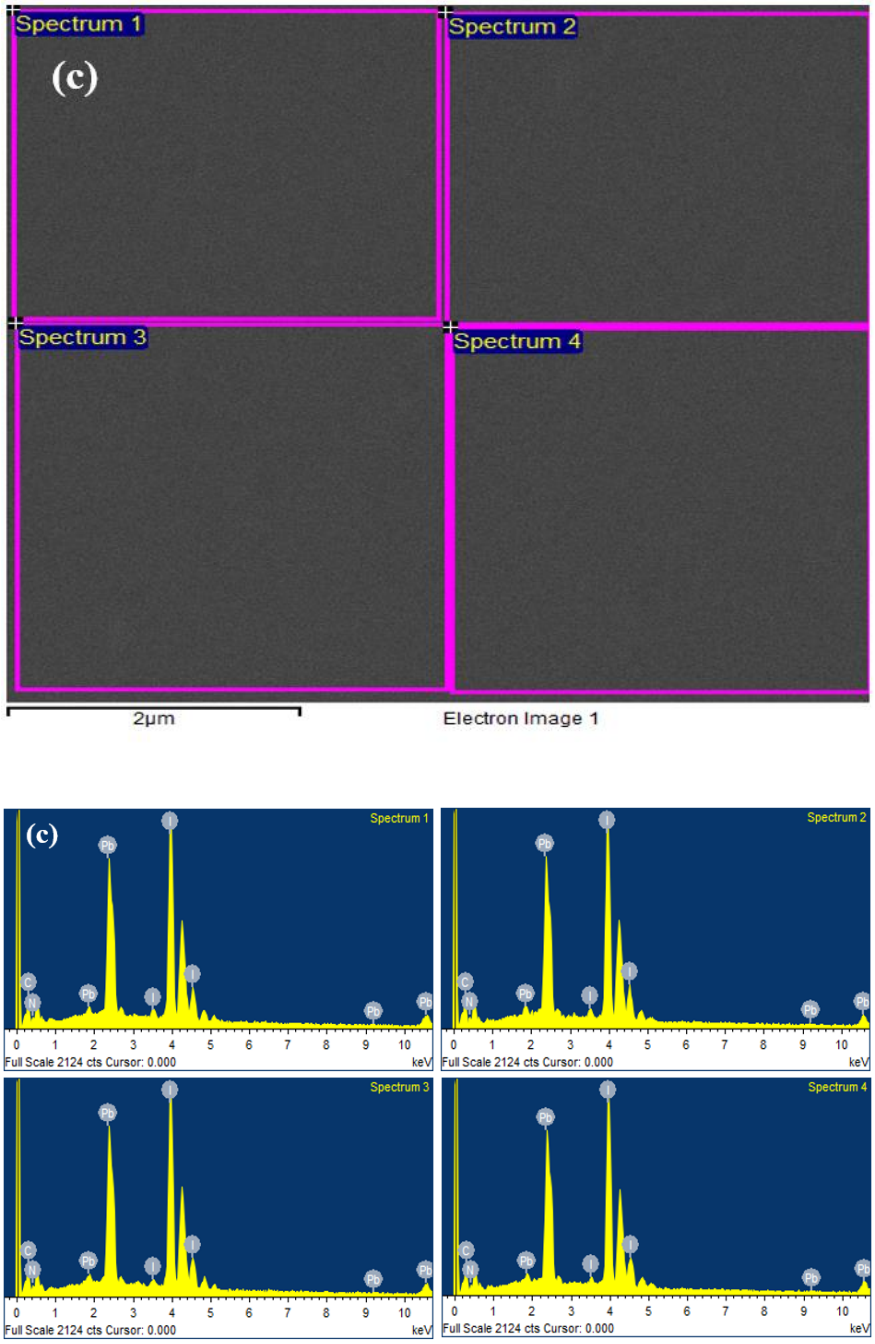

Figure 54 EDX analysis of PAI: $MAPbI_3$ perovskite bulk single crystal.

Table 15 EDX analysis of PAI: $MAPbI_3$ single crystal

Spectrum	In stats.	C	N	I	Pb	Total
Spectrum 1	Yes	7.81	2.36	58.57	31.26	100.00
Spectrum 2	Yes	7.90	3.08	57.94	31.07	100.00
Spectrum 3	Yes	8.25	2.40	58.22	31.14	100.00
Spectrum 4	Yes	7.45	1.61	58.76	32.18	100.00
Mean		7.85	2.36	58.37	31.41	100.00
Std. deviation		0.33	0.60	0.36	0.52	
Max.		8.25	3.08	58.76	32.18	
Min.		7.45	1.61	57.94	31.07	

4.4.10 X-ray mapping analysis

X-ray mapping analysis is a powerful tool to confirm the distribution of the materials in the scanned area. Here we carried out mapping analysis for all the three grown single crystals. The mapping conditions include the 20kv as applied potential and 50 frames were recorded. The mapping analysis again confirm the compositional as well as distribution of the materials. The mapping analysis for each single crystal is provided below.

4.4.11 $MAPbI_3$ Mapping analysis

The mapping analysis of $MAPbI_3$ single crystal is given in Figure 55, which shows proper distribution of the Carbon, Nitrogen, Lead and Iodide. This X-ray graphs confirm elements as well as their distribution.

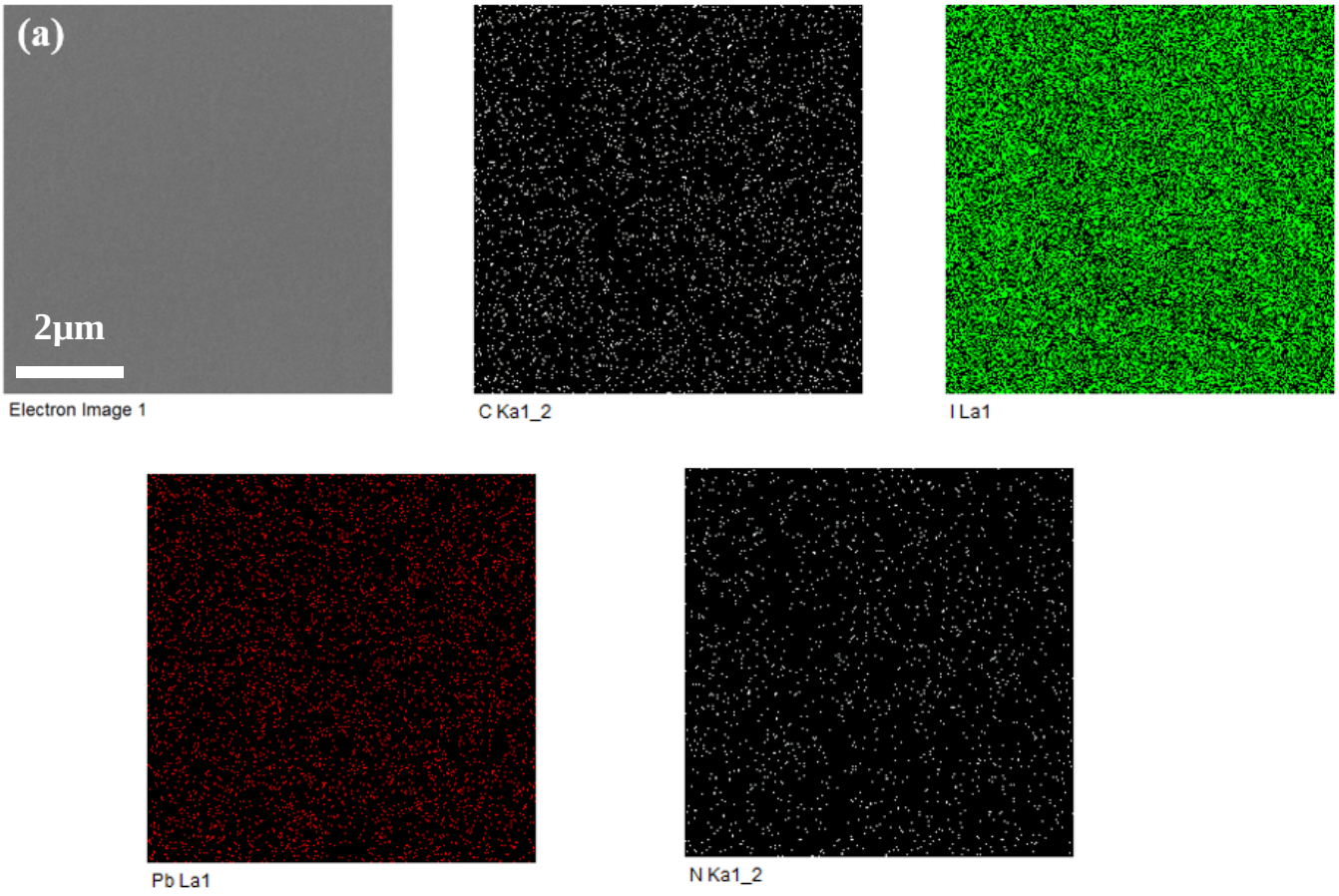

Figure 55 Mapping analysis of $MAPbI_3$ perovskite bulk single crystal.

4.4.12 BAI: $MAPbI_3$ Mapping analysis

The mapping analysis of BAI: $MAPbI_3$ single crystal is given in Figure 56, which shows proper distribution of the Carbon, Nitrogen, Lead and Iodide. This X-ray graphs confirm elements as well as their distribution.

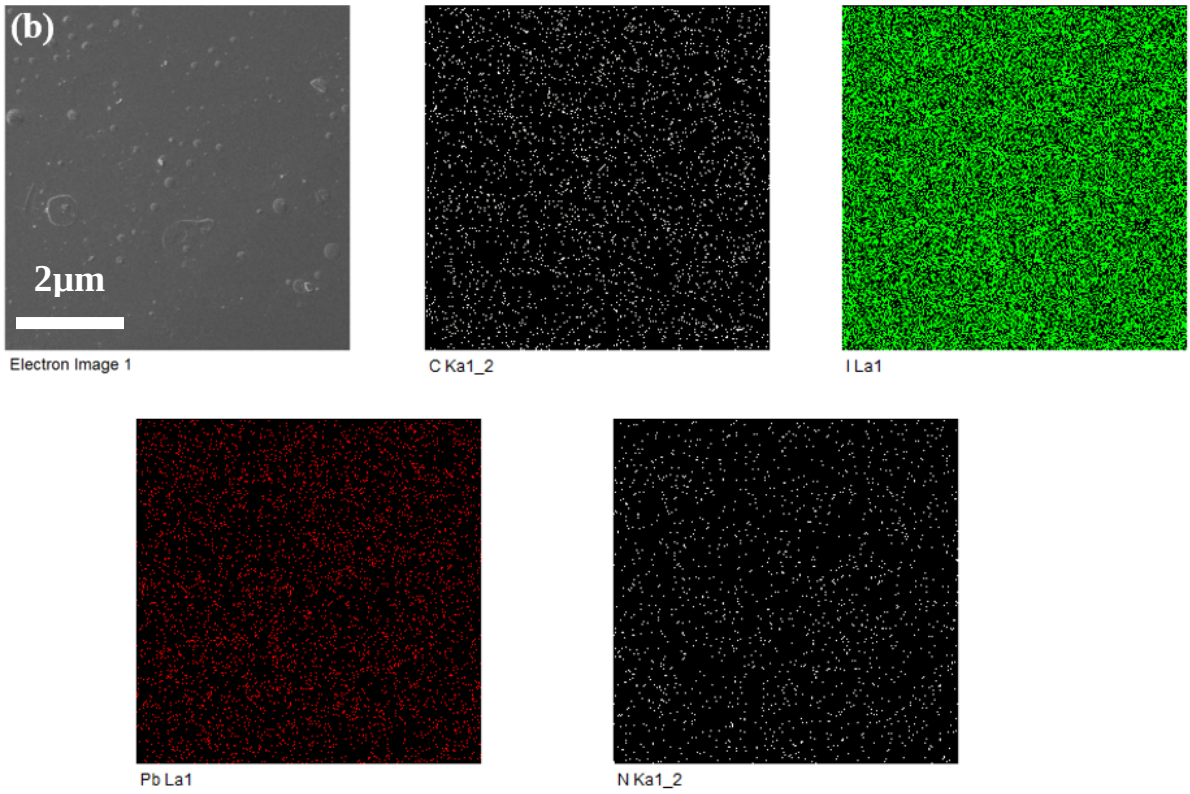

Figure 56 Mapping analysis of BAI: $MAPbI_3$ perovskite bulk single crystal.

4.4.13 PAI: $MAPbI_3$ Mapping analysis

The mapping analysis of $MAPbI_3$ single crystal is given in Figure 57, which shows proper distribution of the Carbon, Nitrogen, Lead and Iodide. This X-ray graphs confirm elements as well as their distribution.

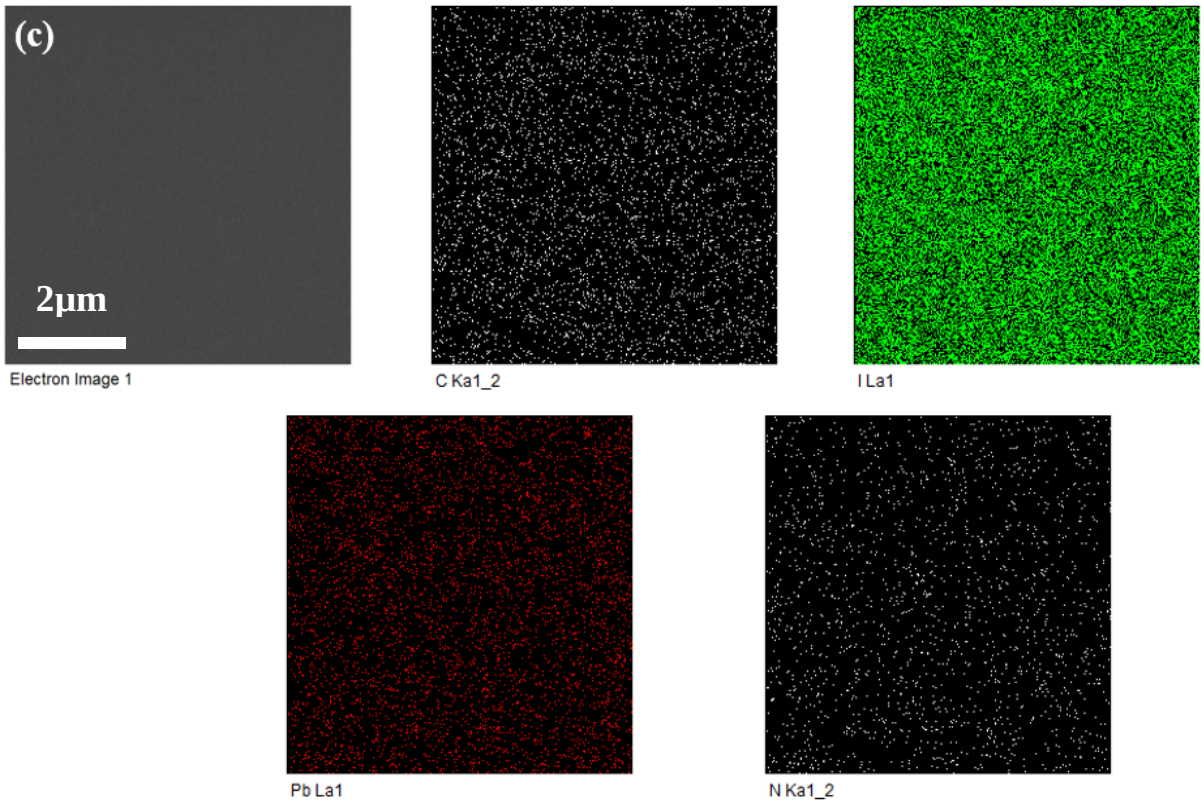

Figure 57 Mapping analysis of PAI: $MAPbI_3$ perovskite bulk single crystal.

4.4.14 XRD analysis of single crystals

The XRD analysis was carried out using miniflex X-ray diffractometer. The as grown bulk single crystal was loaded into the XRD by adjusting the height of single crystal with surface of the holder. The XRD spectra is provided in Figure 58 for all the three bulk single

crystals. Later, these single crystals were crushed with mortar and pestle and XRD analysis was again carried out. The XRD spectra of the crushed single crystals is provided in Figure 59. From the comparison of Figure 58 and 59 we can easily conclude the perfection of single crystals. The number of peaks in as grown bulk single crystals are very less as compared to the crushed ones, which confirms the less orientations available for diffraction of incoming X-rays.

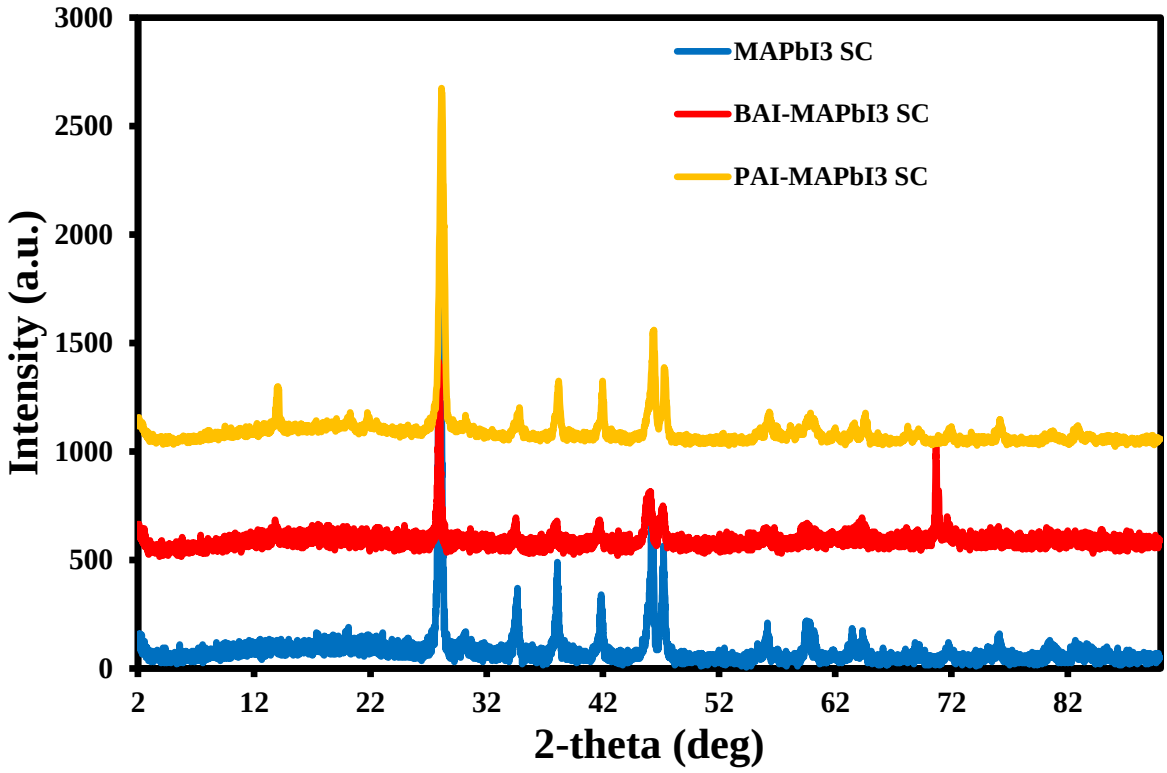

Figure 58 XRD analysis of $MAPbI_3$, BAI: $MAPbI_3$ and PAI: $MAPbI_3$ single crystals.

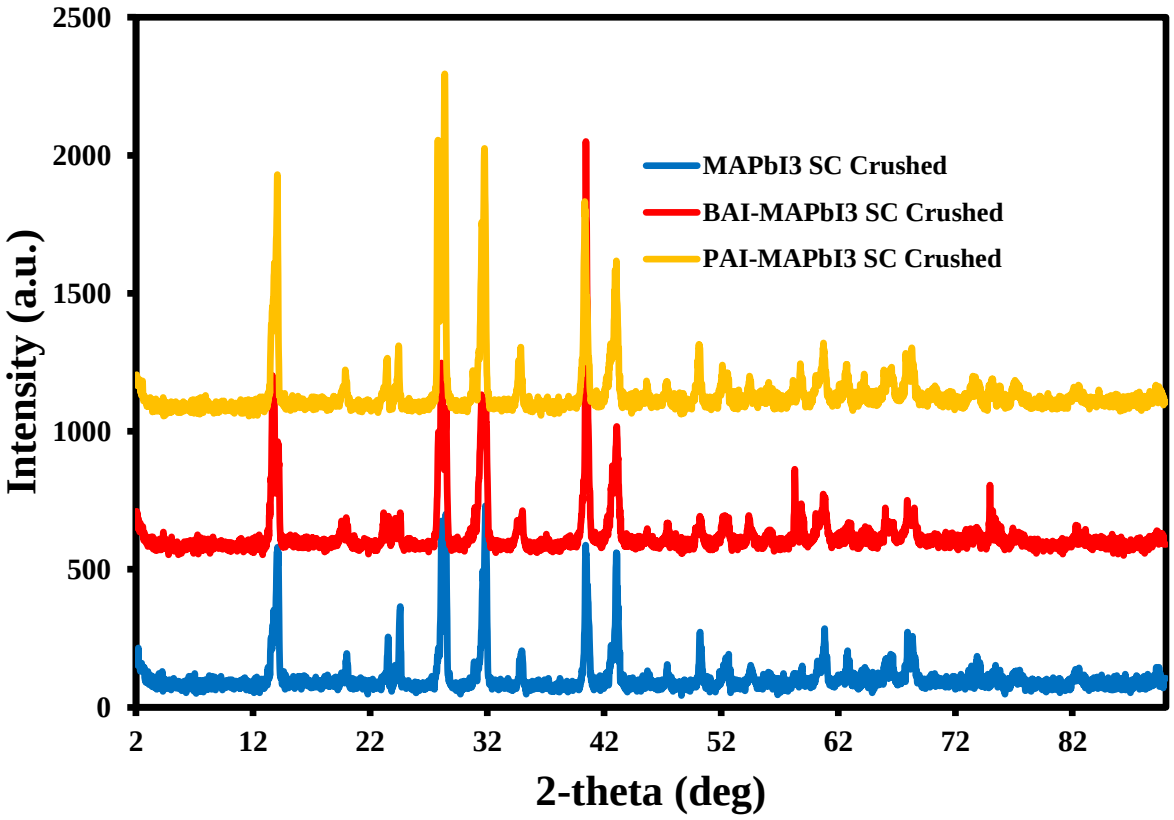

Figure 59 XRD analysis of crushed $MAPbI_3$, BAI: $MAPbI_3$ and PAI: $MAPbI_3$ single crystals with mortar and pestle.

4.4.15 UV-Vis Spectroscopy of perovskite solutions

The UV-Vis spectroscopic analysis of perovskite solutions was carried out in GBL. The UV-Vis spectra show the absorbance mostly in UV region when perovskite materials are in solution forms. Furthermore, it is also clear from the spectra, the absorbance for BAI: $MAPbI_3$ and PAI: $MAPbI_3$ is more as compared to pure $MAPbI_3$.

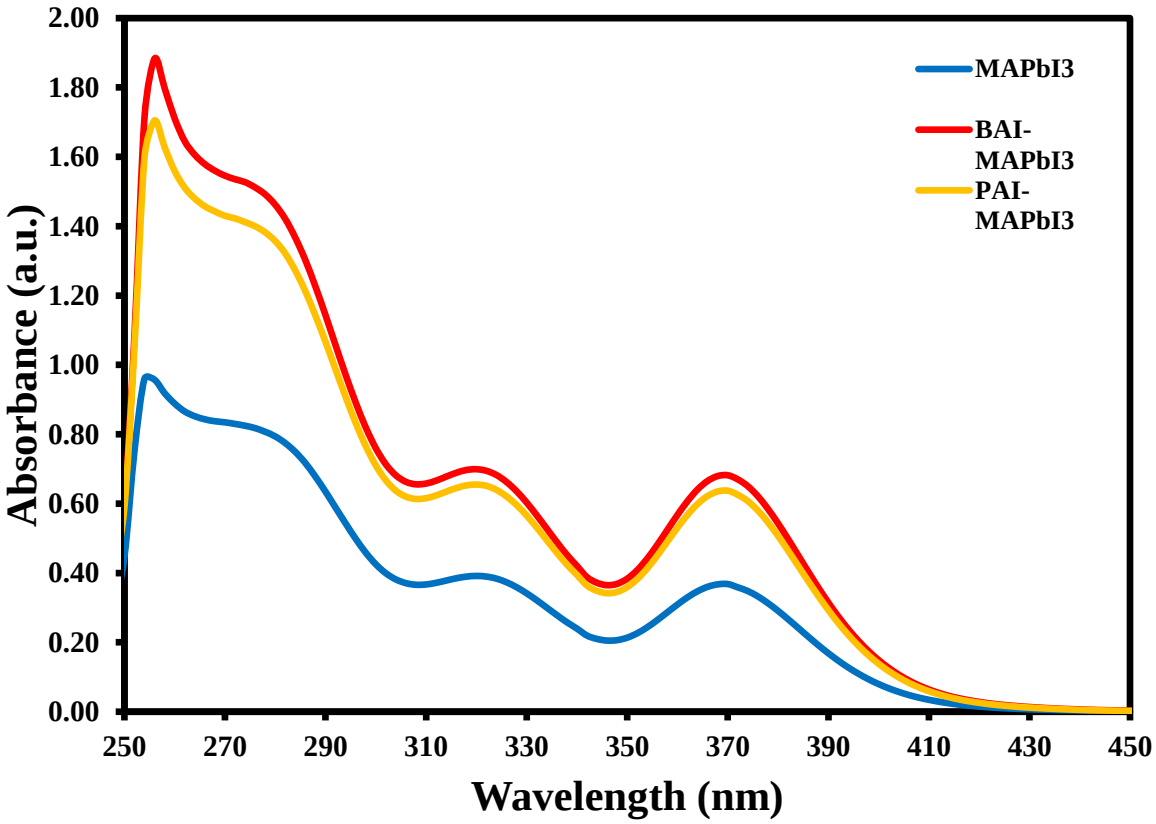

Figure 60 UV-Vis Spectra of Perovskite solution in GBL.

4.4.16 Transmission Electron Microscopy analysis of perovskite solutions

TEM analysis of the same perovskite solutions was carried out. The TEM images at low and high resolutions are provided in Figure 61. From TEM analysis the presence of BAI and PAI was confirmed. Moreover, from TEM images the perovskite materials structure is confirmed [113].

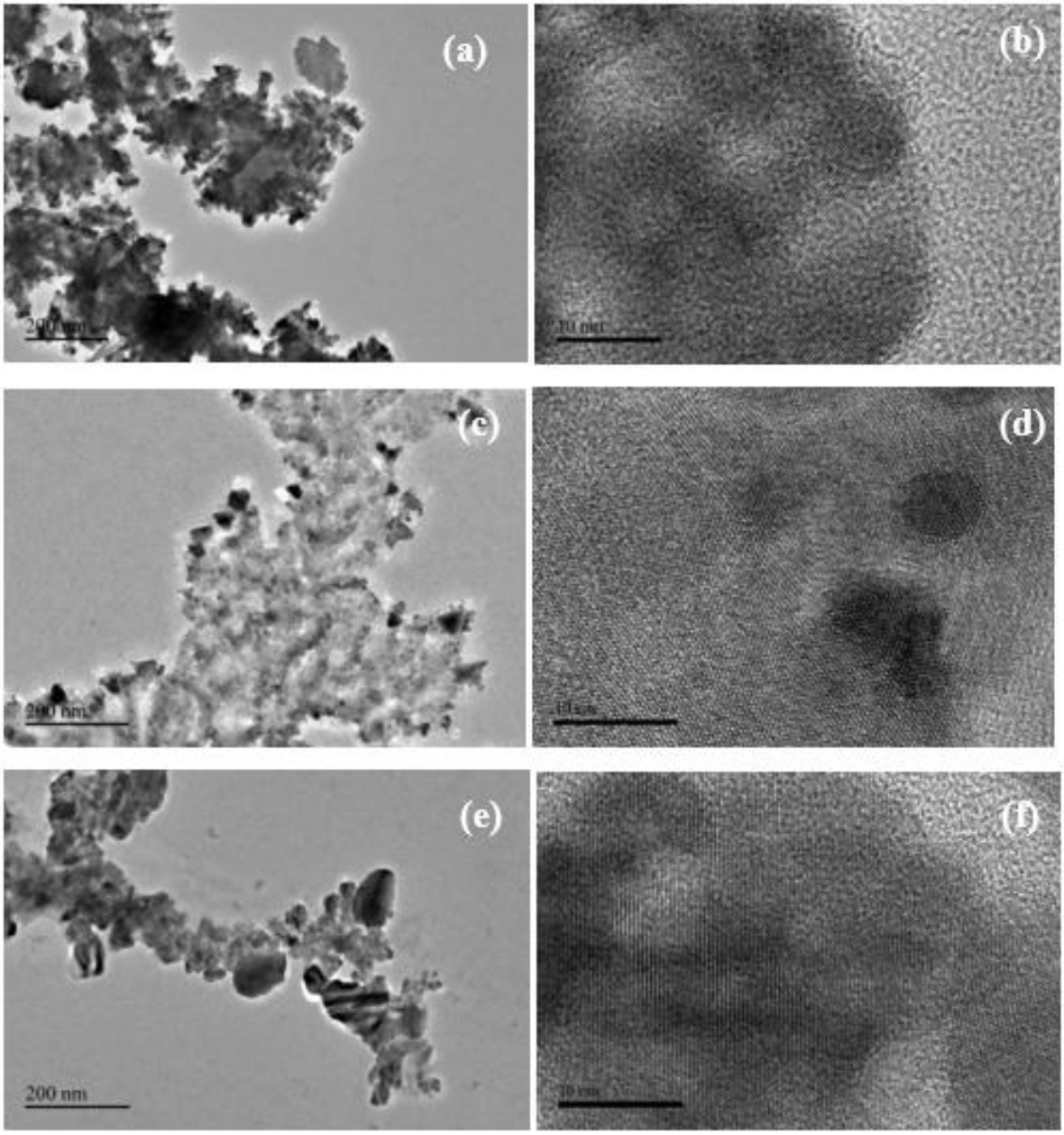

Figure 61 TEM analysis of **(a & b)** $MAPbI_3$ in GBL at low and high magnifications **(c & d)** BAI: $MAPbI_3$ in GBL at low and high magnifications **(e & f)** PAI: $MAPbI_3$ in GBL at low and high magnifications.

4.4.17 Nuclear Magnetic Resonance analysis of perovskite single crystals

Solid NMR C^{13} analysis was carried out for the three types of grown single crystals. The NMR spectra are provided in Figure 62. From the NMR spectra we can observe the small change in the chemical shift of BAI: $MAPbI_3$ and PAI: $MAPbI_3$, which confirms the different environments of the nuclei in these materials as compared to the pure $MAPbI_3$.

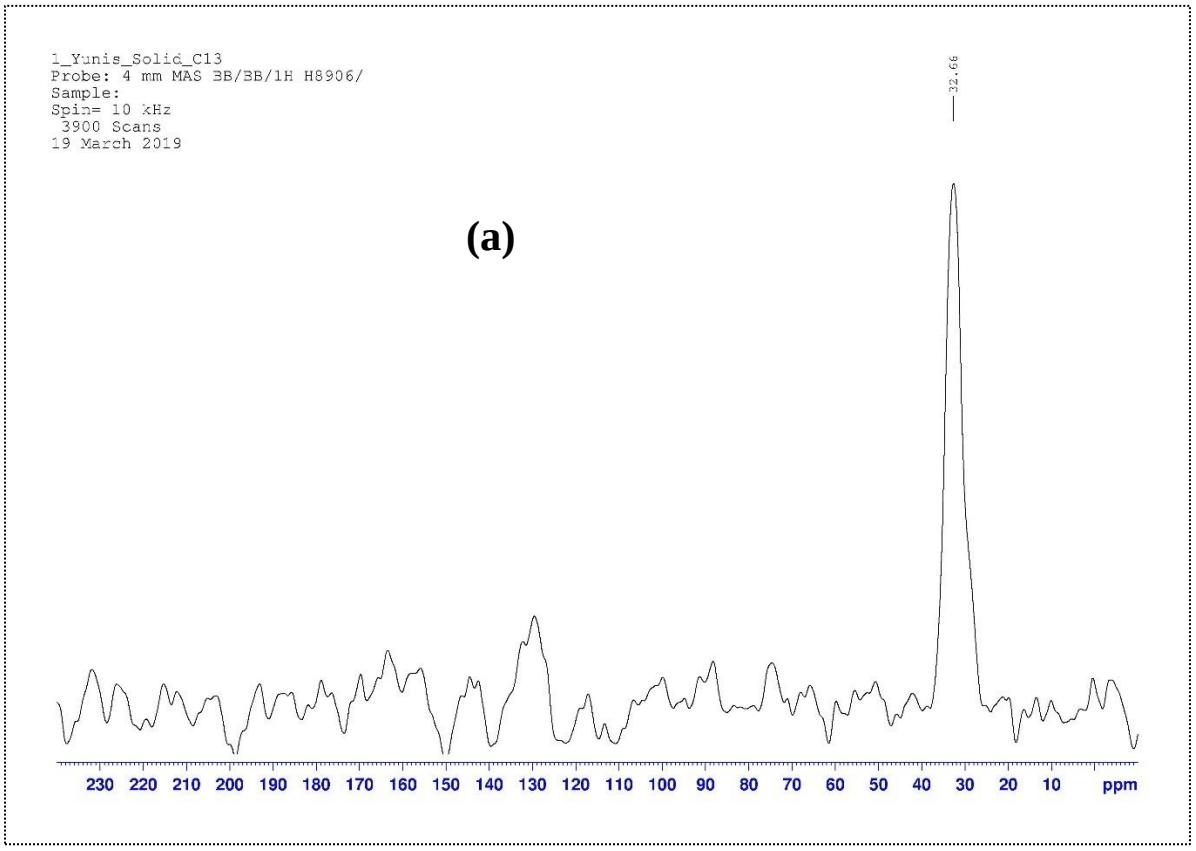

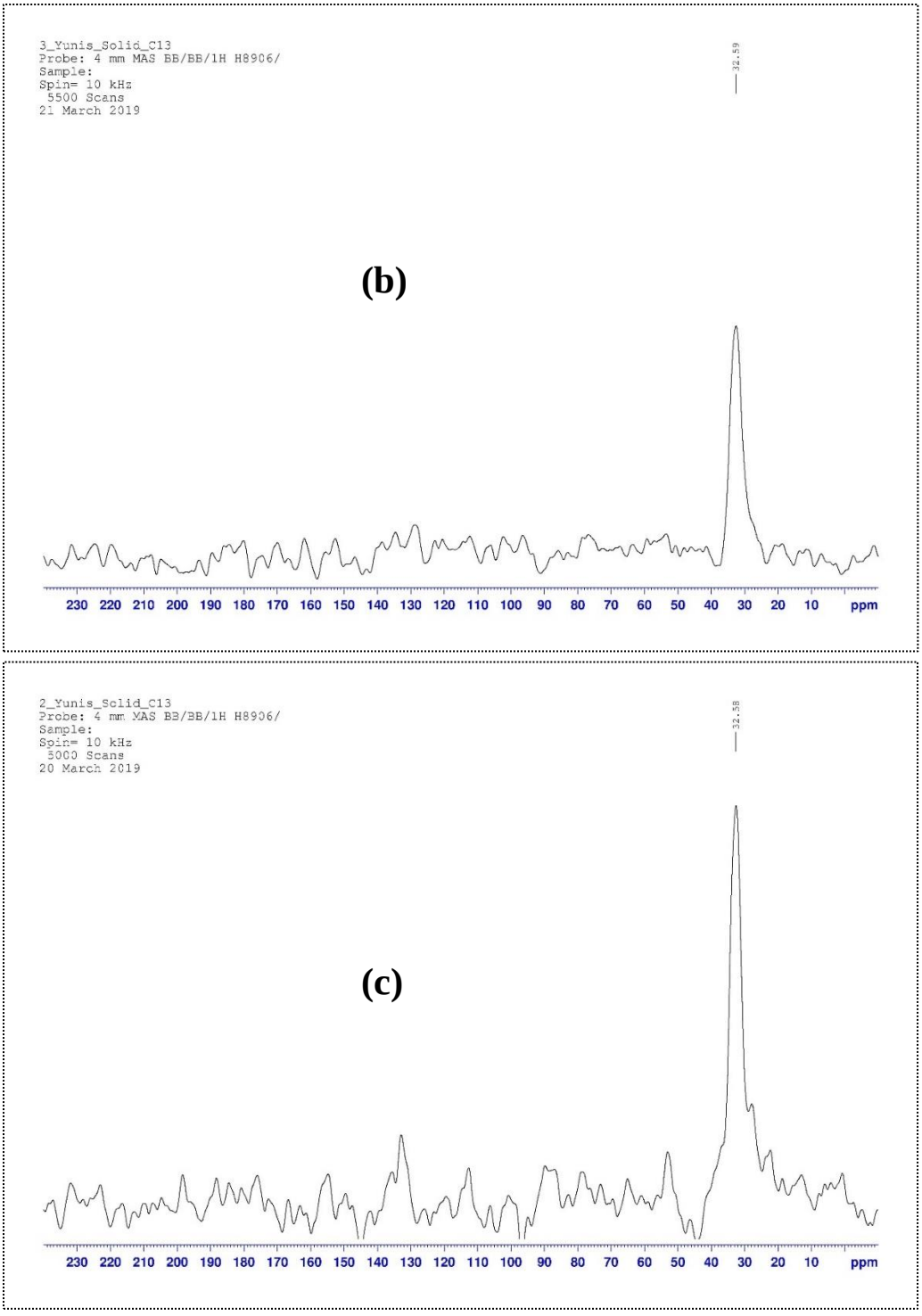

Figure 62 Solid NMR analysis of crushed single crystal **(a)** $MAPbI_3$ **(b)** BAI: $MAPbI_3$ **(c)** PAI: $MAPbI_3$.

CHAPTER FIVE

RESULTS AND DISCUSSIONS

This chapter provides the results and their discussions carried out for this thesis. These results include current-voltage (J-V) characteristics, ultra-violet visible (UV-Vis) spectroscopy, electrochemical impendence spectroscopy (EIS), cyclic voltammetry (CV), Tafel studies, chronoamperometry, and Auto lab potentiostat studies.

The detailed theoretical background of current-voltage characteristics and important parameters of solar cells are discussed in section 5.1 below.

5.1. Current-voltage Characteristics and Important Parameters of Solar Cell

There are four important parameters of solar cells.

(a) Short-circuit current density J_{sc}
(b) Open-circuit voltage V_{oc}
(c) Fill factor FF
(d) Power conversion efficiency η

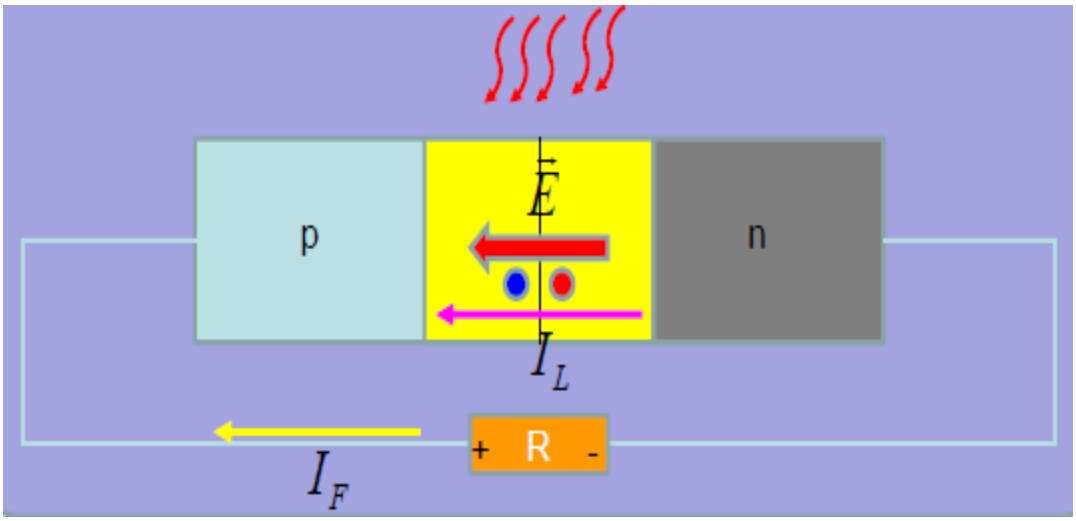

Figure 63 The working diagram of pn junction solar cell.

When an electron-hole pair generated as shown in process 1 of Figure 1 and above figure 63, the current generated is called photocurrent in the reverse bias direction is represented by I_L. When this current drop voltage across the load in the external circuit it made the circuit forward bias and producing a dark current represented by I_F. The total current in the reverse bias direction will be

$$I = I_L\text{-}I_F \qquad (5.1)$$

The forward bias current can be represented in terms of reverse saturation current as

$$I = I_L\text{-}I_S\,[\exp\,(\frac{eV}{kT})\text{-}1] \qquad (5.2)$$

Where k is Boltzmann constant, T is temperature.

There are two limiting cases of interest; short-circuit current and open-circuit voltage. The short-circuit current condition occurs when R=0, so V=0, so from equation 5.2, we can write;

$$I = I_{sc} = I_L \qquad (5.3)$$

In the second case the open-circuit voltage occurs when R → ∞, so V = V_{oc}

From equation 5.2

$$I = 0 = I_L\text{-}I_S\,[\exp(\frac{eV_{oc}}{kT})\text{-}1] \qquad (5.4)$$

$$V_{oc} = V_t \ln(1+\frac{I_L}{I_S}) \qquad (5.5)$$

Where $V_t = \frac{kT}{e}$

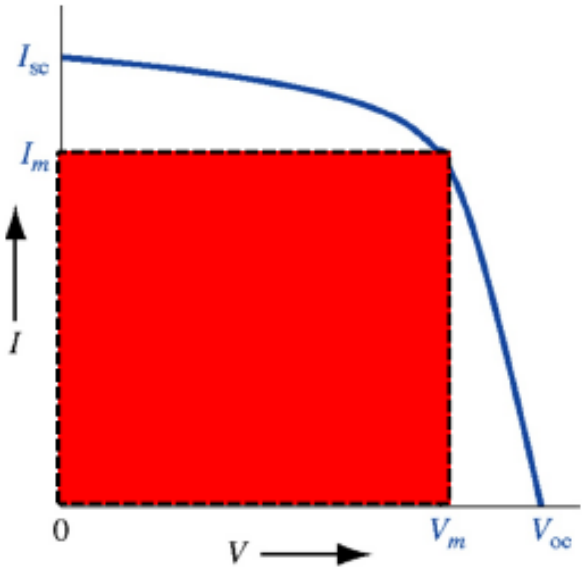

Figure 64 Current-voltage characteristics of a solar cell.

The power delivered to the load is

$$P = I.V \qquad (5.6)$$

By using equation 5.2, we can write equation 5.6 as

$$P = I_L.V - I_s\left[\exp\left(\frac{eV}{kT} - 1\right) - 1\right].V \qquad (5.7)$$

The maximum power delivered to the load can be find as

$$\frac{dp}{dV} = 0 \qquad (5.8)$$

From equation 5.7 and 5.8, we have

$$I_L - I_s\left[\exp\left(\frac{eV_m}{kT} - 1\right) - 1\right] - I_s \times V_m \times \left(\frac{eV_m}{kT}\right) \times \exp\left(\frac{eV_m}{kT} - 1\right) = 0 \qquad (5.9)$$

By solving equation 5.9, we have

$$\left(1 + \frac{V_m}{V_t}\right) \times \exp\left(\frac{eV_m}{kT}\right) = 1 + \frac{I_L}{I_s} \qquad (5.10)$$

The 3rd important parameter of solar cell is Fill Factor (FF). The FF is defined as

$$FF = \frac{I_m V_m}{I_{sc} V_{oc}} \qquad (5.11)$$

Where I_m & V_m are maximum current and maximum power. In other words, the FF can be defined as "the perfection of the solar cell". The FF vary between 0 to 1. The maximum FF can be one in an ideal case when $I_m = I_{sc}\ and\ V_m = V_{oc}$, i.e. no recombination of charges (dark current). Usually the FF is in the range of 0.7 ~ 0.8 for efficient solar cells.

The 4th more important parameter of solar cell is its power conversion efficiency (PCE). The PCE can be defined as;

$$\eta = \frac{P_m}{P_{in}} \times 100\% \qquad (5.12)$$

Where P_m and P_{in} are maximum and incident power.

$$\eta = \frac{I_m \times V_m}{P_{in}} \times 100\% \qquad (5.13)$$

By using equation 5.12, we can write equation 5.13 as

$$\eta = \frac{I_{sc} \times V_{oc} \times FF}{P_{in}} \times 100\% \qquad (5.14)$$

The IV characteristics of solar cells are represented in terms of current density and voltage as shown in Figure 65 below;

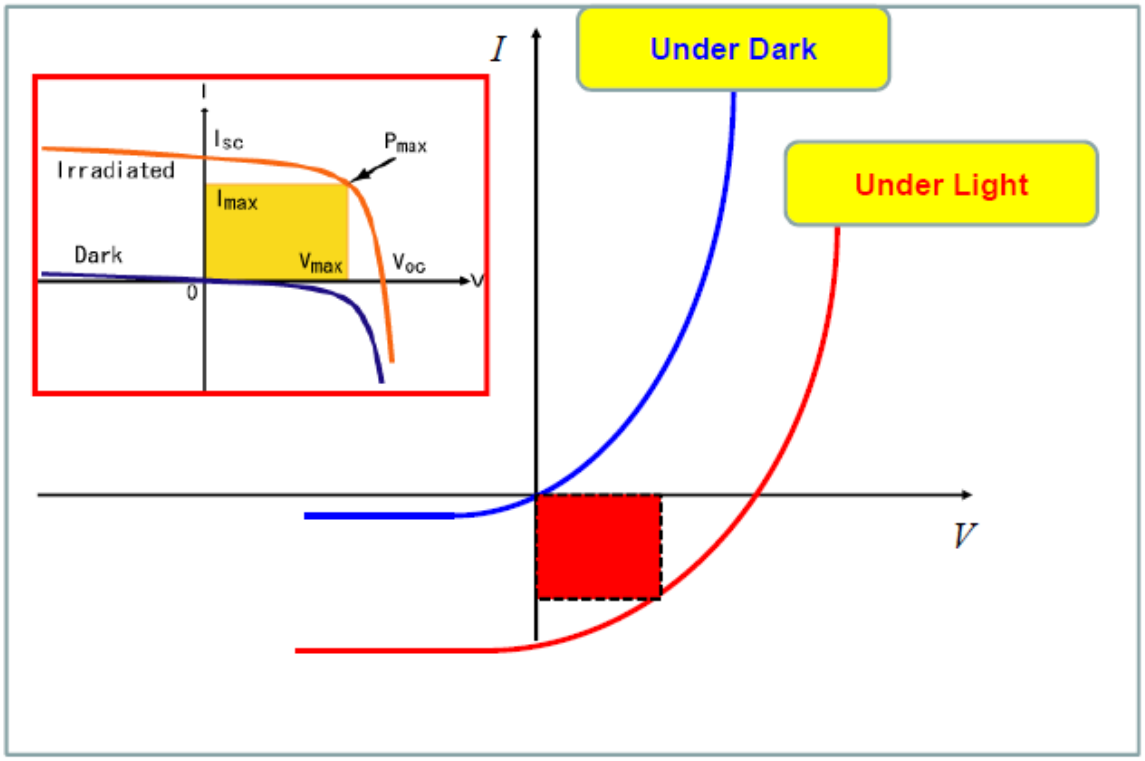

Figure 65 Current-voltage characteristics of solar cell under dark and illumination.

Figure 65 shows the IV characteristics of solar cells under dark and illuminated conditions. Under dark condition, it is evident that there is no photocurrent due to no exposure of light on solar cells. However, when we illuminate solar cells with incident light having energy (energy of photons) more than band gap energy of illuminated material, electrons will be removed from the surface of the material due to photovoltaic effect. The current generated is called photocurrent and can be observed from Figure 65 as a red curve. The maximum current and maximum voltage which we can obtained from the solar cell is represented in Figure 64 and 65 as red area. The FF is the difference between the experimental IV curve and ideal square curve which can be drawn from the J_{sc} point to V_{oc} point.

5.2. Performance enhancement of dye sensitized solar cells via co-sensitization of ruthenizer Z907 and organic sensitizer SQ2

5.2.1 Brief introduction

Energy plays an important role in modernization, automation and economic growth of any country and society at large. Escalating energy demand and ecological issues have encouraged researchers to focus on clean and eco-friendly new energy sources [114]–[116]. Solar energy enjoys the fact that it is easily attainable, most wide and approachable source of renewable energy on our planet. The annual estimated sun energy accessible on our planet is about $3x10^{24}$ J, which is about 10^4 times greater than that currently consumed by the world population [117], [118]. Solar energy is considered among the top available alternatives to mitigate the carbon dioxide (CO_2) emission to the environment due to the burning of fossil fuels [119]–[121]. High emission of CO_2 into the atmosphere has caused many catastrophic effects in terms of global warming, forest declining, and climate change. To utilize this energy various kind of photovoltaic cells have been developed since 1954. DSSCs are third generation solar cells which is a quite new version of photovoltaic devices [122]. DSSC was first developed by Grätzel and co. workers in 1991. DSSCs gained considerable attention due to their low cost, easy fabrication, less toxicity and moderate power conversion efficiency (PCE) as compared to silicon-based solar cells [33], [123].

DSSCs consist of three major components: 1) photoanode, 2) counter electrode, 3) electrolyte. Photoanode, one of the major components of DSSC performs two important functions, (i) collection of electrons from the photo-excited dye and their transportation to the outer circuit, and (ii) acts as scaffolding which needed for dye adsorption. Usually

anode are porous in morphology for sufficient dye adsorption and wide band gap materials e.g. TiO_2, ZnO, Nb_2O_5 etc. [124]. The main functions of the counter electrode (CE) are (i) the reduction of oxidized electrolyte due to the regeneration of dye, and (ii) transportation of the positive charges (holes) toward the CE. Various types of CE have been used for DSSC including platinum (Pt), carbon nanotubes (CNT) and other carbonaceous materials etc. [125]. Electrolyte, which is sandwiched between photoanode and CE, is one of the most important components in the DSSC. The prime function of the electrolyte is to regenerate photo-exited dye [118]. There are different types of electrolytes e.g. liquid, gel polymer, and other polymer electrolytes, which have been used in DSSC. Liquid electrolyte e.g. iodine/triiodide (I^-/I_3^-) are commonly used due to their outstanding characteristics like the couple have a good solubility, not absorbing much of the incident light, containing an appropriate redox potential and fast dye regeneration. However, due to the liquid nature, the stability, long term durability and performance of the DSSC is compromised. To resolve these issues researchers replaced the liquid electrolyte with hole transport materials, gel polymer and other polymers for stable and flexible DSSCs. Federico Bella et al. report new gel-polymer membranes doped with iodine salts for the enhancement of photovoltaic performance. Matteo Gerosa et al. used Ti grid for the fabrication of completely flexible DSSC. An important work to enhance the thermal and long-term stability of DSSC has been carried out by Federico Bella et al. by introducing the finely dispersed nanosized silica particles with the iodide/triiodide electrolytes and obtained promisingly encouraging results. The group also carried out the polymeric approach to patterning the DSSC anode, in addition with polymer electrolytes, for stable and efficient DSSC [126]–[129]. Photosensitizer (dye) is the main component of DSSC which is

adsorbed on the semiconducting material, for instance, TiO_2, ZnO [130]–[132]. The PCE of DSSC mainly depends on photosensitizer. The main function of dye in DSSC is to absorb incident photons and produce the electron-hole pairs which can be transferred to the external circuit through the semiconducting material. In the last fifteen years, remarkable progress has been observed at many aspects of this technology, approaching record efficiencies over 14% [133]. However, still, there is room for efficiency enhancement of these photovoltaic devices and their commercial applications at large scale. The specific reason for low PCE is the low absorption range of photosensitizer (dye) [9], [114]. Presently, there is no such single sensitizer having the ability to absorb sunlight in a broad spectral range (400-900 nm) [8].

Co-sensitization is highly successful technique to boost the PCE of DSSC [10], [11]. It improves the absorption spectral range, hence light harvesting efficiency of solar cells [12]. Many combinations of photosensitizers like porphyrin co-sensitized with ruthenium complexes [13], organic dye co-sensitized with ruthenium complexes [14], [15], [134], or co-sensitization of phthalocyanine with an organic sensitizer [16]–[18], and an organic sensitizer that has been co-sensitized with different organic dyes [19], [20] has been employed. Daibin Kuang et al. used two organic dyes (SQ1 and JK2), and found PCE of 6.4% using solvent-free electrolyte [20]. Yousheng Chen et al. used different organic dyes for co-sensitization, a hemicyanine dye, a merocyanine dye, and a dye based on squarylium cyanine and obtained the efficiency of 6.5% [19]. Wenjun Wu et al. synthesized two indolium based organic dyes and used them in DSSCs. They used their mixture to the ratio of 1:3 and got overall PCE of 3.0% under standard 1 sun AM 1.5G illumination [21]. Kun-Mu Lee et al. used co-sensitization technique for plastic DSSCs. They got PCE of 5.1%

by co-sensitization of ruthenium complexes (N719 and N749) and organic dye consisting of the thienylfluorene segment called FL [22]. Chi-Ming Lan et al. used zinc porphyrin dye (LD12) for co-sensitization with an organic sensitizer (CD5) in a stepwise approach and obtained an efficiency of 9% [12]. L. Wei et al. co-sensitized ruthenium dye (N719) with different three organic dyes (DM, DE, and DP) and got an efficiency of 7% [15].

In this work, we used the co-sensitization technique to improve the efficiency of DSSC. The organic SQ2 dye was used as a co-sensitizer with ruthenium Z907 dye. Dye solutions of different concentrations were prepared and used for the sensitization of semiconductor anode. The performance of DSSCs sensitized with individual dyes (Z907 or SQ2) is compared to that of solar cell devices fabricated with co-sensitized (Z907+SQ2) phenomenon under the same conditions of fabrication. The results reveal that the overall photovoltaic performance of the optimized co-sensitized solar cells is significantly enhanced and hence PCE is much superior than that of individually sensitized solar cells.

5.2.2 Results and discussion

5.2.3 Ultra-violet (UV-Vis) spectroscopy of fabricated DSSC

The absorption spectra (UV-Vis spectra) of dyes (Z907, SQ2 and Z907+SQ2) in ethanol and adsorbed on the surface of TiO_2 films coated on FTO conductive glass are shown in Figures 66-69 respectively. Three broader and intense peaks in Z907 at 530, 385 and 310 nm are attributed to metal to ligand charge transfer (MLCT) and intraligand (π-π^*) charge-transfer transitions, respectively, as shown in Figure 66. Similarly, Figure 67 depicts the absorption spectrum of SQ2 with two absorption peaks in the regions 580-620 nm and 620-680 nm. The peak in the region 580-618 nm can be ascribed to π-π^* electronic transitions of the conjugated molecules, while the second peak is due to the donor to acceptor

anchoring groups intermolecular charge transfer (ICT). Figure 68 shows the absorption spectra of mixed dyes in ethanol, which are more intense as compared to that of individual dyes. The results clearly demonstrate that the concentration of co-sensitizer strongly affects the absorption of light. The absorption of Z907 enhanced with the increase in the concentration contents of SQ2 sensitizer because of the synergistic effect of both sensitizers. However, the absorption of *Z907 + SQ2 becomes red* shifted when anchored to TiO_2 as shown in Figure 69, owing to strong interaction among the carboxylate groups and the surface Ti^{4+} ions [117], which enhances the delocalization of the π* orbital**.** The red shift physically can be noted from Figure 68 and 69 as the peaks are shifted from 656 nm to 671 nm. This red shift is due to the strong interaction between carboxylate groups from dyes and Ti^{4+} ions from semiconductor TiO_2 film. Furthermore, the absorption spectrum of *Z907 + SQ2* dyes adsorbed on TiO_2 is more intense, sharp and broader in comparison with the individual dyes anchored to TiO_2 in the same conditions of fabrication. This clearly shows that the co-sensitized TiO_2/ (Z907+SQ2) thin films fabricated in this experiment can absorb more photons from the incident light as compared to that of individual sensitized TiO_2/Z907 or TiO_2/SQ2 films. The more absorptions of photons lead to the more generations of electrons in the dyes adsorbed on TiO_2 semiconducting film i.e. excitation of electrons from HOMO to LUMO level of dyes, which resulted in more available conduction electrons and hence more efficiency.

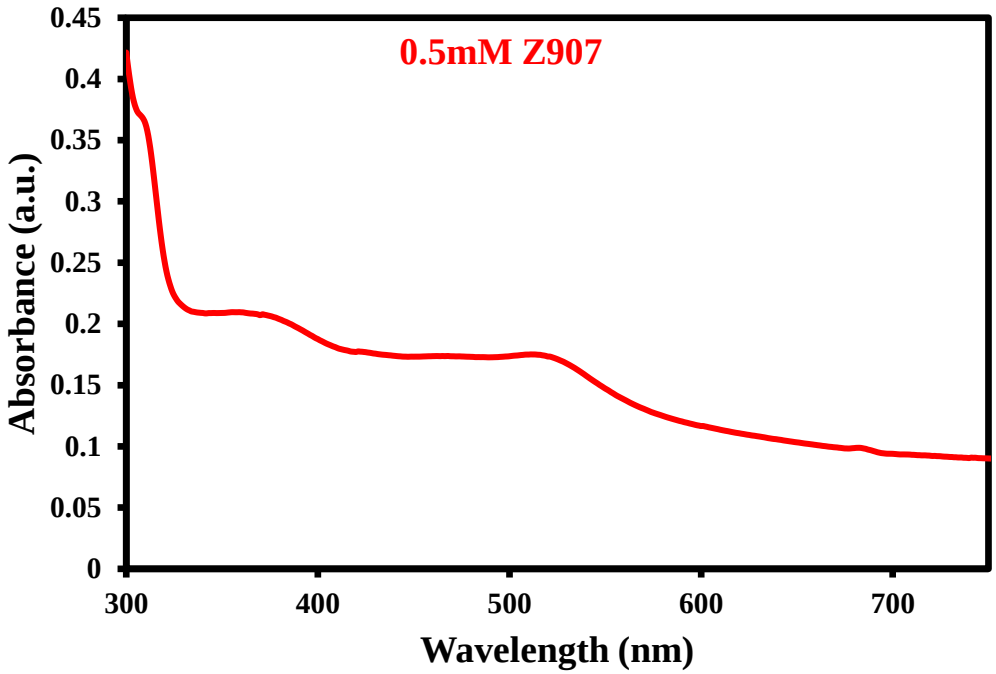

Figure 66 UV-Vis spectra of Z907 in ethanol.

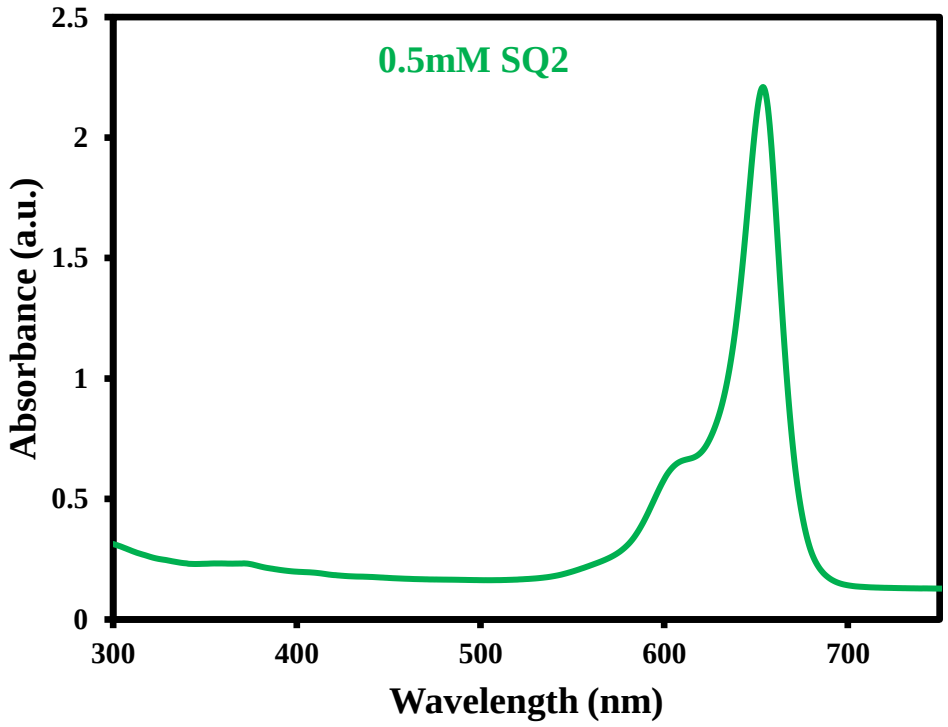

Figure 67 UV-Vis spectra of SQ2 in ethanol.

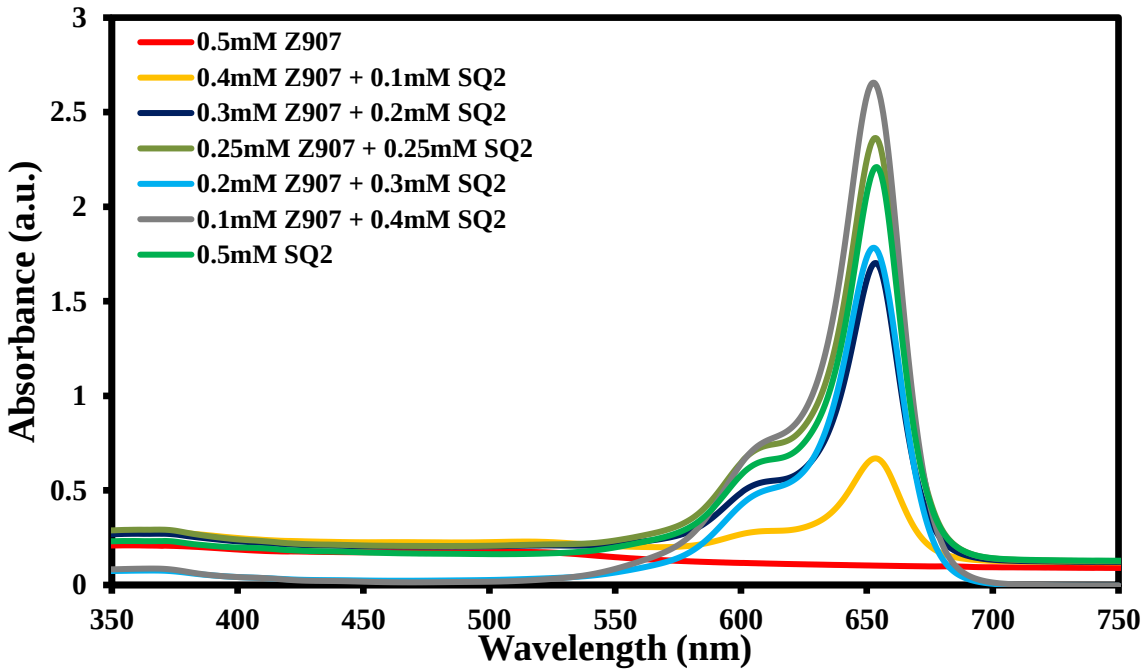

Figure 68 UV-Vis spectra of Z907 + SQ2 in ethanol.

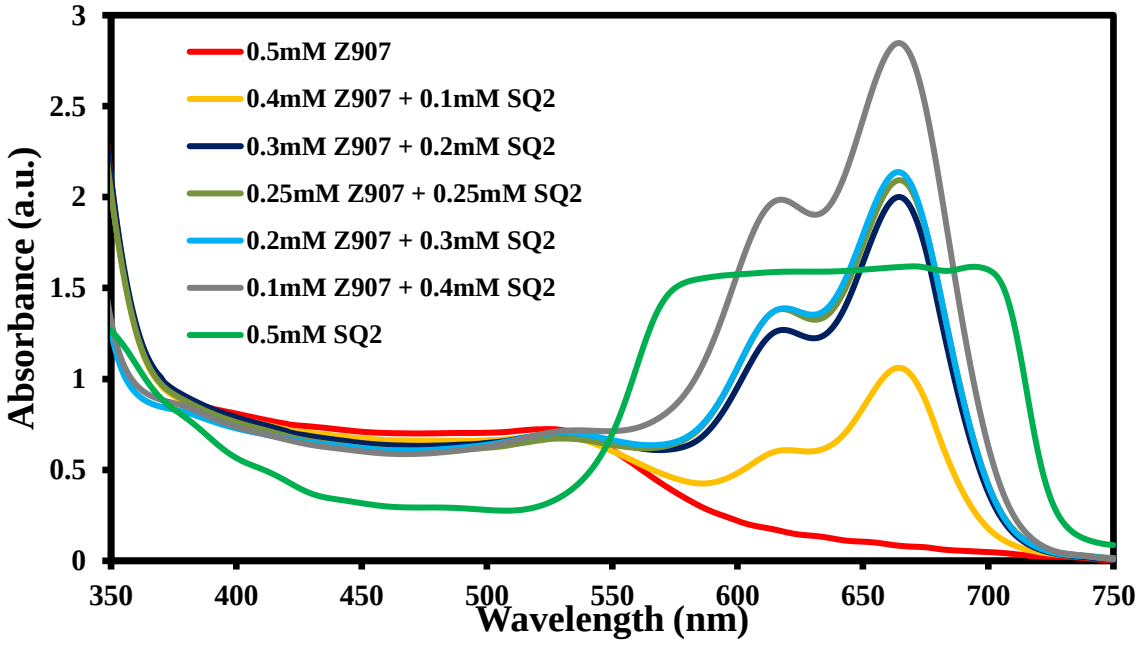

Figure 69 UV-Vis spectra of dyes adsorbed on TiO_2 films.

5.2.4 I-V characteristics of fabricated DSSC

I-V characteristics and their photovoltaic parameters of fabricated co-sensitized solar cells are given in Figure 70 and table 16, respectively. Table 16 shows, the current density (J_{SC}), open circuit voltage (V_{oc}), Fill Factor (FF) and efficiency (η) of the fabricated solar cells. From table 16 it can be clearly noted the current density of the fabricated solar cells is increased until optimized concentration and then it starts decreasing, as for higher concentrations of SQ2 the number of available electrons are reduced due to higher bandgap of organic dye. Similarly, the open circuit voltage and Fill Factor also enhanced until optimized concentrations of dyes and then start decreasing. The overall enhanced performance has been achieved by co-sensitization technique by availing, both maximum absorption due to higher absorption coefficient of organic dye and more current due to less band gap of ruthenium-based dye. The results clearly show that the overall performance of co-sensitized solar cells strongly depends on the concentration of co-sensitizer. Under optimized conditions, the solar cell sensitized with 0.3mM Z907 + 0.2mM SQ2 showed J_{SC} = 21.38 mA/cm^2, V_{oc} = 698.37 mV, FF = 52.46%, and η = 7.83%. This PCE is significantly greater than that of the individual (TiO_2/Z907 or TiO_2/SQ2*)* sensitized devices. The enhancement in PCE of the co-sensitized solar cell is due to increase in J_{SC} (21.38 mAcm^{-2}), V_{oc} (698.37 mV) and fill factor (52.46%). An increase in J_{sc} is primarily owing to strong and intense absorption of light while the suppression of charge recombination due to co-sensitization is the major cause of the increase in V_{oc}.

The uncertainty analysis of the parameters has been provided in the table 17. Five sets of each configuration have been taken to measure uncertainty or error analysis. All the parameters have been averaged over the five values obtained from each cell configuration.

The standard deviation has been calculated to find the uncertainty or error in each parameter for each cell configuration. The overall error has been remained less than 1% among all the parameters in each cell configurations.

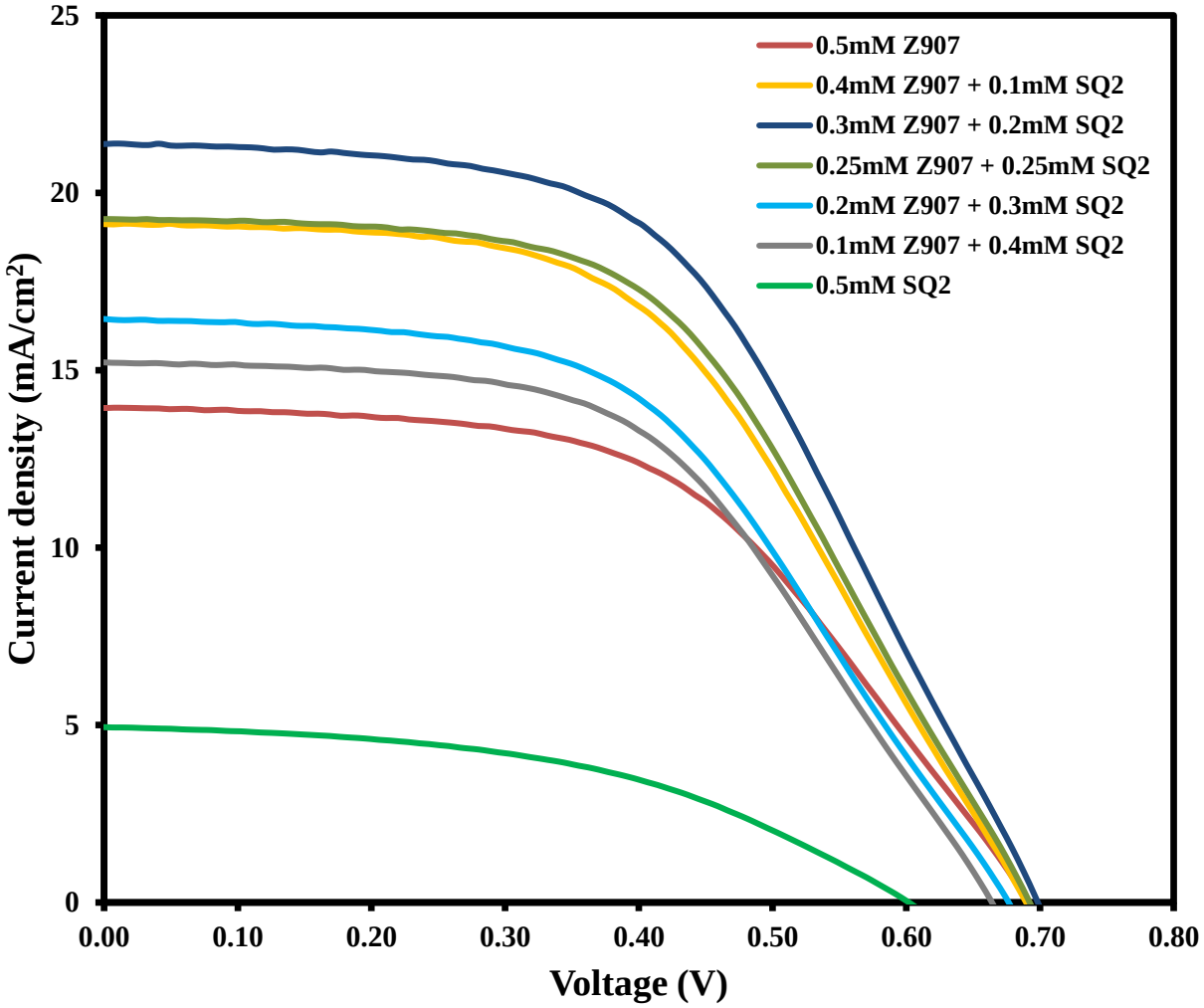

Figure 70 Current − voltage characteristics of DSSCs.

Table 16 Photovoltaic properties of DSSCs.

DSSCs	J_{sc} (mA/cm^2)	V_{oc} (mV)	FF(%)	η (%)
TiO_2/0.5mM Z907	13.94	691.09	52.72	5.08
TiO_2/0.4mM Z907 + 0.1mM SQ2	19.12	689.65	51.62	6.81
TiO_2/0.3mM Z907 + 0.2mM SQ2	**21.38**	**698.37**	**52.46**	**7.83**
TiO_2/0.25mM Z907 + 0.25mM SQ2	19.26	692.27	52.74	7.03
TiO_2/0.2mM Z907 + 0.3mM SQ2	16.44	676.52	51.41	5.72
TiO_2/0.1mM Z907 + 0.4mM SQ2	15.22	664.04	53.05	5.36
TiO_2/0.5mM SQ2	4.94	601.93	46.69	1.39

Table 17 Photovoltaic properties of DSSCs with error analysis.

DSSCs	J_{sc} (mA/cm^2)	V_{oc} (mV)	FF(%)	η (%)
TiO_2/0.5mM Z907	13.91±0.31	690.95±0.14	52.72±0.50	5.07±0.03
TiO_2/0.4mM Z907 + 0.1mM SQ2	18.97±0.22	690.06±0.81	51.71±0.32	6.75±0.06
TiO_2/0.3mM Z907 + 0.2mM SQ2	**20.67±0.52**	**698.46±0.42**	**53.52±0.91**	**7.72±0.08**
TiO_2/0.25mM Z907 + 0.25mM SQ2	19.20±0.04	692.59±0.22	52.64±0.09	7.00±0.03
TiO_2/0.2mM Z907 + 0.3mM SQ2	16.50±0.12	677.04±0.98	51.01±0.41	5.70±0.02
TiO_2/0.1mM Z907 + 0.4mM SQ2	15.23±0.01	664.35±0.22	52.87±0.15	5.35±0.01
TiO_2/0.5mM SQ2	4.87±0.06	600.84±0.76	46.48±0.41	1.36±0.03

5.2.5 EIS analysis of fabricated DSSC

Charge recombination is a major problem in solar cells devices. It is an important factor and can be understood from Figure 71. All the dotted lines in Figure 71 represent the various type of charge recombinations. An electron generated in response of an incident photon due to the excitation of dye usually moved to the conduction band (CB) of the porous semiconductor. In an ideal case an excited electron should be harvested to the external circuit, however, there are three possibilities. This electron can go through the following paths; either recombine with the excited dye generated holes or transferred to semiconductor and recombine with the excited dye generated holes or recombine with the ionized electrolyte atoms [135]. In this work, the charge recombination resistances of DSSCs were investigated by EIS analysis. EIS, evaluates the response of current at different frequencies with applied AC voltage. Figure 72a and 72b depict the EIS spectra (Nyquist plot) of fabricated DSSCs and the equivalent circuit of Nyquist plot, respectively. EIS spectra are represented by three semicircles. The first circle at high frequency shows interface resistance between the counter electrode and electrolyte (R_1). The second arc at intermediate frequency and third arc at low frequency represent interface resistance between photoanode and electrolyte (R_2) and carrier transport internally inside the electrolyte through diffusion of redox couple (Z_w), respectively [10]. In Figure 72b, equivalent circuit of the Nyquist plot contains R_s, the series resistance, i.e. the value of resistance representing the initial point of the first arc at high frequency in Nyquist plot. The resistances R_1 and R_2 show the resistance at back electrode/electrolyte interface and the recombination rate at anode/electrolyte interface, respectively. The symbols C_2 and C_1 indicate the capacitances (constant phase elements) to the respective interfaces, i.e.

anode/electrolyte and counter electrode/electrode. The Z_w indicates the Warburg diffusion impedance. In our case it is clear from Figure 72a, only second arc (R_2) representing resistance at photoanode/dye/electrolyte appears in four devices, and remaining two small arcs may be overshadowed by second arc [136], [137]. However, the other three devices showed two arcs related to R_1 and R_2. Moreover, since the R_2 denotes the recombination resistance to the free carriers at anode/electrolyte interface [10], [114]. Higher the free carriers recombination resistance, larger will be the electron lifetime and vice versa [138]. The charge recombination resistances are listed in Table 18. It can be observed from Table 18 and Figure 72a that the R_2 of 0.3mM Z907 + 0.2mM SQ2 sensitized DSSC possesses the higher resistance to the recombination of free charges and hence longer electron transport lifetime which is verified from the increase in the efficiency. From table 18 it can also be noted that the individual dyes have less charge recombination resistances as compared to the co-sensitized configurations of the fabricated solar cells which shows the effectiveness of co-sensitization technique. The increase in electron lifetime by co-sensitization can be ascribed to the enhancement of surface coverage by dye on TiO_2. Higher the surface coverage by the dye, less will be the electron approach to TiO_2 and hence reduces the recombination process. Physically we can explain this recombination process as shown in Figure 71. The more coverage of TiO_2 surface with dye will leads to more generation of electrons as well as less charge recombination due to the exposure of electrolyte to the TiO_2 surface and hence enhancement of overall performance of the co-sensitized configuration of fabricated solar cells.

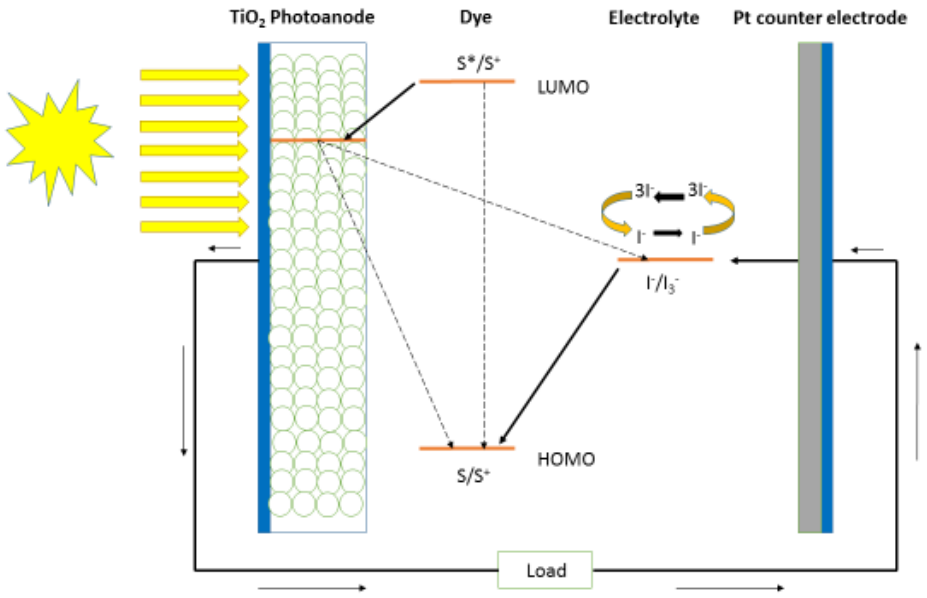

Figure 71 DSSCs energy bandgap diagram.

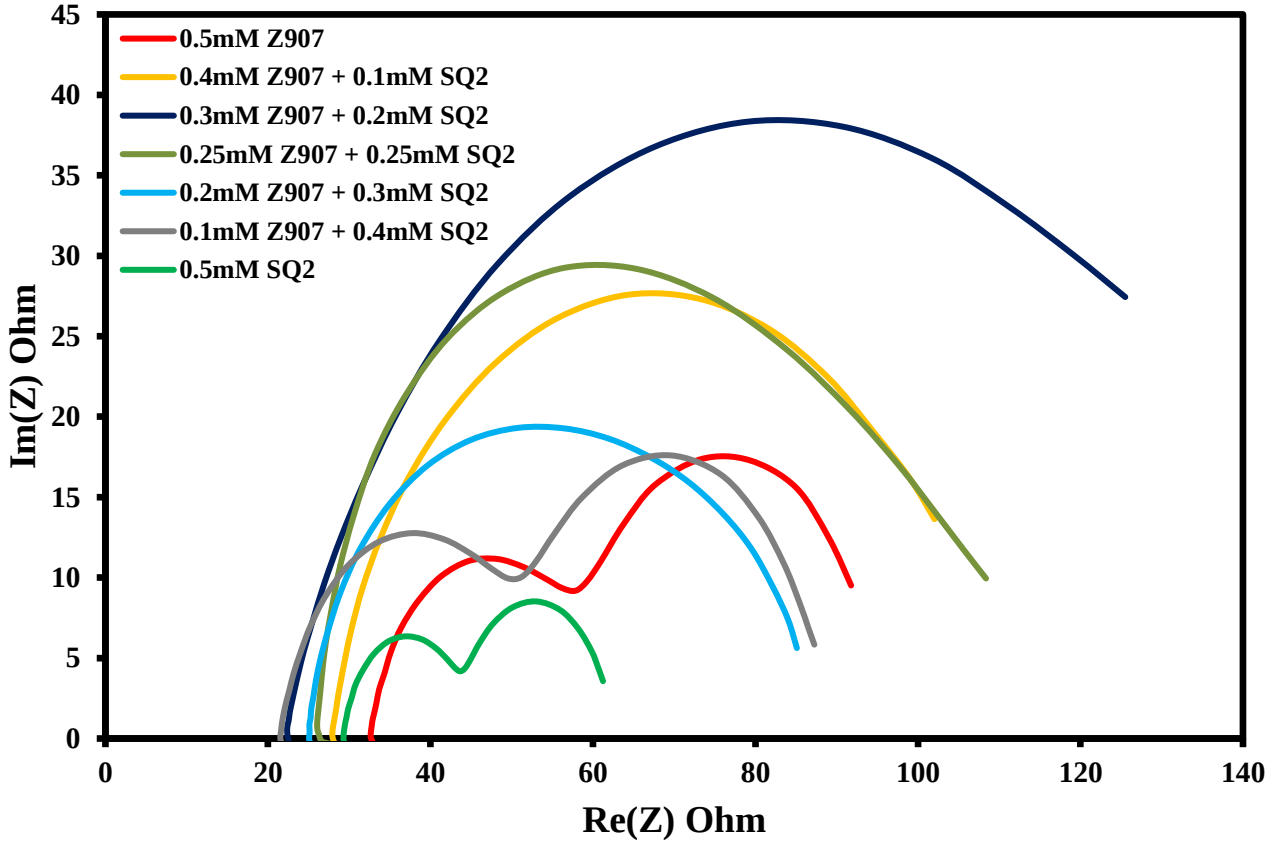

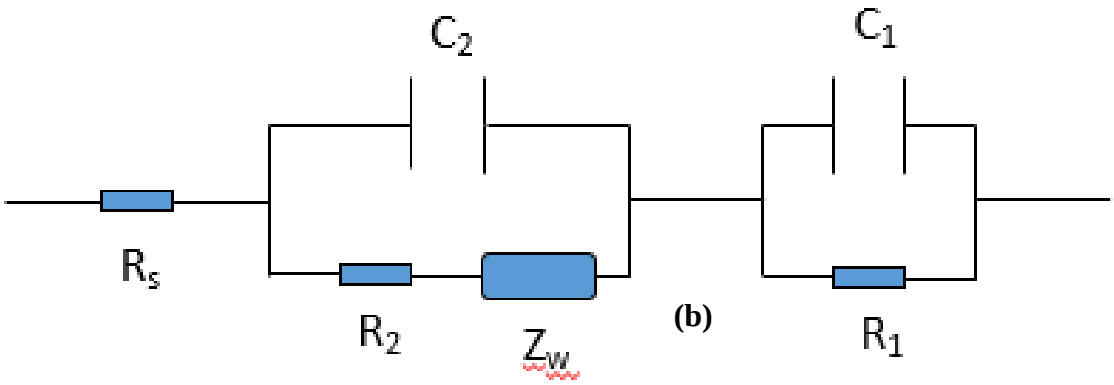

Figure 72 (a) EIS investigation of DSSCs (b) equivalent circuit of DSSC.

Table 18 Charge recombination resistance at anode interface (TiO_2/dye/electrolyte).

Sample#	DSSCs	*R_2 (ohm)*
1	TiO_2/0.5mM Z907	36
2	TiO_2/0.4mM Z907 + 0.1mM SQ2	81
3	**TiO_2/0.3mM Z907 + 0.2mM SQ2**	**122**
4	TiO_2/0.25mM Z907 + 0.25mM SQ2	90
5	TiO_2/0.2mM Z907 + 0.3mM SQ2	62
6	TiO_2/0.1mM Z907 + 0.4mM SQ2	41
7	TiO_2/0.5mM SQ2	31

5.2.6 Summary

In this work we used co-sensitization approach to enhance the performance of DSSC. We used organic sensitizer SQ2 as a co-sensitizer with ruthenium-based dye Z907. Dye solutions of seven different concentrations were prepared for the fabrication of DSSC. The fabricated DSSC were characterized by UV-Vis spectroscopy, I-V characteristics, and EIS analysis. Our main findings are:

- The co-sensitization approach is highly effective method to boost the photovoltaic performance of a DSSC.
- The absorption of dye solution increases with the increase of SQ2 contents. However, spectra become more intense, sharp and broader when anchored to TiO_2 film coated on the FTO surface.
- The PCE, V_{oc}, J_{sc}, FF and charge recombination resistance of solar cells strongly depend on the concentration of SQ2 dye. Under optimal conditions, the DSSC assembled with 0.3mM Z907 + 0.2mM SQ2 delivered PCE of 7.83%, which is significantly higher than the individual sensitized solar cell (Z907 = 5.08% and SQ2 = 1.39%).
- The charge recombination resistance at photoanode/dye/electrolyte interface increases with co-sensitization and thus reduces the dark current.

5.3. Fabrication of Cost Effective and Efficient Dye Sensitized Solar Cells with WO_3-TiO_2 Nanocomposites as Photoanode and MWCNT as Pt-Free Counter Electrode

5.3.1 Brief introduction

Energy is one of the most essential commodities for human progress and development, especially in the world of postindustrial revolution. With the ever-growing population and the standard of living, the demand for energy is skyrocketing in developed and developing nations alike, and it is predicted that by 2050, the energy consumption will rise to 23 terawatt from the current figure of 13 terawatt [139]. Nearly 80% of the world energy requirement is catered by rapidly depleting fossil fuels, and the excessive use of which triggers geological imbalances and environmental impairment due to the disposal of huge amount of greenhouse gases in the fragile atmosphere [140]. Hence, scientists, environmentalists and the policy makers started contemplating alternate renewable sources of energy, and naturally the most abundant, the cleanest and the inexhaustible solar energy, top the list of the alternate energy sources [50]. Ever since, the first discovery of the photovoltaic effect was reported by William Grylls Adams, the development of solar cells has gone through many technological and economic challenges and categorized into three generations. The silicon wafer based 1st generation solar cells, and even slightly less expensive amorphous silicon, CdTe, and CIGS based 2nd generation solar cells encounter the challenge of high material and production cost, despite their remarkable efficiency of about 15-20 % [141]. Hence the research pursuit for developing cost effective and the efficient solar cell has been on for a few decades and culminated in the development of

Dye Sensitized Solar Cell (DSSC) by M. Grätzel et al. in 1991 [33], which is widely considered as the 3rd generation solar cells.

DSSC consists of a basic structure in which an electrolyte is sandwiched between a photoanode sensitized by an organic/ruthenium dye and a counter electrode (CE) [142], and this breed of solar cell has gained an enormous research attention in the last two decades, due to its vast potential scope for making improvisations in various aspects like its structure, assembly, and the constituent materials and thereby enhancing their efficiencies at less production cost [143]. There has been numerous works reporting the modifications and improvements made on the photo anode [130]–[132], [144], [145], back electrode [146]–[148], dyes [149]–[152], and electrolyte [153]–[155] of DSSC. Photo-anode is a crucial component in the DSSC structure, where the collection of vital electrons into the semiconductor is mediated by the photo excitation of the organic/ruthenium dye (photosensitizer) and subsequently transferring the photo-generated electrons to the back electrode through an external circuit. Although several semiconductors such as TiO_2, SnO_2, ZnO_2, In_2O_3, CeO_3 and NbO_3 etc. have been used as photo-anode in DSSC [156], TiO_2 stands out to be the best material owing to its outstanding features like low cost, easy availability, nontoxicity and better dye loading. However, inherently inferior electron transport property (electron mobility) of TiO_2 compared to other semiconductors like ZnO considerably brings down the efficiency in TiO_2 photo-anode based DSSCs [157].

In order to overcome the electron transport deficiency and simultaneously harnessing the positive features of TiO_2 as a promising semiconducting material, it is usually combined with another semiconductor having high electron mobility to form a nanocomposite materials for photo-anode and extensive work has been carried out to develop an efficient

composite photo-anode to improve the performance of DSSC [158]. Owing to the favorable band gap energy (2.6-3.1 eV), better electron mobility, and high stability, tungsten oxide (WO_3) can be considered for a good composite partner with TiO_2 to fabricate an efficient photo-anode [159]. However it should be noted that DSSC based on pure WO_3 as a photo-anode have been proven to be quite inefficient through the work of H. Zheng et al. who got the maximum efficiency of 1.46% with Pt as a CE [160] and also through the work of S. M. Yong et al. who got the maximum efficiency of 1.51% with WO_3 1D nanorods as photoanode and Pt as a CE [161]. On the other hand, TiO_2-WO_3 composite semiconductor as a photo-anode in DSSC has been proven to be much more efficient than pure TiO_2 and pure WO_3 photo-anodes. N. Prabhu et al. reported the enhancement of the performance with the maximum efficiency of 5.03% by using TiO_2-WO_3 composite as photoanode and Pt as CE [162]. J. H Yang et al. tried composite of TiO_2+TNWs+WO_3 and obtained an efficiency of 5.47% with Pt as CE, which is the best reported efficiency from any TiO_2-WO_3 nanocomposite based photo-anode till date [163].

Platinum (Pt: a noble metal), which is extensively used as CE of DSSC because of its high catalytic activity, stability and high exchange current density, however, being expensive, the use of Pt in DSSCs cannot be an economical proposition to scale up DSSC. Several materials such as conductive polymers, carbon, carbon black, single wall carbon nanotubes, multi wall carbon nanaotubes (MWCNT) have been tried as CE in DSSC to replace the conventional Pt based CE and among these counter electrode materials, MWCNT has attained a considerable attention owing to its low cost, high electron mobility and surface area [148].

In this work, *n*WO_3-TiO_2 nanocomposites of three different WO_3-TiO_2 mass ratios (*n* = 1%, 3% and 5%) were synthesized and applied for photovoltaic and photo-catalytic applications. In photovoltaic part, we fabricated DSSCs using synthesized *n*WO_3-TiO_2 nanocomposite paste as photo-anode and replaced the conventional Pt with MWCNT as the CE and to the best of our knowledge; this [*n*WO_3-TiO_2/N719/MWCNT] DSSC combination was developed for the first time. In order to single out the enhancement of the performance brought about by the introduction of *n*WO_3-TiO_2 as photo-anode and MWCNT as CE in DSSC and also to make a comparative evaluation of [*n*WO_3-TiO_2/N719/MWCNT] DSSC, we also fabricated [TiO_2/N719/Pt], [TiO_2/N719/MWCNT] and [*n*WO_3-TiO_2/N719/Pt] combinations of DSSCs. It was found that an efficiency of 6.12 % was achieved with [1%WO_3-TiO_2/N719/ MWCNT] combination, which is around 12 % higher than the highest 5.47% reported efficiency in the literature for any DSSC with photo-anode made up of *n*WO_3-TiO_2 nanocomposite semiconductors. In addition to improving the efficiency of DSSC, the replacement of Pt with MWCNT as a CE can reduce the production cost of this combination of DSSC. We also carried out various material characterization on *n*WO_3-TiO_2 nanocomposite anode films such as FE-SEM, TEM, XPS, EDX and XRD, the photo-anode characterization studies such as UV-Vis spectroscopy and Tauc plot, DSSC characterization such as J-V characteristics, electrochemical impedance spectroscopy (EIS) and finally conducted cyclic voltammetry (CV), tafel, and chronoamperometry tests to examine the catalytic activity and stability of MWCNTs as CE in the fabricated DSSC. In addition, the photo-catalytic reduction of Methylene blue (MB) dye is presented in this work with the intention of proving the superiority of the synthesized *n*WO_3-TiO_2 in terms of its increased inhibition to charge recombination, and increased

light absorption, as these two characteristics are the desired features in photovoltaic applications also. It was found that particularly 1%WO_3-TiO_2 was able to degrade 99.99% of MB dye in 105 minutes and this performance is quite consistent with the photovoltaic results.

5.3.2 Results and Discussions

5.3.3 UV-VIS spectroscopy

The optical spectral responses of plain *n*WO_3-TiO_2 films and N719 dye sensitized *n*WO_3-TiO_2 films each with three different WO_3-TiO_2 mass ratios (*n* = 1%, 3%, and 5%) are shown in Figure 73a as the optical absorption spectra in the visible spectral region. It is quite obvious from absorption spectra that the light absorbance of plain *n*WO_3-TiO_2 films increases with the increase of WO_3 content in it and more importantly, when each of these three *n*WO_3-TiO_2 films are stained with N719 dye, the effects on the absorbance spectra are that they get red shifted in addition to the overall enhancement of absorbance intensity and the broadening of the spectra. The observed enhancement of the optical absorbance and red shift could be brought about by either of or both of the following independent mechanisms. When WO_3 is loaded on TiO_2, W^{6+} ions are replaced by Ti^{4+} ions in TiO_2 lattice and the newly formed W-O-Ti bonds in the TiO_2 lattice result in the charge imbalance. This charge imbalance of W^{6+} ion is neutralized by the introduction of additional oxygen atoms and/or structural defects like cation vacancy and as a result the defect and impurity energy levels are formed within the forbidden region of TiO_2. The absorbance spectra of N719 dye in ethanol are shown in Figure 74, where the absorbance peaks centered at 385 nm and 525 nm are due to metal to ligand charge transfer and the one centered at 310 nm is due to intra ligand $\pi - \pi^*$ charge transfer. When TiO_2 is stained

with N719, the carboxylate group in N719 dye gets attached to Ti^{4+} ion, which leads to the delocalization of π^* energy level to a lower value. Hence, the observed red shift and the enhancement of the optical absorbance could be attributed to either of or both of the independent mechanisms described above. Also to calculate the band gap energies (E_g) of the pure TiO_2 film and *n*WO_3-TiO_2 films with three different WO_3-TiO_2 mass ratios (*n* = 1%, 3%, and 5%) were estimated using Tauc plots [164] and are shown in the Figure 73b.

For a semiconductor material, absorption coefficient (A), the incident photon energy (E), and the band gap energy are related by equation 5.15, where K is a constant known as band tailing parameter and n is the power factor of the transition mode which depends on the nature of the material. Basically there are two types of semiconductor materials: direct band gap materials and indirect band gap materials and in the case of direct band gap materials the energy and momentum conservations in the associated electronic transitions from the valance to conduction band is tallied by the photon itself, whereas in indirect band gap material, for each electronic transition, photons account only the energy conservation but the momentum is not conserved. Hence in the indirect band gap material, phonon transitions intervene to tally the momentum conservation in order to make the electronic transitions possible. Hence, the power factor n in equation 5.15 takes the value ½ and 2 respectively for the direct and indirect band gap materials. In our case the anatase form of TiO_2 is an indirect band gap material, the power factor is taken as 2 in equation 5.16 and transforming this equation into linear form leads to equation 5.17. Equation 5.17 eventually used to estimate band gap energy of the synthesized materials through Tauc plot, which is basically $(A.E)^{0.5}$ versus photon energy (E)plot. It is quite clear from

equation 5.17 that the extrapolation of the linear part of the Tauc plot and its intercept on the X axis directly yield the band gap energy of the material.

$$A = \frac{K(E-E_g)^n}{E} \qquad (5.15)$$

$$A = \frac{K(E-E_g)^2}{E} \qquad (5.16)$$

$$(A.E)^{0.5} = K(E - E_g) \qquad (5.17)$$

It is quite clear from the Tauc plots, that the band gap energies of the WO_3 modified TiO_2 decrease with the increase of WO_3 content in TiO_2.

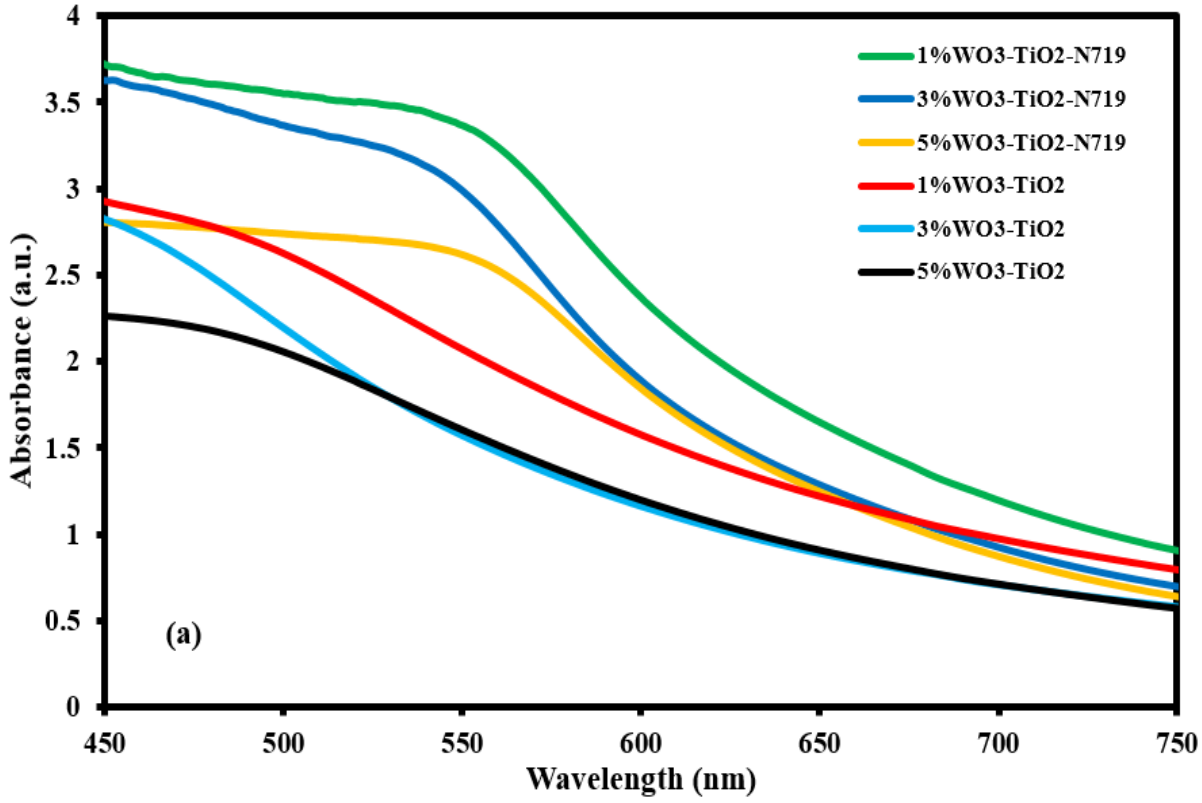

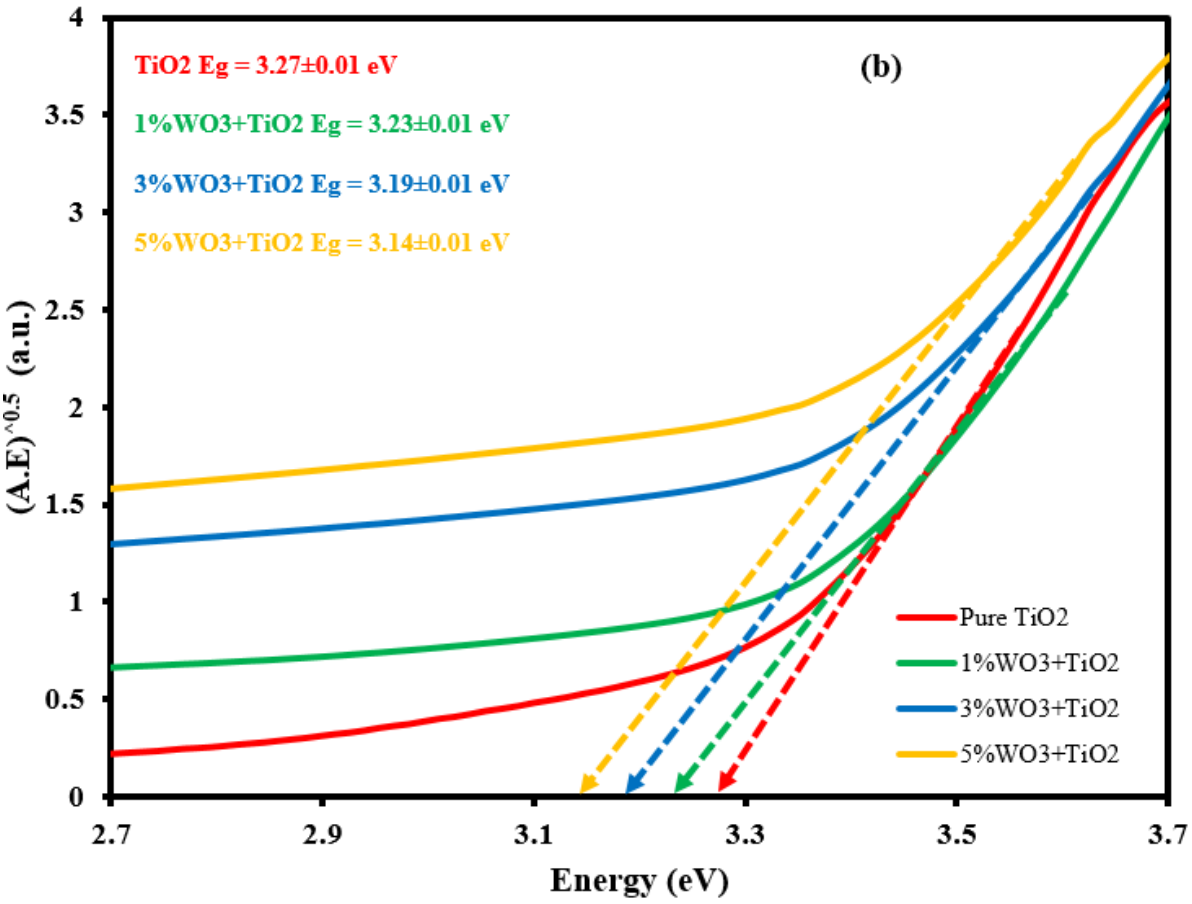

Figure 73 (a) UV-VIS spectroscopy of 1%WO_3-TiO_2, 3%WO_3-TiO_2, and 5%WO_3-TiO_2, films sensitized with and without N719 (b) Tauc plot for the estimation of the band gap energies of pure TiO_2, 1%WO_3-TiO_2, 3%WO_3-TiO_2, and 5%WO_3-TiO_2 films.

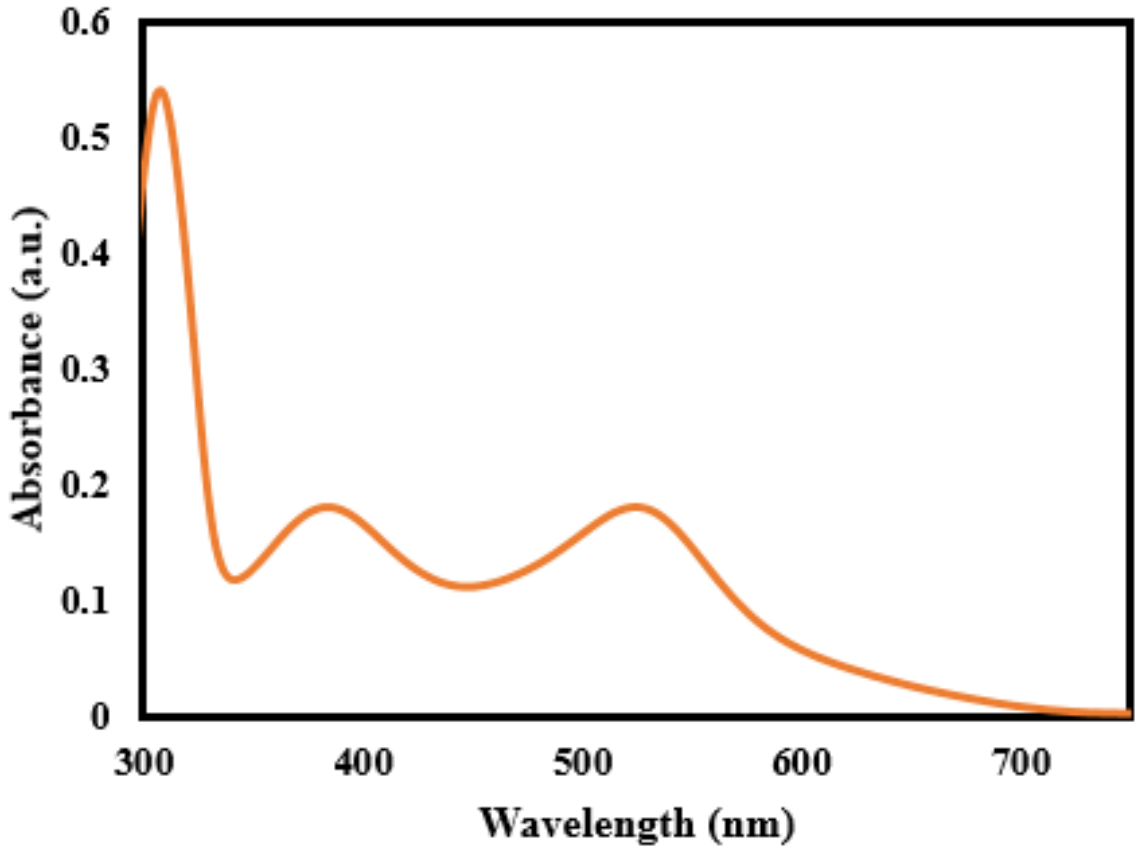

Figure 74 UV-VIS spectroscopy of N719 dye in ethanol.

5.3.4 The current-voltage (J-V) characteristics

The J-V characteristics of the solar cell is an essential characterization study to deduce the key performance indicators of solar cells, e.g. short circuit current density (J_{sc} mA/cm^2), open circuit voltage (V_{oc} mV), fill factor (FF %), and efficiency (η %) . These important figures of merit of a DSSC, intricately depends on characteristics of the materials used in photo-anode, dye, electrolyte, and counter electrode and all these factors can be improved by improvising the properties of materials used in the components of DSSC. Figure 75a shows a set of nine J-V characteristic curves, [*n*WO_3-TiO_2/N719/MWCNT] and [*n*WO_3-

TiO_2/N719/pt] DSSCs with three different WO_3-TiO_2 mass ratios (n = 1%, 3%, and 5%) for each, along with standard bench mark [TiO_2/ N719/Pt], [TiO_2/ N719/MWCNT] and [TiO_2/ N719/TiO_2] DSSCs for comparison and also these parameters are listed in Table 19. In order to single out the enhancement brought about by the introduction of *n*WO_3-TiO_2 as a photo-anode, we compared the performance of [*n*WO_3-TiO_2/N719/Pt] DSSCs with [TiO_2/N719/Pt] DSSC and [*n*WO_3-TiO_2/N719/MWCNT] DSSCs with [TiO_2/N719/MWCNT] DSSC in Figure 57a, where we can notice that the presence of WO_3 in TiO_2 in fact enhanced the efficiency and fill factors of the DSSCs with the maximum value at the WO_3-TiO_2 mass ratio of 1%. The increased J_{sc} in the WO_3-TiO_2 based DSSCs in Figure 75a could be due to the shifting of the edge of the conduction band to more positive level [165], [166] as shown in Figure 75b and c, which facilitates the increased flow of photo-excited electrons to the conduction band of *n*WO_3-TiO_2 anode and reduced charge recombination. It is quite clear from the band gap energies of WO_3 and TiO_2 that the conduction band of WO_3 lies favorably in such a way that the photo excited electrons in the conduction band of TiO_2 tunnels its way out to the conduction band of WO_3, while the photo generated holes remain in TiO_2. This excellent charge separation of photo-generated electrons and holes inhibits the recombination of electron hole pairs in the anode film and make these charge carriers available more for the photovoltaic process. Also, we notice that [1%WO_3-TiO2/N719/ MWCNT] yielded a better efficiency than ones for [3%WO_3-TiO_2/N719/ MWCNT] and 5%WO_3-TiO_2/N719/ MWCNT. This is because, although the charge separation is promoted by the presence of WO_3, the higher WO_3 contents in TiO_2 causes less dye adsorption on the anode film [160], which in turn leads to the generation of less electron hole pair. These two mutually competing factors resulted in

the optimum efficiency in [1%WO_3-TiO_2/N719/ MWCNT]. Also, as the position of conduction band edge is directly related to V_{oc}, the reduction of V_{oc} in *n*WO_3-TiO_2 nanocomposite based DSSCs is quite expected, which has been observed in both modified photoanode [*n*WO_3-TiO_2/N719/Pt] and [*n*WO_3-TiO_2/N719/MWCNT] DSSCs with respect to their unmodified photoanode [TiO_2/N719/Pt] and [TiO_2/N719/MWCNT] DSSC respectively. The reduced V_{oc} with the increased WO_3 content in TiO_2 observed in Figure 75a is in good agreement with reduced band gap energies with the increased WO_3 content in TiO_2 observed in Tauc plot provided in Figure 75b and c. On the other hand, it is also quite obvious from Figure 75a that values of J_{sc} and FF enhanced with the increased WO_3 content in TiO_2 till the WO_3 content in TiO_2 is as high as 1%, which can be attributed to the availability of a greater number of conduction electrons and the enhanced suppression of charge recombination brought about by the modified photoanode as explained above. Further increase of WO_3 in TiO_2, leads to the reduction of the current density (J_{sc}) due to the reduction in dye loading on *n*WO_3-TiO_2 photoanode [160]. Figure 75a and Table 19 also show that the photovoltaic performance in terms of J_{sc}, FF and overall efficiency η of the *n*WO_3-TiO_2 based DSSCs is further enhanced when the Pt counter electrode was replaced with MWCNT, which may be attributed to the faster redox reduction at the CE due to the better catalytic activity of MWCNT along with reduced charge recombination at photoanode due to the addition of WO_3 in TiO_2 [167].

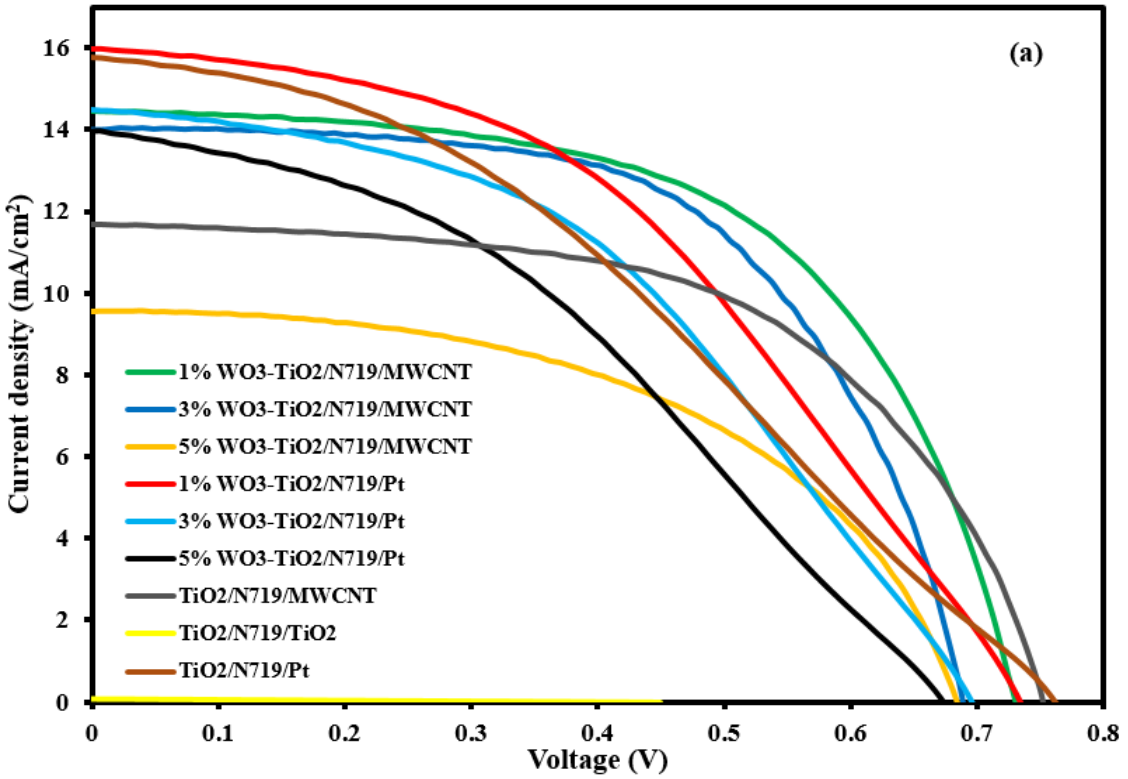
(a)
Current density (mA/cm²)
Voltage (V)
1% WO3-TiO2/N719/MWCNT
3% WO3-TiO2/N719/MWCNT
5% WO3-TiO2/N719/MWCNT
1% WO3-TiO2/N719/Pt
3% WO3-TiO2/N719/Pt
5% WO3-TiO2/N719/Pt
TiO2/N719/MWCNT
TiO2/N719/TiO2
TiO2/N719/Pt

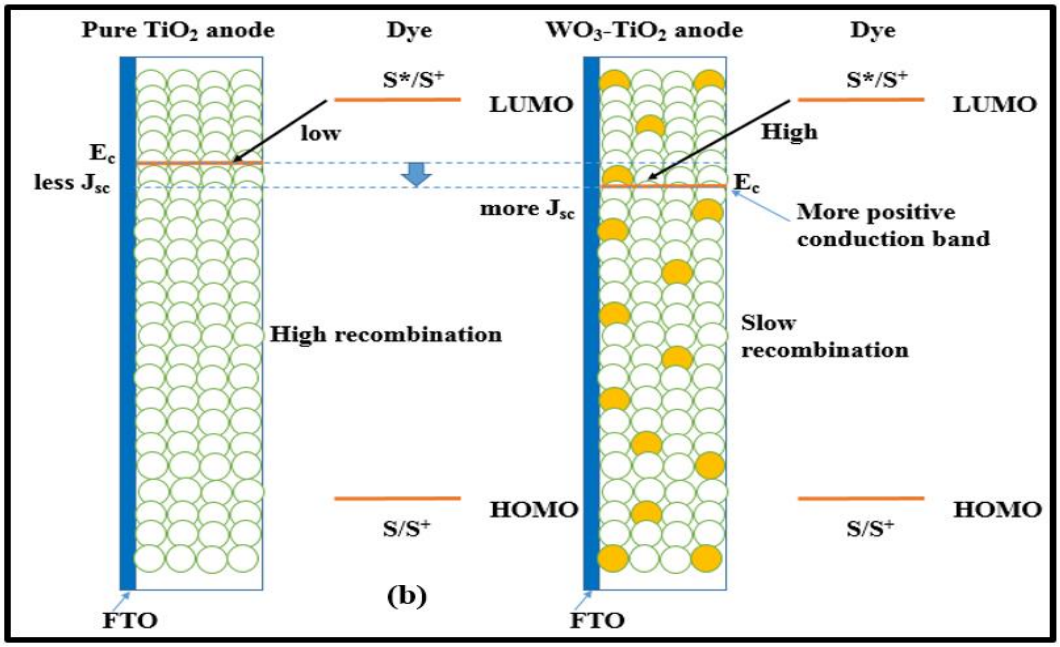
Pure TiO2 anode
Dye
WO3-TiO2 anode
Dye
S*/S+
LUMO
low
Ec
less Jsc
High
more Jsc
More positive conduction band
High recombination
Slow recombination
HOMO
S/S+
FTO
(b)

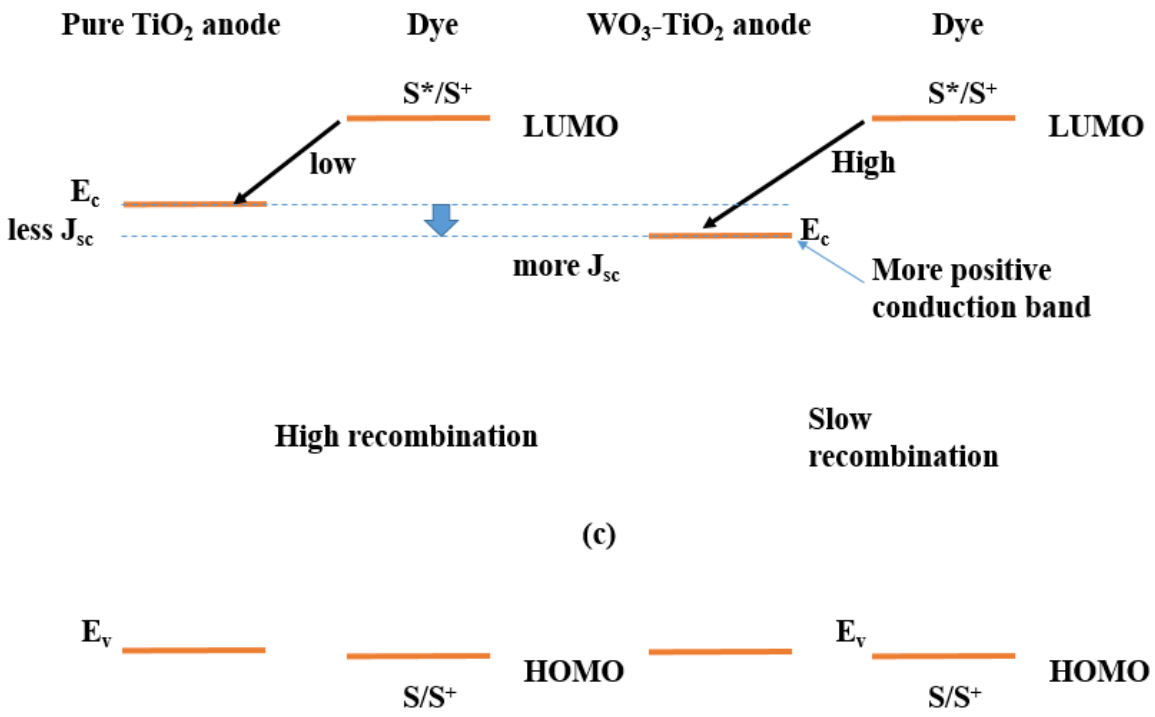

Figure 75 (a) Current-Voltage (J-V) characteristics of fabricated DSSC with different configurations of photo-anodes and counter electrodes (b & c) Schematic and energy band diagram of pure TiO_2 (left) and *n*WO_3-TiO_2 (right) based photo-anode fabricated for DSSC.

Table 19 Photovoltaic parameters of fabricated DSSCs

Cell Structure	J_{sc} (mA/cm^2)	V_{oc} (mV)	FF (%)	η (%)
[TiO_2/N719/ TiO_2]	0.079	443	25	0.01
[TiO_2/N719/Pt]	15.76	761	36	4.36
[1%WO_3-TiO_2/N719/Pt]	15.96	734	44	5.18

[3%WO_3-TiO_2/N719/Pt]	14.49	695	45	4.50
[5%WO_3-TiO_2/N719/Pt]	13.97	673	38	3.62
[TiO_2/N719/MWCNT]	11.67	752	57	5.01
[1%WO_3-TiO_2/N719/MWCNT]	**14.46**	**730**	**58**	**6.12**
[3%WO_3-TiO_2/N719/MWCNT]	14.01	689	59	5.75
[5%WO_3-TiO_2/N719/MWCNT]	9.63	683	51	3.34

5.3.5 Electrochemical impendence spectroscopy (EIS) analysis

EIS is a very common technique used for the characterization of interfacial charge transport properties of DSSC. EIS is measured by applying an AC voltage to the DSSC and observe the current response at different frequencies. EIS data shown in Figure 76 is depicted as a Nyquist plot, for the three variants of [*n*WO_3-TiO_2/N719/Pt] and [*n*WO_3-TiO_2/N719/MWCNT] DSSCs, where the real and imaginary parts of the impedance of the combined equivalent circuit are presented respectively in X and Y axes (complex plane) as a function of varying frequency. The semicircle in the Nyquist plot is the characteristic of a resistor capacitor parallel combination with a unique time constant. Inset of Figure 58 shows the equivalent circuit deduced from the Nyquist plot. The capacitances (C_1 and C_2) in the equivalent circuit come into being as a result of the formation of charge double layer between electrode and electrolyte (counter electrode/electrolyte and anode/dye/electrolyte interfaces), when the ions from the solution are adsorbed on the surface of electrode and

separated from the ions by an intervening insulating space. R_s is the sheet resistance that comes initially in series with the parallel circuit combination, R_1 and R_2 are the charge transfer resistances at counter electrode/electrolyte and semiconductor/dye/electrolyte interfaces respectively, and Z_w (Warburg impedance) is the impendence faced by the charge carriers during their diffusion through the electrolyte. The semi-circle at higher frequency and at the intermediate frequency is respectively due to the capacitance and resistance combinations at the back electrode/electrolyte interface and semiconductor/dye/electrolyte interface in addition to Warburg diffusion impedance at low frequency. Ideally Nyquist plot is expected to display the semicircles representing each of the circuit elements, however, the absence of expected third semicircles in all the fabricated DSSC are seen due to very large resistance R_2 as compared to Z_w, which may overshadowed the third semicircle. Therefore, in Figure 76, the two semi-circles appear in the Nyquist plot correspond to R_1 and R_2, and also it is quite clear from the plots that R_2 corresponding to the DSSC with [1%WO_3-TiO_2/N719/MWCNT] is the largest among the six variants. This highest resistance for the charge recombination in [1%WO_3-TiO_2/N719/MWCNT] makes more charges available for the photovoltaic performance and better charge transportation, which is quite instrumental in enhancing J_{sc} and makes this particular DSSC combination the best among all the 6 variants under study, which is evident from Table 19 [10].

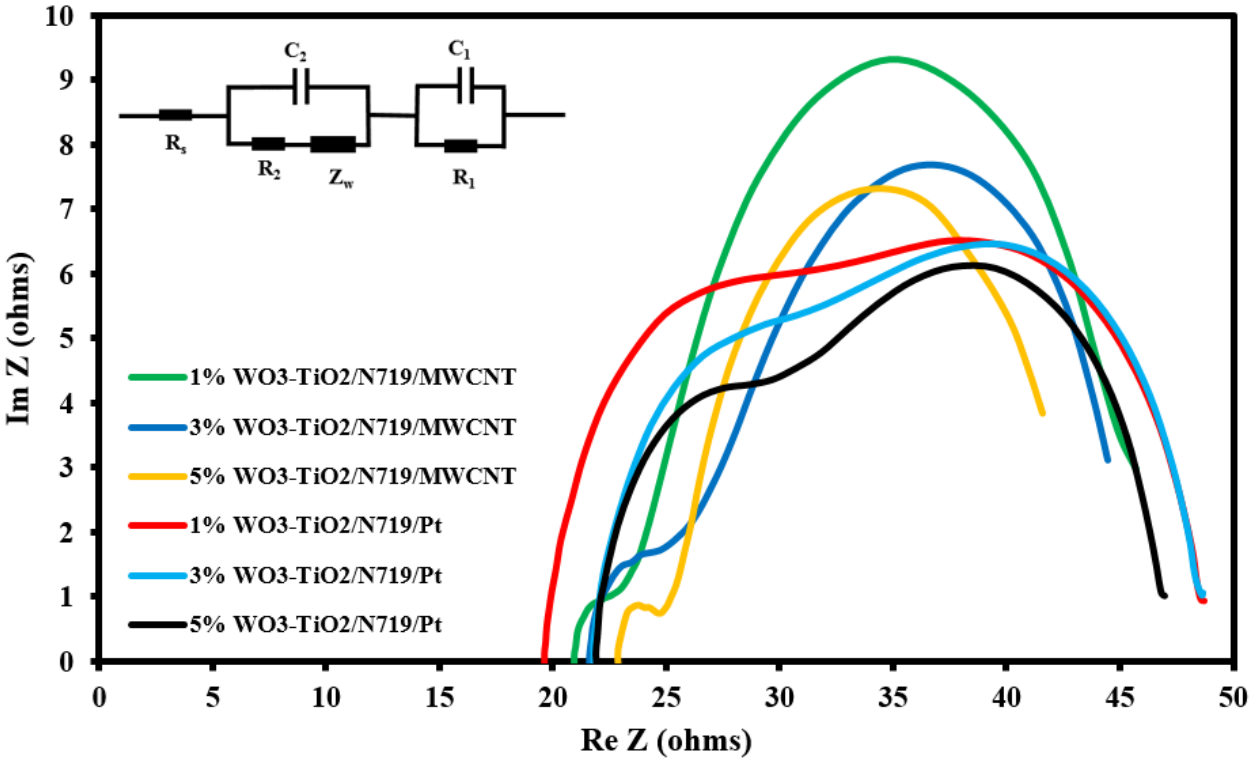

Figure 76 Electrochemical impendence spectroscopy (EIS) of fabricated DSSC along with equivalent circuit of DSSCs (inset).

5.3.6 Catalytic activity and stability measurements of MWCNT as counter electrode

5.3.7 Cyclic voltammetry, Chronoamperometry

In order to verify the stability of MWCNT, used as a CE in the fabricated DSSCs the cyclic voltammetry (CV) was carried out using 10 mM acetonitrile solution of Iodolyte (AN-50) as an electrolyte, platinum electrode as a working electrode, and Ag/AgCl electrode as reference electrode. It is quite clear from Figure 77a that the hysteresis effect due to the forward and reverse ramp of the applied voltage remain intact after multiple cycles of sweeping at the ramp rate of 50 mV/sec, which is the clear indication that MWCNT is quite

stable. The stability of MWCNT is further substantiated by varying the ramp rate in the CV study which is shown in Figure 77b. The two distinct peaks manifested in the CV hysteresis curve in Figure 77a are due to the chemical processes that leads to the regeneration of oxidized dye molecule by the donation of electrons from iodolyte electrolyte and also the reduction of iodide by the oxidation of triiodide ions at CE as depicted in the following two chemical equations 5.18 and 5.19 [168].

$$3I^- \rightarrow I_3^- + 2e^- \quad (5.18)$$

$$2I_3^- \rightarrow 3I_2 + 2e^- \quad (5.19)$$

The stability of the MWCNTs as the CE was further tested by the chronoamperometry analysis, where 600 mV potential was applied, and the current density was recorded for one hour (3600 seconds). It is clear from Figure 77c that although the current density initially drops, it becomes quite stable after 500 seconds and remains stable.

5.3.8 Tafel Studies

The catalytic activity at the electrolyte/counter electrode interface were further investigated by Tafel plot, where the logarithmic current density (log *J*) is plotted against the potential. The two important parameters that can be deduced from that plot to evaluate catalytic performance of the CE are exchange current density (J_0) and the limiting diffusion current density (J_{lim}). Figure 77d shows the Tafel plots recorded for Pt and MWCNT counter electrode based dummy cells with Iodolyte (Z-50) as electrolyte. It is found that the estimated value of J_0 is almost equal for both Pt and MWCNT counter electrodes, which ensures that the catalytic activity of MWCNT counter electrode is sufficient enough for the

reduction of iodide by tri-iodide ions. The exchange current density J_0 has an inverse relation with charge transfer resistance (R_1) at the electrolyte/counter electrode interface as

$$J_0 = \frac{RT}{nFR_1} \qquad (5.20)$$

Where n, F, R, and T respectively are number of transferred (exchanged) electrons in reduction reaction, Faraday's constant, the gas constant, and temperature. The R_1 value for MWCNT based CE is less than Pt based CE, and hence higher current density J_0 for MWCNT as compared to Pt based CE and is in good agreement with Figure 76.

Also from Figure 77d the limiting diffusion current density J_{lim} for MWCNT counter electrode is greater than that of Pt counterpart, which means the former has greater diffusion coefficient (D) of the I^-/I_3^-redox couples in the DSSC according to the relation [169], [170].

$$D = \frac{l}{2nFC} J_{lim} \qquad (5.21)$$

Where *F*, C, *l*, and *n*, respectively are Faraday's constant and triiodide ion concentration, the spacer thickness, and number of transferred (exchanged) electrons in reduction reaction. The better J_0 and J_{lim} in MWCNT back electrode made it a good choice for counter electrode in the proposed structure of DSSC.

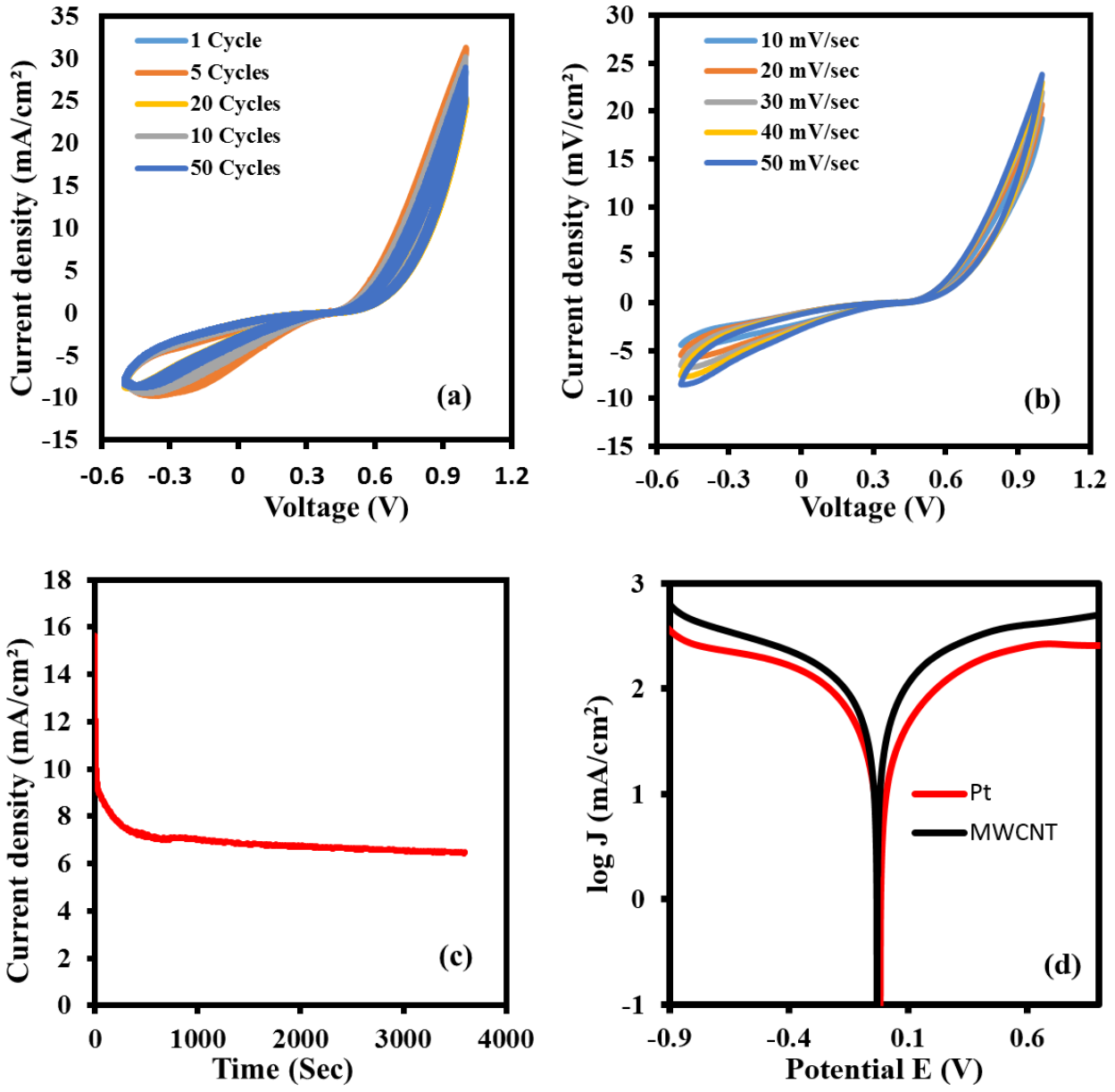

Figure 77 (a) Cyclic voltamograms for different cycles at the scan rate of 50 $mVsec^{-1}$, (b) CV curves at various scan rates (c) Stability test of MWCNT as a catalyst for counter electrodes with 10mM Iodolyte Z-50as electrolyte, Pt as auxiliary electrode and Ag/AgCl as reference electrode and (d) Tafel curves of symmetrical cells (dummy) fabricated with MWCNT and Pt.

5.3.9 Photocatalytic performance of WO_3-TiO_2 nanocomposites films

In order to understand the photocatalytic behavior of *n*WO_3-TiO_2 nanocomposite films with three different WO_3-TiO_2 mass ratios (*n* = 1%, 3%, and 5%), we investigated the photo-catalytic degradation of MB dye in water under UV irradiation. In order to confirm that the degradation of MB dye is not due to non-photo-catalytic (photo-induced) effect, the decay curve in the absence of photo-catalytic thin film on FTO (i.e. only light) under the same irradiation conditions was also examined. The decay curve for photocatalytic degradation of MB dye in the absence of photo-catalytic film and also with *n*WO_3-TiO_2 nanocomposite films (*n* = 1%, 3%, and 5% WO_3-TiO_2 mass ratios) under UV irradiation are shown in Figure 78a. In addition to this, the photo-catalytic degradation curves of MB, presented as $\ln(C/C_o)$ versus time is depicted in Figure 78b, where it is quite clear that in the presence of *n*WO_3-TiO_2 nanocomposite films (*n* = 1%, 3%, and 5% WO_3-TiO_2 mass ratio), the photo-catalytic degradation of MB dye is much faster compared to the one without *n*WO_3-TiO_2 nanocomposite films (only UV illumination). Also, by linearizing the decay curve, we estimated the rate of degradation (k) of MB and their values are 0.424 min^{-1}, 0.320 min^{-1} and 0.273 min^{-1} respectively for 1%, 3%, and 5% WO_3-TiO_2 mass ratios in *n*WO_3-TiO_2, nanocomposite films compared to a significantly lower k value of 0.0033 min^{-1} in the absence of photo-catalytic film. The bar diagram in Figure 78c demonstrates the percentage photo-catalytic degradation efficiency of MB in water at different irradiation times, where it is evident that the photocatalytic degradation efficiency of *n*WO_3-TiO_2 nanocomposite films (*n* = 1%, 3%, and 5%) are approximately 99.99%, 96.82% and 96.15% as compare to 34.11% without photo-catalytic film after 120 minutes of UV irradiation. The absorbance spectrum of degradation of MB dye with *n*WO_3-TiO_2

nanocomposite films (n = 1%, 3%, and 5%), from which the above results were deduced are presented in Figure 79(a-c).

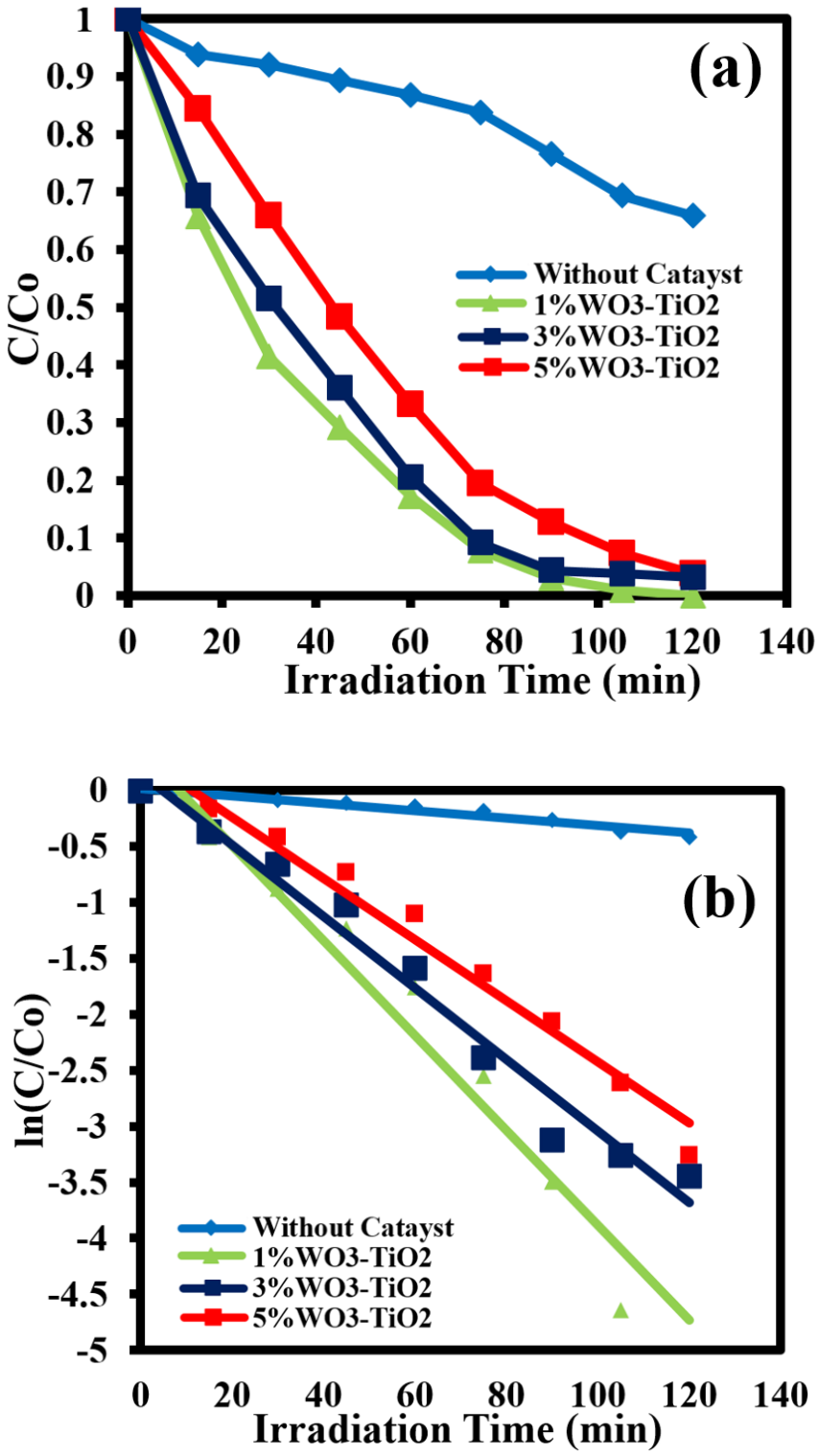

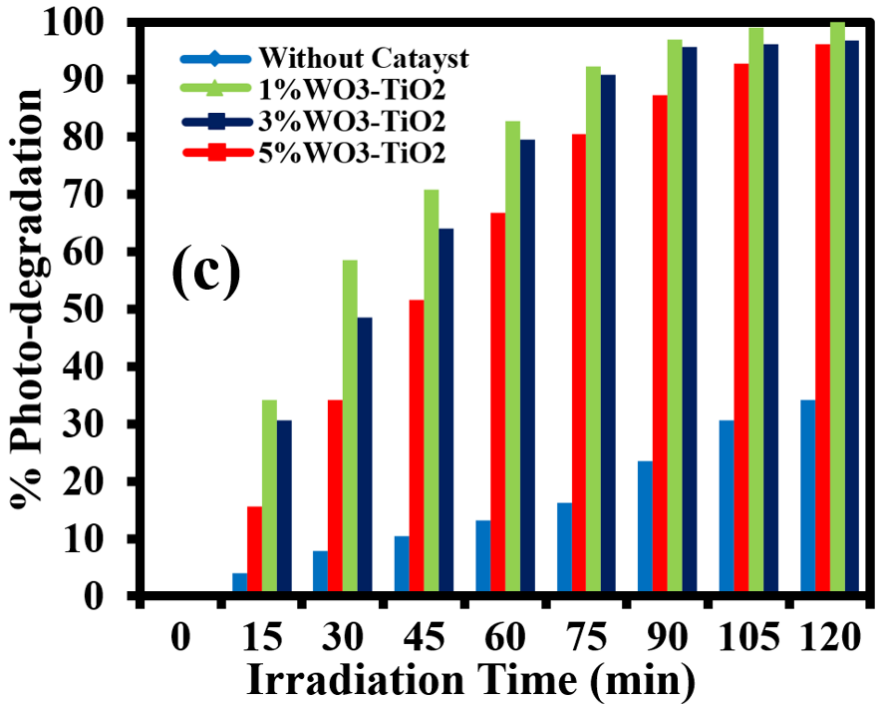

Figure 78 (a) Decay curves for photocatalytic degradation of MB dye with *n*WO_3-TiO_2 films with three different WO_3-TiO_2 mass ratios (*n* = 1%, 3% and 5%) and also in the absence of catalyst under UV light irradiation. (b) Plots of ln(C/C_o) vs. irradiation time for the photo-catalytic degradation of MB dye with *n*WO_3-TiO_2 films with three different WO_3-TiO_2 mass ratios (*n* = 1%, 3% and 5%) and also in the absence of catalyst under UV light irradiation. (c) Percentage of photocatalytic degradation of MB dye with *n*WO_3-TiO_2 films with three different WO_3-TiO_2 mass ratios (*n* = 1%, 3% and 5%) and also in the absence of catalyst under UV light irradiation.

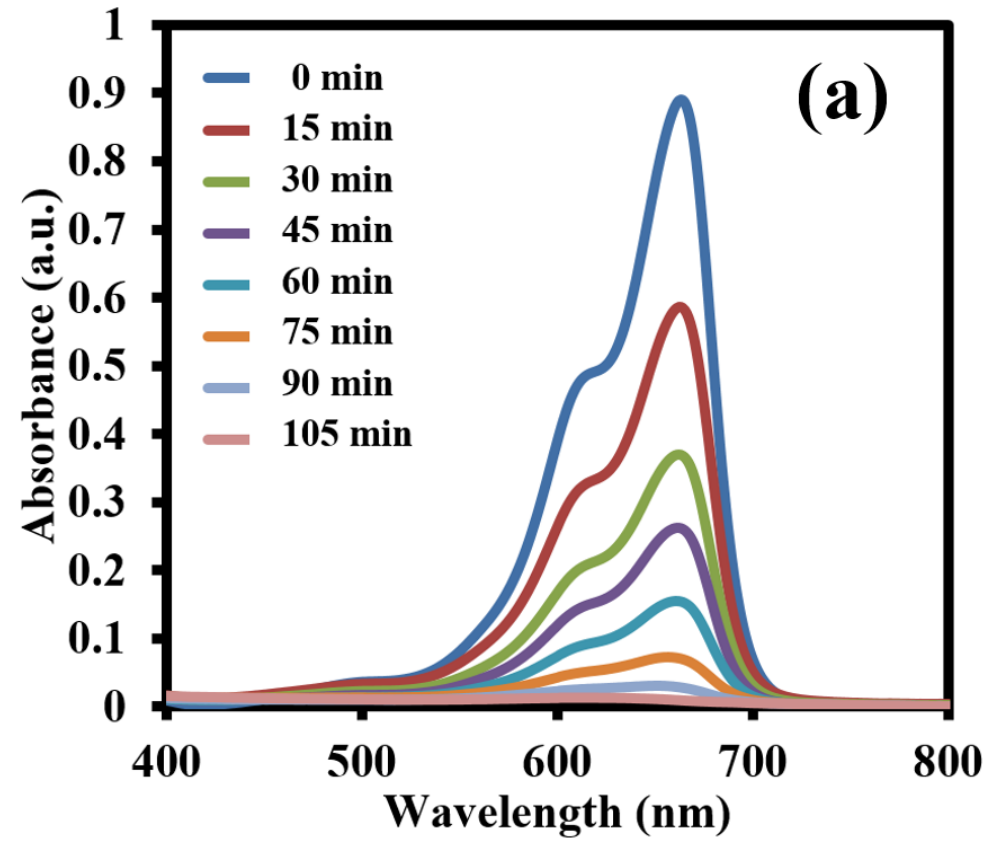
(a)
0 min
15 min
30 min
45 min
60 min
75 min
90 min
105 min
Absorbance (a.u.)
Wavelength (nm)
1
0.9
0.8
0.7
0.6
0.5
0.4
0.3
0.2
0.1
0
400
500
600
700
800

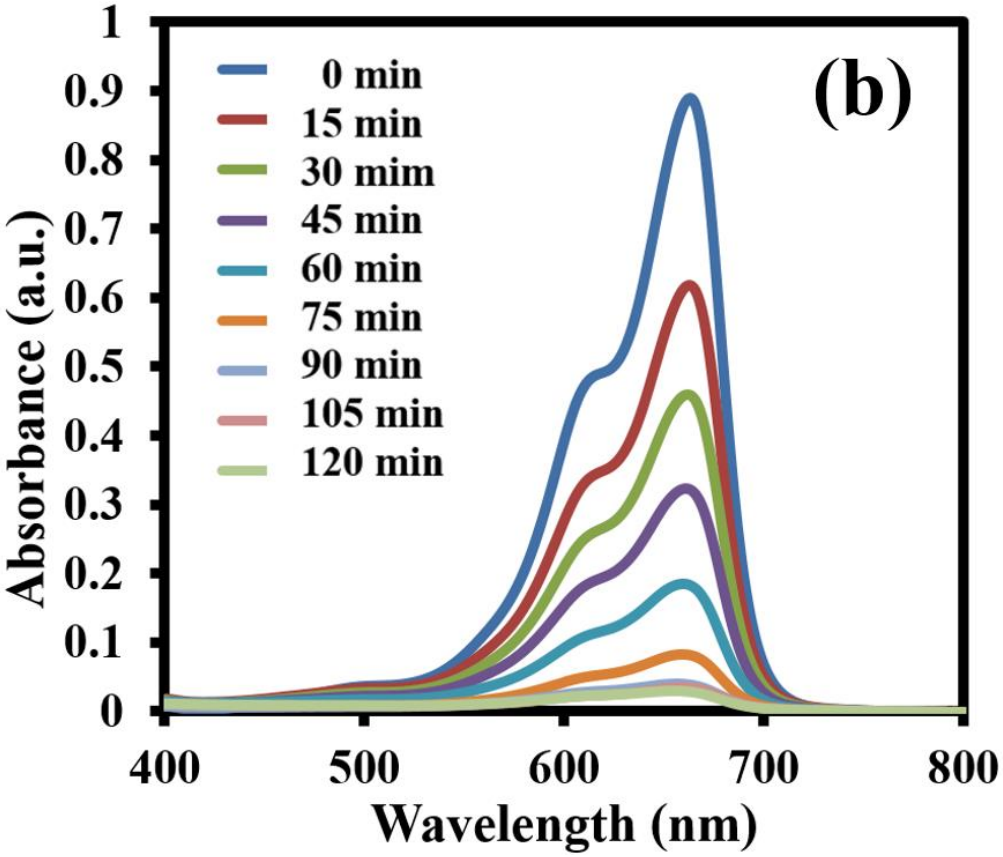
(b)
0 min
15 min
30 mim
45 min
60 min
75 min
90 min
105 min
120 min
Absorbance (a.u.)
Wavelength (nm)
1
0.9
0.8
0.7
0.6
0.5
0.4
0.3
0.2
0.1
0
400
500
600
700
800

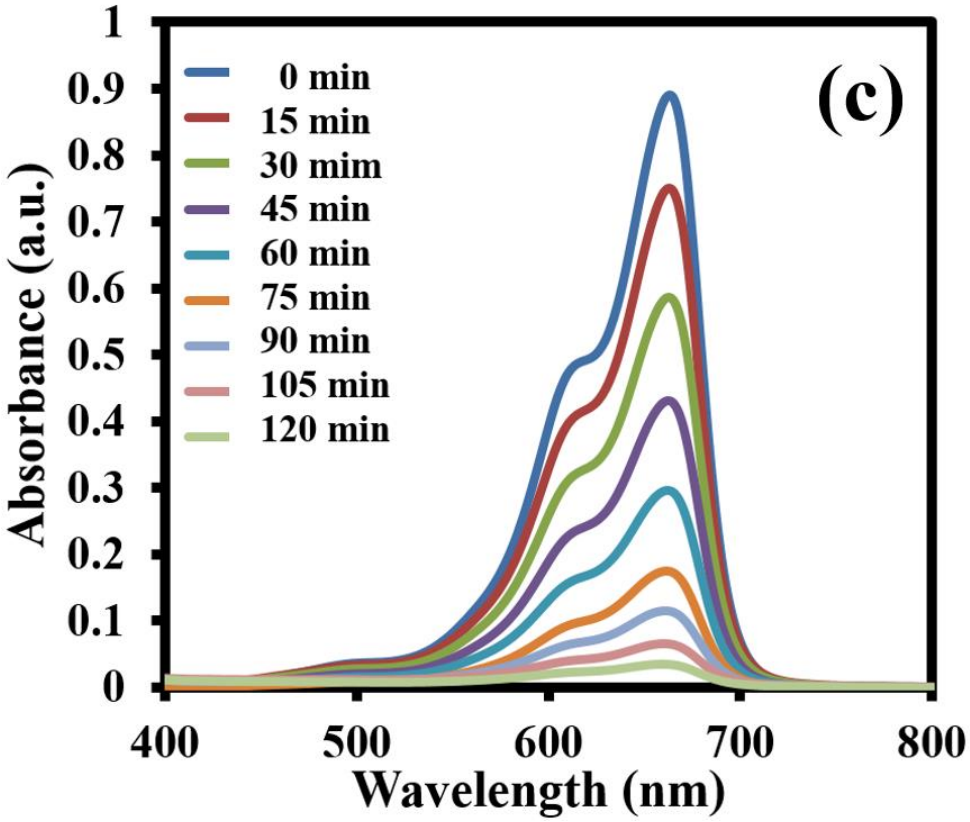

Figure 79 Absorption spectra taken at a regular time interval in the process of photo-catalytic degradation of MB dye with (a) 1%WO_3-TiO_2, (b) 3%WO_3-TiO_2, and (c) 5%WO_3-TiO_2 films as photo-catalyst under UV radiation.

5.3.10 Summary

In this study, three different mass ratios of synthesized *n*WO_3-TiO_2 nanocomposite films (*n* = 1%, 3%, and 5%), and MWCNT were used as photoanode and back electrode respectively to fabricate [*n*WO_3-TiO_2/N719/MWCNT] combination of DSSC. In addition to this, a set of [*n*WO_3-TiO_2/N719/Pt] combination of DSSC were also fabricated in order to single out the improvement in the performance of DSSC due to the use of MNCNT as the back electrode. The structural, morphological and optical characterizations of

synthesized *n*WO_3-TiO_2 nanocomposite photoanode films and the stability test of back electrode were carried out. By comparing the photovoltaic performance of all the DSSCs, it is quite clear that the cell with 1%WO_3-TiO_2 in *n*WO_3-TiO_2 as a photoanode and MWCNT as back electrode [1%WO_3-TiO_2/N719/MWCNT] has the best efficiency of all the six variants of fabricated DSSCs. It was found that an efficiency of 6.12 % was achieved with [1%WO_3-TiO_2/N719/MWCNT] combination, which is around 12 % higher than the highest reported in the literature for any *n*WO_3-TiO_2 nanocomposite photo-anode in DSSC. The enhancement of photovoltaic performance of fabricated [*n*WO_3-TiO_2/N719/ MWCNT] DSSC in general could be attributed to the reduced charge recombination and increased electron injection into the conduction band of the composite semiconductor. In addition to this the photo-catalytic degradation of Methylene blue (MB) dye was also carried out using all three mass ratios of synthesized *n*WO_3-TiO_2 nanocomposites under UV radiation and it was found that particularly 1%WO_3-TiO_2 was able to degrade 99.99% of MB dye in 105 minutes, which is quite consistent with the photovoltaic results. The photo-catalytic degradation experiment is presented with the aim that enhanced rate of dye degradation would prove the increased inhibition to charge recombination and light absorption of *n*WO_3-TiO_2, the features essential for the better performance of photovoltaic cells, the result of which supports the photovoltaic obtained performance.

5.4. Efficient and Cost-effective Dye-Sensitized Solar Cells using MWCNT-TiO_2 Nanocomposite as Photoanode and MWCNT as Pt-free counter electrode

5.4.1 Brief introduction

Ever increasing global need, over dependency on the fast depleting fossil fuels and consequent environmental repercussions due to CO_2 emission instigated the quest for renewable energy sources particularly from abundant solar energy through photovoltaic process [50], [139], [140]. Photovoltaic technology has been going through three generations of research and development, mainly focusing on novel materials that could replace ubiquitous, yet expensive silicon based first generation solar cells, which achieved an efficiency of 20% [141]. The second generation solar cells are developed from the thin films of semiconducting materials such as cadmium telluride (CdTe), amorphous silicon, or copper indium gallium selenide (CIGS) and the major constraint in the maturity of the second generation solar cell is the use of rare elements that restrict large scale production [171]. Dye-sensitized solar cells (DSSC) are the third generation low-cost multi junction solar cells pioneered by Brain O' Regan and M Grätzel in 1991, in which an organic dye is excited by solar radiation, the photo generated electrons are injected to the conduction band of mesoporous semiconductor, the oxidized dye is regenerated by iodide/ triiodide redox mediator and this circuit is completed by the reduction of redox couple by the incoming electron at a platinum counter electrode [33], [142], [172].

The output voltage of DSSC depends on the energy difference between the quasi Fermi level of the semiconductor and the redox potential of the redox mediator under illumination

and the photo-generated current depends on the absorption coefficient of the dye and the charge transportation characteristics of the dye stained semiconductor as well as the dye/TiO_2 interface. Having more dye stained mesoporous semiconductor in the photoanode (larger surface area) leads to the creation of more photo generated electrons and consequently it leads to the enhancement in the efficiency of DSSC, however, with the increase of interfacial area between the photoanode and the electrolyte, the probability of recombination of conduction electrons of the semiconductor (or in any trap state) and the diffused cations of the redox couple increases, which contributes negatively to the cell efficiency. So in order to get good efficiency of a fabricated dye-sensitized solar cell, the dye in the photoanode should have high visible light absorption coefficient and the excited energy levels of the dye and the level of conduction band of the semiconductor should be favorable for a good electron transfer from the excited dye to the conduction band of the semiconducting material, compatible redox potential that enables effective regeneration of dye and the faster catalytic activity of the counter electrode in reducing the oxidized electrolyte [9], [152].

Unlike in the p-n junction photovoltaics, where the separation of the charges is mediated by the induced field in the junction, in DSSC the charge separation is realized by different competing kinetic and diffusion processes. The rate of injection of photo generated electron from the excited dye to the conduction band of the semiconductor should be higher than that of the relaxation time of the dye. In this process effective charge separation is achieved in which the electron moved from the excited dye to the conduction band of the semiconductor and the hole remained behind in the oxidized dye molecule. Then the oxidized dye molecules are reduced by the redox mediator. This process is called dye

regeneration and this process should be faster than the process in which the electrons in the semiconductor are recombined with the oxidized dye and the redox mediator called as dark current or charge recombination. Also the time taken for the electron to diffuse through the semiconductor should be faster than recombination time and the diffusion length of the conduction electrons should be more than the thickness of the semiconductor coating for the efficient charge extraction [72], [143].

The intrinsic properties of semiconductor material and the dye used in the photoanode, redox mediator and the catalyst as counter electrode along with the thickness and structure are the key parameters that decides the interplay of different kinetic and diffusion processes leading up to the enhanced efficiency of DSSC. The light absorbance, electron injection from the dye, inhibition of recombination, electron transport is the key properties of semiconductor material in the photoanode. Although different pure doped and composite semiconducting materials have been used in the photo-anode of DCCS, TiO_2 remains to be quite ubiquitous in DSSC fabrication due to its abundance, cost effectiveness, non-toxicity and strong adsorption of dye, besides its remarkable properties mentioned above [158]. In spite of all these positive characteristics of TiO_2, electron transport property of TiO_2, which decides the key photocurrent in DSSC is weaker than other semiconductors like ZnO [157] and this deficiency of this wonderful material can be improved by synthesizing nanocomposite of TiO_2 with other suitable material and several works in the area of DSSC with composite photoanode, with improved electron transport, dye adsorption and overall increase of efficiency have been reported [130]–[132], [145], [173], [174]. Multiwall carbon nanotubes (MWCNT) discovered by Sumio Iijima [175] in 1991 has unique electrical and morphological characteristics, that addition of small amount of MWCNT in

TiO_2 can enhance the key electron transport characteristics, when this composite is used as a semiconductor material in the photoanode of DSSC. The enhancement of electron transport in this material can be attributed to one dimensional structure and the formation of complex interpenetrating network of MWCNTs [176].

The role of material of the counter electrode (CE) of DSSC is to catalyze effective reduction of oxidized electrolyte in order to win over the recombination of conduction electrons of the photo anode semiconducting material with electrolytic cations. As platinum (Pt) is well known for its chemical stability, catalytic activity and high exchange current densities, this expensive noble metal is widely used as a CE in DSSC. However, the use of platinum raises the cost of production and hence the very purpose of using DSSC in the place of silicon solar cell is not completely justified. Many cost effective materials such as carbon black, conductive polymer and carbon nanotubes have been used as a counter electrode material [172], [177], [178]. In this focus of improvisation of the counter electrode, MWCNT has also been tried owing to its positive attributes like high surface area and rapid electron transport [179].

In this work, *n*-MWCNT-TiO_2 nanocomposite with four varying mass ratios of MWCNT in TiO_2 (n = 0.03%, 0.06%, 0.09 and 0.12%) were synthesized, coated on FTO and soaked in N3 dye and these dye soaked *n*-MWCNT-TiO_2 films on FTO were used as photo anodes for the fabrication of DSSC, in conjunction with iodide/triiodide redox mediator and pure MWCNT coated FTO as counter electrode. The performance evaluation of the fabricated DSSC was carried out by IV characterization, which showed the highest efficiency of 7.15 % in [0.06%-MWCNT-TiO_2/N3/MWCNT] DSSC configuration, which accounts for 13 % enhancement in the overall efficiency compared to the conventional [TiO_2/N3/Pt] DSSC.

The improved efficiency of DSSC brought about by 0.06%-MWCNT-TiO_2 photo anode is explained in the light of the results of morphological (SEM, TEM), elemental and chemical state (XPS) and optical (absorption spectrum) of characterizations of *n*-MWCNT-TiO_2 and electrochemical (EIS) analysis of the fabricated DSSC. The improved light absorbance in the visible spectral region, high electron recombination resistance with oxidized dye and redox mediator, improved electron transportation and better catalytic activity of MWCNT at the counter electrode are some positive attributes for the improved performance of the [0.06%-MWCNT-TiO_2/N3/MWCNT] DSSC. As for this proposed [*n*-MWCNT-TiO_2/N3/MWCNT] DSSC configuration in particular, it has not been reported in the literature to the best of our knowledge.

5.4.2 Results and Discussions

5.4.3 Optical Absorption Spectroscopy

The absorbance spectrum for N3 dye in ethanol in Figure 80, (also in Figure 81) shows two absorbance peaks in the visible spectral regions centered at 419 nm and 547 nm and one absorbance peak in the UV region centered at 322 nm. The visible region absorbance peaks, originate from the characteristic low energy metal to ligand charge transfer (MLCT), involving the excitation of electrons from 4d orbital of Ru to the unoccupied π^* molecular orbitals and also the absorbance peak in the ultra-violet (UV) region is due to ligand centered π- π^* excitation. When TiO_2 is added to N3, an electronic coupling between the N3 dye molecule and TiO_2 is established and this coupling reorganizes the energy structure in the intermolecular MLCT states. The titanium dioxide (TiO_2) effect of on the dynamics of the adsorbed N3 dye on its surface, is primarily due to both mode-specific vibrational

and electronic de-phasing, where the latter process is more dominant. The restructuring of the intermolecular MLCT states, brought about by the presence of TiO_2, accompanied by efficient photo-induced charge transfer enhances the visible light absorbance on TiO_2-N3 dye as seen in Figure 80. This visible light absorbance is further enhanced with the addition of MWCNT with the maximum visible light absorbance with 0.06% MWCNT in *n*-MWCNT-TiO_2 in the presence of N3 dye, as it is quite obvious from Figure 80 and this further enhancement of visible light absorbance could be due to the photosensitizing property of MWCNT [180]. However, with higher MWCNT content, the light transmission is restricted and also the agglomeration sets in, leading to reduced absorbance. In addition to the enhancement of overall absorbance in the visible spectral region, there is a slight red shift in the absorbance spectrum *n*-MWCNT-TiO_2, originating from the creation of defect states from the oxygen vacancy and/or structural defects in the MWCNT-TiO_2 composite, resulting from the formation of Ti-O-C bonds in the TiO_2 lattice. The observed red shift in the absorbance spectrum is attributed to the lowering of π^* energy level due to the bonding between carboxylic group in N3 dye and Ti^{4+} ion.

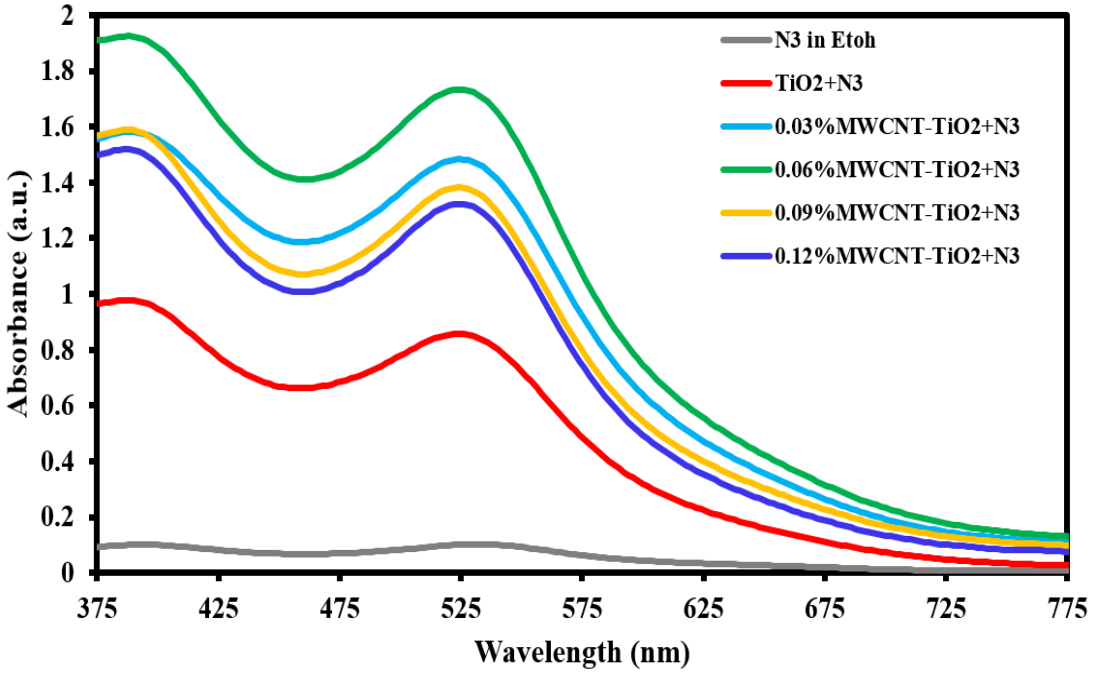

Figure 80 UV-Vis spectra of N3 dye in Etoh, TiO_2/N3 and *n*-MWCNT-TiO_2/N3 films.

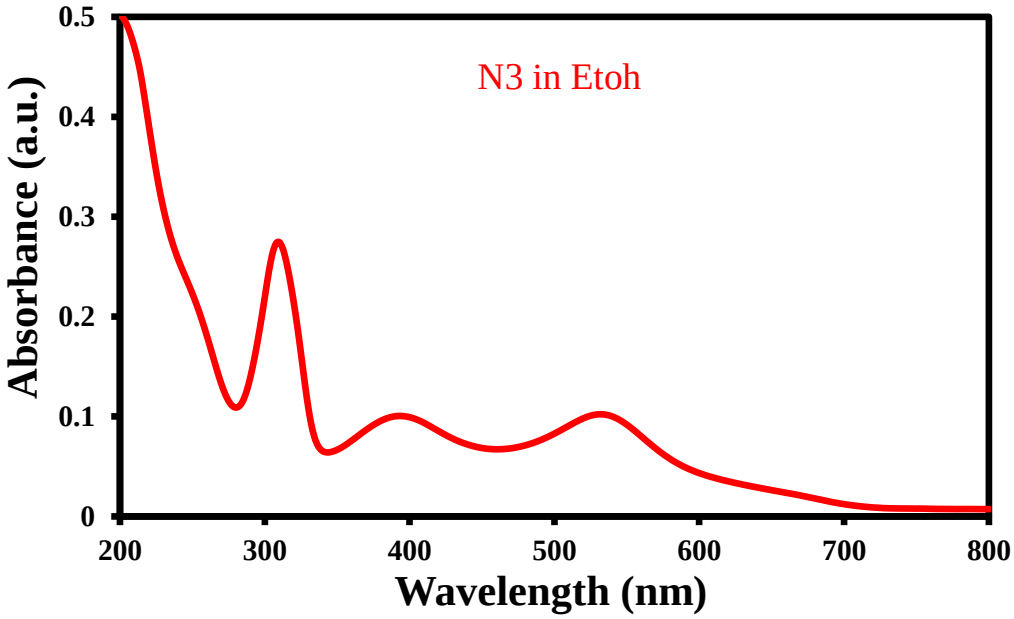

Figure 81 UV-Vis spectra of N3 dye in Etoh.

5.4.4 The current-voltage (J-V) characteristics of fabricated DSSC

The performance of the fabricated DSSC, having *n*-MWCNT-TiO_2 photosensitized by N3 dye as a photo-anode, and MWCNT as a counter electrode was evaluated by typical I-V characteristic study under standard test conditions (ambient temperature of 25 ^oC and 1 sun illumination, equivalent to 1000 W/ cm^2 at air mass AM 1.5G) and the J-V curves are depicted in Figure 82 for six different DSSC configurations. The key DSSC performance indicators like open circuit voltage V_{oc} (mV), short circuit current density J_{sc} (mA/cm^2), fill factor FF (%), and overall photovoltaic efficiency η (%) of all the configurations of DSSC, deduced from the I-V characteristics are listed in table 20. In Figure 82 the photovoltaic output indicators of our proposed [*n*-MWCNT-TiO_2/N3/MWCNT] DSSC configuration with four different *n*-MWCNT-TiO_2 mass ratios (*n* = 0.03%, 0.06%, 0.09% and 0.12%) in photo anode are shown along with the standard [TiO_2/N719/Pt] and [TiO_2/N3/MWCNT] DSSC configurations for bench marking.

Table 20 indicates a systematic enhancement of short circuit current density J_{sc} for all the MWCNT based DSSCs and this is due to the improved electron transport property brought about by the presence of MWCNT. In the case of both [0.09%-MWCNT-TiO_2/N3/MWCNT] and [0.12%-MWCNT-TiO_2/N3/MWCNT] configurations, all the photovoltaic performance indicators are less than that of four other configurations presented in Figure 82. This reduced photovoltaic performance in the above two configurations is due to the reduced visible light absorbance due to the agglomeration of MWCNT in the higher concentrations of MWCNT in photo anode, and also could be due to the formation of undesired trap states that facilitates the rapid photo induced charge recombination. Also, the higher recombination resistance (R_2) as explained in

electrochemical impedance spectroscopy analysis of these fabricated DSSC provided in next section and the more intense visible light absorbance in [0.06%-MWCNT-TiO_2/N3/MWCNT] configuration should yield a higher short circuit current density J_{sc} for [0.06%-MWCNT-TiO_2/N3/MWCNT] configuration than that for [TiO_2/N719/Pt] configuration. But J_{sc} for [0.06%-MWCNT-TiO_2/N3/MWCNT] configuration listed in table 20 is less than that of [TiO_2/N719/Pt] configuration and this discrepancy is due to the fact that the MWCNT presence in photoanode reduced the transparency and hence the number of electrons generated could be slightly lower in MWCNT-TiO_2 photo anodes than in [TiO_2/N719/Pt]. On the other hand, the fill factors and the efficiencies of [0.03%-MWCNT-TiO_2/N3/MWCNT] and [0.06%-MWCNT-TiO_2/N3/MWCNT] configurations are higher than that of [TiO_2/N3/MWCNT] and [TiO_2/N719/Pt] DSSC configurations, with the highest efficiency of 7.15% in the case of and [0.06%-MWCNT-TiO_2/N3/MWCNT]. This performance enhancement could be due to (i) the presence of optimum level of MWCNT in TiO_2, that serve as bridge for the better transport of electrons without being trapped in the grain boundaries, thereby providing a conducting network for the transfer of photoelectron to the outer circuit of DSSC [176], [181] (ii) the observed enhancement of visible light absorbance originating from the trap states formed due to the Ti-O-C bonds in the TiO_2 lattice, resulted in the generation of more photocurrents and (iii) the better catalytic performance at the counter electrode side, resulted in the enhancement of charges available for the efficient reduction of electrolyte [167]. It is quite clear from this study that there is a 13% increase of efficiency in [0.06%-MWCNT-TiO_2/N3/MWCNT] DSSC configuration, compared to that of conventional DSSC configuration [TiO_2/N719/Pt].

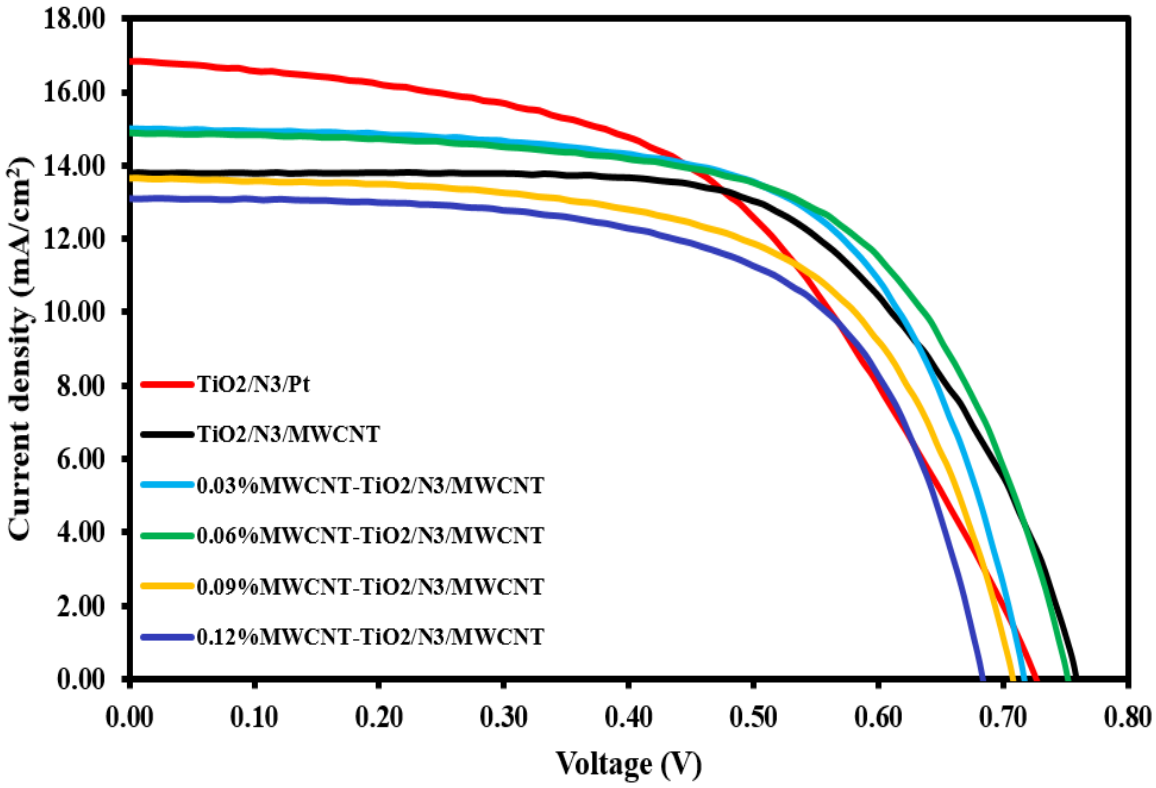

Figure 82 J-V characteristics of fabricated DSSCs.

Table 20 Photovoltaic properties of DSSCs

Cell Structure	J_{sc} (mA/cm^2)	V_{oc} (mV)	FF (%)	η (%)
TiO_2/N3/MWCNT	13.8	759	63	6.65
0.03%MWCNT-TiO_2/N3/MWCNT	14.9	717	64	6.94
0.06%MWCNT-TiO_2/N3/MWCNT	**15.4**	**752**	**62**	**7.15**
0.09%MWCNT-TiO_2/N3/MWCNT	13.6	707	62	6.03
0.12%MWCNT-TiO_2/N3/MWCNT	13.1	683	63	5.69
TiO_2/N3/Pt	16.8	726	52	6.33

5.4.5 Electrochemical Impendence Spectroscopy (EIS) analysis of fabricated DSSCs

In order to elucidate the electrochemical charge transfer and transport behavior in different pairs of charged surface layers and the media in DSSC during its operation, we carried out the EIS analysis at the open circuit voltage, in the 0.1 Hz - 10^5 Hz frequency range. The EIS results of all the six variants of DSSC are presented as Nyquist plots in Figure 83. Further, the proposed equivalent circuit is provided in the inset of Figure 83 and the numerical values of the fitted resistance and capacitance are listed in table 21. Nyquist plot (in complex plane) is basically the wide range of frequency response of the imaginary and components of the cell impedance of the equivalent parallel RC circuits at different interfaces of DSSC. The smaller semicircles at the high frequency region (left) of the Nyquist plots in Figure 83 arise due to the interface of MWCNT counter electrode and electrolyte, where R_1 is the charge transfer resistance and double layer C_1 represents capacitance due to the charge formation in back electrode layer and the electrolyte constitute RC network in the interface. The large semicircles at the mid frequency range are due to MWCNT-TiO_2/dye and electrolyte interface where R_2, the electron recombination (back reaction or dark current) resistance and C_2, the capacitance between the MWCNT-TiO_2 layer and the electrolyte constitute RC network in the interface. The third semicircles which is expected to appear at small frequency is due to characteristics of diffusion of the I^-/I^{3-} redox electrolytes are obscured due to much higher resistance of R_2 than that of Z_w (Warburg impedance). The Z_w is the impendence that is resistance encountered by the charge carriers when they diffused through the electrolyte. In addition to these, there is sheet resistance R_s that is in series with the RC parallel circuit, which is

more or less similar for all the fabricated DSSCs. Except [TiO_2/N719/Pt] configuration, in all the other 5 variants of DSSCs, we use same MWCNT as the counter electrode, R_1 values are almost same with slight variations. On the other hand, in the photo anode interface, the value of R_2 should vary according to the amount of MWCNT present in the photo anode material. The increased level of MWCNT photo anode facilitates the easy transport of the electrons within the semiconductor and also helps to reduce the recombination. It is quite clear from Figure 83 and table 21 that the recombination resistance R_2 corresponding to the configuration [0.06%-MWCNT-TiO_2/N3/MWCNT] based DSSC is the highest among the all six different fabricated configurations. This largest R_2 in [0.06%-MWCNT-TiO_2/N3/MWCNT] configuration offers high resistance for the charge recombination (also called dark current) between the photosensitized electron in MWCNT-TiO_2 semiconducting surface and the electrolytic cationic layer surrounding MWCNT-TiO_2 directly from the conduction band of the photoanode (MWCNT-TiO_2) or through some trap states below [10].

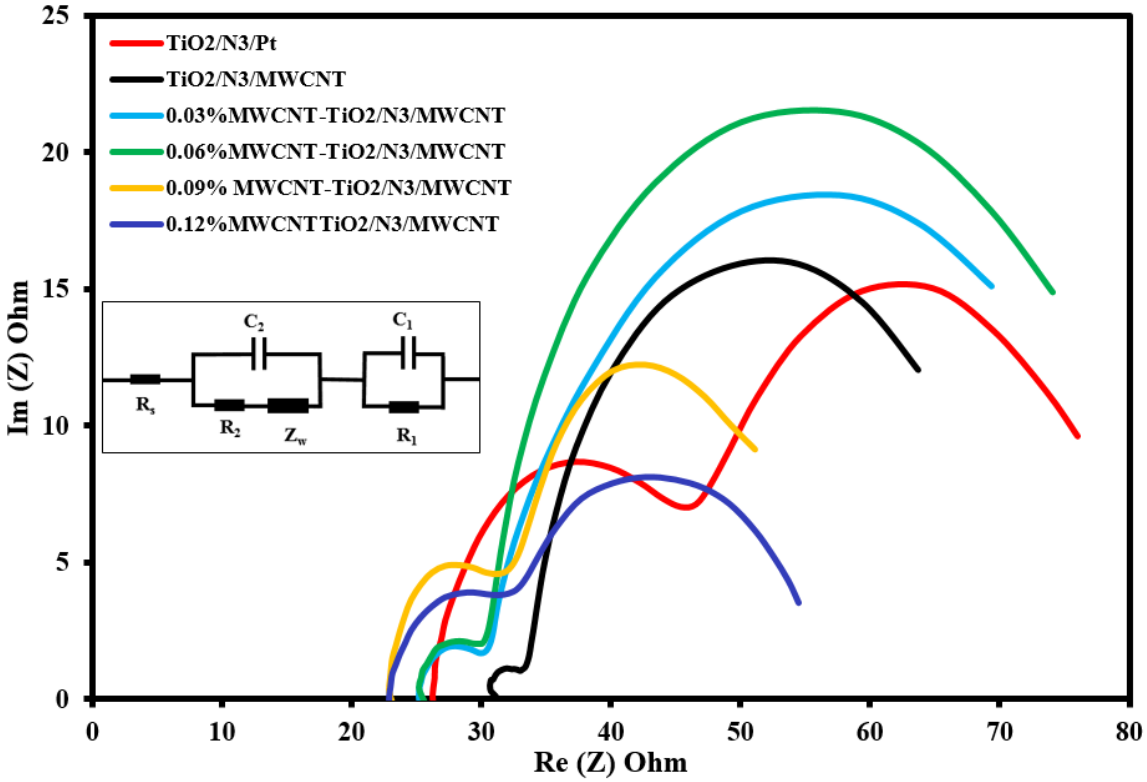

Figure 83 EIS spectra of fabricated DSSCs with equivalent circuit of DSSC (inset).

Table 21 Equivalent circuit parameters of fabricated DSSCs

Cell Structure	R_1 (Ω)	R_2 (Ω)	C_1 (μF)	C_2 (mF)
TiO_2/N3/MWCNT	15.31	39.37	5.52	0.16
0.03%MWCNT-TiO_2/N3/MWCNT	8.95	41.54	20.57	0.26
0.06%MWCNT-TiO_2/N3/MWCNT	**7.22**	**55.09**	**38.6**	**0.29**
0.09%MWCNT-TiO_2/N3/MWCNT	19.74	27.28	19.7	0.23
0.12%MWCNT-TiO_2/N3/MWCNT	25.66	26.02	7.73	0.23
TiO_2/N3/Pt	23.45	36.67	5.28	0.25

5.4.6 Catalytic activity of MWCNT

Besides the optical, electron transport and material characteristics of photo anode, the catalytic nature of the counter electrode (cathode), composition and configuration of DSSC, the nature of redox electrolytes and the sensitizing dye are the crucial factors that influence the performance of DSSC. Another improvisation introduced in the DSSC is the use of MWCNT as the catalytic material to replace the expensive platinum electrode. Although the [MWCNT-TiO_2/N3/MWCNT] DSSC is found to be more promising than the conventional [TiO_2/N3/Pt] configuration, it is quite interesting to single out the contribution of MWCNT counter electrode in the overall photovoltaic performance enhancement. In DSSC counter electrode functions as catalyst in the chemical process of efficiently reducing the redox mediator so that the dye molecules are rapidly regenerated. The rapid reduction of redox mediator and the regeneration of dye can also effectively inhibit the charge recombination at the conduction band of TiO_2 and electrolytic cations interface and also recombination of conduction electrons with the oxidized dye molecule. As the exchange current for the reduction of oxidized species in DSSC is proportional to the catalytic performance of the counter electrode material, we carried out Tafel analysis to estimate and compare the exchange current produced by the catalytic activity of Pt and MWCNT in the DSSC. We fabricated dummy cells for both MWCNT and Pt materials with Iodolyte I^-/I_3^- as electrolyte. Tafel plot is bases on the Tafel equation, in which the log *J;* logarithmic current density is plotted against the V; excess potential, and the exchange current can be deduced by taking the antilog of the y intercept (at V=0) of the tangent of the curve. Figure 66a shows the Tafel curves of dummy cells (also called symmetrical cells) fabricated with Pt and MWCNT, from which it is clear that the exchange

current J_0 for MWCNT catalyst is considerably higher than that for Pt and hence it is quite obvious that the MWCNT as a counter electrode is found to be better than that of Pt in terms of catalytic activity in this DSSC configuration. The resistance R_1, at the electrolyte I^-/I_3^- /counter electrode interface called charge transfer has an inverse relation with exchange current density J_0 as shown in equation (5.22)

$$J_0 = \frac{RT}{nFR_1} \qquad (5.22)$$

Where, F, R, T and n are Faraday's constant, the gas constant, temperature, and the number of electrons involved in the reduction reaction respectively. Hence according to equation 1, the increased J_0 for MWCNT is quite anticipated as the R_1 of the MWCNT as counter electrode estimated from the EIS study is found to be much less than that of Pt counter electrode (table 21). Another important electrochemical parameter that can be deduced from Tafel plot is the limiting current (J_{lim}), which is the saturated level of current in the Tafel plot and from the Tafel plot in Figure 84a, the limiting current for MWCNT catalyst is also found to be-higher than that for Pt. The limiting current density (J_{lim}), is related to the diffusion coefficient (D) of the I^-/I_3^-redox mediator as depicted in equation 5.23.

$$D = \frac{l}{2nFC} J_{lim} \qquad (5.23)$$

Where, F is Faraday's constant, C is electrolyte concentration, l is the spacer thickness and n is the number of exchange electrons involved in the reduction reaction. Hence the improved exchange current and limiting current (improved diffusion coefficient) testify the role of MWCNT counter electrode to partially enhance the efficiency of [*n*-MWCNT-TiO_2/N3/MWCNT] DSSC.

5.4.7 Stability of MWCNT

Another desired feature of the counter electrode is that it should be chemically and electrochemically stable in the electrolytic environment. In this work chronoamperometry and cyclic voltammetry (CV) were carried out to study the chemical and electrochemical stability of MWCNTs as the CE. Figure 84b is the results of chronoamperometric analysis, where the current density is found to be quite stable for the duration of 3600 seconds, when 600 mV potential was applied. Also cyclic voltammetry (CV) study was also carried out and the hysteresis loops formed due to the oxidation process (forward ramp of the voltage) and reduction process (reverse ramp of the voltage) remain quite similar in Figure 84c and 84d, which are respectively for different number of cycles of forward/reverse voltage ramping (with the scan rate of 50 mV/sec) and for different voltage ramp rates. Therefore, it is quite evident from the chronoamperometric and cyclic voltammetric analyses that MWCNT counter electrode is electrochemically very stable.

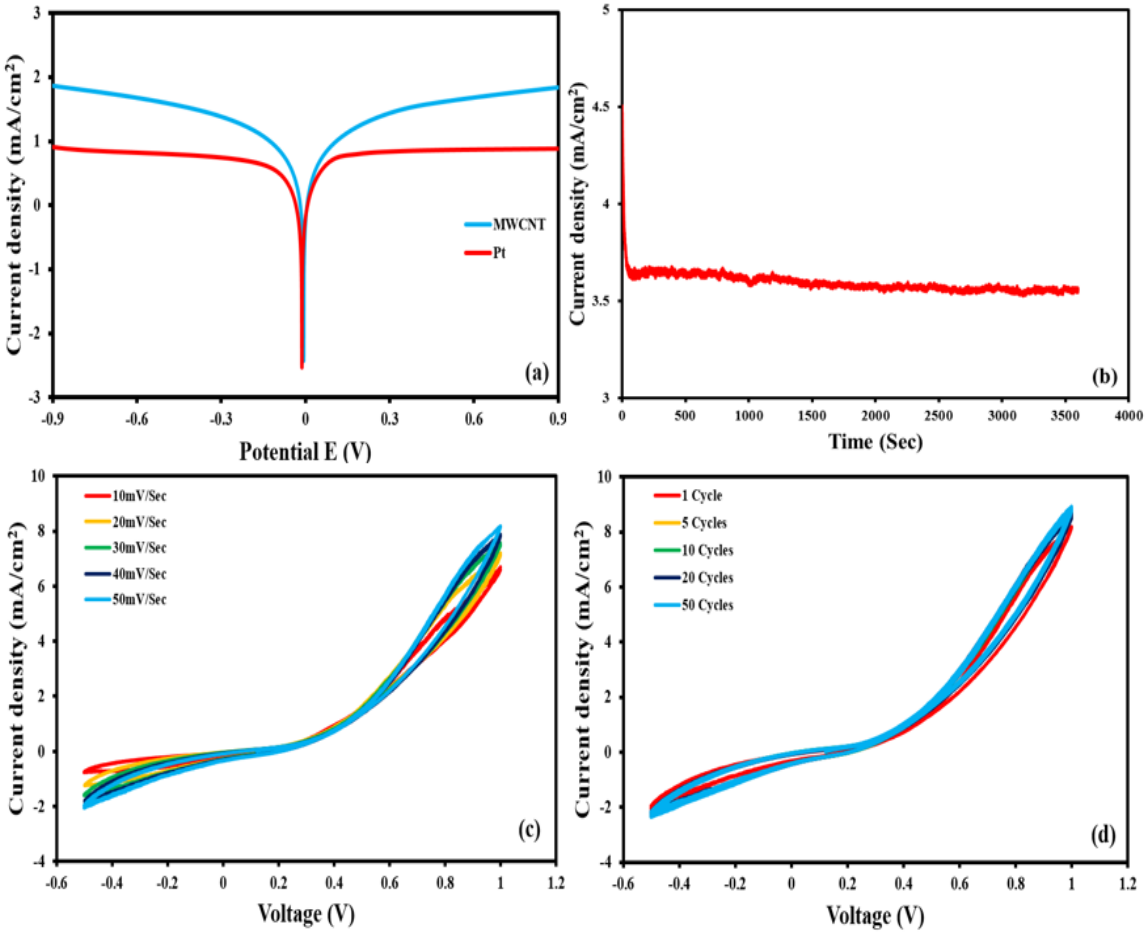

Figure 84 **(a)** Tafel curves of symmetrical cells (dummy cells) fabricated with MWCNT and Pt. **(b)** Stability test of MWCNT as a catalyst for counter electrodes with 7.5mM Iodolyte Z-50 as electrolyte, Pt as auxiliary electrode and Ag/AgCl as reference electrode, **(c)** Cyclic voltamograms for different scan rates, **(d)** CV curves at different number of cycles at the scan rate of 50 $mVsec^{-1}$.

5.4.8 Summary

In this work, MWCNT based DSSC was fabricated, where the synthesized MWCNT-TiO_2 nanocomposites with different levels of MWCNT were used as a photoanode in conjunction with MWCNT based, Pt free counter electrode. In photoanode, the

presence of MWCNT in TiO_2 brought about many positive attributes like enhanced light absorbance in the visible spectral region, high electron recombination resistance and improved electron transportation. MWCNT in counter electrode showed better catalytic effect than Pt in the reduction reaction of the oxidized iodine/triiodine redox mediator in DSSC. All these improved features resulted in the enhancement of photovoltaic efficiency in the [*n*-MWCNT-TiO_2/N3/MWCNT] DSSCs, and among the four different compositions of MWCNT-TiO_2 nanocomposites used as a photoanode, the one with 0.06%-MWCNT-TiO_2, i.e.[0.06%-MWCNT-TiO_2/N3/MWCNT] DSSC configuration showed the highest photovoltaic efficiency of 7.15 %, which accounts for an enhancement of 13% photovoltaic efficiency compared to the conventional [TiO_2/N3/Pt] DSSC configuration. This photovoltaic performance improvement and use of low cost MWCNT in the place of expensive platinum will make MWCNT based DSSCs efficient and cost effective. Morphological, optical, elemental and electrochemical studies of the material and DSSC were carried out and the improved photovoltaic efficiency of [*n*-MWCNT-TiO_2/N3/MWCNT] DSSC configuration is explained on the basis of these results.

5.5 Rapid growth of 2D/3D Perovskite Single Crystals and their Application as Efficient and Stable Solar Cells and Photodetectors

5.5.1 Brief introduction

A perovskite is any material with the following structure $^{XII}A^{2+}\,^{VI}B^{4+}X_3^{2-}$ as shown in Figure 85, where 'A' and 'B' are two cations, and X is an anion that bonds to both A and B. Perovskite materials exhibit many interesting and intriguing properties especially their

superconductivity, which makes them very promising for different uses in technology. Moreover, perovskite can be very beneficial due to their abundant availability and low cost [182].

There are different types of perovskite materials. They include, more common 3D and also 2D, 1D and 0D perovskite materials [183]. The 3D perovskite materials have stacking of layers as shown in unit cell in Figures 86 and 87. However, if we replace cation “A” with some bigger ionic radius cation, e.g. replacing methylammonium with buthylammonium or propylammonium the stacking of 3D structures can be broken into different layers and it can be controlled in many ways in terms of concentrations as shown in Figures 86 and 87.

There are two types of perovskite crystal (1) Polycrystalline and (2) Single crystal. Polycrystalline growth of perovskite materials has many small crystals at nano level and hence many grain boundaries. Many charge carriers are recombining at these grain boundaries. Additionally, water molecules from the moisture are staked on these grain boundaries and leads to the instability of the perovskite polycrystalline materials. A single crystal is a solid in which the crystal lattice is continuous and unbroken throughout the sample i.e. it does not contain any grain boundaries like polycrystals. Usually polycrystalline perovskite materials are used to grow for various applications because of their easy growth. However, single crystals have much more advantages over their counterpart’s poly crystals. The single crystals have unique electrical and optical properties due to the absence of the grain boundaries which decreases the loss of charge carriers at grain boundaries. In addition to this important factor, single crystal has much more advantages over poly crystal such as long diffusion length, long lifetime, higher mobility

and low density of defects [184]**.** On the other hand, the polycrystalline perovskite materials have a shorter lifetime and short diffusion length, many grain boundaries and less mobility. Thus, single crystals were a better choice for this study which are subsequently selected.

Crystallization is a process in which the stable crystalline phase emerges from the metastable disordered phase. Various methods for the synthesis of perovskite single crystals have been developed to date. These methods mainly include solution-processed crystallization methods. There is the Classical Cooling Crystallization (CCC) and the Top-Seeded Solution Growth (TSSG) methods which are both based on the loss of solubility upon cooling the saturated solution [185]. We also have the anti-solvent vapor-assisted Crystallization (AVC) that is based on a slow diffusion of an antisolvent vapor into a solution containing the crystal precursors. Recently Bakr et. al discover a new method to grow single crystals in minutes [186]. This method is called Inverse Temperature Crystallization (ITC) method which we have used in this study.

The Inverse Temperature Crystallization (ITC) method is based on the loss of solubility by solutes in a particular solvent upon heating, favoring their crystallization at elevated temperatures as shown in Figure 88. In most of the solids, the solubility increases with temperature thus cooling crystallization methods are used. However, in a few number of solids the solubility trend is the opposite (inverse), they become less dissolve at high temperatures [187]. Therefore, they are called inverse temperature crystallization. The process of crystallization in ITC is reversible. The grown crystals can re-dissolve in the solution upon cooling to the room temperature [188].

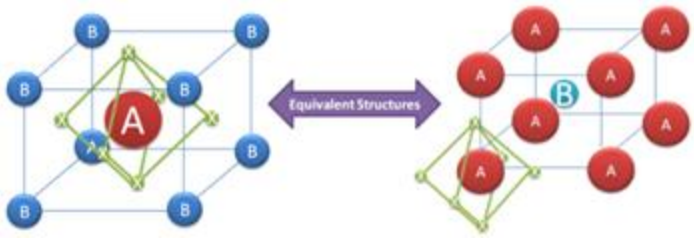

Figure 85 Perovskite structure.

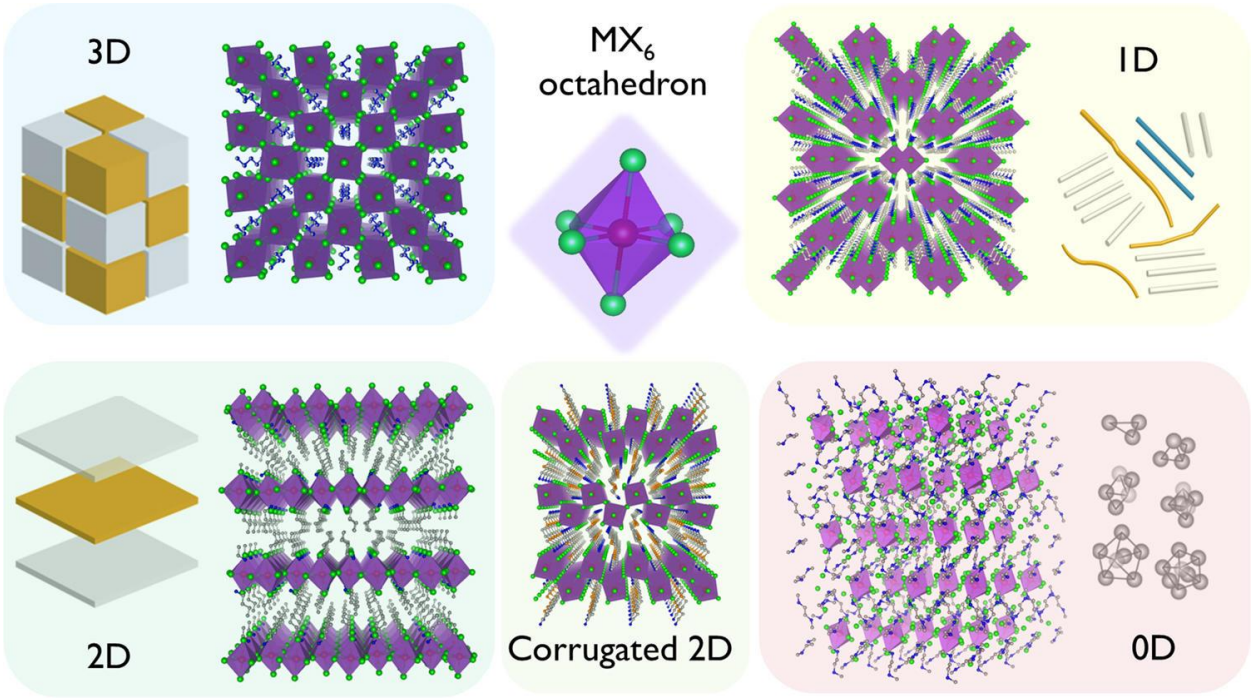

Figure 86 Different structures of perovskite [183].

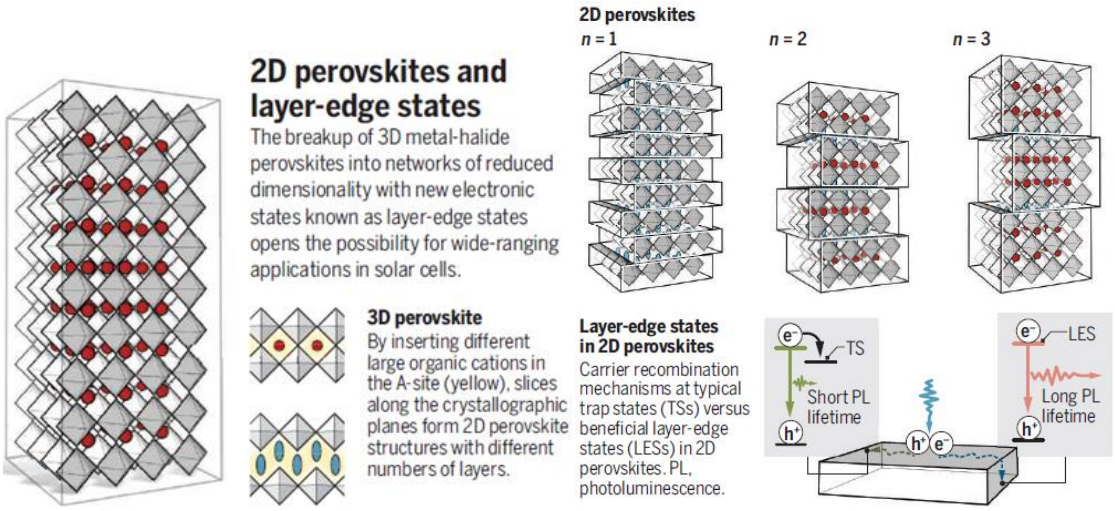

Figure 87 Perovskite structures including 3D and 2D with different number of layers. The figure also explaining the beneficial layer-edge states[189].

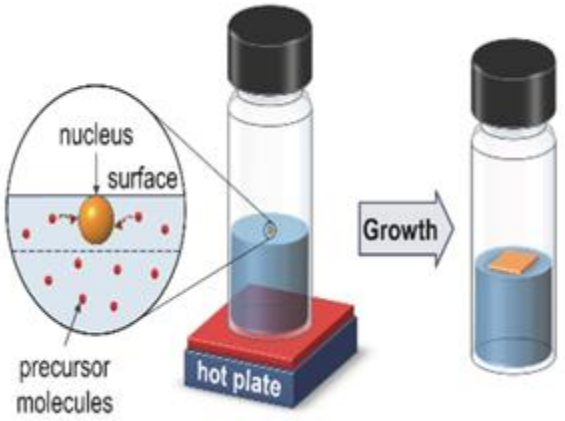

Figure 88 Inverse temperature crystallization method to grow perovskite single crystals [190].

Perovskites can be used in many applications such as solar cells, photodetectors and X-ray detection [191]. Here we are aimed to fabricate perovskite-based photodetectors and solar cells.

Photodetectors are a class of optoelectronic devices that respond to the change of light: absence, presence or intensity variations. Photodetectors can also translate light into electrical current. This property can help us innovate and develop better technologies to help humanity. Photodetectors are also used in optical communications, medical and scientific instruments (X-ray detection, fluorescence), surveillance and other applications [192]. Solar cell is a device which convert sunlight to electrical energy. Unlike other photovoltaics the efficiency of perovskite solar cells raised from 3.8% to 23.7% in just nine years [193] which is best achievement for any type of solar cell in the history of photovoltaic. However, instead of outstanding performance of perovskite solar cells they cannot be commercialized at this stage due to their stability issues. These materials are unstable when expose to ambient environment. 2D perovskite materials are hydrophobic in nature and much more stable as compared to their 3D counterparts.

In this study, we prepared pure 3D and 2D/3D perovskite materials and then used them to grow single crystals. The grown single crystals are used to fabricate photodetector and solar cells. The 2D/3D materials are found more efficient and more stable.

5.5.2 Results and Discussions

5.5.3 Bulk Single Crystals

5.5.4 $MAPbI_3$ bulk single crystals

The $MAPbI_3$ bulk single crystal was grown using inverse temperature crystallization method. The size of the grown single crystal is ~ 7mm as shown in Figure 89. The temperature was elevated from 70 ^oC to 110 ^oC with 5 ^oC/hour.

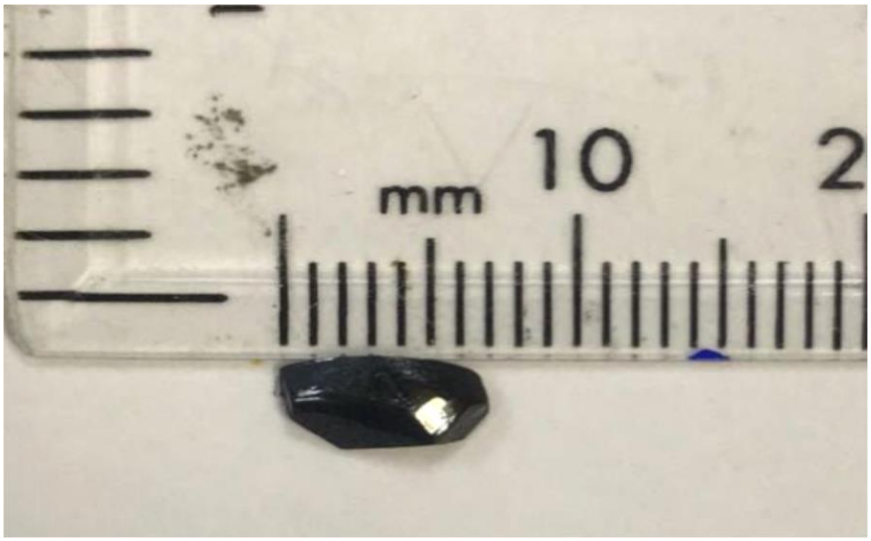

Figure 89 The 3D $MAPbI_3$ perovskite bulk single crystal.

5.5.5 BAI: $MAPbI_3$ bulk single crystals

The BAI: $MAPbI_3$ bulk single crystal was grown using inverse temperature crystallization method. The size of the grown single crystal is ~ 5mm as shown in Figure 90. The temperature was elevated from 70 ^oC to 110 ^oC with 5 ^oC/hour. It was observed that the surface of the grown single crystal was very smooth, and its SEM images are provided in characterization chapter 4.

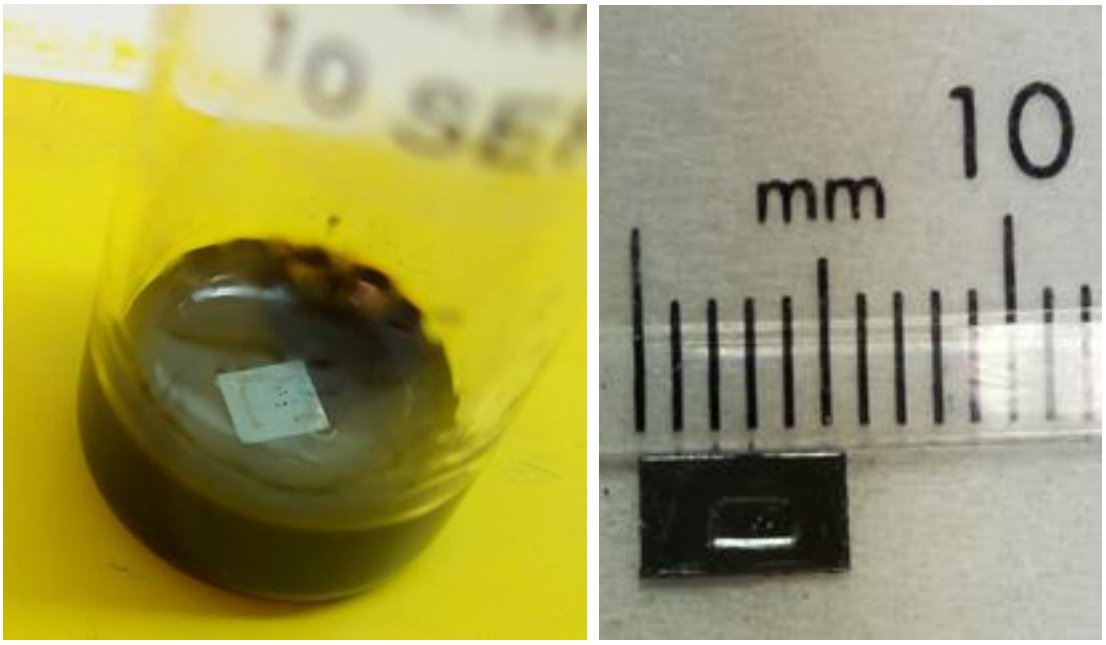

Figure 90 The 2D/3D BAI: $MAPbI_3$ perovskite bulk single crystal.

5.5.6 PAI: $MAPbI_3$ bulk single crystals

The PAI: $MAPbI_3$ bulk single crystal was grown using inverse temperature crystallization method. The size of the grown single crystal is ~ 6mm as shown in Figure 91. The temperature was elevated from 70 ^oC to 110 ^oC with 5 ^oC/hour. It was observed that the surface of the grown single crystal was very smooth, and its SEM images are provided in characterization chapter 4.

Figure 91 The 2D/3D PAI: $MAPbI_3$ perovskite bulk single crystal.

5.5.7 Thin Single Crystals

5.5.8 MAPbI3 thin single crystals

The $MAPbI_3$ thin single crystal were grown using inverse temperature crystallization method. The size of the grown single crystal is ~ 5mm as shown in Figure 92. The perovskite solution was poured between two ITO glasses and case-capping technique was used. The temperature was elevated from 70 ^oC to 110 ^oC with 5 ^oC/hour. It was confirmed that there are no grain boundaries on the surface of the grown single crystal, and its optical microscope images are provided in characterization chapter 4.

Figure 92 The 3D $MAPbI_3$ perovskite thin single crystal between two ITO coated glasses.

5.5.9 BAI: $MAPbI_3$ thin single crystals

The BAI: $MAPbI_3$ thin single crystal were grown using inverse temperature crystallization method. The size of the grown single crystal is ~ 4mm as shown in Figure 93. The perovskite solution was poured between two ITO glasses and case-capping technique was used. The temperature was elevated from 70 ^{o}C to 110 ^{o}C with 5 ^{o}C/hour. It was confirmed that there are no grain boundaries on the surface of the grown single crystal, and its optical microscope images are provided in characterization chapter 4.

Figure 93 The 2D/3D BAI: $MAPbI_3$ perovskite thin single crystal between two ITO coated glasses.

5.5.10 PAI: $MAPbI_3$ thin single crystals

The PAI: $MAPbI_3$ thin single crystal were grown using inverse temperature crystallization method. The size of the grown single crystal is ~ 3-4mm as shown in Figure 94. The shape of these single crystal was star like as shown in the Figure 94 below. The perovskite solution was poured between two ITO glasses and case-capping technique was used. The temperature was elevated from 70 ^oC to 110 ^oC with 5 ^oC/hour. It was confirmed that there are no grain boundaries on the surface of the grown single crystal, and its optical microscope images are provided in characterization chapter 4.

Figure 94 The 2D/3D PAI: $MAPbI_3$ perovskite thin single crystal between two ITO coated glasses.

The response of single crystals was measured using an advanced multimeter for calculating the resistance in ohms to check if the grown single crystals are responding to the shinned light or not. The response for all the three types of single crystals are tabulated below in table 22.

Table 22 Experimental results for the photodetectors fabricated in this study.

Bottle#	**Perovskite Materials**	**Crystal (Thin/bulk)**	**Substrate type**	**Without light (MΩ)**	**With room light (MΩ)**	**With mobile light (MΩ)**
1	$MAPbI_3$	Thin	FTO	21	19	18
			ITO	14	13	12
			FTO	13	8	3

		Bulk	ITO	23.9	20.9	11.9
2	BAI: $MAPbI_3$	Thin	FTO	38	31	27
			ITO	92	68	47
		Bulk	FTO	26	20	14
			ITO	76	61	52
3	PAI: $MAPbI_3$	Thin	FTO	40	30	22
			ITO	135	100	72
		Bulk	FTO	31	26	21
			ITO	92	81	73

Note: Responsiveness of these photodetectors can be determined by the difference rate in the resistance when light luminosity changes.

5.5.11 Photodetector response by potentiostat and xnon lamp

For better understanding the response of the fabricated single crystal photodetector was further tested using autolab potentiostat. Xnon lamp was used as a light source to check the response of the fabricated photodetectors. The test was performed for 200 seconds with an interval of 10 seconds for shinning of UV-Vis light to the photodetector and next 10 seconds keeping the photodetector under dark which are given below in Figures 95 to 100. The response was very clear and quite satisfactory which confirmed the readings taken by

the voltmeter. The overall current remained constant with slight changes for this period which are due to the small degradation of perovskite materials because of 5% UV exposure in the used lamp light.

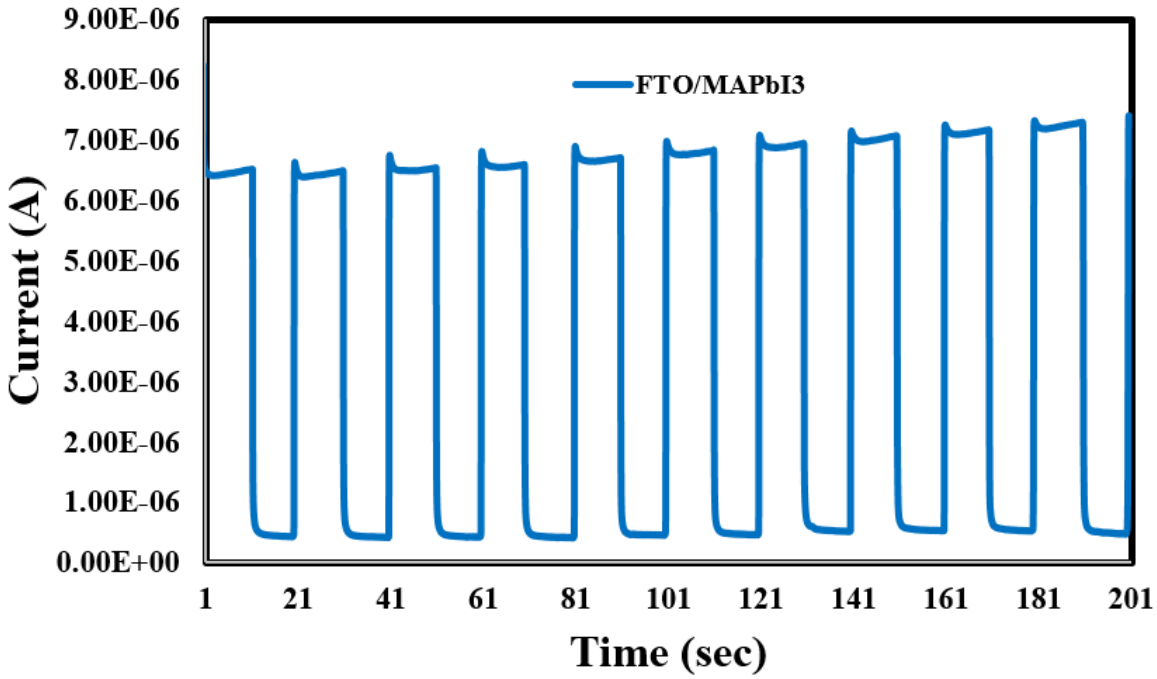

Figure 95 Planar photodetector fabricated using $MAPbI_3$ perovskite single crystal grown on FTO glass substrates response to the UV-Vis Xenon lamp light.

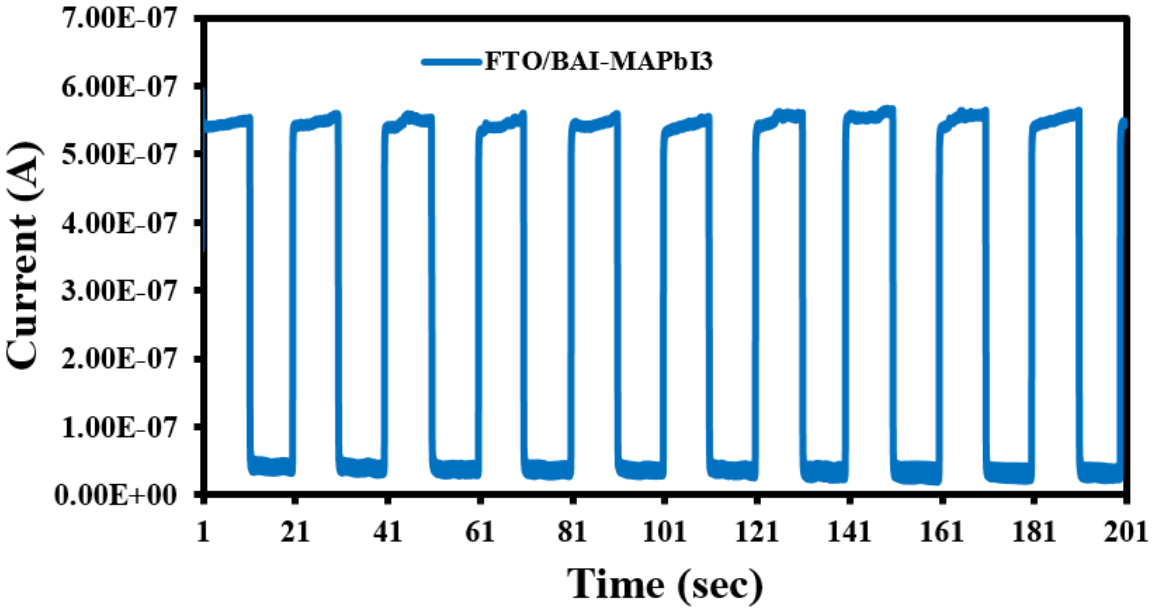

Figure 96 Planar photodetector fabricated using BAI: $MAPbI_3$ perovskite single crystal grown on FTO glass substrates response to the UV-Vis Xenon lamp light.

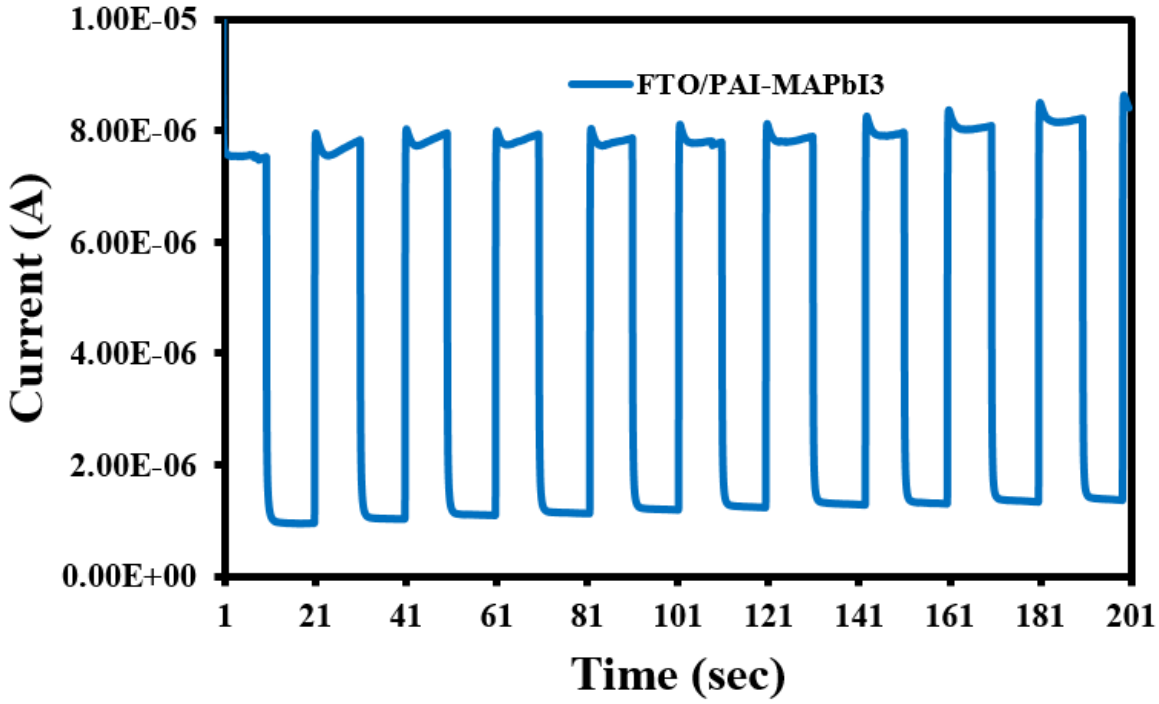

Figure 97 Planar photodetector fabricated using PAI: $MAPbI_3$ perovskite single crystal grown on FTO glass substrates response to the UV-Vis Xenon lamp light.

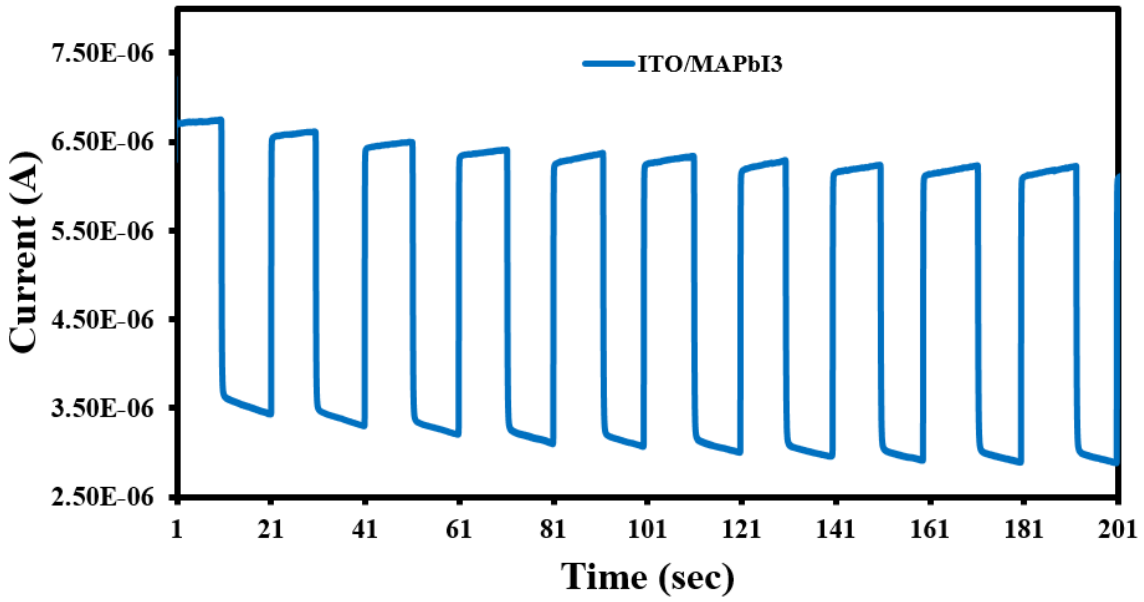

Figure 98 Planar photodetector fabricated using $MAPbI_3$ perovskite single crystal grown on ITO glass substrates response to the UV-Vis Xenon lamp light.

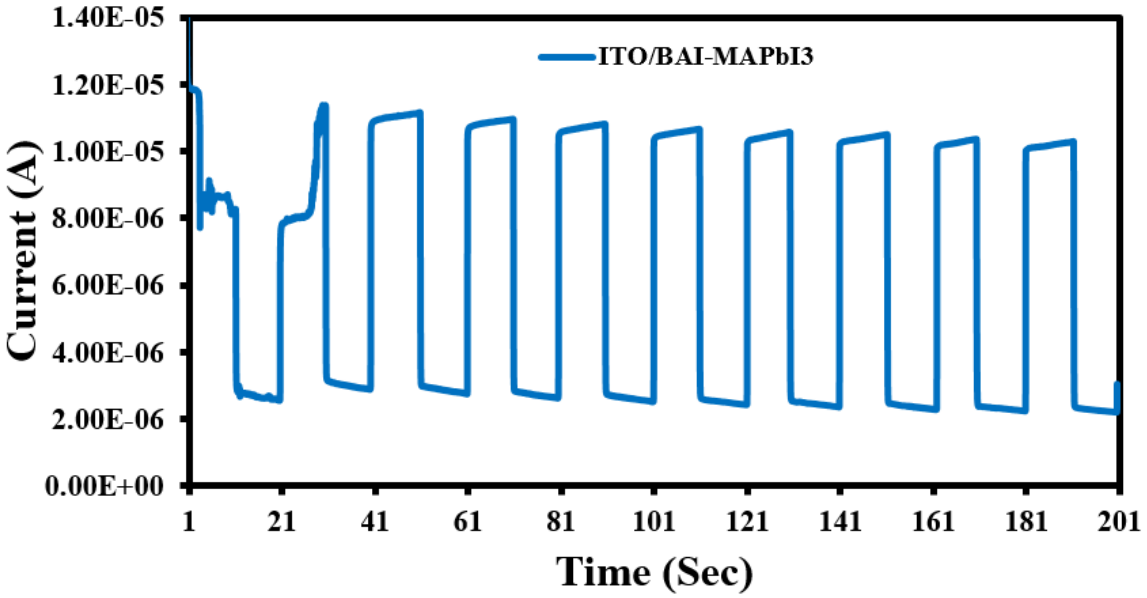

Figure 99 Planar photodetector fabricated using BAI: $MAPbI_3$ perovskite single crystal grown on ITO glass substrates response to the UV-Vis Xenon lamp light.

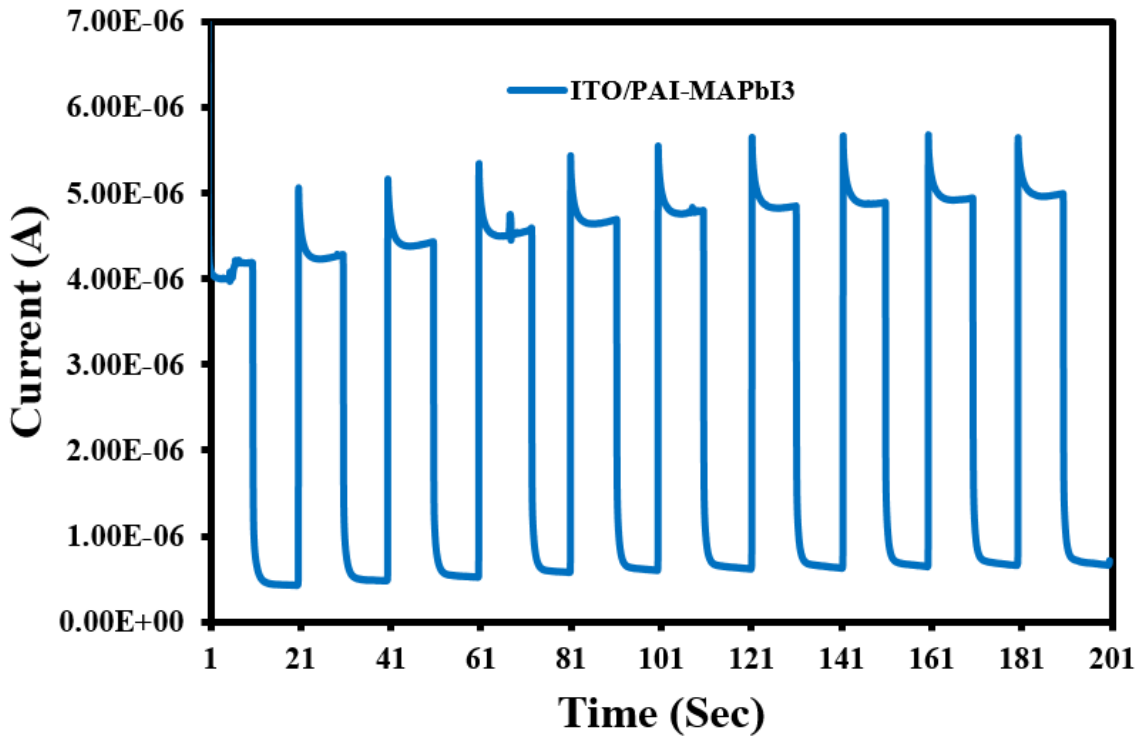

Figure 100 Planar photodetector fabricated using PAI: $MAPbI_3$ perovskite single crystal grown on ITO glass substrates response to the UV-Vis Xenon lamp light.

5.5.12 Fabrication of carbon-based printed perovskite solar cells using inverse temperature crystallization (ITC) technique

The carbon-based printed perovskite solar cells were fabricated using ITC technique. The schematic diagram for the fabrication of carbon-based printed perovskite solar cells using ITC technique is shown in Figure 101 below. First, the FTO glass were masked for the desired area and then etched using zinc powder and hydrochloric acid. After cleaning of the etched FTO substrates, the substrates were tape casted for the desired area to be coated. The tape casted FTO substrates were spin coated with titanium dioxide (TiO_2) blocking layer using spin coater with speed 5000 rpm for 30 seconds. The spin coated blocking layers substrates were annealed at 500 ^oC for 60 mints. Subsequently, the FTO substrates

were tape casted again for desired area to be coated with TiO_2 layer to provide the electron transporting layer. We used doctor blade method to coat this layer and annealed it at 475 ^oC for 30 mints. The FTO substrates were tape casted again to coat the third layer of ZrO_2 using doctor blade method and annealed at 475 ^oC for 30 mints. In the next step, the FTO substrates were tape casted again for the desired area to be coated with carbon paste to prepare porous carbon layer to replace both hole transporting layer as well as counter electrode. This layer was coated using doctor blade method and annealed at 450 ^oC for 30 mints. Finally, the prepared kits were poured with perovskite solutions. The four samples were prepared, one with conventional method and three with ITC technique.

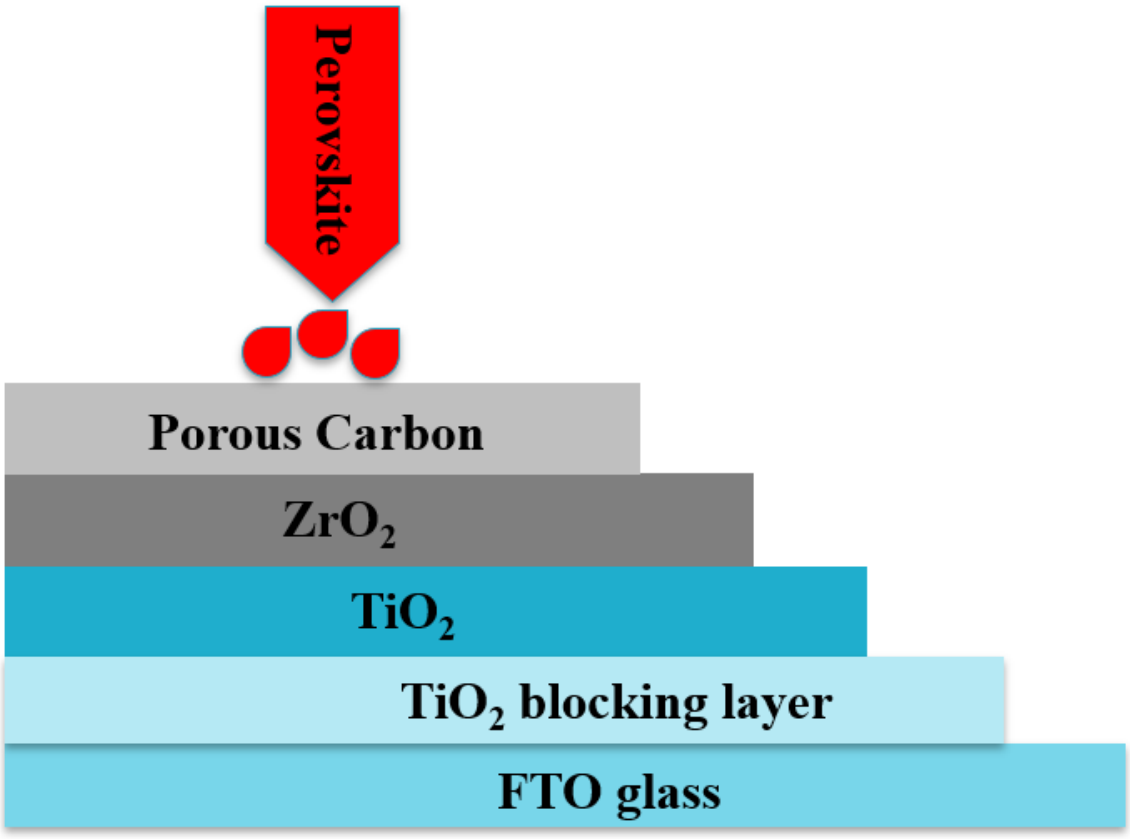

Figure 101 Schematic diagram for the fabrication of carbon-based printed perovskite solar cells using ITC technique.

5.5.13 Current-voltage characteristics of Carbon-based printed perovskite solar cells using ITC technique

The current-voltage characteristics of the fabricated solar cells were measured using class AAA solar simulator equipped with standard simulated light AM 1.5G and data acquisition system (IV-5 solar simulator, Sr. No. 83, PV measurements, USA). The IV curves for all four carbon-based printed perovskite solar cells using ITC technique can be found in Figure 102.

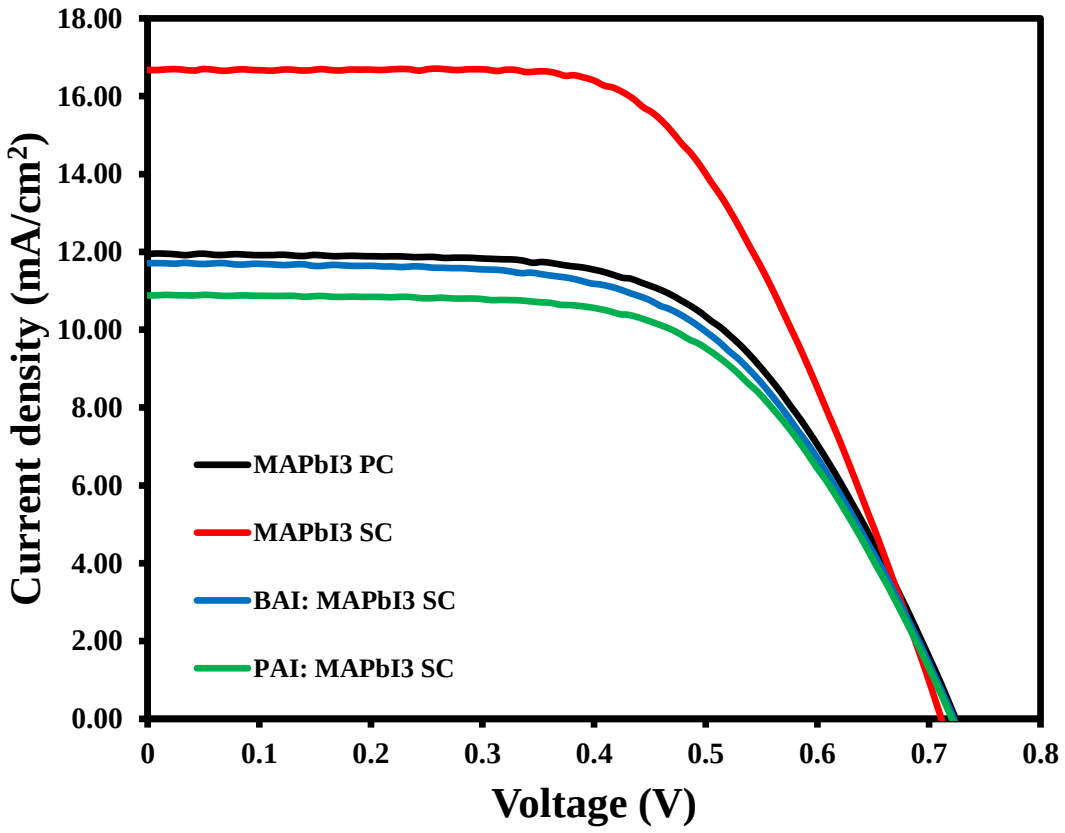

Figure 102 Current-voltage characteristics of carbon-based printed perovskite solar cells fabricated using ITC technique.

The current-voltage characteristics parameters i.e. current density J_{sc} (mA/cm^2), open circuit voltage V_{oc} (mV), Fill Factor (%) and power conversion efficiency η (%) for the fabricated solar cells are provided in the table 23 below. It is evident that the current density became better for $MAPbI_3$ single crystals based solar cells. This is due to reduced recombination of the charge carriers. It is also observed that the current density of the 2D/3D perovskite single crystal based solar cells decreased due to the long chain perovskite 2D material layers which behave as charge barriers. However, single crystal based solar cell are more stable as there are no grain boundaries, so no moisture will be sticking on the grain boundaries, ultimately no degradation of the single crystals.

Table 23 Current voltage characteristics of carbon-based printed perovskite solar cells fabricated using ITC technique.

Cell structure	**J_{sc} (mA/cm^2)**	**V_{oc} (mV)**	**FF (%)**	**η (%)**
$MAPbI_3$ PC	11.9	724	60	5.17
$MAPbI_3$ SC	**16.7**	**711**	**60**	**7.09**
BAI: $MAPbI_3$ SC	11.7	722	59	4.98
PAI: $MAPbI_3$ SC	11.2	721	59	4.76

Through the analysis of all these fabricated solar cells, we can conclude that single crystal based solar cells are more efficient and more stable due to absence of grain boundaries. Further research can lead these solar cells to large scale application due to utilization of inexpensive carbon as counter electrode instead of costly gold as well as removal of hole expensive hole transporting material like Spiro-OMeTAD.

5.5.14 Summary

Perovskite bulk and thin single crystals were grown using ITC technique. Three types of single crystals were grown including pure $MAPbI_3$, BAI: $MAPbI_3$ and PAI: $MAPbI_3$. The 2D/3D perovskite single crystals (BAI: $MAPbI_3$) showed a more significant difference in the resistance at the three different circumstances (room light, without light and with mobile light) than the other perovskite single crystals i.e. $MAPbI_3$ and PAI: $MAPbI_3$, which means greater responsiveness to light that makes it an excellent photodetector. The photodetector responses to the light were measured using auto lab potentiostat, which further verify the better efficiency of BAI: $MAPbI_3$. Furthermore, 2D/3D perovskite materials-based single crystals shown more smooth and shiny surfaces. Finally, we fabricated solar cells based on perovskite single crystals which shows better efficiency as compared to the poly crystalline solar cells. The carbon-based printed perovskite solar cells were fabricated using ITC technique to grow single crystals. The current-voltage characteristics confirm the better efficiency in case of single crystal method.

CHAPTER SIX

CONCLUSION AND FUTURE RECOMMENDATIONS

In this chapter the conclusion of the entire work carried out for this thesis and future recommendations are presented.

6.1. Conclusion

The two main reasons for low efficiency of DSSCs are (i) low absorption coefficient (ii) the recombination of photogenerated electrons with the oxidized electrolyte/dye. This recombination of charges is also called dark current. On the other hand, platinum which is an expensive noble metal, is conventionally used as a counter electrode in DSSC. In this thesis we used various strategies to reduce the fabrication cost and enhancement of the efficiency of the DSSCs by improving its absorption coefficient as well as reducing dark current. The first strategy to enhance absorption coefficient, and hence ultimately enhancing the efficiency of DSSC is co-sensitization technique. Co-sensitization approach is an effective approach to enhance the performance of DSSC. We used organic sensitizer SQ2 as a co-sensitizer with ruthenium-based dye Z907. Dye solutions of seven different concentrations were prepared for the fabrication of DSSC. The fabricated DSSC were characterized by UV-Vis spectroscopy, I-V characteristics, and EIS analysis. Our main findings from this study demonstrated that the co-sensitization approach is a highly effective method to boost the photovoltaic performance of a DSSC. Additionally, our results proved that the absorption of dye solution increases with the increase of SQ2

content. However, absorption spectra become more intense, sharp and broader when anchored to TiO_2 film coated on the FTO surface. It has been also observed that the PCE, V_{oc}, J_{sc}, FF and charge recombination resistance of solar cells strongly depend on the concentration of SQ2 dye. This study also confirmed that the charge recombination resistance at photoanode/dye/electrolyte interface increases with co-sensitization and thus reduces the dark current. Under optimal conditions, the DSSC assembled with 0.3mM Z907 + 0.2mM SQ2 delivered PCE of 7.83%, which is significantly higher than the individual sensitized solar cell (Z907 = 5.08% and SQ2 = 1.39%). This research has been published in International Journal of Energy Research.

The costly platinum as counter electrode and the dark current which is the second main problem of DSSC low efficiency was investigated using different approaches. We fabricated hybrid composite using WO_3-TiO_2 which showed reduced recombination of free carriers at photoanode/electrolyte interface. Additionally, we replaced expensive platinum with cost-effective MWCNTs as counter electrode. In this study, three different mass ratios of synthesized *n*WO_3-TiO_2 nanocomposite films (*n* = 1%, 3%, and 5%), and MWCNT were used as photoanode and back electrode respectively to fabricate [*n*WO_3-TiO_2/N719/MWCNT] combination of DSSC. In addition, a set of [*n*WO_3-TiO_2/N719/Pt] combination of DSSC were also fabricated in order to single out the improvement in the performance of DSSC due to the use of MNCNT as the back electrode. The structural, morphological and optical characterizations of synthesized *n*WO_3-TiO_2 nanocomposite photoanode films and the stability tests of back electrode were carried out. By comparing the photovoltaic performance of all the DSSCs, it is quite clear that the cell with 1%WO_3-TiO_2 in *n*WO_3-TiO_2 as a photoanode and MWCNT as back electrode [1%WO_3-

TiO_2/N719/MWCNT] has the best efficiency of all the six variants of fabricated DSSCs. It was found that an efficiency of 6.12 % was achieved with [1%WO_3-TiO_2/N719/MWCNT] combination, which is around 12 % higher than the highest reported in the literature for any *n*WO_3-TiO_2 nanocomposite photo-anode in DSSC. The enhancement of photovoltaic performance of fabricated [*n*WO_3-TiO_2/N719/ MWCNT] DSSC in general could be attributed to the reduced charge recombination and increased electron injection into the conduction band of the composite semiconductor. This study has been published in Ceramics International journal.

From the motivation of the previous study we used another strategy to enhance the efficiency of the DSSC using a completely new cost-effective approach. We prepared hybrid composite anodes using MWCNT-TiO_2 and used them for photoanode and at the same time MWCNT were used as counter electrode to replace the expensive platinum. In this study, MWCNT based DSSC was fabricated where the synthesized nanocomposites of MWCNT and TiO_2 used as a material for photoanode with variant compositions and MWCNT with the precise fixed composition as Pt free counter electrode. In photoanode, the presence of MWCNT in TiO_2 brought about many positive attributes like improved light absorbance in the visible region, high electron recombination resistance, improved electron transportation and MWCNT in counter electrode showed improved catalytic effect in the reduction reaction of the oxidized iodine/triiodine redox mediator in DSSC. All these improved features resulted in the enhancement of photovoltaic efficiency in the [*n*-MWCNT-TiO_2/N3/MWCNT] DSSCs, particularly the efficiency enhanced as high as 7.15 % in the case of [0.06%-MWCNT-TiO_2/N3/MWCNT] DSSC configuration. This photovoltaic performance improvement and use of low cost MWCNT in the place of

expensive platinum will make MWCNT based DSSCs efficient and cost effective. Morphological, optical, elemental and electrochemical studies of the material and DSSC were carried out and the improved photovoltaic efficiency of [*n*-MWCNT-TiO_2/N3/MWCNT] DSSC configuration is explained on the basis of these results. This study is under review in Solar Energy journal.

Perovskite are more efficient materials as compared to dyes due to their better absorption coefficient in the visible region. However, the perovskite solar cells are not stable yet. The usual 3D perovskite materials are more efficient, while 2D perovskites are more stable. We carried out our research to make perovskite more efficient as well as stable. For this purpose, we mixed 2D/3D perovskite materials to achieve both efficiency as well as stability. Furthermore, we worked to grow 2D/3D perovskite single crystals e.g. BAI: $MAPbI_3$, PAI: $MAPbI_3$. Finally, these grown perovskite single crystals were used for fabrication of photodetectors. The fabricated photodetector using 2D/3D perovskite single crystals i.e. BAI: $MAPbI_3$ and PAI: $MAPbI_3$ showed a more significant difference in the resistance at the three different circumstances (room light, without light, and with mobile light) as compared to the 3D perovskite materials $MAPbI_3$, which showed more efficient photodetector. Additionally, these 2D/3D photodetectors showed great stability in comparison with the 3D perovskite materials-based photodetectors. Moreover, we fabricated perovskite solar cells using 3D as well as 2D/3D perovskite materials. The results show more efficiency and stability in case of 2D/3D perovskite materials single crystals. Concludingly, as DSSC is more stable but less efficient as compared to PSC, and PSC is more efficient but less stable. In this thesis we worked to fix these gaps. Additionally, we worked to make them more cost-effective.

6.2. Future recommendations

Low efficiency and high cost for platinum counter electrode are the major challenges for the commercial growth of DSSCs. The following factors are responsible for the low efficiency and expensive counter electrode of DSSCs,

1) Non-optimized dark current
2) Poor performance of dyes in the NIR region
3) Poor contact between the electrodes
4) High cost of platinum being a noble metal

Following steps are recommended in order to further enhance the efficiency and cost effectiveness of DSSCs;

1) Improvement in the morphology of semiconductors to reduce dark current like addition of MWCNT or any other efficient and cost-effective materials
2) Dyes design can be improved to enhance extinction coefficient
3) Contact improvement at interfacial surfaces
4) Use of additives for dyes and electrolytes that enhance their properties.

On the other hand, perovskite solar cells are efficient, but they are not stable as well as they have toxicity problem. The stability and toxicity problem of perovskite solar cells could be improved by the following steps and actions,

1) Use of 2D perovskite materials in combination with the 3D perovskite materials
2) Growth of single crystals using pure 3D perovskite materials as well as quasi 2D materials.
3) Growth of large as well as controlled single crystals
4) Use of Sn, Ge i.e. lead-free materials to avoid toxicity problem.

References

[1] T. Suzuki, “Nuclear Energy Policy after the Fukushima Nuclear Accident: An Analysis of ‘Polarized Debate’ in Japan,” in *Energy Policy*, IntechOpen, 2019.

[2] “Annual Energy Outlook 2018 with projections to 2050,” *U.S. Energy Inf. Adm.*, vol. Feb, 2018.

[3] F. S. Huraib, S. M. Hasnain, and S. H. Alawaji, “Lessons learned from solar energy projects in Saudi Arabia,” *Renew. Energy*, vol. 9, no. 1–4, pp. 1144–1147, Sep. 1996.

[4] S. H. Alawaji, “Evaluation of solar energy research and its applications in Saudi Arabia — 20 years of experience,” *Renew. Sustain. Energy Rev.*, vol. 5, no. 1, pp. 59–77, 2001.

[5] Saleh A. Al-Athel, “Solar energy in the Kingdom of Saudi Arabia,” *Int. J. Glob. Energy Issues*, vol. 9, no. 1/2, pp. 53–67, 1997.

[6] “http://www.nrel.gov/ncpv/images/efficiency_chart.jpg.”

[7] M. A. Green, K. Emery, Y. Hishikawa, W. Warta, and E. D. Dunlop, “Solar cell efficiency tables (version 48),” *Prog. Photovoltaics Res. Appl.*, vol. 24, no. 7, pp. 905–913, Jul. 2016.

[8] J.-H. Yum *et al.*, “Efficient co-sensitization of nanocrystalline TiO(2) films by organic sensitizers.,” *Chem. Commun. (Camb).*, no. 44, pp. 4680–2, 2007.

[9] A. Hagfeldt, G. Boschloo, L. Sun, L. Kloo, and H. Pettersson, “Dye-Sensitized Solar

Cells," *Chem. Rev.*, vol. 110, no. 11, pp. 6595–6663, Nov. 2010.

[10] U. Mehmood, I. A. Hussein, K. Harrabi, N. Tabet, and G. R. Berdiyorov, "Enhanced photovoltaic performance with co-sensitization of a ruthenium(II) sensitizer and an organic dye in dye-sensitized solar cells," *RSC Adv.*, vol. 6, no. 10, pp. 7897–7901, 2016.

[11] S. P. Singh, M. Chandrasekharam, K. S. V. Gupta, A. Islam, L. Han, and G. D. Sharma, "Co-sensitization of amphiphilic ruthenium (II) sensitizer with a metal free organic dye: Improved photovoltaic performance of dye sensitized solar cells," *Org. Electron.*, vol. 14, no. 5, pp. 1237–1241, May 2013.

[12] C.-M. Lan *et al.*, "Enhanced photovoltaic performance with co-sensitization of porphyrin and an organic dye in dye-sensitized solar cells," *Energy Environ. Sci.*, vol. 5, no. 4, p. 6460, Mar. 2012.

[13] H.-P. Wu *et al.*, "Molecular engineering of cocktail co-sensitization for efficient panchromatic porphyrin-sensitized solar cells," *Energy Environ. Sci.*, vol. 5, no. 12, p. 9843, Nov. 2012.

[14] H. Ozawa, R. Shimizu, and H. Arakawa, "Significant improvement in the conversion efficiency of black-dye-based dye-sensitized solar cells by cosensitization with organic dye," *RSC Adv.*, vol. 2, no. 8, p. 3198, Mar. 2012.

[15] L. Wei *et al.*, "Enhance the performance of dye-sensitized solar cells by co-sensitization of 2,6-bis(iminoalkyl)pyridine and N719," *RSC Adv.*, vol. 3, no. 48, p. 25908, Nov. 2013.

[16] J. N. Clifford, A. Forneli, H. Chen, T. Torres, S. Tan, and E. Palomares, “Co-sensitized DSCs: dye selection criteria for optimized device Voc and efficiency,” *J. Mater. Chem.*, vol. 21, no. 6, p. 1693, Jan. 2011.

[17] M. Kimura, H. Nomoto, N. Masaki, and S. Mori, “Dye molecules for simple co-sensitization process: fabrication of mixed-dye-sensitized solar cells.,” *Angew. Chem. Int. Ed. Engl.*, vol. 51, no. 18, pp. 4371–4, Apr. 2012.

[18] L. Jin, Z. L. Ding, and D. J. Chen, “Zinc octacarboxylic phthalocyanine/lutein dyads co-adsorbed nanocrystalline TiO2 electrode: enhancement in photovoltaic performance of dye-sensitized solar cells,” *J. Mater. Sci.*, vol. 48, no. 14, pp. 4883–4891, Mar. 2013.

[19] Y. Chen, Z. Zeng, C. Li, W. Wang, X. Wang, and B. Zhang, “Highly efficient co-sensitization of nanocrystalline TiO2 electrodes with plural organic dyes,” *New J. Chem.*, vol. 29, no. 6, p. 773, 2005.

[20] D. Kuang *et al.*, “Co-sensitization of organic dyes for efficient ionic liquid electrolyte-based dye-sensitized solar cells.,” *Langmuir*, vol. 23, no. 22, pp. 10906–9, Oct. 2007.

[21] W. Wu, F. Meng, J. Li, X. Teng, and J. Hua, “Co-sensitization with near-IR absorbing cyanine dye to improve photoelectric conversion of dye-sensitized solar cells,” *Synth. Met.*, vol. 159, no. 11, pp. 1028–1033, 2009.

[22] K.-M. Lee *et al.*, “Co-sensitization promoted light harvesting for plastic dye-sensitized solar cells,” *J. Power Sources*, vol. 196, no. 4, pp. 2416–2421, 2011.

[23] P. Ravirajan *et al.*, "Hybrid Polymer/Zinc Oxide Photovoltaic Devices with Vertically Oriented ZnO Nanorods and an Amphiphilic Molecular Interface Layer," *J. Phys. Chem. B*, vol. 110, no. 15, pp. 7635–7639, Apr. 2006.

[24] H. J. Snaith, "Perovskites: The Emergence of a New Era for Low-Cost, High-Efficiency Solar Cells," *J. Phys. Chem. Lett.*, vol. 4, no. 21, pp. 3623–3630, Nov. 2013.

[25] M. H. Kumar *et al.*, "Flexible, low-temperature, solution processed ZnO-based perovskite solid state solar cells," *Chem. Commun.*, vol. 49, no. 94, p. 11089, 2013.

[26] N. G. Park, "Organometal perovskite light absorbers toward a 20% efficiency low-cost solid-state mesoscopic solar cell," *J. Phys. Chem. Lett.*, vol. 4, no. 15, pp. 2423–2429, 2013.

[27] T. A. Berhe *et al.*, "Organometal halide perovskite solar cells: degradation and stability," *Energy Environ. Sci.*, vol. 9, p. Advance Article, 2016.

[28] N. Elumalai, M. Mahmud, D. Wang, and A. Uddin, "Perovskite Solar Cells: Progress and Advancements," *Energies*, vol. 9, no. 11, p. 861, 2016.

[29] J. Burschka *et al.*, "Sequential deposition as a route to high-performance perovskite-sensitized solar cells," *Nature*, vol. 499, no. 7458, pp. 316–319, Jul. 2013.

[30] M. Liu, M. B. Johnston, and H. J. Snaith, "Efficient planar heterojunction perovskite solar cells by vapour deposition," *Nature*, vol. 501, no. 7467, pp. 395–398, Sep. 2013.

[31] D. B. Mitzi, "Organic-inorganic perovskites containing trivalent metal halide layers:

The templating influence of the organic cation layer," *Inorg. Chem.*, vol. 39, no. 26, pp. 6107–6113, 2000.

[32] D. B. Mitzi, "Thin-film deposition of organic-inorganic hybrid materials," *Chem. Mater.*, vol. 13, no. 10, pp. 3283–3298, 2001.

[33] B. O'Regan and M. Grätzel, "A low-cost, high-efficiency solar cell based on dye-sensitized colloidal TiO2 films," *Nature*, vol. 353, no. 6346, pp. 737–740, Oct. 1991.

[34] H. Tributsch, "Dye sensitization solar cells: A critical assessment of the learning curve," *Coord. Chem. Rev.*, vol. 248, no. 13–14, pp. 1511–1530, 2004.

[35] A. Tiwari and M. Snure, "Synthesis and characterization of ZnO nano-plant-like electrodes.," *J. Nanosci. Nanotechnol.*, vol. 8, no. 8, pp. 3981–7, Aug. 2008.

[36] F. Gao *et al.*, "Enhance the optical absorptivity of nanocrystalline TiO2 film with high molar extinction coefficient ruthenium sensitizers for high performance dye-sensitized solar cells," *J. Am. Chem. Soc.*, vol. 130, no. 32, pp. 10720–10728, 2008.

[37] A. Hagfeldt and M. Grätzel, "Molecular photovoltaics," *Acc. Chem. Res.*, vol. 33, no. 5, pp. 269–277, 2000.

[38] B. O'Regan, F. Lenzmann, R. Muis, and J. Wienke, "A Solid-State Dye-Sensitized Solar Cell Fabricated with Pressure-Treated P25−TiO 2 and CuSCN: Analysis of Pore Filling and IV Characteristics," *Chem. Mater.*, vol. 14, no. 12, pp. 5023–5029, Dec. 2002.

[39] J. Hagen *et al.*, "Novel hybrid solar cells consisting of inorganic nanoparticles and an organic hole transport material," *Synth. Met.*, vol. 89, no. 3, pp. 215–220, Sep.

1997.

[40] K. Murakoshi, R. Kogure, Y. Wada, and S. Yanagida, “Fabrication of solid-state dye-sensitized TiO2 solar cells combined with polypyrrole,” *Sol. Energy Mater. Sol. Cells*, vol. 55, no. 1–2, pp. 113–125, 1998.

[41] T. Taguchi, X. Zhang, I. Sutanto, K. Tokuhiro, and T. N. Rao, “Improving the performance of solid-state dye-sensitized solar cell using MgO-coated TiO 2 nanoporous film,” *Chem. Comm.*, pp. 2480–2481, 2003.

[42] Z. Lan, J. Wu, D. Wang, S. Hao, J. Lin, and Y. Huang, “Quasi-solid-state dye-sensitized solar cells based on a sol-gel organic-inorganic composite electrolyte containing an organic iodide salt,” *Sol. Energy*, vol. 81, no. 1, pp. 117–122, 2007.

[43] L. Han, N. Koide, Y. Chiba, and T. Mitate, “Modeling of an equivalent circuit for dye-sensitized solar cells,” *Appl. Phys. Lett.*, vol. 84, no. 13, pp. 2433–2435, 2004.

[44] Q. Wang, J.-E. Moser, and M. Grätzel, “Electrochemical impedance spectroscopic analysis of dye-sensitized solar cells.,” *J. Phys. Chem. B*, vol. 109, no. 31, pp. 14945–53, 2005.

[45] “DSSC: Dye Sensitized Solar Cells Basic Principles and Measurements.”

[46] M. K. Nazeeruddin *et al.*, “Conversion of Light to Electricity by SCN-) on Nanocrystalline Ti02 Electrodes,” *J. Am. Chem. Soc.*, vol. 115, no. 4, pp. 6382–6390, 1993.

[47] M. K. Nazeeruddin, P. Péchy, and M. Grätzel, “Efficient panchromatic sensitization of nanocrystalline TiO2 films by a black dye based on a trithiocyanato-ruthenium

complex," *Chem. Commun.*, vol. 1, no. 18, pp. 1705–1706, 1997.

[48] M. K. Nazeeruddin *et al.*, "Engineering of efficient panchromatic sensitizers for nanocrystalline TiO2-based solar cells," *J. Am. Chem. Soc.*, vol. 123, no. 8, pp. 1613–1624, 2001.

[49] Y. Chiba, A. Islam, Y. Watanabe, R. Komiya, N. Koide, and L. Han, "Dye-sensitized solar cells with conversion efficiency of 11.1%," *Japanese J. Appl. Physics, Part 2 Lett.*, vol. 45, no. 24–28, pp. 23–26, 2006.

[50] M. Grätzel, "Recent Advances ins sensitized Mesoscopic Solar Cells," *Acc. Chem. Res.*, vol. 42, no. 11, pp. 1788–1798, 2009.

[51] S. Hwang *et al.*, "A highly efficient organic sensitizer for dye-sensitized solar cells," *Chem. Commun.*, no. 46, p. 4887, 2007.

[52] N.-G. Park, J. van de Lagemaat, and a J. Frank, "Comparison of Dye-Sensitized Rutile- and Anatase-Based TiO2 Solar Cells," *J. Phys. Chem. B*, vol. 104, no. 38, pp. 8989–8994, 2000.

[53] M. Grätzel, "Visible Light Sensitization by cis-Bis(thiocyanato)bis(2,2'-bipyridal-4,4'-dicarboxylato)ruthenium(II) of a Transparent Nanocrystalline ZnO Film Prepared by Sol-Gel Techniques," *Chem. Mater.*, vol. 6, no. 5, pp. 686–691, 1994.

[54] J. Qian *et al.*, "TiO2-coated multilayered SnO2 hollow microspheres for dye-sensitized solar cells," *Adv. Mater.*, vol. 21, no. 36, pp. 3663–3667, 2009.

[55] Y. Fukai, Y. Kondo, S. Mori, and E. Suzuki, "Highly efficient dye-sensitized SnO2 solar cells having sufficient electron diffusion length," *Electrochem. commun.*, vol.

9, no. 7, pp. 1439–1443, 2007.

[56] B. Tan, E. Toman, Y. Li, and Y. Wu, “Zinc stannate (Zn2SnO4) dye-sensitized solar cells,” *J. Am. Chem. Soc.*, vol. 129, no. 14, pp. 4162–4163, 2007.

[57] L. Huang, L. Jiang, and M. Wei, “Metal-free indoline dye sensitized solar cells based on nanocrystalline Zn2SnO4,” *Electrochem. commun.*, vol. 12, no. 2, pp. 319–322, 2010.

[58] I. Hamberg and C. G. Granqvist, “Evaporated Sn-doped In2O3 films: Basic optical properties and applications to energy-efficient windows,” *J. Appl. Phys.*, vol. 60, no. 11, 1986.

[59] S. Ngamsinlapasathian, T. Sreethawong, Y. Suzuki, and S. Yoshikawa, “Doubled layered ITO/SnO2 conducting glass for substrate of dye-sensitized solar cells,” *Sol. Energy Mater. Sol. Cells*, vol. 90, no. 14, pp. 2129–2140, 2006.

[60] M. Adachi, Y. Murata, J. Takao, J. Jiu, M. Sakamoto, and F. Wang, “Highly Efficient Dye-Sensitized Solar Cells with a Titania Thin-Film Electrode Composed of a Network Structure of Single-Crystal-like TiO 2 Nanowires Made by the ‘Oriented Attachment’ Mechanism,” *J. Am. Chem. Soc.*, vol. 126, no. 45, pp. 14943–14949, Nov. 2004.

[61] M. Law, L. E. Greene, J. C. Johnson, R. Saykally, and P. Yang, “Nanowire dye-sensitized solar cells,” *Nat. Mater.*, vol. 4, no. 6, pp. 455–459, Jun. 2005.

[62] K. Tennakone, G. R. R. A. Kumara, A. R. Kumarasinghe, K. G. U. Wijayantha, and P. M. Sirimanne, “A Dye-sensitized Nano-porous Solid-state Photovoltaic Cell,”

Semicond. Sci. Technol., vol. 10, no. 12, pp. 1689–1693, 1995.

[63] B. O'Regan and D. T. Schwartz, "Efficient Photo-Hole Injection from Adsorbed Cyanine Dyes into Electrodeposited Copper(1) Thiocyanate Thin Films," *Chem. Mater.*, vol. 7, no. 1, pp. 1349–1354, 1995.

[64] G. R. A. Kumara, S. Kaneko, M. Okuya, and K. Tennakone, "Fabrication of dye-sensitized solar cells using triethylamine hydrothiocyanate as a CuI crystal growth inhibitor," *Langmuir*, vol. 18, no. 26, pp. 10493–10495, 2002.

[65] R. Hazen, "Perovskites," *Scientific American*, vol. 6. pp. 52–61, 1988.

[66] M. I. Ahmed, A. Habib, and S. S. Javaid, "Perovskite Solar Cells : Potentials , Challenges , and Opportunities," *Int. J. Photoenergy*, vol. 2015, 2015.

[67] H.-S. Kim *et al.*, "Lead iodide perovskite sensitized all-solid-state submicron thin film mesoscopic solar cell with efficiency exceeding 9%.," *Sci. Rep.*, vol. 2, no. 7436, p. 591, 2012.

[68] S. S. M. Abstracts, *214 th ECS Meeting Abstracts Pacific Rim Meeting on Electrochemical and*. 2008.

[69] G. Peng, X. Xu, and G. Xu, "Hybrid Organic-Inorganic Perovskites Open a New Era for Low-Cost, High Efficiency Solar Cells," *J. Nanomater.*, vol. 2015, pp. 1–10, 2015.

[70] J.-H. Im, C.-R. Lee, J.-W. Lee, S.-W. Park, and N.-G. Park, "6.5% efficient perovskite quantum-dot-sensitized solar cell," *Nanoscale*, vol. 3, no. 10, p. 4088, 2011.

[71] I. Chung, B. Lee, J. He, R. P. H. Chang, and M. G. Kanatzidis, “All-solid-state dye-sensitized solar cells with high efficiency,” *Nature*, vol. 485, no. 7399, pp. 486–489, May 2012.

[72] B. E. Hardin, H. J. Snaith, and M. D. McGehee, “The renaissance of dye-sensitized solar cells,” *Nat. Photonics*, vol. 6, no. 3, pp. 162–169, Feb. 2012.

[73] F. Hao, C. C. Stoumpos, D. H. Cao, R. P. H. Chang, and M. G. Kanatzidis, “Lead-free solid-state organic–inorganic halide perovskite solar cells,” *Nat. Photonics*, vol. 8, no. 6, pp. 489–494, May 2014.

[74] M. Grätzel *et al.*, “Solid-state dye-sensitized mesoporous TiO2 solar cells with high photon-to-electron conversion efficiencies,” *Nature*, vol. 395, no. 6702, pp. 583–585, Oct. 1998.

[75] M. M. Lee, J. Teuscher, T. Miyasaka, T. N. Murakami, and H. J. Snaith, “Efficient Hybrid Solar Cells Based on Meso-Superstructured Organometal Halide Perovskites,” *Science (80-.).*, vol. 338, no. 6107, pp. 643–647, Nov. 2012.

[76] J. M. Ball, M. M. Lee, A. Hey, and H. J. Snaith, “Low-temperature processed meso-superstructured to thin-film perovskite solar cells,” *Energy Environ. Sci.*, vol. 6, no. 6, p. 1739, 2013.

[77] J. H. Noh, S. H. Im, J. H. Heo, T. N. Mandal, and S. Il Seok, “Chemical management for colorful, efficient, and stable inorganic-organic hybrid nanostructured solar cells,” *Nano Lett.*, vol. 13, no. 4, pp. 1764–1769, 2013.

[78] P. Qin *et al.*, “Inorganic hole conductor-based lead halide perovskite solar cells with

12.4% conversion efficiency," *Nat Commun*, vol. 5, no. May, pp. 1–6, 2014.

[79] T. Song *et al.*, "Perovskite solar cells: film formation and properties," *J. Mater. Chem. A*, vol. 3, no. 17, pp. 9032–9050, 2015.

[80] N. J. Jeon, J. H. Noh, Y. C. Kim, W. S. Yang, S. Ryu, and S. Il Seok, "Solvent engineering for high-performance inorganic–organic hybrid perovskite solar cells," *Nat. Mater.*, vol. 13, no. 9, pp. 897–903, Jul. 2014.

[81] H. Zhou *et al.*, "Interface engineering of highly efficient perovskite solar cells," *Science (80-.).*, vol. 345, no. 6196, pp. 542–546, Aug. 2014.

[82] R. F. Service, "Perovskite Solar Cells Keep On Surging," *Science (80-.).*, vol. 344, no. 6183, pp. 458–458, May 2014.

[83] J.-Y. Jeng *et al.*, "CH 3 NH 3 PbI 3 Perovskite/Fullerene Planar-Heterojunction Hybrid Solar Cells," *Adv. Mater.*, vol. 25, no. 27, pp. 3727–3732, Jul. 2013.

[84] J. You *et al.*, "Low-Temperature Solution-Processed Perovskite Solar Cells with High Efficiency and Flexibility," *ACS Nano*, vol. 8, no. 2, pp. 1674–1680, Feb. 2014.

[85] P. Docampo, J. M. Ball, M. Darwich, G. E. Eperon, and H. J. Snaith, "Efficient organometal trihalide perovskite planar-heterojunction solar cells on flexible polymer substrates.," *Nat. Commun.*, vol. 4, p. 2761, 2013.

[86] Z.-L. Tseng, C.-H. Chiang, and C.-G. Wu, "Surface Engineering of ZnO Thin Film for High Efficiency Planar Perovskite Solar Cells.," *Sci. Rep.*, vol. 5, p. 13211, 2015.

[87] Z. Xiao *et al.*, “Efficient, high yield perovskite photovoltaic devices grown by interdiffusion of solution-processed precursor stacking layers,” *Energy Environ. Sci.*, vol. 7, no. 8, p. 2619, 2014.

[88] J. You *et al.*, “Improved air stability of perovskite solar cells via solution-processed metal oxide transport layers,” *Nat. Nanotechnol.*, vol. 11, no. October, pp. 1–8, 2015.

[89] “2016-Stability of PSC.” .

[90] N. G. Park, “Perovskite solar cells: An emerging photovoltaic technology,” *Mater. Today*, vol. 18, no. 2, pp. 65–72, 2015.

[91] J. You *et al.*, “A polymer tandem solar cell with 10.6% power conversion efficiency.,” *Nat. Commun.*, vol. 4, p. 1446, 2013.

[92] J. Y. Kim *et al.*, “Efficient Tandem Polymer Solar Cells Fabricated by All-Solution Processing,” *Science (80-.).*, vol. 317, no. 5835, pp. 222–225, Jul. 2007.

[93] M. A. Green, “Silicon wafer-based tandem cells: The ultimate photovoltaic solution?,” 2014, p. 89810L.

[94] A. A. Zhumekenov, M. I. Saidaminov, and O. M. Bakr, “Perovskite Single Crystals: Synthesis, Properties and Devices,” 2018, pp. 241–283.

[95] C. Sleigh, A. P. Pijpers, A. Jaspers, B. Coussens, and R. J. Meier, “On the determination of atomic charge via ESCA including application to organometallics,” *J. Electron Spectros. Relat. Phenomena*, vol. 77, no. 1, pp. 41–57, Feb. 1996.

[96] D. Gonbeau, C. Guimon, G. Pfister-Guillouzo, A. Levasseur, G. Meunier, and R. Dormoy, “XPS study of thin films of titanium oxysulfides,” *Surf. Sci.*, vol. 254, no. 1–3, pp. 81–89, Aug. 1991.

[97] A. K. L. Sajjad, S. Shamaila, B. Tian, F. Chen, and J. Zhang, “Comparative studies of operational parameters of degradation of azo dyes in visible light by highly efficient WOx/TiO2 photocatalyst,” *J. Hazard. Mater.*, vol. 177, no. 1–3, pp. 781–791, May 2010.

[98] S. Bai *et al.*, “Improvement of TiO2 photocatalytic properties under visible light by WO3/TiO2 and MoO3/TiO2 composites,” *Appl. Surf. Sci.*, vol. 338, pp. 61–68, May 2015.

[99] S. A. K. Leghari, S. Sajjad, F. Chen, and J. Zhang, “WO3/TiO2 composite with morphology change via hydrothermal template-free route as an efficient visible light photocatalyst,” *Chem. Eng. J.*, vol. 166, no. 3, pp. 906–915, Feb. 2011.

[100] R. P. Netterfield, P. J. Martin, C. G. Pacey, W. G. Sainty, D. R. McKenzie, and G. Auchterlonie, “Ion-assisted deposition of mixed TiO 2 -SiO 2 films,” *J. Appl. Phys.*, vol. 66, no. 4, pp. 1805–1809, Aug. 1989.

[101] U. Mehmood, “Efficient and economical dye-sensitized solar cells based on graphene/TiO2 nanocomposite as a photoanode and graphene as a Pt-free catalyst for counter electrode,” *Org. Electron.*, vol. 42, pp. 187–193, Mar. 2017.

[102] H. Perron *et al.*, “Combined investigation of water sorption on TiO2 rutile (110) single crystal face: XPS vs. periodic DFT,” *Surf. Sci.*, vol. 601, no. 2, pp. 518–527,

Jan. 2007.

[103] W. GRUNERT, “Reduction behavior and metathesis activity of WO3/Al2O3 catalysts I. An XPS investigation of WO3/Al2O3 catalysts,” *J. Catal.*, vol. 107, no. 2, pp. 522–534, Oct. 1987.

[104] A. Katrib, F. Hemming, P. Wehrer, L. Hilaire, and G. Maire, “The multi-surface structure and catalytic properties of partially reduced WO3, WO2 and WC + O2 or W + O2 as characterized by XPS,” *J. Electron Spectros. Relat. Phenomena*, vol. 76, pp. 195–200, Dec. 1995.

[105] S. Nakade, Y. Saito, W. Kubo, T. Kitamura, Y. Wada, and S. Yanagida, “Influence of TiO 2 Nanoparticle Size on Electron Diffusion and Recombination in Dye-Sensitized TiO 2 Solar Cells,” *J. Phys. Chem. B*, vol. 107, no. 33, pp. 8607–8611, Aug. 2003.

[106] T. P. Chou, Q. Zhang, B. Russo, G. E. Fryxell, and G. Cao, “Titania Particle Size Effect on the Overall Performance of Dye-Sensitized Solar Cells,” *J. Phys. Chem. C*, vol. 111, no. 17, pp. 6296–6302, May 2007.

[107] F. Gracia, J. P. Holgado, and A. R. González-Elipe, “Photoefficiency and Optical, Microstructural, and Structural Properties of TiO 2 Thin Films Used as Photoanodes,” *Langmuir*, vol. 20, no. 5, pp. 1688–1697, Mar. 2004.

[108] B. A. Gregg, F. Pichot, S. Ferrere, and C. L. Fields, “Interfacial Recombination Processes in Dye-Sensitized Solar Cells and Methods To Passivate the Interfaces,” *J. Phys. Chem. B*, vol. 105, no. 7, pp. 1422–1429, Feb. 2001.

[109] R. Sanjinés, H. Tang, H. Berger, F. Gozzo, G. Margaritondo, and F. Lévy, "Electronic structure of anatase TiO 2 oxide," *J. Appl. Phys.*, vol. 75, no. 6, pp. 2945–2951, Mar. 1994.

[110] D. Shuttleworth, "Preparation of metal-polymer dispersions by plasma techniques. An ESCA investigation," *J. Phys. Chem.*, vol. 84, no. 12, pp. 1629–1634, Jun. 1980.

[111] B. Qiu *et al.*, "Facile synthesis of the Ti3+ self-doped TiO2-graphene nanosheet composites with enhanced photocatalysis," *Sci. Rep.*, vol. 5, no. 1, p. 8591, Jul. 2015.

[112] S. A. Ganiyu, O. Muraza, A. S. Hakeem, K. Alhooshani, and M. A. Atieh, "Carbon nanostructures grown on 3D silicon carbide foams: Role of intermediate silica layer and metal growth," *Chem. Eng. J.*, vol. 258, pp. 110–118, Dec. 2014.

[113] A. B. K. Chen, S. G. Kim, Y. Wang, W.-S. Tung, and I.-W. Chen, "A size-dependent nanoscale metal–insulator transition in random materials," *Nat. Nanotechnol.*, vol. 6, no. 4, pp. 237–241, Apr. 2011.

[114] U. Mehmood, S. Ahmed, I. A. Hussein, and K. Harrabi, "Co-sensitization of TiO2-MWCNTs hybrid anode for efficient dye-sensitized solar cells," *Electrochim. Acta*, vol. 173, pp. 607–612, 2015.

[115] M. Hasanuzzaman, N. A. Rahim, R. Saidur, and S. N. Kazi, "Energy savings and emissions reductions for rewinding and replacement of industrial motor," *Energy*, vol. 36, no. 1, pp. 233–240, Jan. 2011.

[116] M. Hasanuzzaman, N. A. Rahim, M. Hosenuzzaman, R. Saidur, I. M. Mahbubul,

and M. M. Rashid, “Energy savings in the combustion based process heating in industrial sector,” *Renew. Sustain. Energy Rev.*, vol. 16, no. 7, pp. 4527–4536, Sep. 2012.

[117] U. Mehmood, I. A. Hussein, K. Harrabi, M. B. Mekki, S. Ahmed, and N. Tabet, “Hybrid TiO2–multiwall carbon nanotube (MWCNTs) photoanodes for efficient dye sensitized solar cells (DSSCs),” *Sol. Energy Mater. Sol. Cells*, vol. 140, pp. 174–179, Sep. 2015.

[118] B. V. S. R. Umer Mehmood, Saleem-ur Rahman, Khalil Harrabi, Ibnelwaleed A. Hussein, “Recent Advances in Dye Sensitized Solar Cells,” *Adv. Mater. Sci. Eng.*, vol. 2014, p. 12, 2014.

[119] J. G. Canadell *et al.*, “Contributions to accelerating atmospheric CO2 growth from economic activity, carbon intensity, and efficiency of natural sinks,” *Proc. Natl. Acad. Sci.*, vol. 104, no. 47, pp. 18866–18870, Nov. 2007.

[120] M.-Q. Yang, N. Zhang, M. Pagliaro, and Y.-J. Xu, “Artificial photosynthesis over graphene–semiconductor composites. Are we getting better?,” *Chem. Soc. Rev.*, vol. 43, no. 24, pp. 8240–8254, Sep. 2014.

[121] K. W. J. Barnham, M. Mazzer, and B. Clive, “Resolving the energy crisis: nuclear or photovoltaics?,” *Nat. Mater.*, vol. 5, no. 3, pp. 161–164, Mar. 2006.

[122] J. Yan and B. R. Saunders, “Third-generation solar cells: a review and comparison of polymer:fullerene, hybrid polymer and perovskite solar cells,” *RSC Adv.*, vol. 4, no. 82, pp. 43286–43314, 2014.

[123] M. Bashir *et al.*, “Performance investigation of photovoltaic modules by back surface water cooling,” *Therm. Sci.*, no. 00, pp. 290–290, 2016.

[124] M.-E. Yeoh and K.-Y. Chan, “Recent advances in photo-anode for dye-sensitized solar cells: a review,” *Int. J. Energy Res.*, vol. 41, no. 15, pp. 2446–2467, Dec. 2017.

[125] W. Wei, D. J. Stacchiola, and Y. H. Hu, “3D graphene from CO 2 and K as an excellent counter electrode for dye-sensitized solar cells,” *Int. J. Energy Res.*, vol. 41, no. 15, pp. 2502–2508, Dec. 2017.

[126] F. Bella, E. D. Ozzello, S. Bianco, and R. Bongiovanni, “Photo-polymerization of acrylic/methacrylic gel–polymer electrolyte membranes for dye-sensitized solar cells,” *Chem. Eng. J.*, vol. 225, pp. 873–879, Jun. 2013.

[127] M. Gerosa *et al.*, “Toward Totally Flexible Dye-Sensitized Solar Cells Based on Titanium Grids and Polymeric Electrolyte,” *IEEE J. Photovoltaics*, vol. 6, no. 2, pp. 498–505, Mar. 2016.

[128] F. Bella, A. Verna, and C. Gerbaldi, “Patterning dye-sensitized solar cell photoanodes through a polymeric approach: A perspective,” *Mater. Sci. Semicond. Process.*, vol. 73, pp. 92–98, Jan. 2018.

[129] F. Bella, J. Popovic, A. Lamberti, E. Tresso, C. Gerbaldi, and J. Maier, “Interfacial Effects in Solid–Liquid Electrolytes for Improved Stability and Performance of Dye-Sensitized Solar Cells,” *ACS Appl. Mater. Interfaces*, vol. 9, no. 43, pp. 37797–37803, Nov. 2017.

[130] A. M. Ilyas, M. A. Gondal, U. Baig, S. Akhtar, and Z. H. Yamani, “Photovoltaic

performance and photocatalytic activity of facile synthesized graphene decorated TiO 2 monohybrid using nanosecond pulsed ablation in liquid technique," *Sol. Energy*, vol. 137, pp. 246–255, Nov. 2016.

[131] M. A. Gondal, A. M. Ilyas, and U. Baig, "Facile synthesis of silicon carbide-titanium dioxide semiconducting nanocomposite using pulsed laser ablation technique and its performance in photovoltaic dye sensitized solar cell and photocatalytic water purification," *Appl. Surf. Sci.*, vol. 378, pp. 8–14, Aug. 2016.

[132] M. A. Gondal *et al.*, "Synthesis of green TiO 2 /ZnO/CdS hybrid nano-catalyst for efficient light harvesting using an elegant pulsed laser ablation in liquids method," *Appl. Surf. Sci.*, vol. 357, pp. 2217–2222, Dec. 2015.

[133] K. Kakiage, Y. Aoyama, T. Yano, K. Oya, J. Fujisawa, and M. Hanaya, "Highly-efficient dye-sensitized solar cells with collaborative sensitization by silyl-anchor and carboxy-anchor dyes," *Chem. Commun.*, vol. 51, no. 88, pp. 15894–15897, 2015.

[134] G. D. Sharma *et al.*, "Stepwise co-sensitization as a useful tool for enhancement of power conversion efficiency of dye-sensitized solar cells: The case of an unsymmetrical porphyrin dyad and a metal-free organic dye," *Org. Electron.*, vol. 15, no. 7, pp. 1324–1337, Jul. 2014.

[135] J. W. Ondersma and T. W. Hamann, "Recombination and redox couples in dye-sensitized solar cells," *Coord. Chem. Rev.*, vol. 257, no. 9–10, pp. 1533–1543, May 2013.

[136] S. Li *et al.*, “Preparation and performance of dye-sensitized solar cells based on ZnO-modified TiO2 electrodes,” *Int. J. Miner. Metall. Mater.*, vol. 17, no. 1, pp. 92–97, Feb. 2010.

[137] A. S. Nair, R. Jose, Y. Shengyuan, and S. Ramakrishna, “A simple recipe for an efficient TiO2 nanofiber-based dye-sensitized solar cell.,” *J. Colloid Interface Sci.*, vol. 353, no. 1, pp. 39–45, Jan. 2011.

[138] U. Mehmood, S. Ahmed, I. A. Hussein, and K. Harrabi, “Improving the efficiency of Dye sensitized solar cells by TiO2–graphene nanocomposite photoanode,” *Photonics Nanostructures - Fundam. Appl.*, Aug. 2015.

[139] U. Mehmood, S. Rahman, K. Harrabi, I. A. Hussein, and B. V. S. Reddy, “Recent Advances in Dye Sensitized Solar Cells Recent Advances in Dye Sensitized Solar Cells,” no. April, pp. 0–13, 2014.

[140] B. Li, L. Wang, B. Kang, P. Wang, and Y. Qiu, “Review of recent progress in solid-state dye-sensitized solar cells,” *Sol. Energy Mater. Sol. Cells*, vol. 90, no. 5, pp. 549–573, Mar. 2006.

[141] M. Dale, “A Comparative Analysis of Energy Costs of Photovoltaic, Solar Thermal, and Wind Electricity Generation Technologies,” *Appl. Sci.*, vol. 3, no. 2, pp. 325–337, Mar. 2013.

[142] A. N. B. Zulkifili, T. Kento, M. Daiki, and A. Fujiki, “The Basic Research on the Dye-Sensitized Solar Cells (DSSC),” *J. Clean Energy Technol.*, vol. 3, no. 5, pp. 382–387, 2015.

[143] M. Grätzel, “Dye-sensitized solar cells,” *J. Photochem. Photobiol. C Photochem. Rev.*, vol. 4, no. 2, pp. 145–153, Oct. 2003.

[144] K. Zhu, N. R. Neale, A. Miedaner, and A. J. Frank, “Enhanced Charge-Collection Efficiencies and Light Scattering in Dye-Sensitized Solar Cells Using Oriented TiO 2 Nanotubes Arrays,” *Nano Lett.*, vol. 7, no. 1, pp. 69–74, Jan. 2007.

[145] M. A. Gondal, A. M. Ilyas, and U. Baig, “Pulsed laser ablation in liquid synthesis of ZnO/TiO 2 nanocomposite catalyst with enhanced photovoltaic and photocatalytic performance,” *Ceram. Int.*, vol. 42, no. 11, pp. 13151–13160, Aug. 2016.

[146] H. Choi, H. Kim, S. Hwang, W. Choi, and M. Jeon, “Dye-sensitized solar cells using graphene-based carbon nano composite as counter electrode,” *Sol. Energy Mater. Sol. Cells*, vol. 95, no. 1, pp. 323–325, Jan. 2011.

[147] S. S. Jeon, C. Kim, J. Ko, and S. S. Im, “Pt Nanoparticles Supported on Polypyrrole Nanospheres as a Catalytic Counter Electrode for Dye-Sensitized Solar Cells,” *J. Phys. Chem. C*, vol. 115, no. 44, pp. 22035–22039, Nov. 2011.

[148] S. Thomas, T. G. Deepak, G. S. Anjusree, T. A. Arun, S. V. Nair, and A. S. Nair, “A review on counter electrode materials in dye-sensitized solar cells,” *J. Mater. Chem. A*, vol. 2, no. 13, pp. 4474–4490, 2014.

[149] A. Mishra, M. K. R. Fischer, and P. Bäuerle, “Metal-Free Organic Dyes for Dye-Sensitized Solar Cells: From Structure: Property Relationships to Design Rules,” *Angew. Chemie Int. Ed.*, vol. 48, no. 14, pp. 2474–2499, Mar. 2009.

[150] K. Hara *et al.*, "Molecular Design of Coumarin Dyes for Efficient Dye-Sensitized Solar Cells," *J. Phys. Chem. B*, vol. 107, no. 2, pp. 597–606, Jan. 2003.

[151] M. R. Narayan, "Review: Dye sensitized solar cells based on natural photosensitizers," *Renew. Sustain. Energy Rev.*, Sep. 2011.

[152] M. Younas, M. A. Gondal, U. Mehmood, K. Harrabi, Z. H. Yamani, and F. A. Al-Sulaiman, "Performance enhancement of dye-sensitized solar cells via cosensitization of ruthenizer Z907 and organic sensitizer SQ2," *Int. J. Energy Res.*, Jul. 2018.

[153] L. Wang, S.-B. Fang, and Y. Lin, "Novel polymer electrolytes containing chemically crosslinked gelators for dye-sensitized solar cells," *Polym. Adv. Technol.*, vol. 17, no. 7–8, pp. 512–517, Jul. 2006.

[154] J. Wu, Z. Lan, J. Lin, M. Huang, and P. Li, "Effect of solvents in liquid electrolyte on the photovoltaic performance of dye-sensitized solar cells," *J. Power Sources*, vol. 173, no. 1, pp. 585–591, Nov. 2007.

[155] E. Guillén, C. Fernández-Lorenzo, R. Alcántara, J. Martín-Calleja, and J. A. Anta, "Solvent-free ZnO dye-sensitised solar cells," *Sol. Energy Mater. Sol. Cells*, vol. 93, no. 10, pp. 1846–1852, Oct. 2009.

[156] X. Liu, J. Fang, Y. Liu, and T. Lin, "Progress in nanostructured photoanodes for dye-sensitized solar cells," *Front. Mater. Sci.*, vol. 10, no. 3, pp. 225–237, Sep. 2016.

[157] A. K. Chandiran, M. Abdi-Jalebi, M. K. Nazeeruddin, and M. Grätzel, "Analysis of

Electron Transfer Properties of ZnO and TiO 2 Photoanodes for Dye-Sensitized Solar Cells," *ACS Nano*, vol. 8, no. 3, pp. 2261–2268, Mar. 2014.

[158] M. Ye *et al.*, "Recent advances in dye-sensitized solar cells: from photoanodes, sensitizers and electrolytes to counter electrodes," *Mater. Today*, vol. 18, no. 3, pp. 155–162, Apr. 2015.

[159] M. Gillet, K. Aguir, C. Lemire, E. Gillet, and K. Schierbaum, "The structure and electrical conductivity of vacuum-annealed WO3 thin films," *Thin Solid Films*, vol. 467, no. 1–2, pp. 239–246, Nov. 2004.

[160] H. Zheng, Y. Tachibana, and K. Kalantar-zadeh, "Dye-Sensitized Solar Cells Based on WO 3," *Langmuir*, vol. 26, no. 24, pp. 19148–19152, Dec. 2010.

[161] S.-M. Yong, T. Nikolay, B. T. Ahn, and D. K. Kim, "One-dimensional WO3 nanorods as photoelectrodes for dye-sensitized solar cells," *J. Alloys Compd.*, vol. 547, pp. 113–117, Jan. 2013.

[162] N. Prabhu, S. Agilan, N. Muthukumarasamy, and T. S. Senthil, "Enhanced photovoltaic performance of WO3 nanoparticles added dye sensitized solar cells," *J. Mater. Sci. Mater. Electron.*, vol. 25, no. 12, pp. 5288–5295, Dec. 2014.

[163] J. H. Yang, K. H. Kim, C. W. Bark, and H. W. Choi, "Synthesis and Characterization of WO 3 Doped TiO 2 Particle/Nanowire Layer in Dye-Sensitized Solar Cells," *Mol. Cryst. Liq. Cryst.*, vol. 598, no. 1, pp. 32–39, Jul. 2014.

[164] J. Tauc, "Optical properties and electronic structure of amorphous Ge and Si," *Mater. Res. Bull.*, vol. 3, no. 1, pp. 37–46, Jan. 1968.

[165] X. Lü *et al.*, “Improved-Performance Dye-Sensitized Solar Cells Using Nb-Doped TiO 2 Electrodes: Efficient Electron Injection and Transfer,” *Adv. Funct. Mater.*, vol. 20, no. 3, pp. 509–515, Feb. 2010.

[166] M. Yang, D. Kim, H. Jha, K. Lee, J. Paul, and P. Schmuki, “Nb doping of TiO 2 nanotubes for an enhanced efficiency of dye-sensitized solar cells,” *Chem. Commun.*, vol. 47, no. 7, pp. 2032–2034, 2011.

[167] J. G. Nam, Y. J. Park, B. S. Kim, and J. S. Lee, “Enhancement of the efficiency of dye-sensitized solar cell by utilizing carbon nanotube counter electrode,” *Scr. Mater.*, vol. 62, no. 3, pp. 148–150, Feb. 2010.

[168] C. H. Yoon, R. Vittal, J. Lee, W.-S. Chae, and K.-J. Kim, “Enhanced performance of a dye-sensitized solar cell with an electrodeposited-platinum counter electrode,” *Electrochim. Acta*, vol. 53, no. 6, pp. 2890–2896, Feb. 2008.

[169] Z. Zhang *et al.*, “Electrodeposition of nanostructured cobalt selenide films towards high performance counter electrodes in dye-sensitized solar cells,” *RSC Adv.*, vol. 3, no. 37, p. 16528, 2013.

[170] C.-K. Cheng, J.-Y. Lin, K.-C. Huang, T.-K. Yeh, and C.-K. Hsieh, “Enhanced Efficiency of Dye-Sensitized Solar Counter Electrodes Consisting of Two-Dimensional Nanostructural Molybdenum Disulfide Nanosheets Supported Pt Nanoparticles,” *Coatings*, vol. 7, no. 10, p. 167, Oct. 2017.

[171] M. Jacoby, “The future of low-cost solar cells,” *Chem. Eng. News*, vol. 94, no. 18, pp. 30–35, 2016.

[172] M. Z. Iqbal and S. Khan, “Progress in the performance of dye sensitized solar cells by incorporating cost effective counter electrodes,” *Sol. Energy*, vol. 160, pp. 130–152, Jan. 2018.

[173] U. Mehmood, A. Ul Haq Khan, A. Ali Qaiser, S. Bashir, and M. Younas, “Nanocomposites of carbon allotropes with TiO 2 as effective photoanodes for efficient dye-sensitized solar cells,” *Mater. Lett.*, vol. 228, pp. 125–128, Oct. 2018.

[174] M. Younas, M. A. Gondal, M. A. Dastageer, and U. Baig, “Fabrication of cost effective and efficient dye sensitized solar cells with WO3-TiO2 nanocomposites as photoanode and MWCNT as Pt-free counter electrode,” *Ceram. Int.*, Sep. 2018.

[175] S. Iijima, “Helical microtubules of graphitic carbon,” *Nature*, vol. 354, no. 6348, pp. 56–58, 1991.

[176] P. Du *et al.*, “Dye-sensitized solar cells based on anatase TiO2/multi-walled carbon nanotubes composite nanofibers photoanode,” *Electrochim. Acta*, vol. 87, pp. 651–656, Jan. 2013.

[177] J. Wu *et al.*, “Counter electrodes in dye-sensitized solar cells,” *Chem. Soc. Rev.*, vol. 46, no. 19, pp. 5975–6023, 2017.

[178] U. Mehmood *et al.*, “Electrochemical Impedance Spectroscopy and Photovoltaic Analyses of Dye-Sensitized Solar Cells Based on Carbon/TiO 2 Composite Counter Electrode,” *J. Electrochem. Soc.*, vol. 163, no. 5, pp. H339–H342, 2016.

[179] J. M. Nugent, K. S. V. Santhanam, A. Rubio, and P. M. Ajayan, “Fast Electron Transfer Kinetics on Multiwalled Carbon Nanotube Microbundle Electrodes,” *Nano*

Lett., vol. 1, no. 2, pp. 87–91, Feb. 2001.

[180] K. Woan, G. Pyrgiotakis, and W. Sigmund, "Photocatalytic Carbon-Nanotube-TiO 2 Composites," *Adv. Mater.*, vol. 21, no. 21, pp. 2233–2239, Jun. 2009.

[181] Munkhbayar Batmunkh Mark J. Biggs Joseph G. Shapter, "Carbonaceous Dye-Sensitized Solar Cell Photoelectrodes," *Adv. Sci.*, vol. 2, no. 3, p. 16, 2015.

[182] Z. Shi and A. Jayatissa, "Perovskites-Based Solar Cells: A Review of Recent Progress, Materials and Processing Methods," *Materials (Basel).*, vol. 11, no. 5, p. 729, May 2018.

[183] H. Lin, C. Zhou, Y. Tian, T. Siegrist, and B. Ma, "Low-Dimensional Organometal Halide Perovskites," *ACS Energy Lett.*, vol. 3, no. 1, pp. 54–62, Jan. 2018.

[184] D. Shi *et al.*, "Low trap-state density and long carrier diffusion in organolead trihalide perovskite single crystals," *Science (80-.).*, vol. 347, no. 6221, pp. 519–522, Jan. 2015.

[185] V. Belruss, J. Kalnajs, A. Linz, and R. C. Folweiler, "Top-seeded solution growth of oxide crystals from non-stoichiometric melts," *Mater. Res. Bull.*, vol. 6, no. 10, pp. 899–905, Oct. 1971.

[186] M. I. Saidaminov *et al.*, "High-quality bulk hybrid perovskite single crystals within minutes by inverse temperature crystallization," *Nat. Commun.*, vol. 6, no. 1, p. 7586, Dec. 2015.

[187] M. I. Saidaminov, A. L. Abdelhady, G. Maculan, and O. M. Bakr, "Retrograde solubility of formamidinium and methylammonium lead halide perovskites enabling

rapid single crystal growth," *Chem. Commun.*, vol. 51, no. 100, pp. 17658–17661, 2015.

[188] J. M. Kadro, K. Nonomura, D. Gachet, M. Grätzel, and A. Hagfeldt, "Facile route to freestanding CH3NH3PbI3 crystals using inverse solubility," *Sci. Rep.*, vol. 5, no. 1, p. 11654, Dec. 2015.

[189] J.-C. Blancon *et al.*, "Extremely efficient internal exciton dissociation through edge states in layered 2D perovskites," *Science (80-.).*, vol. 355, no. 6331, pp. 1288–1292, Mar. 2017.

[190] A. A. Zhumekenov *et al.*, "The Role of Surface Tension in the Crystallization of Metal Halide Perovskites," *ACS Energy Lett.*, vol. 2, no. 8, pp. 1782–1788, Aug. 2017.

[191] H. Wang and D. H. Kim, "Perovskite-based photodetectors: materials and devices," *Chem. Soc. Rev.*, vol. 46, no. 17, pp. 5204–5236, 2017.

[192] J. Yu *et al.*, "A high-performance self-powered broadband photodetector based on a CH 3 NH 3 PbI 3 perovskite/ZnO nanorod array heterostructure," *J. Mater. Chem. C*, vol. 4, no. 30, pp. 7302–7308, 2016.

[193] "https://www.nrel.gov/pv/assets/images/efficiency-chart.png accessed on 22 Feb 2019."

Vitae

Name	Muhammad Younas
Nationality	Pakistani
Date of Birth	1/3/1988
Email	muhammad.younas006@gmail.com
Address	House#3/III, Street#3, Star Colony, Opposite Government Zamindar College, Bhimber Road Gujrat, Zip code 50700, Pakistan.
Academic Background	Provided below

Academic Profile

2014 – 2019 Doctor of Philosophy (Ph.D.) in Physics

King Fahd University of Petroleum & Minerals, Dhahran, Kingdom of Saudi Arabia

Thesis Title: “Fabrication of perovskite & dye sensitized solar cells and their parametric optimization”.

2008 – 2011 Master of Philosophy (M.Phil.) in Physics

Quaid-i-Azam University Islamabad, Pakistan

Thesis Title: “The Kondo Effect”.

2006 – 2008 Master of Science (M.Sc.) in Physics

University of the Punjab Lahore, Pakistan.

CGPA: 3.93/4.0, Percentage: 87.71%, Grade: A+

Distinction: 1st Position in M.Sc. (Session 2006-2008)

Publications

1. **M. Younas**, M.A. Gondal, U. Mehmood, K. Harrabi, Z.H. Yamani, F.A. Al-Sulaiman, Performance enhancement of dye-sensitized solar cells via cosensitization of ruthenizer Z907 and organic sensitizer SQ2, Int. J. Energy Res. (2018). doi:10.1002/er.4154.
2. **M. Younas**, M.A. Gondal, M.A. Dastageer, U. Baig, Fabrication of cost effective and efficient dye sensitized solar cells with WO3-TiO2 nanocomposites as photoanode and MWCNT as Pt-free counter electrode, Ceram. Int. (2018). doi:10.1016/j.ceramint.2018.09.269.
3. **M. Younas**, M.A. Gondal, M.A. Dastageer, K. Harrabi, Fabrication of cost effective and efficient dye sensitized solar cells with MWCNT-TiO2 nanocomposites as photoanode and MWCNT as Pt-free counter electrode, Solar Energy Volume 188, August 2019, Pages 1178-1188, doi: 10.1016/j.solener.2019.07.009.
4. M. Mansha, **M. Younas**, M. A. Gondal, N. Ullah "1,5-Naphthyridine-based conjugated polymers as co-sensitizers for dye-sensitized solar cells" Dyes and pigments (Under review).
5. **M. Younas**, A. Al-Ahmed, M. A. Gondal, U. Mehmood, FA Al-Sulaiman, K. Harrabi , Highly efficient dye sensitized solar cells based on Single wall carbon nanotube doped titanium dioxide nanocomposites as photoanode and SWCNT as Pt-free counter electrode (ready for submission).

6. **M. Younas**, A. Al-Ahmed, M. A. Gondal, A. Helal, FA Al-Sulaiman, "Dye sensitiezed solar cells Photoanode modificaiton using MOFs" (ready for submission).
7. **M. Younas**, A. Al-Ahmed, M. A. Gondal, FA Al-Sulaiman, "Dye sensitiezed solar cells study using novel two metal-complex dye" (ready for submission).
8. **M. Younas**, T. N. Baroud, M. A. Gondal, M.A. Dastageer"Pore size and pore volume of CE electrode mesoporous carbon material's effect on the performance of Dye sensitized Solar cells" (ready for submission).
9. **M. Younas**, M. A. Gondal "Fabrication of carbon based efficient and cost effective perovskit solar cells" (Manuscript in prepartion).